Measurement of D Meson Production

Probing QCD and LFV τ decay with the ATLAS detector

Edwin Yun Sang Chow

ISBN: 978-90-834422-1-1

Measurement of *D* Meson Production
Probing QCD and LFV τ decay with the ATLAS detector

Thesis, Radboud University Nijmegen

Cover design: Chloe Xu

Printing: proefschriftenprinten.nl

This work has been performed at the National Institute for Subatomic Physics (Nikhef) which is funded by the Dutch Research Council (NWO). The research was financially supported by the NWO Innovational Research Incentives Scheme (Vici).

Measurement of D Meson Production

Probing QCD and LFV τ decay with the ATLAS detector

Proefschrift ter verkrijging van de graad van doctor
aan de Radboud Universiteit Nijmegen
op gezag van de rector magnificus prof. dr. J.M. Sanders,
volgens besluit van het college voor promoties
in het openbaar te verdedigen

op maandag 26 augustus 2024
om 14.30 uur precies

door

Edwin Yun Sang Chow

geboren op 22 april 1993
te Hong Kong

Promotor:	Prof. dr. N. de Groot
Copromotor:	Dr. ir. P. Kluit (Nikhef)
Manuscriptcommissie:	Prof. dr. B. Krishnan Dr. F. Filthaut Dr. C. F. Galea Dr. K. Vos (Maastricht University) Prof. dr. W. Verkerke (Universiteit van Amsterdam)

Contents

Introduction

Physics - perhaps that is the most ambitious dream of human beings. The word physics comes from Ancient Greek; it means the knowledge of nature. Over the past centuries, physics theories have been proven successful in unfolding the laws of nature. Modern physics offers explanations for a wide range of phenomena, from tiny processes like the neutron decay to colossal events like the merging of black holes. The development of physics has given rise to many technologies and innovations that revolutionized the world. Despite the success so far, humanity is not satisfied with just *some* knowledge of nature; the dream is to understand *everything* of nature.

Particle physics is a field of study that pushes such an ambition to the extreme. Within particle physics, matter and fundamental forces are modelled by fundamental particles and their interaction. The ultimate objective is to build a theory that describes all matter, all the interactions and the Universe, revealing the complete set of the laws of nature; such theory is called the Theory of Everything (TOE).

Currently, the state-of-the-art theory is the Standard Model, which provides an excellent description of three out of the four fundamental forces, including the strong force, the weak force and the electromagnetic force. While the current theory offers valuable insights, it has notable limitations, leaving questions unanswered. For instance, the Standard Model does not account for neutrino masses, baryogenesis, or gravity. To construct a more comprehensive theory, extensions to the Standard Model are essential. In the quest for a theory beyond the Standard Model, experimental tests are crucial for distinguishing between competing theories. It is especially important to test these theories in areas where the most significant disagreements arise. Among various phenomena, neutrino oscillation and lepton flavor violation stand out, showing some of the most pronounced deviations between the Standard Model and extended theories.

Besides seeking extensions to the Standard Model, experimental input is also necessary for precise description of physical phenomena. For instance, quantum chromodynamics, the theory that describes quarks, suffers from large uncertainties because of the non-perturbative nature of the strong force. Experimental measurements are therefore particularly important to provide feedback to the theory.

In light of the motivations presented above, the $D_s^{\pm}$ meson emerges as a valuable candidate for research. Firstly, the $D_s^{\pm}$ meson is abundantly produced in hadron colliders. This allows for the study of quark production, hadronization and the decay of B mesons into the $D_s^{\pm}$ meson. Moreover, the $D_s^{\pm}$ meson also has a significant branching fraction to the τ lepton, serving as a reliable source of τ lepton for lepton flavour violation searches.

This thesis presents the work on the measurement of $D^{\pm}$ and $D_s^{\pm}$ meson production using the rare decay $D \to \phi(\mu\mu)\pi$, and the prospect of using the $D_s^{\pm}$ meson as a source for τ lepton flavour violation searches with the ATLAS experiment. This thesis consists of five chapters as follows:

- **Chapter 1** describes the theoretical frameworks: the Standard Model of particle physics and various beyond the Standard Model theories. To highlight the need for a more comprehensive model, the limitations of the Standard Model are discussed. Neutrino mixing, hypothetical sterile neutrinos and lepton flavour violation are also presented.
- **Chapter 2** describes the Large Hadron Collider and the ATLAS detector located at CERN. The design and the structure of the detector are presented layer-by-layer.
- **Chapter 3** describes the particle detection and reconstruction algorithms used by the ATLAS experiment. The definition of the physics objects and the performance of the algorithms are presented.
- **Chapter 4 and 5** describe the measurement of $D^{\pm}$ and $D_s^{\pm}$ meson production with the ATLAS experiment. The result is also compared to state-of-the-art theoretical predictions.
- **Chapter 6** describes the prospect of searches for the lepton-flavour-violating $D_s^{\pm} \to \tau(3\mu)\nu$ decay with the ATLAS experiment.

The measurements described in Chapter 4 and 5 are the original work of the author; the results have not been published in any other format at the time of writing. The prospect study in Chapter 6 is a review and extension of the previous work in the ATLAS collaboration.

Chapter 1.

The Standard Model and Beyond

1.1. The Standard Model

The Standard Model of particle physics (SM) [1–4] is a quantum field theory that describes the physics of the fundamental particles and their interactions. Except for the gravitational interaction, the other three out of the four fundamental interactions (i.e. the electromagnetic interaction, the weak interaction and the strong interaction) are well described by the SM.

1.1.1. Fundamental Particles

The SM introduces 17 fundamental particles, which are not composed of other particles. The fundamental particles are divided into fermions, which are the constituents of matter; and bosons, which are the force carriers. Figure 1.1 shows all the fundamental particles with their basic properties.

Fermions

Particles with half-integer spin are fermions (f), which can be grouped into quarks (q) and leptons (l) according to their charge or the interactions that they are involved in. Both quarks and leptons are spin-1/2 particles with different masses.

Quarks are further classified into three generations, with two flavours per generations, for a total of six flavours. All six flavours of quarks carry color charge and electric charge. The first-generation includes the up (u) and down (d) quarks, which are the lightest quarks. The second-generation includes the charm (c) and strange (s) quarks, which are heavier than the first-generation quarks. The third-generation includes the top (t) and bottom (b) quarks, which are the heaviest quarks; the top quark is also the heaviest fundamental particle in the SM.

Analogous to quarks, leptons are further classified into three generations, with an electrically charged lepton and an electrically neutral lepton per generation. On the other

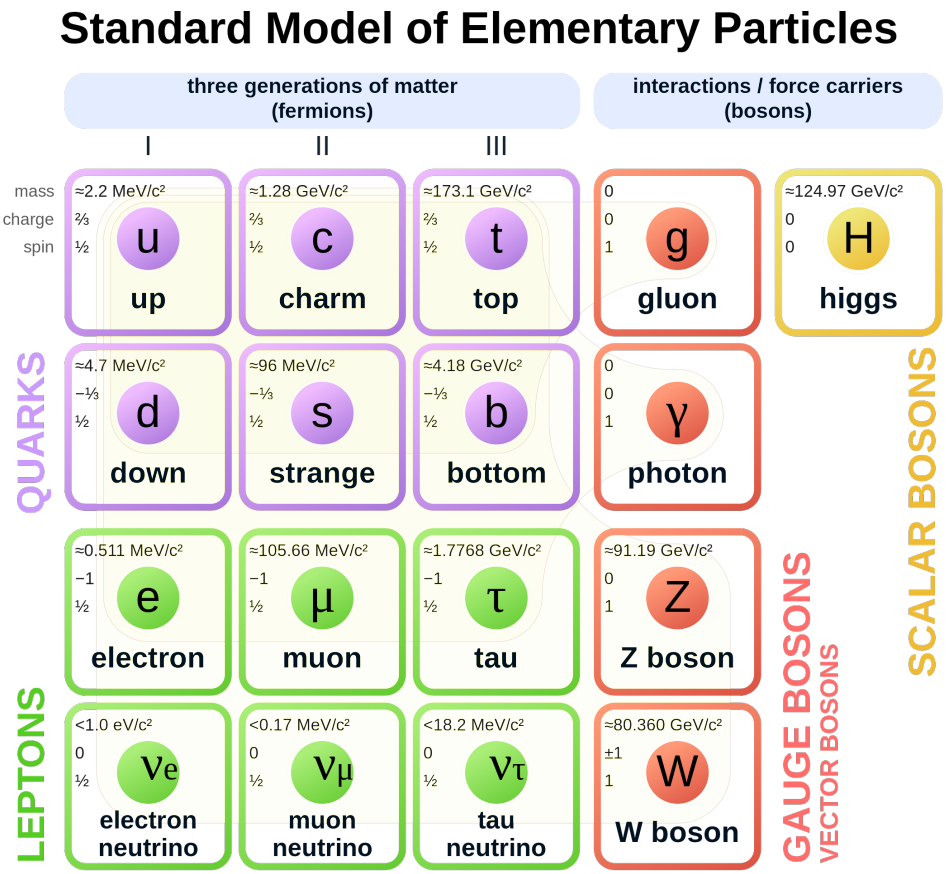

Figure 1.1.: Fundamental particles in the Standard Model, grouped into different sectors. The mass, electric charge and spin are also shown for each particle [5].

hand, leptons are distinct from quarks in that they carry no color charge. The electrically charged leptons are referred to as charged leptons while the electrically uncharged leptons are referred to as neutrinos (ν); the charged lepton and neutrino pair in the same generation have a corresponding flavour. Listing from the first-generation to the third-generation, the charged leptons are: the electron (e), the muon (μ) and the tau (τ); the corresponding neutrinos are: the electron neutrino (ν_e), the muon neutrino (ν_μ), and the tau neutrino (ν_τ).

Bosons

Particles with integer spin are bosons; fundamental bosons can either be spin-0 or spin-1. In the SM, spin-1 bosons are called gauge bosons, including the gluon (g), the photon (γ), the Z boson (Z) and the W boson (W); they are the carriers of the fundamental interactions. The Higgs boson (H), with spin-0, is the only fundamental scalar boson, which is essential in the Higgs mechanism [6–9].

Anti-particles

For every particle, a corresponding anti-particle also exists. These anti-particles are identical to their counterparts, except that they have opposite charges. The anti-particle is denoted by an overline (e.g. $\overline{b}$, $\overline{e}$, $\overline{\nu_e}$). For some particles (e.g. the photon and the Higgs boson), they are their own anti-particles; they are not denoted by an overline.

1.1.2. Fundamental Interactions

The Standard Model is based on the Yang-Mills theory [10, 11], which requires the existence of bosonic fields to describe the fundamental interactions (excluding gravity). For each interaction, the corresponding charges and force carrier bosons can be viewed as a consequence of the gauge groups. The gauge group of the Standard Model can be written as:

$$SU(3)_C \times SU(2)_L \times U(1)_Y, \tag{1.1}$$

where the subscript "C" denotes color, the subscript "L" denotes left-handed and the subscript "Y" denotes hypercharge. For each interaction in a gauge group $SU(N)$, the number of gauge bosons is given by:

$$N^2 - 1. \tag{1.2}$$

The strong interaction is described by Quantum Chromodynamics (QCD) [12–15], which is based on the $SU(3)_C$ gauge theory. Because of the $SU(3)_C$ symmetry, the force carriers are eight independent types of gluon, each carrying different color charges; they only interact with particles that carry color charges.

The weak interaction and the electromagnetic interaction can be unified into the electroweak interaction [16–18], which possesses the $SU(2)_L \times U(1)_Y$ symmetry. Given the gauge symmetry, there are three W bosons (W_1, W_2, W_3) and one B boson (B). After the electroweak symmetry breaking (EWSB), the $SU(2)_L \times U(1)_Y$ group breaks down to the $U(1)_{EM}$ group, where the subscript "EM" represents electromagnetic interaction to distinguish itself from the $U(1)_Y$ group. As a result, the W_1 boson and the W_2 boson mix to produce the W^+ and W^- bosons. Similarly, the W_3 and the B boson mix to produce the Z boson and the photon. The weak interaction bosons (W^+, W^-, Z) couple to weak isospin, and therefore only interact with left-handed fermions and right-handed anti-fermions. In the Standard Model, the weak interaction is the only interaction that allows flavour changing via the mediation of a $W^\pm$ boson; to account for quark transitions between generations, the Cabibbo-Kobayashi-Maskawa (CKM) matrix is introduced [19, 20].

The electromagnetic interaction is described by Quantum Electrodynamics (QED) [21–23], which is based on the residual $U(1)_{EM}$ symmetry from the EWSB. The force carrier

of the electromagnetic interaction is the photon, which only interacts with electrically charged particles.

In addition to the gauge interactions, the Standard Model also incorporates the Higgs interaction [24–26]. Unlike gauge interactions, the Higgs interaction is not governed by gauge theories, and there is no corresponding charge. Instead, the Higgs boson directly interacts with all particles that have mass. With a non-zero vacuum expectation value of the Higgs field, particles with mass experience interactions as they interact with the Higgs field, resulting in the acquisition of mass. On the other hand, photons and gluons, which are massless, remain massless because they do not interact with the Higgs field.

For easier visualization, the above interactions and corresponding processes can be represented by means of Feynman diagrams. Figure 1.2 shows the Feynman diagrams of the fundamental processes in the Standard Model; each of these simple diagrams contains one simple vertex, where the particles interact with each other.

1.1.3. The Lagrangian

The Standard Model Lagrangian [2, 28] encapsulates all the interactions and particles discussed with Lorentz invariance and local gauge symmetry in mind. Assuming each term implies a summation over all the gauge fields and particle types, it can be written in a short-handed form as:

$$\begin{aligned}\mathcal{L} = &-\frac{1}{4}F_{\mu\nu}F^{\mu\nu} \\ &+ i\bar{\psi}\not{D}\psi + h.c. \\ &+ \bar{\psi}_i y_{ij}\psi_j\phi + h.c. \\ &+ |D_\mu\phi|^2 - V(\phi),\end{aligned} \tag{1.3}$$

where $F_{\mu\nu}$ is the gauge field tensor, ψ is the fermion field, D_μ is the covariant derivative that consist of derivatives and gauge field tensors, $\not{D}$ is the slashed covariant derivative, y_{ij} is the Yukawa matrix, $V(\phi)$ is the Higgs potential as a function of the Higgs field, and $h.c.$ represents the hermitian conjugate.

In Equation (1.3), the first line includes the sum of scalar products of all the gauge field strength tensors $F_{\mu\nu}F^{\mu\nu}$, which describes the field and gauge boson dynamics. The second line, which consists of the matter fields and the covariant derivative in the form $i\bar{\psi}\not{D}\psi$, describes how the fermions interact with the gauge bosons. The third line consists of the matter fields, the Yukawa matrix and the Higgs field in the form $\bar{\psi}_i y_{ij}\psi_j\phi$; this term describes how matter particles couple to the Higgs field to acquire mass. The term $|D_\mu\phi|^2$ is called the Higgs kinetic term; it describes the propagation of the Higgs field and how the massive gauge bosons interact with the Higgs field to obtain masses. The last term $V(\phi)$ is the potential of the Higgs field, which has a set of minima that allows for spontaneous symmetry breaking. The hermitian conjugates are also added to make sure the Lagrangian remains real-valued.

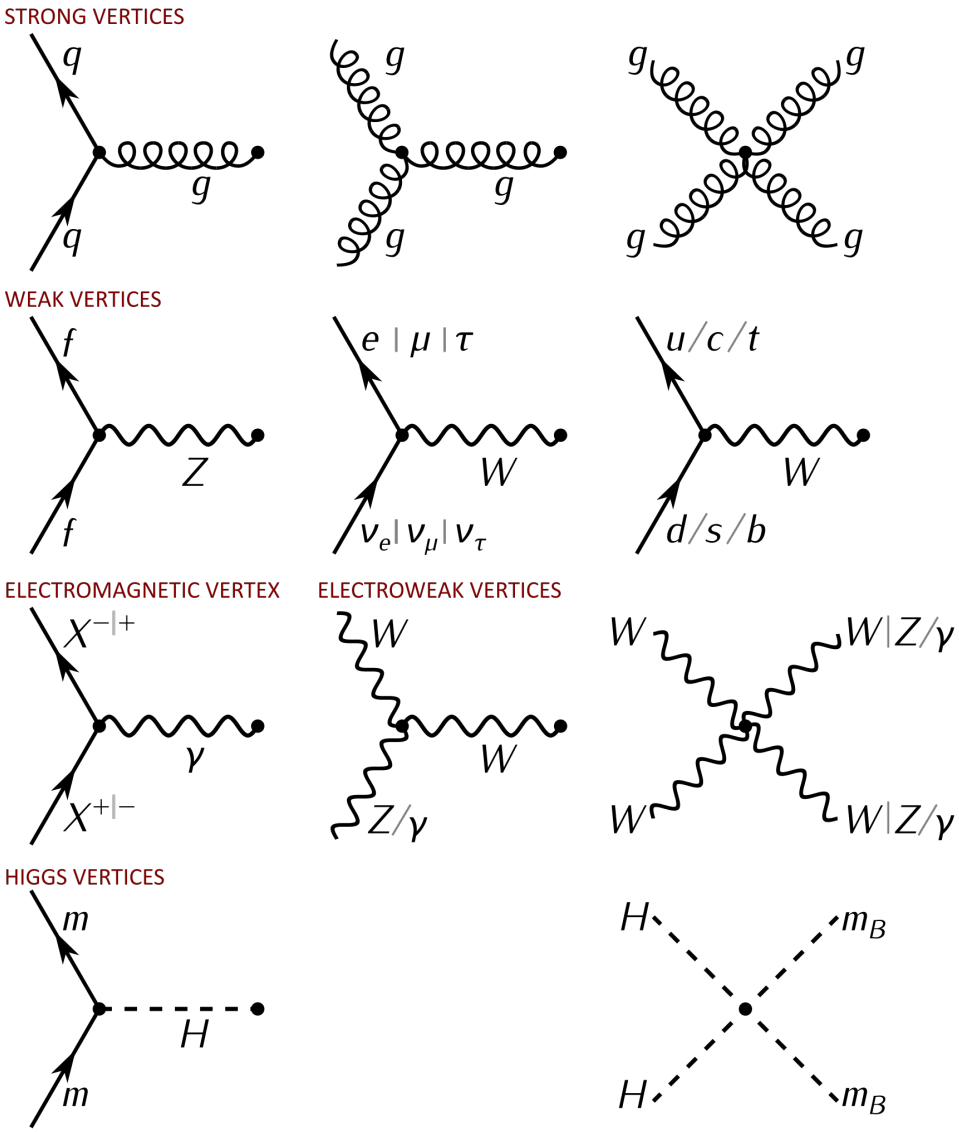

Figure 1.2.: Feynman diagrams of fundamental interactions in the Standard Model. In addition to the common notation introduced, $X^{-|+}$ represents any electrically charged particles, m represents any particle with mass and m_B represents any boson with mass [27].

The CKM Matrix

In the Standard Model, quark mixing arises from the Yukawa interactions with the Higgs condensate described in the $\bar{\psi}_i y_{ij} \psi_j \phi$ term in Equation (1.3). To describe the connection between the mass eigenstates and the weak interaction eigenstates of quarks, the Cabibbo-Kobayashi-Maskawa (CKM) matrix V_{CKM} is introduced. The CKM matrix can be written

as:

$$V_{\text{CKM}} = \begin{bmatrix} V_{ud} & V_{us} & V_{ub} \\ V_{cd} & V_{cs} & V_{cb} \\ V_{td} & V_{ts} & V_{tb} \end{bmatrix}, \tag{1.4}$$

where each element V_{ij} correspond to the transition of an up type quark i to a down type quark j via the weak interaction. For each possible transition, the probability of the transition is proportional to the square of the element $|V_{ij}|^2$.

Although there are 9 elements in the CKM matrix, the true degrees of freedom can be further reduced. Because of the unitarity requirement and common phases absorbed by quark fields, the degree of freedom of the CKM matrix is reduced to 4. To address this, one can rewrite the CKM matrix in the standard parameterization as:

$$V_{\text{CKM}} = \begin{bmatrix} c_{12}c_{13} & s_{12}c_{13} & s_{13}e^{-i\delta_{CP}} \\ -s_{12}c_{23} - c_{12}s_{23}s_{13}e^{i\delta_{CP}} & c_{12}c_{23} - s_{12}s_{23}s_{13}e^{i\delta_{CP}} & s_{23}c_{13} \\ s_{12}s_{23} - c_{12}c_{23}s_{13}e^{i\delta_{CP}} & -c_{12}s_{23} - s_{12}c_{23}s_{13}e^{i\delta_{CP}} & c_{23}c_{13} \end{bmatrix}, \tag{1.5}$$

where $s_{ij} = \sin\theta_{ij}$, $c_{ij} = \cos\theta_{ij}$, θ_{ij} are the mixing angles, and δ_{CP} is the complex phase. In this representation, the remaining parameters therefore become 3 mixing angles and a complex phase. The complex phase is of particular importance, as it is responsible for all the CP-violation in the Standard Model.

Symmetries

Other than the Poincaré symmetry and local gauge symmetry in Equation (1.1) that are implemented by construction, there are other symmetries in the Standard Model [29, 30].

As a result of Lorentz invariance, the Standard Model also possess CPT-symmetry, where CPT represents simultaneous transformation of charge conjugation (C), parity (P), and time reversal (T). However, any individual or combination of these transformations do not yield exact symmetry in general. One symmetry of particular interest is the CP-symmetry; although it is not strictly conserved, the amount of CP-violation has a direct consequence of the matter-antimatter imbalance of the universe.

The additional symmetries that are not postulated by design are called accidental symmetries. For instance, the Lagrangian is also invariant under various $U(1)_X$ transformations. By defining the baryon number B, electron number L_e, muon number L_μ and tau number L_τ, the Lagrangian is found to be invariant under corresponding $U(1)_X$ transformation for $X \in \{B, L_e, L_\mu, L_\tau\}$. Therefore, the baryon number and lepton number for each individual flavour are conserved in Standard Model processes.

Free Parameters

Other than the well-defined symmetries and structures of the interactions of the Standard Model, the model also requires several parameters that need to be determined experimentally. There are multiple common ways to parameterize the free parameters in the Standard Model; the choice of parameterization is a matter of convention and convenience. For instance, one can use the fermion masses instead of the Yukawa couplings or use the mass and vacuum expectation value instead of the parameters of the Higgs potential if desired. Assuming the neutrinos are massless, the number of free parameters is 19; one way to parameterize and categorize the parameters is as follows:

- **9 fermion masses**: Other than the neutrinos, the masses of the charged leptons (m_l) and quarks (m_q) all fall into this category.
- **2 Higgs parameters**: The mass of the Higgs boson (m_H) and the Higgs vacuum expectation value (v), which is responsible for mass generation.
- **3 gauge couplings**: These are the gauge couplings (g_1, g_2 and g_3) for the gauge groups ($U(1)$, $SU(2)$ and $SU(3)$), which represent the strength of the interactions.
- **4 CKM parameters**: These include the quark mixing angles (θ_1, θ_2 and θ_3) and the complex phase (δ_{CP}) in the CKM matrix.
- **1 QCD vacuum angle**: The QCD vacuum angle (θ_{QCD}) represents the amount of CP-violation in the strong interaction.

1.1.4. Open Questions

Although the majority of experimental results to date align with the Standard Model, there are also plenty of unsolved problems in particle physics that are not addressed by the Standard Model. These problems raise open questions that show the limitation of the Standard Model; some of them are described below.

Strong CP Problem

CP-violation in the Standard Model is only observed in processes governed by the weak interaction; the level of violation is dictated by the complex phase δ_{CP} [31, 32]. In the Standard Model, CP-violation is theoretically also permitted via the strong interaction, through a non-zero QCD vacuum angle (θ_{QCD}). However, no CP-violation is observed in the strong sector, as this angle is measured to be smaller than 10^{-10}. The mechanism by which this angle acquires such an unnaturally small value, or the reason CP-violation is forbidden in the strong sector, is not explained by current theories.

Baryogenesis

Astronomical observations have shown that the universe is dominated by matter; the proportion of anti-matter is of the order 10^{-9} compared to matter [33]. For such level of imbalance to exist, a set of three necessary conditions known as the Sakharov conditions [34] must be satisfied. These conditions are:

- Baryon number violation.
- C-symmetry and CP-symmetry violation.
- Non-thermal equilibrium

However, in the known processes, matter and anti-matter are produced equally to conserve the baryon number. Moreover, the level of CP-violation in the weak interaction is still limited. Therefore, new mechanisms and processes that introduce baryon number violation and/or CP violation are needed to explain the large level of imbalance.

Neutrino Masses

In the Standard Model, the masses of the neutrinos have been assumed to be zero. However, neutrino experiments have shown that the neutrinos can oscillate, meaning that neutrinos can transform into neutrinos of another flavour when they travel through space [35–37]. For this to happen, it has been theorized that the neutrinos must have flavour eigenstates that are different from their mass eigenstates, which implies that their mass cannot be zero [38–40]. From the neutrino oscillation frequency, the mass differences of the neutrinos are calculated, which provide constraints on the neutrino mass. Such masses are not permitted nor explained by the Standard Model, therefore an extension of the Standard Model in the lepton sector is needed.

Generation of Fermions

While the number of gauge bosons is dictated by the gauge symmetry, the number of generations of quarks and leptons is assumed to be three in the Standard Model; the existence of additional fermions is not ruled out. Moreover, the large differences in the masses of various flavours are not accounted for. Together with the CKM matrix, the origins of a total of 13 free parameters are unexplained.

Grand Unified Theories

In the Standard Model, the coupling constants g for each interaction are different; such difference is not explained. A Grand Unified Theory (GUT) is a model that merges the three gauge interactions into a single force [41–43], suggesting that the coupling constants converges to a single value at high energy. Besides, the quantization of electric charge in

$\frac{1}{3}e$ is also not explained by the Standard Model. A single interaction can also combine the different charges into a single charge, reducing the necessary input and assumption of the model.

Dark Matter

By measuring the velocities of celestial objects and their distances from their rotation center, the rotation curves of the Milky Way and the other galaxies have shown deviation due to missing mass [44–46]. Astronomical observations have shown that this large proportion of missing matter does not interact electromagnetically; they are referred to as dark matter. Although no electromagnetic radiation from dark matter has been detected, it is believed that dark matter interacts gravitationally. Through the observation of gravitational lensing - bending of light as it traverses a gravitational field, direct evidence for the existence of dark matter has also been established [47–49]. Despite the Standard Model has been successful in describing ordinary matter, no particle serves as a good candidate of dark matter. It is therefore likely that new particles and new forms of interaction, which are not described by the Standard Model, exist in a "dark sector" that is yet to be discovered.

1.2. Beyond the Standard Model

The Standard Model has been proven a successful theory in various experiments. In the past decades, it has been tested by a wide range of experiments at different scales, such as the particle collider experiments, cosmic-ray experiments and even molecular physics experiments. However, the Standard Model does not offer answer to all the phenomena. It is believed that the Standard Model is not a complete theory of particle physics, but modification or extension of the model is needed to build a theory beyond the Standard Model (BSM). In particular, the lepton number has been observed to be violated; based on the observation, several theories are highly motivated. This section describes a number of BSM theories with focus on resolving the neutrino masses and LFV decays.

1.2.1. Neutrino Sector

Since neutrinos have been proven to have mass, a natural extension of the Standard Model is to include neutrino masses as free parameters. This introduces additional complexities in the neutrino sector, such as neutrino mixing and the absence of right-handed neutrinos, which suggests the presence of new physics.

Neutrino Mixing

Neutrino mixing occurs because the mass eigenstates and the flavour eigenstates of the neutrinos do not coincide; the Pontecorvo-Maki-Nakagawa-Sakata (PMNS) matrix U_{PMNS}

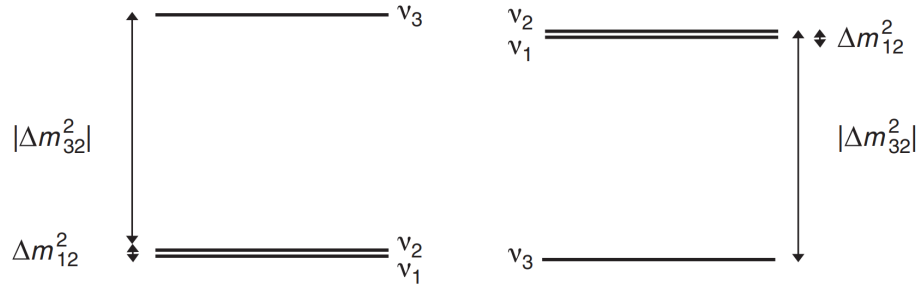

Figure 1.3.: Neutrino mass hierarchies for normal ordering and the inverted ordering [2].

is therefore introduced to connect the eigenstates [39, 50]. The PMNS matrix connects the eigenstates as following:

$$\begin{bmatrix} \nu_e \\ \nu_\mu \\ \nu_\tau \end{bmatrix} = U_{\text{PMNS}} \begin{bmatrix} \nu_1 \\ \nu_2 \\ \nu_3 \end{bmatrix}, \tag{1.6}$$

where ν_i denotes the mass eigenstates and ν_α denotes the flavour eigenstates for $\alpha = e, \mu, \tau$. The PMNS matrix can be explicitly written as:

$$U_{\text{PMNS}} = \begin{bmatrix} U_{e1} & U_{e2} & U_{e3} \\ U_{\mu 1} & U_{\mu 2} & U_{\mu 3} \\ U_{\tau 1} & U_{\tau 2} & U_{\tau 3} \end{bmatrix}, \tag{1.7}$$

where for a neutrino of flavour α, the probability of it collapsing to a mass state m_i is $|U_{\alpha i}|^2$. Similar to the CKM matrix, the PMNS matrix can be parameterized in the same algebraic form as in Equation (1.5), but with different θ_{ij} and δ_{CP}. As a result, 4 PMNS parameters need to be added to the Standard Model to incorporate neutrino mixing.

Experimentally, it is measured that ν_2 is heavier than ν_1, and their mass difference is much smaller than that of ν_3 and ν_2 [51–53]. However, it is uncertain whether ν_2 or ν_3 is the heaviest among the three states, as neutrino oscillation experiments are only sensitive to the mass difference of the neutrinos. Therefore, there are two commonly assumed mass hierarchies: normal ordering and inverted ordering. Normal ordering assumes the relation $m_1 < m_2 < m_3$, while inverted ordering assumes $m_3 < m_1 < m_2$. Figure 1.3 shows the diagram which illustrates the mass difference and the hierarchy of the masses. Table 1.1 shows θ_{ij}, δ_{CP}, and the difference of mass squared Δm^2_{ij} for each assumed ordering. To date, there is no precise measurement of the neutrino mass, but the best upper limit on the neutrino mass is set to sub-eV [54].

Parameter	Normal Ordering	Inverted Ordering
θ_{12} (degrees)	$33.41^{+0.75}_{-0.72}$	$33.41^{+0.75}_{-0.72}$
θ_{23} (degrees)	$42.2^{+1.1}_{-0.9}$	$49.0^{+1.0}_{-1.2}$
θ_{13} (degrees)	$8.58^{+0.11}_{-0.11}$	$8.57^{+0.11}_{-0.11}$
δ_{CP} (degrees)	232^{+36}_{-26}	276^{+22}_{-29}
$\Delta m^2_{21}(10^{-5}\,\mathrm{eV}^2)$	$7.41^{+0.21}_{-0.20}$	$7.41^{+0.21}_{-0.20}$
$\Delta m^2_{31}(10^{-3}\,\mathrm{eV}^2)$	$+2.507^{+0.026}_{-0.027}$	$-$
$\Delta m^2_{32}(10^{-3}\,\mathrm{eV}^2)$	-	$-2.486^{+0.025}_{-0.028}$

Table 1.1.: Neutrino sector parameters extracted by fits to global data for normal ordering and inverted ordering of the neutrino masses [55].

Sterile Neutrinos

In the Standard Model, the neutrinos cannot acquire Dirac mass via interaction of the Higgs field, because no right-handed neutrinos exist in the model. One way to incorporate neutrino masses, while retaining gauge symmetry and renormalizability, is to introduce a number of m right-handed sterile neutrinos ν_s in addition to the three neutrinos in the Standard Model. With the added sterile neutrinos, the Lagrangian mass terms for the neutrino sector (after electroweak symmetry breaking) can be written as [4]:

$$-\mathcal{L}_{M\nu} = M_D \bar{\nu}_s \nu_L + \frac{1}{2} M_N \bar{\nu}_s \nu_s^c + h.c., \tag{1.8}$$

where M_D is a complex matrix of dimension $(m, 3)$, M_N is a symmetric matrix of dimension (m, m), ν_L is neutrino field for the three flavours $\{e, \mu, \tau\}$, ν_s is the sterile neutrino field for the m added neutrinos and the superscript c denotes the charge conjugated field. The first term in Equation (1.8) is the Dirac mass term that is similar to the other particles in the Standard Model. The second term in Equation (1.8) is the Majorana mass term, which allows for the existance of Majorana neutrinos.

To concatenate the neutrinos into one vector, one can rewrite Equation (1.8) as:

$$-\mathcal{L}_{M\nu} = \frac{1}{2} \begin{bmatrix} \bar{\nu}_L^c & \bar{\nu}_s \end{bmatrix} \begin{bmatrix} 0 & M_D^T \\ M_D & M_N \end{bmatrix} \begin{bmatrix} \nu_L \\ \nu_s^c \end{bmatrix} + \text{h.c.} \equiv \vec{\nu^c} M_\nu \vec{\nu}. \tag{1.9}$$

In this representation, $\vec{\nu}$ is a vector of dimension $3+m$ and M_ν is of dimension $(3+m, 3+m)$.

Seesaw Mechanism

With added sterile neutrinos and corresponding mass terms in the Standard Model, the seesaw mechanism provides an explanation of the neutrino masses. To find out the masses of the neutrinos, the matrix M_ν is diagonalized such that the Lagrangian mass terms can

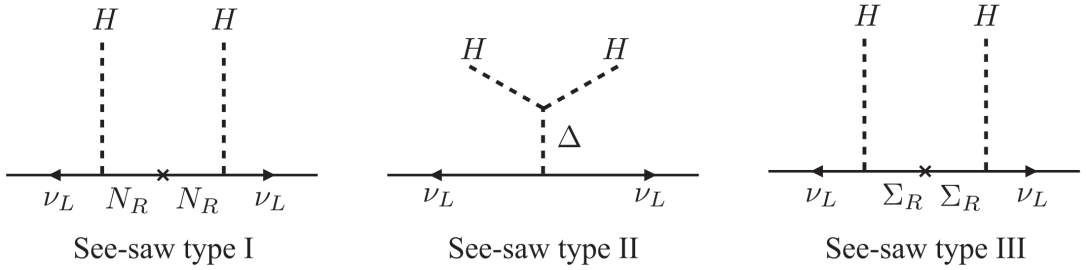

Figure 1.4.: Feynman diagrams showing the additional interactions in different types of seesaw mechanisms, where H indicates the Higgs field, ν_L is a left-handed neutrino, N_R is a sterile neutrino, Δ is a scalar triplet and Σ_R is a neutral fermion triplet [56].

be written as [4, 56]:

$$-\mathcal{L}_{M\nu} = \frac{1}{2}\bar{\nu}_l M^l \nu_l + \frac{1}{2}\bar{\nu}_h M^h \nu_h, \tag{1.10}$$

where M^l and M^h are the diagonalized sub-matrices of M_ν, ν_l are the light neutrino fields in mass basis and ν_h are the heavy neutrino fields in mass basis. Assuming the eigenvalues of M_N in flavour basis are much greater than the electroweak scale, M_ν in the mass basis can be diagonalized with some matrices V and U as:

$$M_\nu \to \begin{bmatrix} -V^T M_D^T M_N^{-1} M_D V & 0 \\ 0 & U^T M_N U \end{bmatrix} \equiv \begin{bmatrix} M^l & 0 \\ 0 & M^h \end{bmatrix}, \tag{1.11}$$

where M^l and M^h are diagonal matrices with dimension $(3, 3)$ and (m, m) respectively.

It can be seen that the mass of the heavy neutrinos has a dependence of M_N, which is assumed to be much greater than the electroweak scale. On the other hand, for the light neutrinos, there is a dependence of M_N^{-1}, which greatly suppresses the neutrino masses. Therefore, with the simple addition of the heavy sterile neutrinos and the corresponding Majorana mass terms, the heavier the neutrino mass, the lighter the three generation of neutrinos; such mechanism is called the type-I seesaw mechanism.

Note that the above mechanism is not the only way to construct or explain neutrino masses; neutrino masses can also be constructed by other types of seesaw mechanisms. For instance, the type-II seesaw mechanism introduces additional heavy triplet scalars to model the mass generation, while the type-III seesaw mechanism introduces new triplet fermions that couple to the neutrinos. Figure 1.4 shows the Feynman diagrams of additional interactions in different types of seesaw mechanisms that are responsible for the neutrino masses.

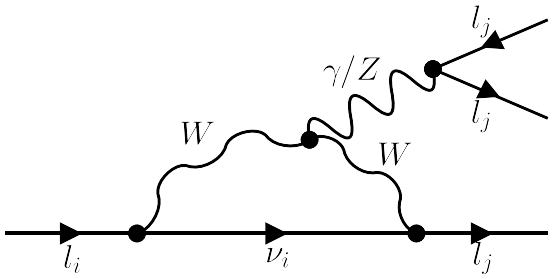

Figure 1.5.: Feynman diagram of LFV decay $l_i \to l_j l_j l_j$ induced by a light neutrino ν_i that changes flavour through a W loop [61].

1.2.2. Lepton Flavour Violation

Although the masses of the neutrinos are tiny compared to other Standard Model particles, this has significant implications. Due to the flavour changing property of the neutrinos, lepton-flavour-violating (LFV) decays for tau leptons and muons are allowed, which contradicts the Standard Model. These processes violate the lepton numbers for individual flavours, breaking the accidental flavour symmetry.

Examples of LFV decays include $\mu \to eee$, $\mu \to e\gamma$ and $\tau \to \mu\mu\mu$. Figure 1.5 shows a Feynman diagram of $l_i \to l_j l_j l_j$, where a lepton l_i, which is heavier than lepton l_j, changes flavour via a W boson loop. Because of the W loop, the neutrino ν_i changes flavour, which breaks the flavour symmetry; the subsequent lepton also mediate a Z/γ, which decays into $l_j l_j$. This diagram can also account for $l_i \to l_j \gamma$ decays, where the only difference is that the photon does not decay into a pair of leptons.

While adding massive neutrinos to the Standard Model allows for LFV processes, these processes are highly suppressed. For the LFV processes via neutrino mixing, the neutrino transition probability is typically associated with a suppression factor $\Delta m_{ij}^2/M_W^2$ [57, 58], which leads to a tiny branching ratio smaller than 10^{-50}. Over the past decades, many measurements have been done in various LFV decay channels as shown in Figure 1.6, most of the upper limits on branching ratio are about 10^{-8} [59, 60]. With new experiments upgrade of current experiments in the coming decade, most of the limits can be improved by a factor of ten times. However, experimental sensitivity is still hopelessly far from the predicted values that are smaller than 10^{-50}. Although such small values are entirely out of reach, the branching ratio is very sensitive to new physics; any enhancement in the branching ratio is a sign of new physics beyond the Standard Model.

1.2.3. Potential Theories

Among the potential BSM theories, most of them extend the Standard Model by adding new fields and new forms of interaction in the Lagrangian, including heavy sterile neutrino fields. The existence of such new terms can lead to a significantly enhanced rate of LFV

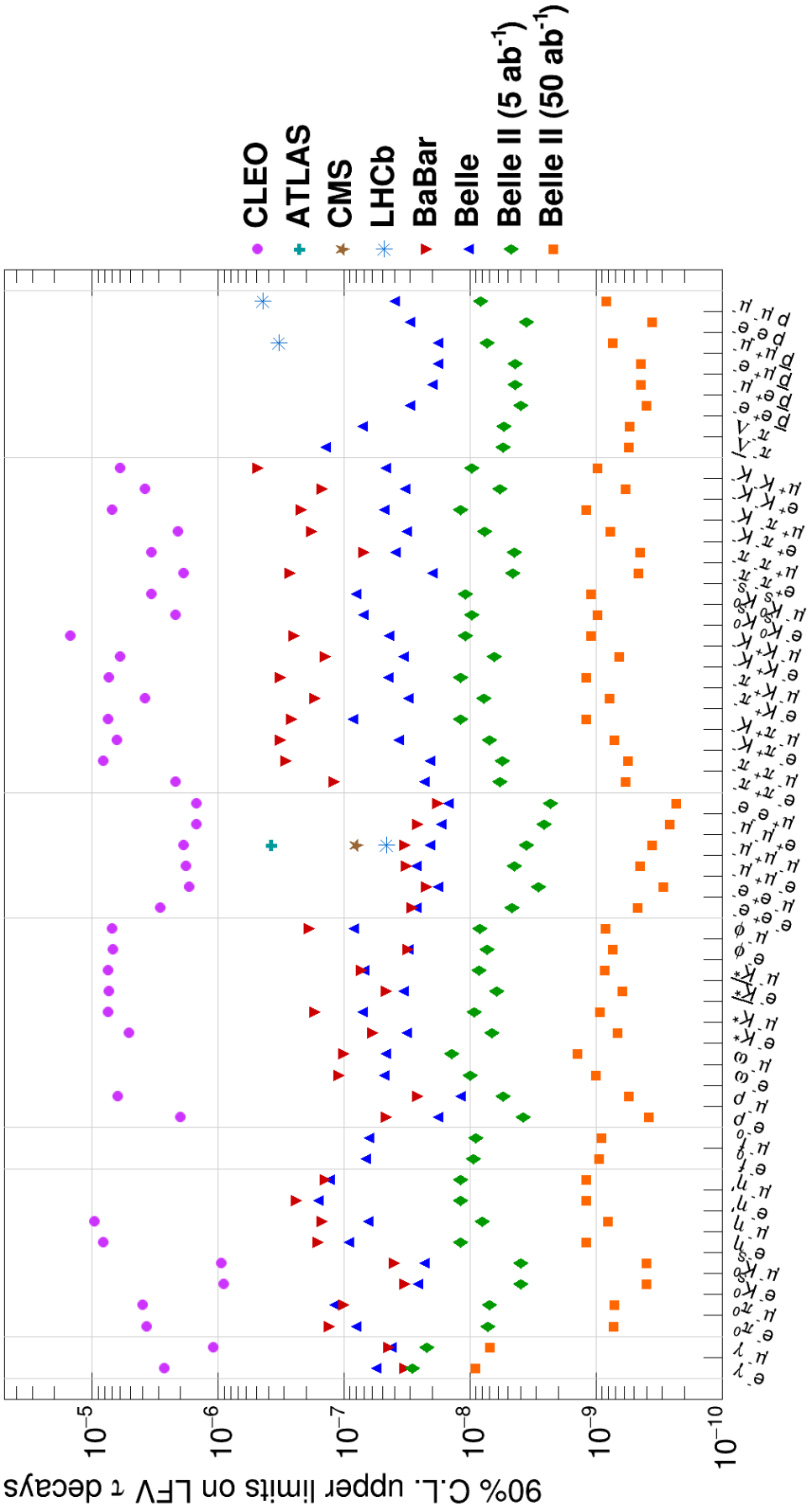

Figure 1.6.: Tau LFV branching fraction upper limits summary plot [60].

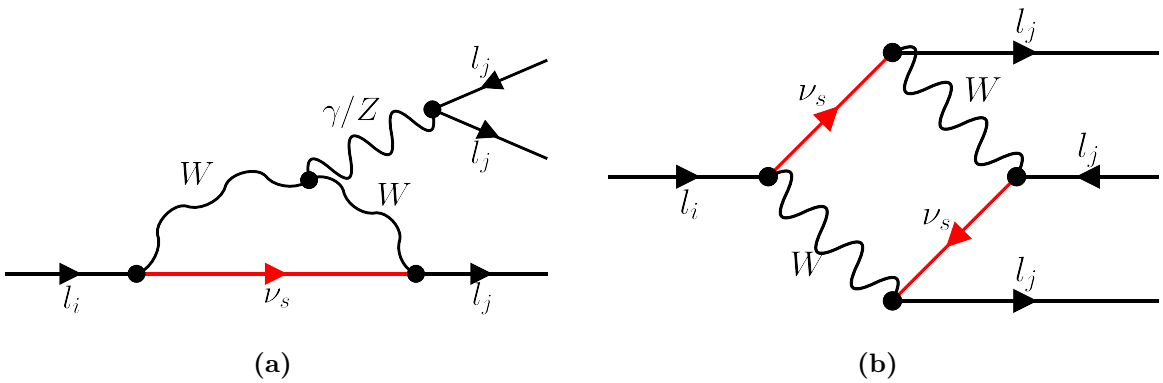

Figure 1.7.: Feynman diagrams of LFV decay $l_i \to l_j l_j l_j$ enhanced by the sterile neutrinos ν_s through (a) a W loop and (b) a box diagram. The BSM sterile neutrinos are indicated by red color [61].

decays compared to that induced by light neutrino mixing; several theories [62] even predict branching ratios in the order of 10^{-10}. Such level of LFV, if detected, is a clear deviation from the Standard Model, as it cannot be explained even with the introduction of neutrino mixing. Some proposed theories and their mechanism to incorporate LFV decays are described below. In particular, the LFV decay of $l_i \to l_j l_j l_j$, where a lepton l_i decays into three leptons of different flavours l_j, is taken as an example for illustration.

Heavy neutral lepton

As motivated in Section 1.2.1, sterile neutrinos, if assumed to be heavy, can naturally explain the small masses of the active left-handed neutrinos. The sterile neutrinos, with a finite mass, can mix with the three active neutrinos through neutrino oscillations and induce charged LFV processes [58, 63, 64]. Figure 1.7 shows some of the additional LFV diagrams induced by the addition of heavy sterile neutrinos in $l_i \to l_j l_j l_j$ decays. For such decay, it is predicted that the branching ratio can be in the order of 10^{-15} to 10^{-13} [64].

Leptoquark

In the Standard Model, there is no vertex containing a quark and a lepton; the direct interaction of quark and lepton is forbidden. In leptoquark theories [65–67], either a scalar or a vector leptoquark (LQ) is introduced to allow for vertices that directly connect a quark, a lepton and a leptoquark. Like quarks, the leptoquark carries both color charge and electric charge. Leptoquarks are encountered in various BSM theories, such as the Pati-Salam model and GUTs based on $SU(5)$ and $SO(10)$.

Figure 1.8 shows the Feynman diagram of the new vertex introduced by the leptoquark. Because of the new vertices, it is also possible for the LFV decays to include leptoquarks and quarks. Figure 1.9 shows the Feynman diagram of the charged lepton decays enabled

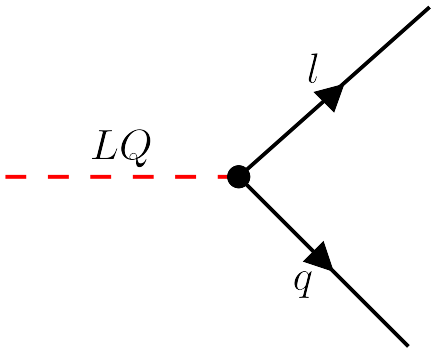

Figure 1.8.: Feynman diagram of a new type of vertex introduced by the hypothetical leptoquark, which is indicated in red color [61].

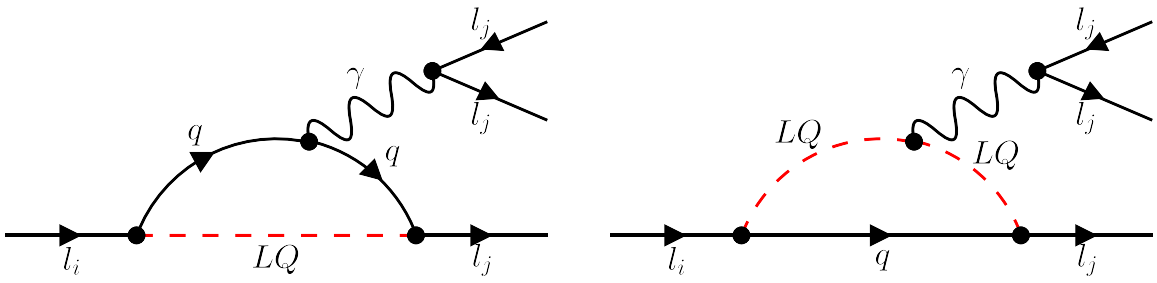

Figure 1.9.: Feynman diagrams of LFV decay $l_i \to l_j l_j l_j$ enhanced by the leptoquarks through (a) a quark loop and (b) a leptoquark loop. The BSM leptoquarks that enables lepton-quark mixing are indicated by red color [61].

by the leptoquark. With the leptoquark, LFV decay no longer relies on neutrino mixing as the only LFV mechanism. Although the leptoquark is typically assumed to be heavy ($m_q << M_{LQ}$) and therefore lead to a small factor m_q^2/M_{LQ}^4 in the branching ratio of LFV decays, such factor is still orders of magnitude greater than the factor $\Delta m_{ij}^2/M_W^2$ in LFV decays induced by light neutrino mixing. Therefore, the existence of leptoquark can lead to a large enhancement of LFV decays. It has also been predicted that the branching ratios of some processes, e.g. $\tau \to eee$, $\tau \to e\mu\mu$ and $\tau \to \mu ee$, can be of order 10^{-8} [68]; such level of sensitivity is achievable in the coming decade.

Multiple Higgs Bosons

In the Standard Model, only one Higgs boson (H) emerges from the Higgs doublet field. However, possibilities of multiple scalar doublet fields are not ruled out. For instance, the two Higgs doublet model (2HDM) [24, 69–71] and the three Higgs doublet model (3HDM) [72–75] models suggest the addition of scalar fields to extend the Higgs sector.

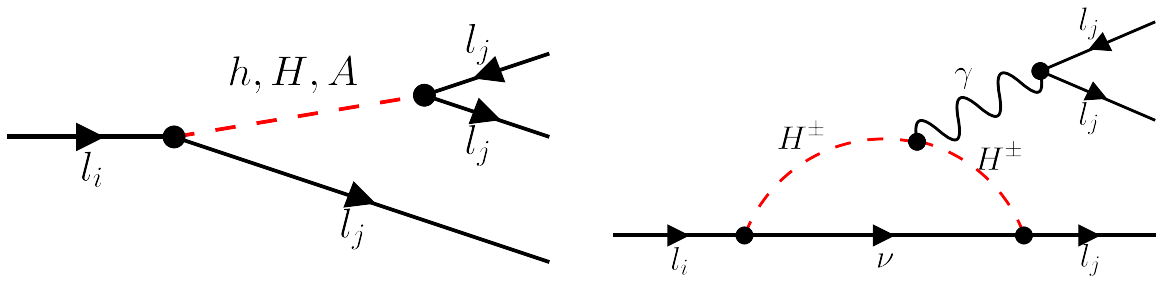

(a) **(b)**

Figure 1.10.: Feynman diagrams of LFV decay $l_i \to l_j l_j l_j$ enhanced by the additional Higgs boson (a) h, H, A and (b) $H^\pm$. The BSM Higgs bosons which enable flavour changing are indicated by red color [61].

In the 2HDM, there are 4 additional Higgs bosons added to the Standard Model; one of them is a CP-even Higgs bosons (h), one of them is a CP-odd pseudoscalar boson (A) and the remaining two are singly charged Higgs bosons (H^+, H^-). One consequence of an additional doublet is that the fermions can couple differently to the two doublet fields. As a result, the Yukawa matrices for the two doublets may not be diagonalised simultaneously, inducing flavour-changing neutral currents (FCNC).

In the Standard Model, FCNC is not allowed; the W boson can change the flavour, but it is not neutral; the Z boson and photon are neutral, but they cannot change the flavour. The 2HDM allows the Higgs bosons to change the flavour of the fermions, leading to the new diagrams in Figure 1.10.

Chapter 2.

The LHC and the ATLAS detector

In the Standard Model, only a handful of the elementary particles are stable, the others either decay or hadronise quickly. This means that most of the elementary particles cannot be readily obtained and studied, but must be first produced, then studied through their decay products. Beyond the Standard Model, various theories also predict the existence of hypothetical particles that can only be produced in high energy processes. Particle accelerators are therefore designed for this exact purpose - inject as much energy as possible into particles, and produce a variety of particles through collisions. The particles produced are then measured and identified by particle detectors to allow various measurements.

As of now, the Large Hadron Collider (LHC) operated by The European Organization for Nuclear Research (better known as CERN) is the most powerful accelerator on Earth, with the highest center-of-mass collision energy achieved. To allow for different physics studies, four main detectors have been constructed, including A Large Ion Collider Experiment (ALICE) detector, A Toroidal LHC ApparatuS (ATLAS) detector, the Compact Muon Solenoid (CMS) detector and the Large Hadron Collider beauty (LHCb) detector. These detectors have a multi-layer structure, allowing efficient measurement and identification of the particles produced. This chapter will focus on the LHC and the ATLAS detector during the second operation run from 2015 to 2018.

2.1. The CERN Accelerator Complex and the LHC

2.1.1. The CERN Accelerator Complex

Over the past decades, CERN has been operating different generations of particle accelerators near the city of Geneva in Switzerland. The energy scale of these accelerators ranges from 50 MeV of the LINear ACcelerator (LINAC) to 209 GeV of the Large Electron-Positron (LEP) collider, up to 13 TeV achieved by the LHC. As higher energy accelerators have been constructed, some of the older accelerators are obsolete, while some of them have been upgraded to form the CERN accelerator complex. Figure 2.1 shows a schematic diagram of the current CERN accelerator complex. It can be seen that the accelerators are connected, allowing injection of particles from one structure into another. In the figure, one can see a sequence of circular colliders advancing from the Proton Synchrotron (PS)

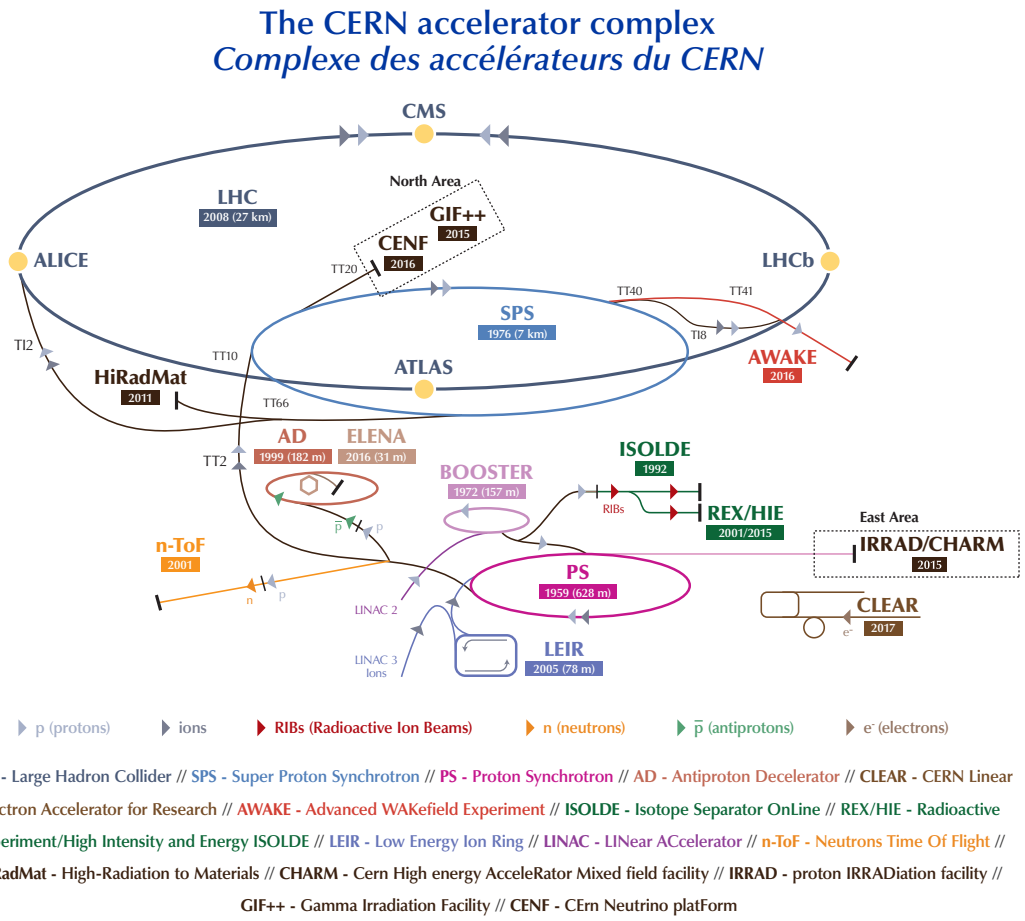

Figure 2.1.: A schematic diagram of the CERN accelerator complex [76].

ring to the Super Proton Synchrotron (SPS) ring, and to the LHC ring; in each generation, the ring size and the energy increases. Note that the accelerator complex also consists of facilities that are not accelerators; for instance, the Antiproton Decelerator (AD) is a facility that decelerates and stores antiprotons.

When the LHC prepares for proton-proton collisions, a series of pre-acceleration steps have to be done. Before injecting protons into the accelerator complex, hydrogen gas is put in an electric field to extract the positively charged hydrogen ions - the protons. The extracted protons are then accelerated by the LINear ACcelerator 2 (LINAC2) to an energy of 50 MeV. The protons are subsequently injected into the Proton Synchrotron Booster (BOOSTER), followed by the Proton Synchrotron (PS), which pump up the energy of the protons to 1.4 GeV and 25 GeV respectively. The PS also groups the protons into bunches with a 25 ns spacing, matching the designed collision rate of 40 MHz at the LHC. The last step of acceleration before injection in the LHC is done by the Super Proton Synchrotron (SPS), which accelerates the protons to 450 GeV. Afterwards, the protons are transferred to the LHC and ramped up to 6.5 TeV over the next 20 minutes.

2.1.2. The LHC

The LHC is a circular collider with a circumference of 27 km placed in the tunnel built for the LEP. Inside the collider, there are two beam pipes, allowing injected protons to travel in opposite directions separately. During operation, the two beams of protons are accelerated, squeezed and collided at four collision points, where the experiment detectors: ATLAS, CMS, ALICE and LHCb are located.

In the LHC, there are 16 radio-frequency (RF) cavities, 8 for each beam, to accelerate the injected protons from 450 GeV to 6.5 TeV. Each RF cavity is tuned to provide an oscillating field of 2 MV at 400 MHz, in order to resonate with the protons. When passing through the RF cavity, protons with the desired energy arriving at the exact timing will not be accelerated, while protons with different energies arriving at a slightly later (earlier) time will be accelerated (decelerated). After passing through the RF cavities more than 10 million times in around 20 minutes, the protons are accelerated to the desired energy of 6.5 TeV and packed tighter inside the bunches.

To direct the beam to travel in a circular path, a total of 1232 superconducting dipole magnets, each capable of generating a magnetic field of 8.3 T, are deployed around the beam. To increase the density of proton bunches, another 392 quadrupole magnets are installed near the collision points to squeeze the beam vertically and horizontally. This is essential to increase the chance of collision, and thus increases the event rate.

2.1.3. Luminosity and Pileup

The instantaneous luminosity $\mathcal{L}$ is a measure of how many particles travel through an area to collide per unit of time. Assuming two identical Gaussian bunches colliding against each other, the instantaneous luminosity can be calculated by

$$\mathcal{L} = \frac{N_\mathrm{b} n_\mathrm{p}^2 f \gamma}{4\pi \varepsilon_\mathrm{n} \beta^*} F, \tag{2.1}$$

where N_b is the number of bunches, n_p is the number of protons per bunch, f is the proton revolution frequency, γ is the relativistic factor, ε_n is the normalized transverse emittance, β^* is the value of the betatron function at the interaction point, and F is the reduction factor caused by the bunch crossing angle, which is about 0.9 in the LHC [77]. With the luminosity known, the number of events N_events of a process is given by

$$N_\mathrm{events} = \sigma \int \mathcal{L}\, \mathrm{d}t, \tag{2.2}$$

where σ is the cross-section of the process and the instantaneous luminosity is integrated over time to give the total luminosity. Figure 2.2a shows the luminosity delivered by the LHC and recorded by ATLAS during the second operation run from 2015 to 2018 [78].

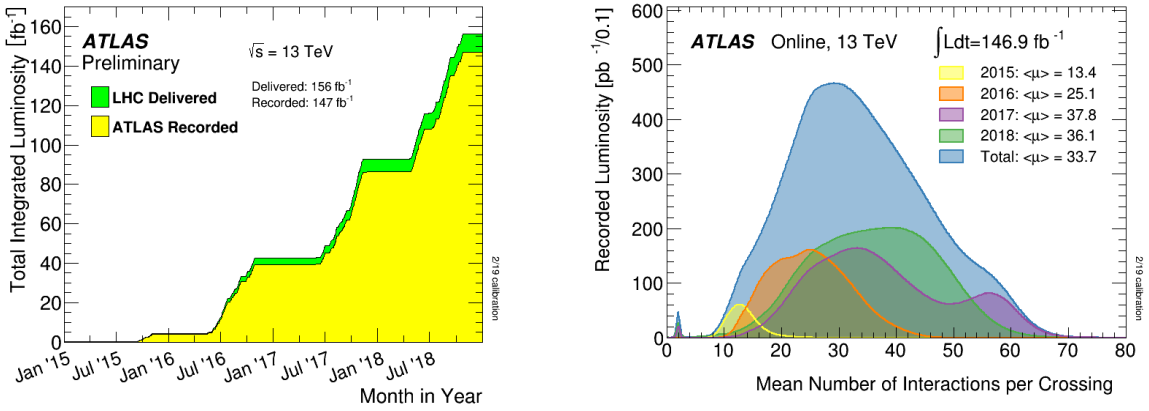

(a) **(b)**

Figure 2.2.: The luminosity (a) and the pileup profile (b) measured by ATLAS [78].

In the LHC, every bunch consists of around 10^{11} protons, but only tens of them undergo inelastic collision during bunch crossing. Out of these collisions, usually only one collision containing the physical process of interest is chosen; the other collisions are denoted as pileup. The number of pileup interactions per bunch crossing μ is given by the formula

$$\mu = \frac{\sigma_{\text{inel}}\mathcal{L}}{fN_{\text{b}}}, \tag{2.3}$$

where σ_{inel} is the cross-section of inelastic scatterings. In a typical physics analysis, only a small number of the proton collisions contain an interesting interaction. A high luminosity is therefore beneficial for collecting useful data. On the other hand, these pileup collisions also produce particles that are measured by particle detectors, leading to challenges in both data handling and associating particles with their collision points. Figure 2.2b shows the pileup averaged over time per year from 2015 till 2018 recorded by ATLAS [78].

Over the past years, the LHC has been running with different setups and therefore operates with a different luminosity. Table 2.1 shows the different parameters of the LHC during the second operation run from year 2015 to 2018 compared to the design values. The LHC operated at a lower center-of-mass energy of 13 TeV, because the magnet training time required to achieve 14 TeV can reduce time for actual data taking [79]. On the other hand, the luminosity and pileup exceeded that of the design values, due to more tightly squeezed beams and a minimized bunch crossing angle [80].

2.2. The ATLAS Detector

The ATLAS detector is a multi-purpose particle detector built around one of the four collision points of the LHC, to efficiently measure and identify the particles produced from the center of the detector. To detect as many particles as possible, the detector has

Parameter	2015	2016	2017	2018	Design
Center-of-mass energy [TeV]	13	13	13	13	14
Typical number of filled bunches	2244	2220	2556	2556	2808
Typical number of protons per bunch [10^{11}]	1.2	1.25	1.25	1.1	1.15
Minimum bunch spacing [ns]	25	25	25	25	25
Peak instantaneous luminosity [$10^{33}\text{cm}^{-2}\text{s}^{-1}$]	5.0	13.8	20.9	21.0	10
Integrated luminosity delivered [fb^{-1}]	4.2	38.5	50.2	63.3	-
Average pileup	13.4	25.1	37.8	36.1	25.0

Table 2.1.: Parameters of the LHC from year 2015 to 2018 compared to the design values [77], showing the beam parameters [80], the luminosity and pileup measured by ATLAS [78].

a cylindrical shape with two end-caps in the forward and backward regions, covering a maximum angle of 1 degree towards the beam line, allowing it to cover a solid angle of almost 4π. Looking inside, the detector has an onion like structure with a multi-layer design. Each layer of the detector is designed using different detection techniques, such that different signatures are measured for different types of particles. Being the single largest detector ever built, the length of the cylindrical detector extends up to 44 m, with a diameter of 25 m; this allows the placement of a large magnet system and muon detector. Figure 2.3 shows the layout of the whole ATLAS detector, showing the subsystems and the size.

2.2.1. Coordinate System

The ATLAS detector adopts a right-handed Cartesian coordinate system, with the origin defined as the nominal collision point. The x-axis points from the origin towards the center of the LHC ring, and the y-axis points vertically upward. To form a right-handed coordinate system, the z-axis is therefore defined to be parallel to the counter-clockwise rotating beam.

As the detector is cylindrical in shape, the use of a cylindrical coordinate system is also common. The azimuthal angle ϕ is measured around the beam axis from the positive x-axis, and the polar angle θ is the angle measured from the positive z-axis. In the transverse plane (x-y plane), the radial distance from the beam axis is defined as $r = \sqrt{x^2 + y^2}$. As most of the particles detected are ultra-relativistic, the pseudorapidity η is a more commonly used quantity instead of θ; it is given by:

$$\eta = -\ln \tan\left(\frac{\theta}{2}\right). \tag{2.4}$$

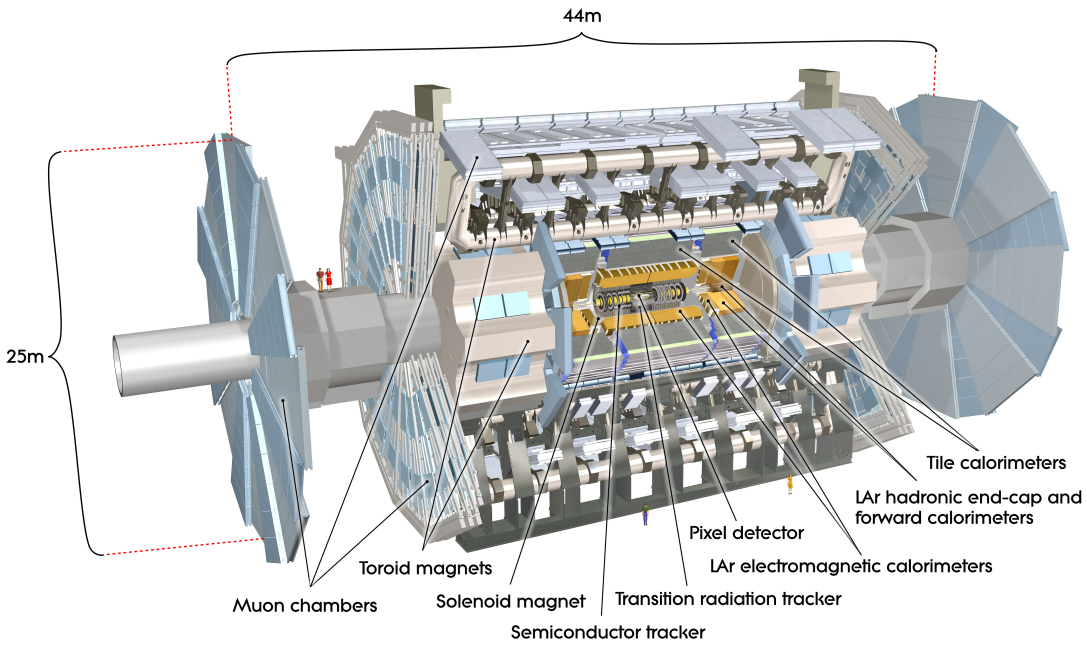

Figure 2.3.: The layout of the ATLAS detector [81].

2.2.2. Subsystem Overview

The ATLAS detector consists of several subsystems which are designed to measure different signatures from different particles. These subsystems include the inner detector, the electromagnetic calorimeter, the hadronic calorimeter and the muon spectrometer. Moreover, there are a magnet system and a trigger system, which do not directly measure the particles, but they are important for the operation of the detector.

Magnet System

Sets of magnets are implemented in the ATLAS detector to create a strong magnetic field. The magnetic field bends the charged particles to allow for momentum and charge measurements. Figure 2.4 shows the layout of the magnets. A magnetic field of 2 T in the z-direction, which the inner detector is submerged in, is created by the solenoid magnet. The larger toroidal magnets, which are outside of the calorimeters, provide a magnetic field that surrounds the detector in the transverse direction. The two smaller toroidal magnets are located in the end-cap regions. The magnetic field strength is about 0.5 T in the barrel region and 1 T in the end-cap regions.

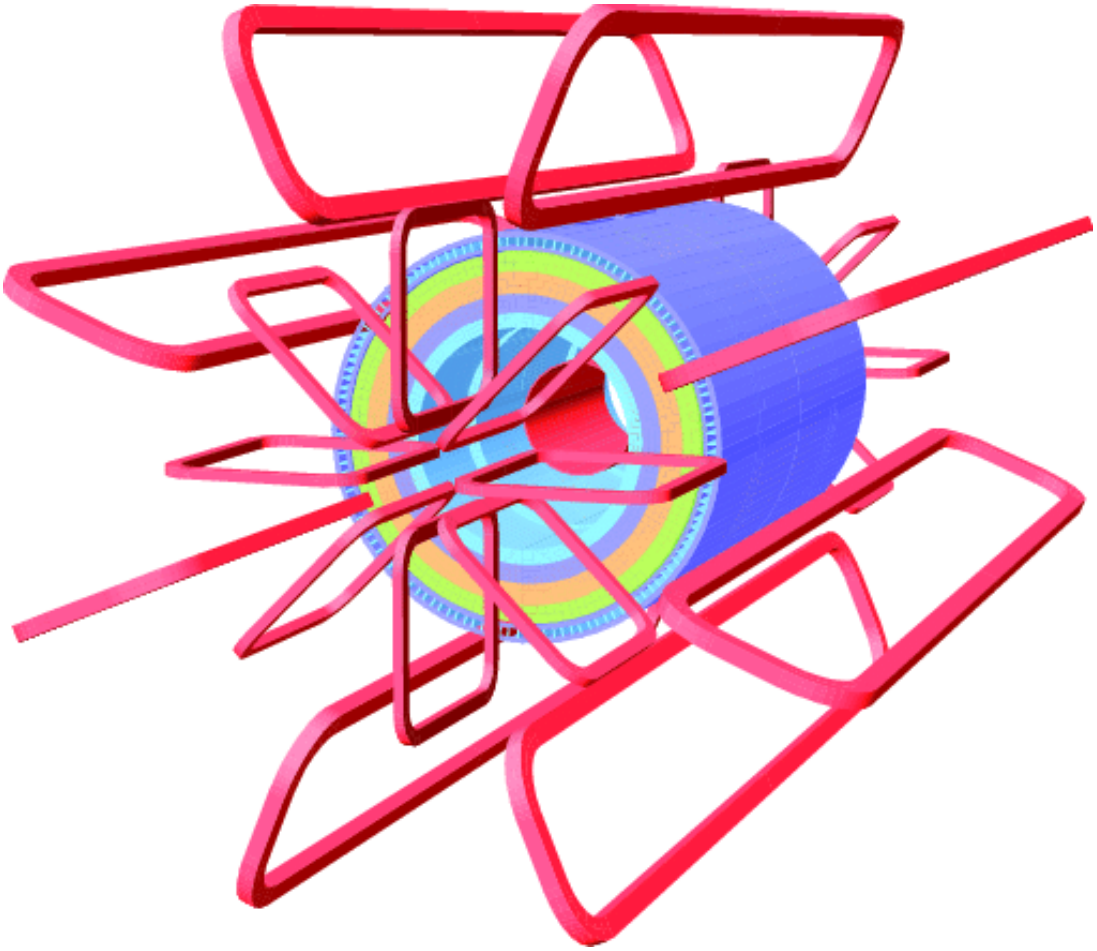

Figure 2.4.: The layout of the magnets in the atlas detector [81].

Inner Detector

The inner detector (ID) is the sub-detector of ATLAS that is the closest to the beam axis. It consists of three sub-detectors, including a silicon pixel detector (pixel) with the Insertable B-Layer (IBL), a silicon micro-strip detector (SCT), and a transition radiation tracker (TRT). With the high granularity silicon based pixel detector and SCT placed close to the collision point, accurate space points can be measured when charged particles pass through. Figure 2.5 shows the layout of the ID. For each tracking sub-detector, the distance from the beam axis is also shown.

The IBL was installed in May 2014 as an upgrade to the ID. It is the innermost pixel layer, which is only 33.25 mm from the beam axis. The system consists of 14 staves made up of over 12 million silicon pixels of a typical size of 50 µm × 250 µm each. With such small pixel size, the position resolution is 8 µm in the transverse plane and 40 µm along the beamline. With the addition of the IBL, the impact parameter resolution of low momentum particles (transverse momentum of 0.5 GeV) was improved by more than 40%.

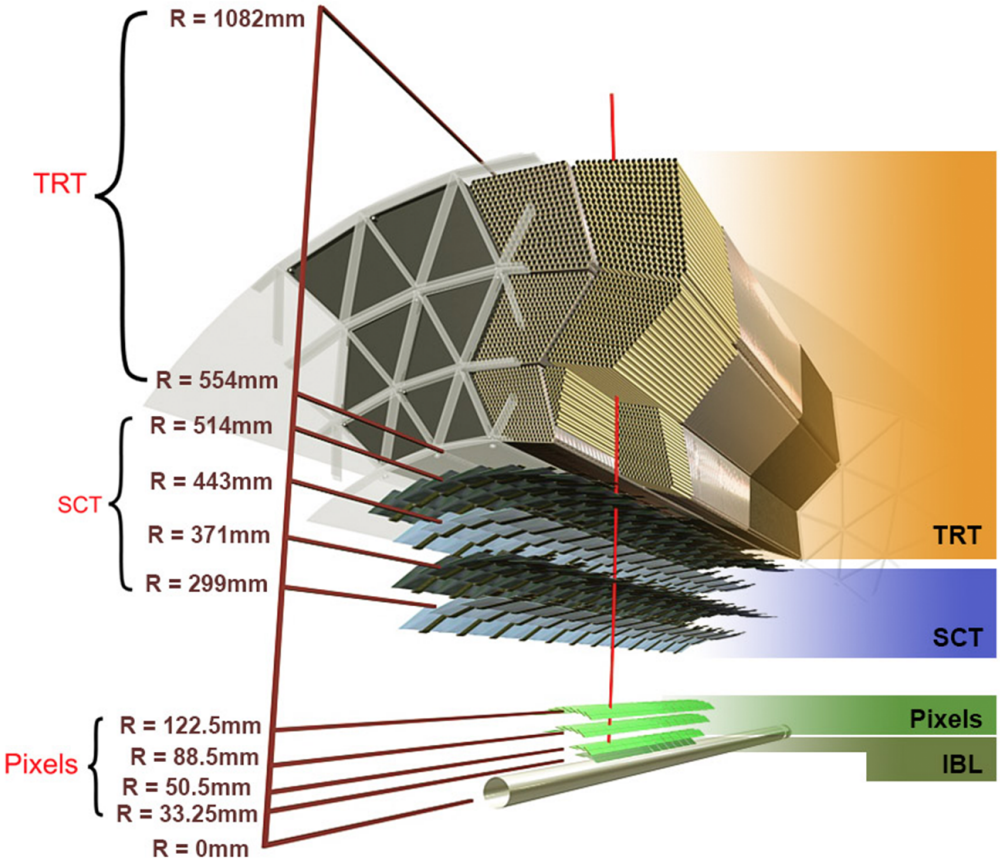

Figure 2.5.: The layout of the ID [81].

The other parts of the pixel detector consist of three layers in the barrel, and three disks for each in the end-caps, together covering the region of $|\eta| < 2.5$. The three layers in the barrel are 50.5 mm, 88.5 mm and 122.5 mm away from the beam axis. There are 1744 pixel-sensor modules, each containing 46080 pixels with a typical size of 50 µm × 400 µm. The intrinsic position resolution is 10 µm in the transverse plane and 115 µm along the beamline.

The SCT consists of 4088 silicon micro-strip modules, arranged in four layers in the barrel and 9 wheels for each of the two end-caps. The four layers in the barrel are 299 mm, 371 mm, 443 mm and 514 mm away from the beam axis; because of the further distance from the beam axis, the particle density is lower and a lower granularity is required. Each micro-strip is 80 µm in the barrel and 60 µm or 80 µm in the end-cap. In the barrel (endcap) region, the position resolution is 17 µm for the transverse coordinate and 580 µm for the longitudinal (radial) coordinate.

The TRT is a sub-detector based on drift tube detectors instead of silicon modules. Each of the 300 thousand drift tubes is 4 mm in diameter, with length varying from 37 cm up to 144 cm. Xenon gas is put in each of the tubes, to allow ionization to take place when particles pass through. Each tube also consists of a wire in the middle to collect

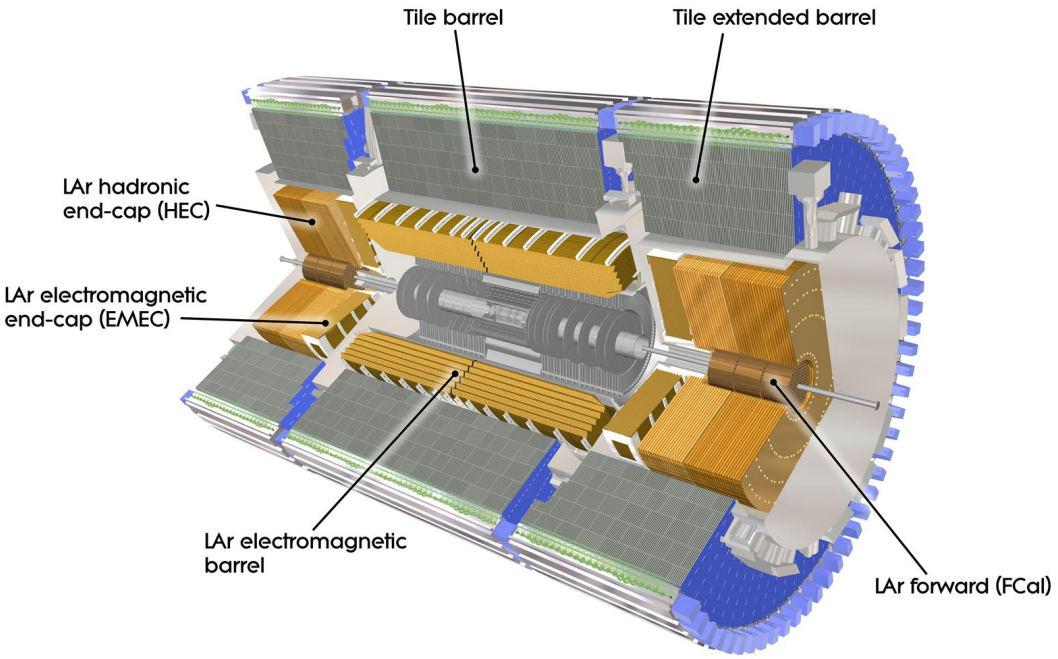

Figure 2.6.: The layout of the calorimeters [81].

the ionized particles and measure the drift time. The space between the tubes is filled with polymer fibers and foils, to create transition radiation when relativistic particles pass through. The position resolution is 130 µm in the transverse coordinate, which is worse than the silicon based sub-detector. Despite the low resolution in spatial coordinates, TRT provides the unique measurement of transition radiation, which is important for identifying electrons.

Electromagnetic Calorimeter

After particles escape from the ID, they need to be absorbed and measured. In particular, electrons and photons can induce electromagnetic showers via bremsstrahlung and pair production. The electromagnetic calorimeter, which is placed just outside of the ID and the superconducting solenoid, is therefore designed as a sampling calorimeter, to induce, absorb and measure the showers with alternated layers of materials. The ATLAS calorimeter uses lead plates as the absorbing material, causing the incoming particles to shower. The lead plates are also filled in-between with the active material - liquid argon, to measure the energy of the shower. For an electromagnetic shower with energy E, the designed energy resolution σ_E is given by the relation:

$$\frac{\sigma_E}{E} = \frac{10\%}{\sqrt{E(\text{GeV})}} \oplus \frac{0.5\%}{E(\text{GeV})} \oplus 0.7\%, \tag{2.5}$$

where E is the energy of the particle measured in the unit of GeV and $\oplus$ is the operator of sum in quadrature.

Hadronic Calorimeter

The hadronic calorimeter is located just behind the electromagnetic calorimeter. Analogously, hadrons also produce particle showers, but with both hadronic interactions and electromagnetic interactions. Therefore, the hadronic calorimeter is designed to absorb showers with a similar principle. Because of the relatively large size of showers induced by hadrons, the showers can be initially induced in the electromagnetic calorimeter, but not fully absorbed, and extend to the hadronic calorimeter. For instance, a shower from a 100 GeV hadron can extend for an order of 2 m, easily exceeding the thickness of the electromagnetic calorimeter. Figure 2.6 shows the layout of the calorimeters, which together cover a region of $|\eta| < 5$. The barrel and extended barrel region consist of scintillating tiles as active material and steel as absorber material, while the forward region consists of lead-liquid argon as active material and copper as absorber material. The materials are structured in alternating layers as in the electromagnetic calorimeter; the main difference is the choice of materials of lower atomic number, which are better at absorbing hadrons. For a hadronic shower with an energy E, depending on η, the energy resolution σ_E is given by:

$$\frac{\sigma_E}{E} = \frac{50\%}{\sqrt{E(\text{GeV})}} \oplus 3\%, \text{ for } |\eta| \leq 3, \tag{2.6}$$

$$\frac{\sigma_E}{E} = \frac{100\%}{\sqrt{E(\text{GeV})}} \oplus 10\%, \text{ for } 3 \leq |\eta| \leq 5. \tag{2.7}$$

Muon Spectrometer

The muon spectrometer is the outermost and largest sub-detector of ATLAS. As the name suggests, the main purpose of the system is to detect and identify muons, which are not absorbed by the calorimeters. Given the large size, the muon spectrometer can measure high momentum muons more efficiently compared to the inner detector, due to the low curvature. The muon spectrometer consists of four sub-systems, and they are categorized into Precision Chambers and Trigger Chambers. The Precision Chambers include the Monitored Drift Tubes (MDT) and Cathode Strip Chambers (CSC). The MDT measure positional information with a resolution of 35 µm in the z direction, while the CSC has a resolution of 40 µm in the bending direction and 5 mm in the orthogonal direction. The Trigger Chambers include the Resistive Plate Chambers (RPCs) and the Thin Gap Chambers (TGCs). These sub-systems are wired gas chambers that provide timing information and fast identification of muons for triggering. Signals detected by the muon system and the ID can be combined together and refitted to provide a significant improvement of the momentum resolution.

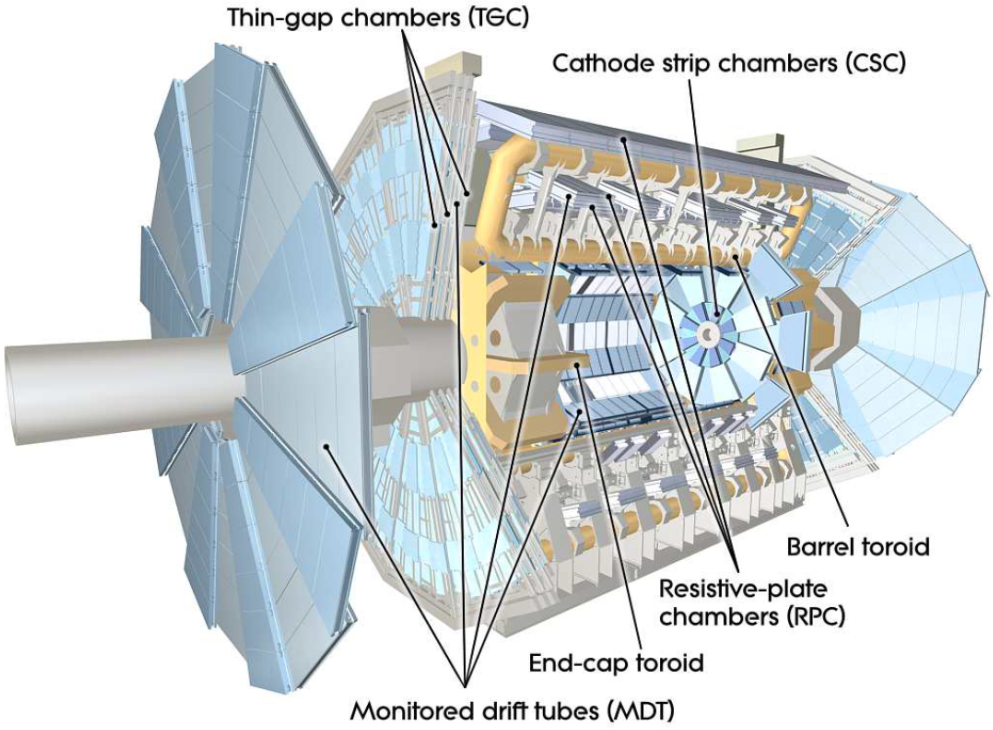

Figure 2.7.: The layout of the muon spectrometer [81].

Trigger System

Given a proton bunch spacing of 25 ns, bunch crossing occurs at a rate of 40 MHz. This means raw data of the whole detector is being produced at a rate of petabytes per second, which is impossible to store and analyze by the standard of today. Therefore, a trigger system has been developed to partially analyze the events, in order to identify the interesting ones to store, while discarding the others. With this pre-selection system, events of different physical signatures can be kept at a desired proportion, allowing a large variety of physics study in ATLAS. Currently, the ATLAS trigger system consists of two levels, each reducing the event rate significantly.

The first level is the Level-1 (L1) triggers, which are implemented at a hardware level in the detector for the fastest decision possible. The L1 triggers are mostly driven by the calorimeter and muon systems, targeting specifically muons, photons, electrons and jets. With fast processing, information like muon momentum and invariant mass are also estimated, allowing a decision based on physical signatures of particles. Since the specific particles are typically localized, the L1 trigger system also defines Regions of Interest (RoI), within which the information of the detector is fully read out and sent to the next level. With the L1 trigger system, the event rate is reduced from 40 MHz to 100 kHz.

After the L1 triggers, the events are sent to the software-based High-level triggers (HLT). With a much reduced incoming event rate, the HLT can perform a more detailed

event selection. At this level, physics objects are reconstructed and tracking information can be obtained; for instance, quantities like the goodness of fit, sum of momenta and angular separation of particles are available. The HLT also consists of more specific triggers with stricter topological requirements. With the HLT, the event rate is further reduced from 100 kHz to 1 kHz, which corresponds to around 1 gigabyte per second of data being recorded.

Chapter 3.

Event and Object Reconstruction

During the operation of ATLAS, proton-proton collisions produce a large variety of particles with a wide range of energy. When the particles produced traverse through the detector layers, they can interact with different sub-detectors, leaving a variety of signatures that are recorded as digital signals. By using dedicated reconstruction algorithms, these digital signals are reconstructed and combined into physics objects such as tracks, vertices, muons, jets, tau leptons and more. These objects store kinematic and positional information of different particles, which are crucial for further analysis.

3.1. Tracks

Tracks represent the trajectories of charged particles. As charged particles traverse through the Inner Detector, they can ionize the pixel and strip silicon sub-detectors and the gases of the TRT sub-detector, leaving energy in different detector layers; such signature on the detector layers is referred to as a hit. By reading out and clustering the hits, followed by a pattern recognition approach to perform track finding and track fitting, the trajectory and kinematics of the particles are reconstructed, and stored in the track objects. Tracks are therefore one of the most fundamental physics objects reconstructed in ATLAS.

3.1.1. Parameterization

Since the inner detector is immersed in the magnetic field provided by the central solenoid magnet, the trajectory of a charged particle can be approximately described by a helix. The tracks are conventionally parameterized using the perigee parameterization. Figure 3.1 illustrates the perigee parameterization for a track with momentum p. The five perigee parameters with respect to a reference point are defined as follows:

- q/p is the charge of the particle divided by its momentum.
- ϕ is the angle between the track and the x-axis in the x-y plane.
- θ is the angle between the track and the z-axis in the x-z plane.

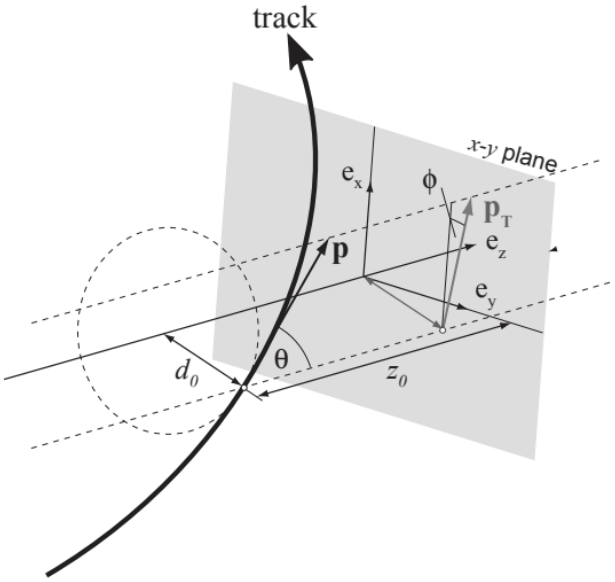

Figure 3.1.: Illustration of the perigee parameters of a track [82].

- d_0 is the shortest distance between the track and the reference point in the x-y plane.
- z_0 is the distance in z between the reference point and the point on the track used to evaluate d_0.

Additionally, the transverse momentum p_{T} and the pseudorapidity η are also commonly used when describing tracks and particles. The pseudorapidity is calculated by the same formula as in Equation (2.4), while the transverse momentum is given by:

$$p_{\mathrm{T}} = p \cos\theta \tag{3.1}$$

3.1.2. Fitting Strategy

ATLAS mainly uses an inside-out strategy, which starts with building tracks from hits measured by the pixel and SCT detectors, then extrapolate the track candidates to add in more hits from the SCT and TRT detectors [83, 84]. Starting with hits in the SCT and TRT detectors, a threshold on the amount of charge is first set to measure the time-over-threshold (ToT), which is directly proportional to the energy deposit. Based on the energy deposit and the positional information, a clustering algorithm [85] is used to group the hits to form clusters. The resultant clusters contain the three-dimensional position, with the corresponding error, that charged particles travelled through. The track seeds, which are track segments, are then formed by fitting three clusters in different layers of the ID.

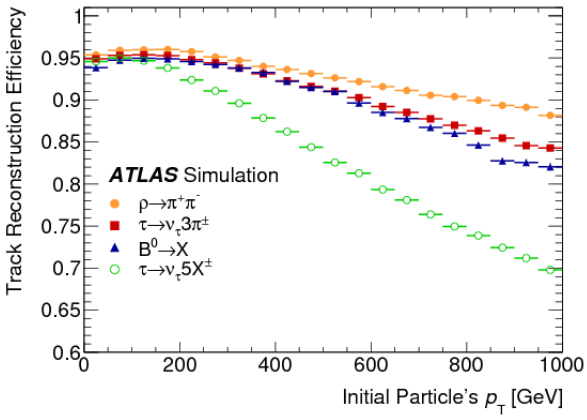

Figure 3.2.: Track reconstruction efficiency as a function of the p_{T} of the initial particle for daughter particles from different decays [84].

With the set of initial track seeds, a combinatorial Kalman filter [86] is then used to build track candidates by refitting the track seeds with additional clusters from the pixel and SCT detectors. This process is repeated until the track candidates contain at least 7 pixel and SCT clusters. To allow for maximum number of combinations of track candidates, different track candidates are allowed to share clusters. Moreover, the filter also creates multiple track candidates per seed if there is more than one compatible cluster. With such an approach, many incomplete or fake tracks (tracks that do not correspond to the trajectories of charged particles) are also created at the same time. Moreover, ambiguity of track-cluster-association exists, because multiple track candidates built this way may share the same clusters that correspond to a single particle.

To solve the above problem, an ambiguity solver based on track score, which is a measure of the track quality, is employed. In general, clusters associated to a track increase the score, while missing clusters in a layer reduce the score. The goodness of fit χ^2 is also considered, to reduce the score for candidates with a poor fit. The ambiguity solver then processes the tracks in descending order of track score, imposing the criterion that no cluster can be shared by more than two tracks and a track can have no more than two shared clusters, giving priority to tracks with higher track score.

The tracks are finally extrapolated outward to the TRT and then refitted with the additional TRT hits to recalculate the track score. The track score is then compared to the original track score and TRT hit is added to the track only if the track score is improved. The resulting tracks are referred to as ID tracks. Figure 3.2 shows the track reconstruction efficiency. Figure 3.3 shows the resolution of impact parameters.

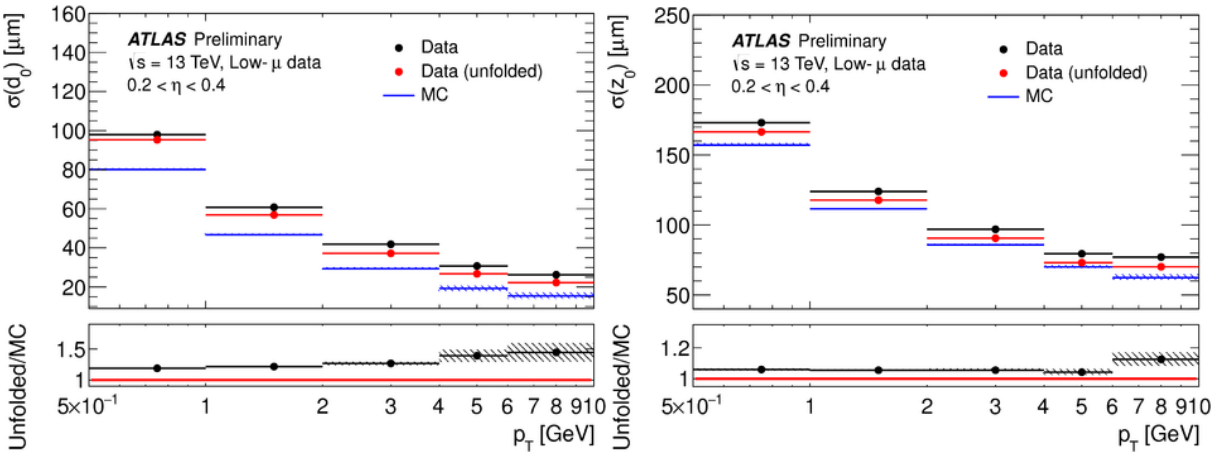

(a) (b)

Figure 3.3.: Resolution of (a) d_0 and (b) z_0 of tracks as a function of p_{T} compared to Monte Carlo simulation [87].

3.2. Vertices

A vertex is the spatial position where particles are produced or decay. Several vertices can be present in a collision event. In ATLAS, the primary vertex is the position at which a p-p collision occurs, while the secondary vertex is where a particle decays after flight.

3.2.1. Primary Vertices

Primary vertex reconstruction in ATLAS is based on a collection of ID tracks for that particular event, and is separated into two stages: seed finding and vertex fitting [88, 89]. For the tracks to be considered in the construction of a vertex, the tracks must pass the following requirements:

- p_{T}>500 MeV and $|\eta| < 2.5$
- Number of silicon hits $\geq 9(11)$ if $|\eta| < 1.65$ ($|\eta| \geq 1.65$)
- Hits in the first two pixel layers ≥ 1
- Additional criteria on shared hits and holes (missing hits in layers)

In the seed finding stage, vertex seeds are first formed in the vicinity of the beam spot in the x-y plane. The beam spot is the beam envelope of where the p-p collisions occur. To obtain the z-coordinates, a finder recursively scans the z_0 of the tracks to estimate the point of maximum track density along the beam axis. After the seeds are formed, the set of tracks with the closest impact parameter significance are assigned to seed the vertex fit.

Before fitting, the track parameters are linearized at the position of the fit. The fitting of the vertices is done using an annealing method with an adaptive Kalman filter on

weighted tracks [90]. For a track with a track-to-vertex distance d_i and uncertainty σ_i, the track compatibility (goodness of fit) with the vertex position can be written as:

$$\chi_i^2 = \frac{d_i^2}{\sigma_i^2} \tag{3.2}$$

The track weight ω_i is defined as:

$$\omega_i = \frac{1}{1 + e^{-\frac{1}{2}(\chi^2_{\text{cut}} - \chi_i^2)/T}} \tag{3.3}$$

where $\chi^2_{\text{cut}} = 9$ is a constant criterion value on χ^2 and T is the temperature for annealing. During annealing, the temperature is decremented in stages, slowly going from one to zero, increasing the importance of the compatibility gradually. As the temperature approaches closer to zero, the exponential term decreases closer to zero for tracks with $\chi^2 < 9$ (or three standard deviations), compatible tracks therefore will have a weight close to unity. On the other hand, the exponential term increases drastically for incompatible tracks with $\chi^2 > 9$, decreasing the weight close to zero.

After the vertex is fitted and the position is determined, the new vertex is required to contain at least two tracks. For each accepted vertex, tracks with weight greater than 0.01 or less than seven deviations away from the vertex are removed from the pool of available tracks for further iterations; while tracks failing both criteria are disassociated from the vertex and remain available for further iterations.

The above procedure is repeated iteratively until there are fewer than two tracks available for vertex fit, or fewer than two tracks are close enough for fitting or the maximum allowed number of vertices are reached (currently 200). After the entire procedure, a list of primary vertices is obtained and ranked in descending order of sum of associated track transverse momentum $\sum p_{\text{T}}^2$. The primary vertex with the highest $\sum p_{\text{T}}^2$ in each event is identified as the default hard scattering vertex, which is taken as the default position where particles are produced, and where short-lived particles decay.

3.2.2. Secondary Vertices

Unlike short-lived particles, long-lived particles can travel for a few mm or more before they decay, therefore their decay points are displaced from the primary vertices. A simple method to construct secondary vertices is to select ID tracks that satisfy kinematic criteria of a target resonance, then fit the selected tracks with the same model used for primary vertex reconstruction. Since these tracks do not originate from a p-p collision, they should not be used in reconstruction of primary vertices. Therefore, the fitting procedure of the primary vertices has to be re-done without the above-mentioned tracks; this is known as primary vertex refit. Moreover, the tracks associated to the secondary vertices can also be refitted with the position of the secondary vertices to improve the precision of the track parameters; this is known as track refit.

3.3. Muons

In ATLAS, muons are of particular importance; the reconstruction and identification of muons are key to many different physics results, including the discovery of the Higgs boson and Standard Model measurements. Due to its minimum-ionising nature and long lifetime, it is the only type of particle that leaves a signature in every layer of the ATLAS detector. Because of this, muon reconstruction is performed independently in the ID and MS and then combined to give more precise measurements [91].

The combined ID-MS muon reconstruction is performed using different algorithms and strategies, to give the following four types of muons:

- **Combined (CB) muons**: ID tracks and MS tracks are reconstructed independently and combined with a global refit that uses the hits from both the ID and MS. An outside-in strategy is used, in which the MS track is extrapolated inward to look for an ID track. Figure 3.4 shows the resolution of CB muon compared to that of ID tracks.
- **Segment-tagged (ST) muons**: ID tracks are extrapolated to MDT or CSC chambers to match with local MS track segments. This is useful for muons with low p_{T} that cross only one layer of MS chambers.
- **Calorimeter-tagged (CT) muons**: ID tracks are extrapolated to the calorimeters, which measure energy deposit by the muons. Based on the energy deposition, the tagging algorithm then determines whether the track is a muon-like or a pion-like particle with a cut-based approach. CT muons have a relatively low purity; it is designed to specifically identify muons in the region $|\eta| < 0.1$, where the MS has limited coverage.
- **Extrapolated (ME) muons**: MS tracks are extrapolated to the interaction point taking into account the estimated energy loss of the muon in the colorimeters. ME muons can extend the acceptance in the region $2.5 < |\eta| < 2.7$, which is not covered by the ID.

Of the four types of muons, CB muons are by far the most precise ones with the highest purity. Therefore, when multiple muon types share the same ID track, preference is given to CB muons, to ST and followed by CT. While the ME does not make use of ID, the ambiguity of MS track association is resolved by selecting the track with better fit quality and larger number of hits. Multiple working points are defined to reject muons from light hadron decays, which in general result in low quality muon tracks, due to a significant change in trajectory within the detector [93]. Figure 3.5 shows the reconstruction and identification efficiency for different working points.

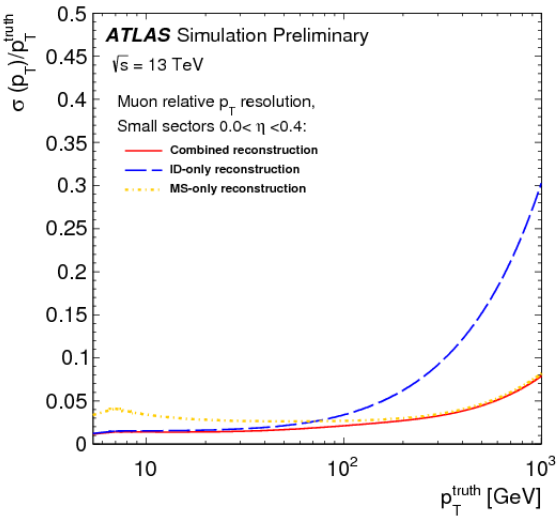

Figure 3.4.: The p_{T} resolution as a function of p_{T} for ID tracks, MS tracks and CB muons [92].

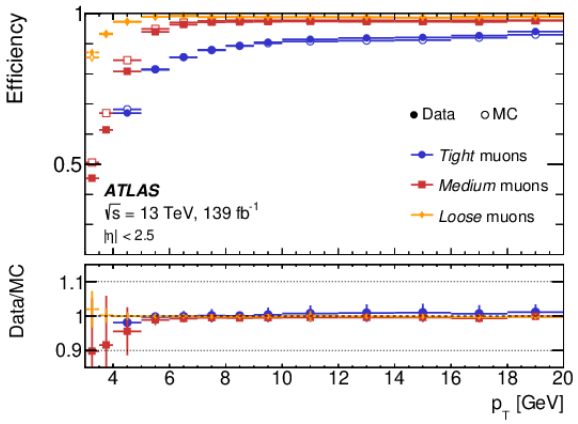

Figure 3.5.: Muon reconstruction and identification efficiency as a function of p_{T} for different working points [93].

3.4. Electrons and Photons

Electrons in ATLAS induce a shower in the EM calorimeter, while photons can convert into an electron-position pair before reaching the EM calorimeter (converted photons), or directly induce a shower in the EM calorimeter (unconverted photon). All of the above interactions produce a similar signature in the EM calorimeter, therefore similar and parallel strategies are used for both electron and photon reconstruction. Other information such as the shape of the EM shower, the compatibility with track, and association to vertex are then considered to further distinguish the processes.

Firstly, a sliding-window algorithm is used to gather energy deposits in nearby calorimeter cells into calorimeter clusters [94]. The tracks are then matched to the calorimeter clusters and refitted. These tracks are then used for building of electron candidates and conversion vertices [95, 96]. The clusters and tracks that match with the conversion vertex further form conversion photon candidates; the conversion photon candidates can either consist of two close-by opposite sign tracks, or a single track in cases where one of the track is too soft for reconstruction.

Since the reconstruction of photons and electrons is done in parallel, a selection procedure is also needed. The determination of whether a cluster is from an electron, a converted photon or an unconverted photon is as follows [97]:

- **Electron**: an electron specific track matching is performed with a tighter requirement on the distance in η and ϕ between the track and the calorimeter cluster. The matching condition also accounts for energy loss due to Bremmstrahlung and the number of hits in the ID. The matched track and cluster are then refitted to form an electron candidate.
- **Converted photon**: clusters matched to a track which is consistent with a conversion vertex candidate are considered converted photon candidates. If the cluster is also reconstructed as an electron candidate, the electron track is compared with the track(s) of the converted photon candidate. If the electron track coincides with the tracks from the conversion vertex, the object is considered as a converted photon. Otherwise, the converted photon candidate is removed, unless the electron track p_{T} is smaller than the p_{T} of the converted photon candidate.
- **Unconverted photon**: clusters that do not match to any of the tracks nor any of the conversion vertex candidates are reconstructed as unconverted photon candidates.

Since tracks are necessary for the reconstruction and distinction of photons and electrons, they are exclusively reconstructed within the central region of the ATLAS detector $|\eta| < 2.7$. Because of high level of hadronic activity in the LHC, dedicated multivariate discriminators are developed to distinguish electrons and photon candidates from hadronic backgrounds. Electron and photon candidates are required to pass a set of criteria to reach a desired purity and efficiency as defined by the algorithms [98]. Figure 3.6 shows the identification efficiency of electron, converted photons and unconverted photons.

3.5. Jets and Hadronic Tau Leptons

As quarks and gluons hadronize, showers of particles are produced; these collimated particles travelling in a cone are known as jets. To study quarks, gluons in the LHC, jet reconstruction and identification is therefore essential. Moreover, jets are also needed for the reconstruction of tau leptons that decay into hadrons.

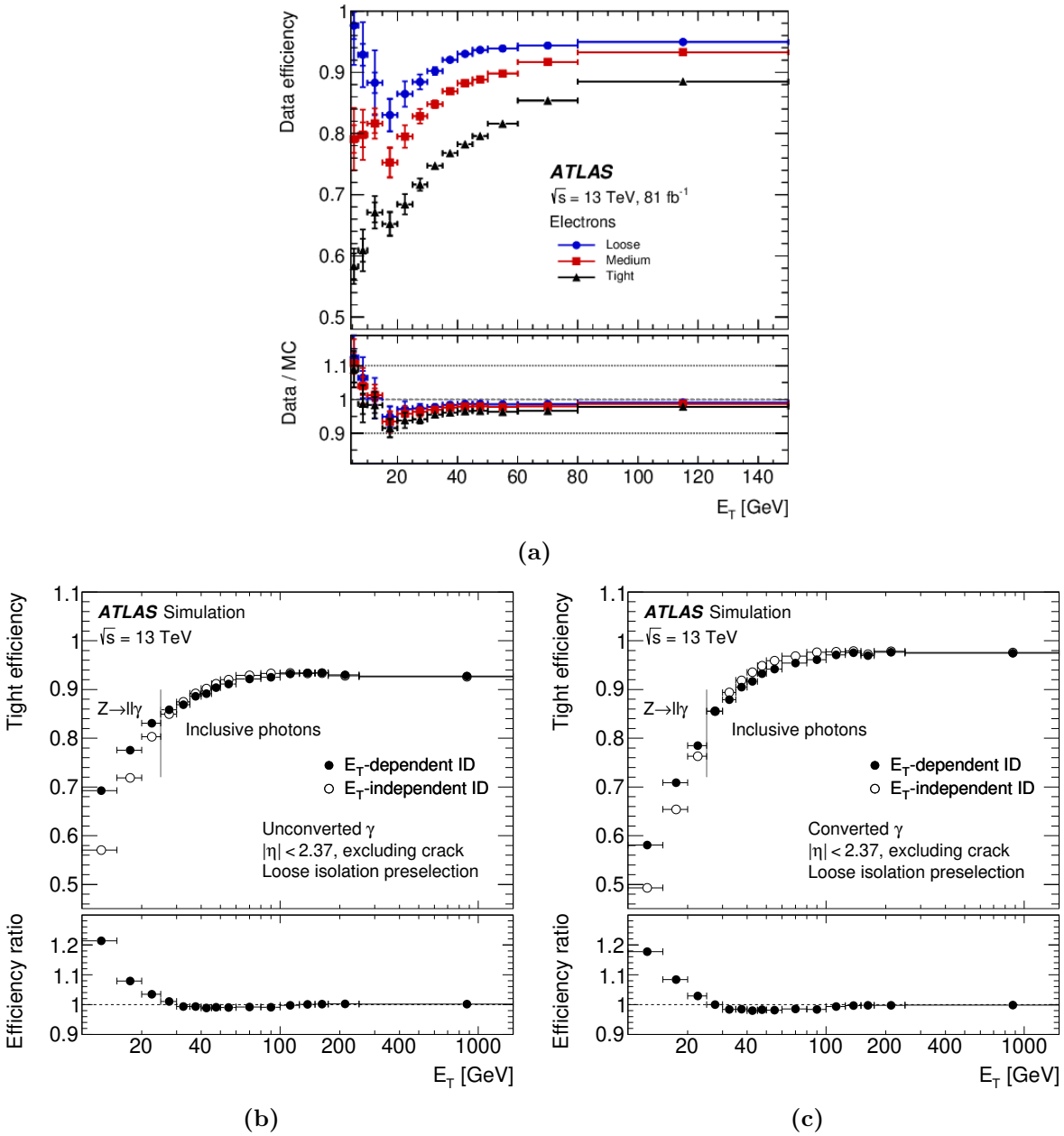

Figure 3.6.: The identification efficiency of (a) electron, (b) converted photons and (c) unconverted photons measured in data as a function of transverse energy E_T [98]. For electron, the efficiency is measured for different working points and also compared to the values measured in Monte Carlo simulation. For photons, the efficiency of the tight working point is displayed.

3.5.1. Jets

Jet reconstruction starts with searching and grouping of calorimeter cells. A seed cell is required to have an energy deposit exceeding 4σ, where σ is the expected noise of the cell [99]. The cells adjacent to the seed cells with larger than 2σ of energy are also added to form a topo-cluster [100].

To form the jets, ATLAS uses the anti-k_t algorithm [101]. In the algorithm, for two topo-clusters i and j, the relative distance between them is defined as:

$$d_{ij} = \min(p_{T,i}^{-2}, p_{T,j}^{-2}) \frac{(\Delta R_{ij})^2}{R^2} \tag{3.4}$$

where $p_{T,i}$ and $p_{T,j}$ are the transverse momentum of the clusters, ΔR_{ij} is the angular separation between the clusters and R is the cone size parameter which is chosen to be 0.4. For two topo-clusters, if d_{ij} is smaller than the distance to the beam line $d_{iB} = p_{T,i}^{-2}$, the two topo-clusters are combined to form a jet candidate. The procedure is repeated iteratively to add in topo-clusters, forming a set of jets.

In general, it is difficult to identify the flavour of the original quark in the jet, except if it is a b-jet (a jet that originates from the b-quark). Because the b-quark can hadronize into B hadrons, which typically have a lifetime of 1.5 ps, the decay vertex of the B hadrons can be a few mm displaced from the collision point. Therefore, the impact parameter of a b-jet is significantly larger than the other jets. In ATLAS, the impact parameters and other variables of jets are used to construct several multivariate algorithms [102] which identify a b-jet. This technique is known as b-tagging. Figure 3.7 shows the outputs of two commonly used b-tagging algorithms in ATLAS.

3.5.2. Hadronic Tau Leptons

Tau leptons decay either leptonically into electrons and muons or hadronically into hadrons; they are often referred to as leptonic tau τ_{lep} and hadronic tau τ_{had} respectively. Around one third of tau leptons decays leptonically and two thirds of tau leptons decay hadronically, containing one or three charged pions (kaons) in 72% and 22% of all cases respectively. Moreover, one or more neutral pions are often produced. These pions can induce hadronic showers in the calorimeters, which are reconstructed as one or more jets. Therefore, jets can be a starting point of reconstruction of τ_{had}.

Candidates of hadronic taus are first seeded by reconstructed jets, and required to have $p_{\text{T}} > 10\,\text{GeV}$ and $|\eta| < 2.5$, but those within the transition region between the barrel and forward calorimeters, $1.37 < |\eta| < 1.52$ are vetoed. To determine the primary vertex that produces the tau, p_{T} of ID tracks in the region $\Delta R < 0.2$ around the jet seed are first selected. The primary vertex that has the largest fraction of total p_{T} contributed by the selected tracks is then chosen as the primary tau vertex. A set of boosted decision trees (BDTs) is used to classify the tracks into core and isolation tracks; in cases where more than one core track exists, a tau secondary vertex is reconstructed from all core

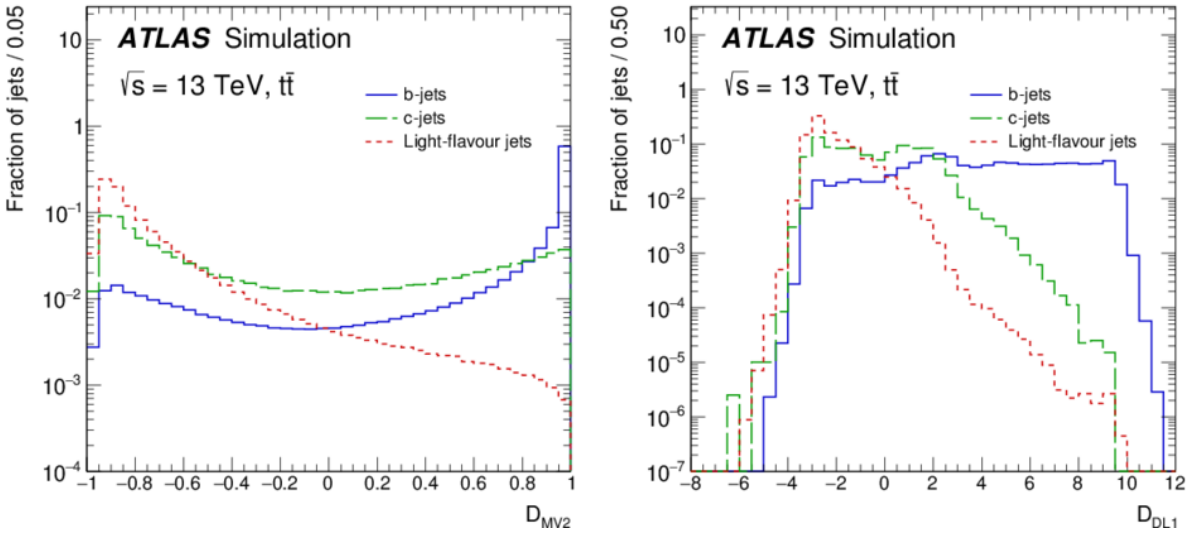

(a) **(b)**

Figure 3.7.: Distribution of the output discriminant of the (a) MV2 and (b) DL1 algorithms for different jets in simulated events [102].

tracks. The direction of the hadronic tau candidate is calculated by the vectorial sum of the vectors pointing from the tau vertex to the calorimeter topo-clusters within $\Delta R < 0.2$ of the seed jet barycenter. The momentum of the hadronic tau candidate is calibrated by a local hadronic calibration (LC) scheme [103, 104].

Unfortunately, jets produced by quarks and gluons can also be misidentified as a hadronic tau. To reject these backgrounds, a multivariate algorithm based on Boosted Decision Tree (BDT) has been developed [104]. The BDT is based on the narrow shower in the calorimeter, distinct number of tracks, and the displaced tau vertex due to a relatively long proper decay length of the tau lepton (87 µm). Several working points have been developed for desired purity and efficiency requirements. Figure 3.8 shows the reconstruction and identification efficiency for different working points. The reduction of efficiency for 3-prong τ_{had} at high-p_{T} is due to the smaller curvature and closer proximity of the decay product tracks.

3.6. Missing Transverse Momentum

At the collision points, the protons collide with no significant transverse momentum. By conservation of momentum, the vectorial sum of transverse momenta for all the particles produced should therefore vanish, which can be written as:

$$\sum_{\text{all particles}} \boldsymbol{p}_{\text{T}} = 0 \tag{3.5}$$

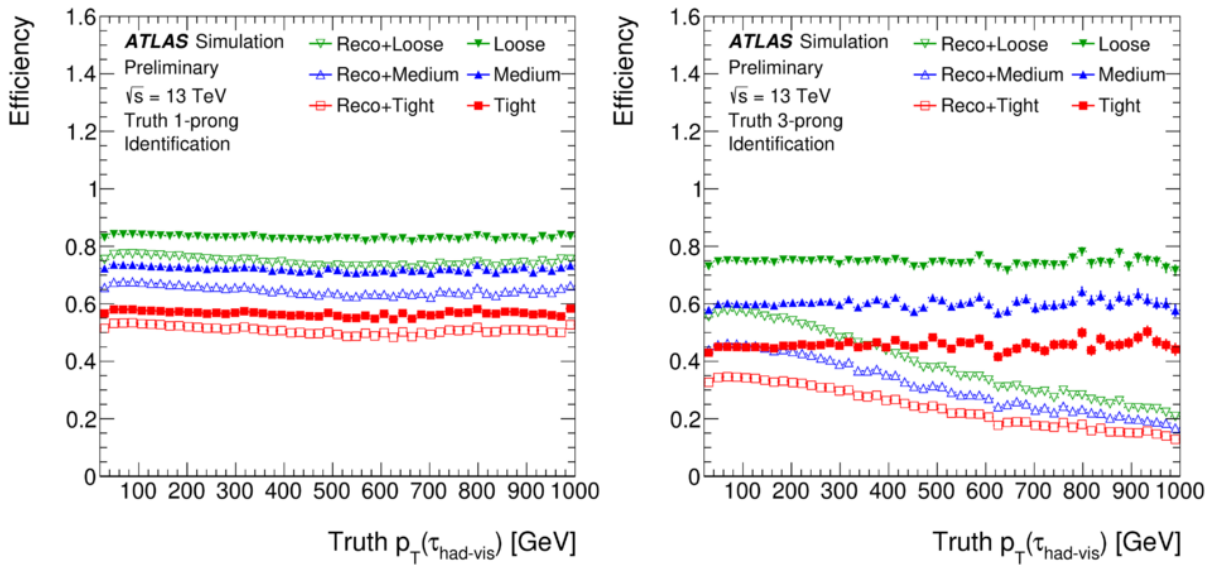

(a) **(b)**

Figure 3.8.: Efficiency of τ_{had} identification only (solid symbols) and combined reconstruction and identification efficiency (open symbols) as a function of τ_{had} p_{T} for (a) 1-track and (b) 3-track τ_{had} candidates; values are shown for three different working points [105].

However, not all the particles can be measured directly by the ATLAS detector. The summation can therefore be broken down into a visible part and an invisible part[106]:

$$\sum_{\text{visible}} \boldsymbol{p}_{\text{T}} + \sum_{\text{invisible}} \boldsymbol{p}_{\text{T}} = 0 \tag{3.6}$$

Since the invisible part is not directly detectable, it is referred to as missing transverse energy $\mathbf{E}_{\text{T}}^{\text{miss}}$, which can be calculated from the visible part:

$$\begin{aligned} \mathbf{E}_{\text{T}}^{\text{miss}} &= \sum_{\text{invisible}} \boldsymbol{p}_{\text{T}} \\ &= -\sum_{\text{visible}} \boldsymbol{p}_{\text{T}} \end{aligned} \tag{3.7}$$

In ATLAS, the visible part consists of contributions from high-p_{T} objects, such as electrons, photons, jets, hadronic tau leptons and muons; it also includes tracks and energy depositions that are not reconstructed as high-pt objects. Therefore, the visible contributions can be separated into two terms:

$$\mathbf{E}_{\text{T}}^{\text{miss}} = -\sum_{\substack{e,\gamma,\tau_{\text{had}} \\ \mu,\text{jet}}} \boldsymbol{p}_{\text{T}} - \sum_{\text{soft}} \boldsymbol{p}_{\text{T}} \tag{3.8}$$

The sum over high-p_{T} objects is referred to as the hard part, while the sum over soft objects is referred to as the soft part. The soft term is often calculated using the ID

tracks, but it is also possible to use the calorimeter topo-clusters. The calorimeter-based calculation is proven to be inferior to the track-based calculation in most cases, due to larger residual dependence on pile-up [107].

Chapter 4.

Motivation and Acquiring D Meson Data

Measurement of D meson production is one of the most fundamental and important measurements in heavy flavour physics. The production of D meson is a crucial background in searches for new physics phenomena, and the measurement of D meson production cross section provides a direct constraint on perturbative quantum chromodynamics (QCD). On the other hand, the presented measurements are important for searches for new physics appearing in heavy flavour decays such as lepton flavour violating tau decays at the LHC. In particular, the search of $D_s^{\pm} \to \tau(3\mu)\nu$ would not be possible without the precise measurement of the $D_s^{\pm}$ production cross section.

To measure the $D^{\pm}$ and $D_s^{\pm}$ mesons produced at the LHC, an analysis has been conducted making use of the decay channel $D^{\pm}/D_s^{\pm} \to \phi(\mu\mu)\pi$. The final state of two muons and one pion is fully reconstructed and identified, allowing the extraction of the yield. Because of the sizeable error contribution from experimental uncertainties and the branching ratios, the analysis strategy is based on a set of loose cuts placed on di-muon mass and vertexing variables to retain statistics; this allows for fitting procedures to be performed in bins of different variables and a data-driven study of systematic uncertainties.

In this chapter, the current QCD calculation scheme of heavy flavour production is introduced. Then, the data collected and the simulated data used in this analysis are described. The pre-processing of data, including candidate reconstruction, event selection and trigger choice, are also presented.

4.1. Motivation

4.1.1. Heavy Quark Production

In the QCD calculation of hadron production, the parton density function (PDF) of the proton and quark masses play an important role. One basic question is whether the heavy quarks, i.e. the charm quark and the bottom quark, should be included in the proton with their own PDF. In traditional calculation schemes, there are two approaches: the Fixed-

Flavor-Number (FFN) scheme and the Zero-Mass Variable-Flavor-Number (ZM-VFN) scheme [108].

In the FFN scheme, the heavy quarks are not included as a parton in the proton, and the heavy quarks are produced only in the hard scattering process. The heavy quark QCD corrections are calculated by expanding the cross section in terms of $\alpha_s(m_Q)$, where m_Q is the mass of the heavy quark. Such calculations are however not reliable for $p_{\mathrm{T}Q} >> m_Q$ due to some neglected $p_{\mathrm{T}Q}$ terms. It is also referred to as the massive scheme.

In the ZM-VFN scheme, also known as the massless scheme, the approach is entirely different; the heavy quarks PDF are included as a parton in the proton. In the calculation scheme, the heavy quark mass is set to zero, and the heavy quark QCD corrections are calculated by expanding the cross section in terms of $\alpha_s(\mu_R)$, where μ_R is the renormalization scale. Unlike the massive scheme, the massless scheme is reliable only for $p_{\mathrm{T}Q} >> m_Q$ due to the zero heavy quark mass assumed.

In the LHC, hadrons of interest have energies ranging from few GeV to hundreds of GeV; therefore $p_{\mathrm{T}Q}$ is in an intermediate range where the above assumption of the schemes are not always valid. To provide more reliable predictions in the intermediate $p_{\mathrm{T}Q}$ range, the fixed-order plus next-to-leading logs (FONLL) and the general-mass variable-flavor-number scheme(GM-VFNS) calculation were developed.

FONLL

The FONLL calculation consists of three components: the heavy quark production cross-section calculated in perturbative QCD $d\sigma_Q^{\mathrm{FONLL}}$, the non-perturbative heavy flavor fragmentation D_Q^{NP} and the decay function describing the heavy hadron decay into leptons $g_{Q\to l}^{\mathrm{weak}}$. The principle of the scheme is to expand the massless scheme computation in powers of the strong coupling α_s, and replace a finite number of terms with their massive scheme counterparts. For instance, the FONLL scheme matches the massive and massless scheme predictions exactly up to $O(\alpha_s^3)$, giving a prediction that is reliable for $p_{\mathrm{T}Q} \approx m_Q$. Currently, the FONLL calculation is available for the $D^{\pm}$ meson, but not for the $D_s^{\pm}$ meson.

GM-VFNS

The GM-VFNS aims to combine the massless scheme with the massive scheme. In the calculation, the charm quark PDF evolves with massless evolution, but the heavy quark mass is retained in the hard-scattering calculation. The leading order processes $\gamma^* c \to c$ and $\gamma^* g \to c\bar{c}$ from the massless scheme and the massive scheme respectively, are both included in the GM-VFNS. With such approach, the calculation agrees with the massless scheme at high $p_{\mathrm{T}Q}$, and with the massive scheme at $p_{\mathrm{T}Q} \approx m_Q$. Unlike other calculations, GM-VFNS also considers the fragmentation to D mesons from light quarks and gluons in addition to the heavy-quark fragmentation. The GM-VFNS prediction is available for both $D^{\pm}$ meson and $D_s^{\pm}$ meson, which are the two D mesons of interest.

4.1.2. Measurements at the LHC

Measurements of heavy quark production at the Large Hadron Collider (LHC) serve as a means for testing perturbative quantum chromodynamics (QCD) calculations at the highest available collision energies. Since the current calculations suffer from large theoretical uncertainties, the experimental constraints on heavy quark production cross sections are important in searches for new physics phenomena, for which heavy quark production is often an significant background process.

Charmed mesons are produced in the hadronization of charm and bottom quarks, which are copiously produced in pp collisions at $\sqrt{s} = 13\,\text{TeV}$. The ATLAS detector [109] at the LHC has been used previously to measure $D^{*\pm}$, $D^{\pm}$ and $D_s^{\pm}$ meson production [110], but no measurement has been performed at 13 TeV nor has the production cross section of $D_s^{\pm}$ meson been measured differentially.

A study conducted by the CMS experiment reported the differential cross section of $D^{*\pm}$, D^0 and $D^{\pm}$ up to 100 GeV based on a partial dataset collected in 2016, but no measurement has been made on the non-prompt production fraction [111]. The ALICE experiment reported the non-prompt production fraction of D^0 and $D^{\pm}$ mesons in the range 1 GeV to 24 GeV, which observed a slight increasing trend in low p_{T} [112].

In light of the high luminosity in Run-II, the ATLAS experiment has collected a large amount of data, which enables the study of D meson production in rarer, but cleaner channels compared to Run-I. Notably, previous studies from Run-I, characterized by the relatively high uncertainties, especially at high p_{T}, underscore the need of statistics to precisely measure the shape of the differential cross section extending into the high p_{T} regime. Such measurements are crucial for validating theoretical models like the FONLL and GM-VFNS calculations, which aim to predict the behavior in the intermediate p_{T} range. Beyond theoretical QCD, the study of D meson production also holds significant implications for new physics searches, particularly in heavy flavour decays, such as lepton flavour violating tau decays, thus offering a dual facet of importance both in refining our understanding of the Standard Model and in probing beyond its current boundaries.

4.2. Dataset

4.2.1. ATLAS Data

The data used in this analysis were collected from 2016 to 2018 with the ATLAS detector in pp collisions at $\sqrt{s} = 13\,\text{TeV}$ at the LHC. Data collected during 2015 were not used for this study, because of the unavailability of low p_{T} di-muon trigger in the target di-muon invariant mass range. The analyzed data sample corresponds to an integrated luminosity of $137\,\text{fb}^{-1}$ after requiring each detector component is fully operational.

4.2.2. Monte Carlo Simulation

To model inelastic events produced in pp collisions, a large sample of Monte Carlo (MC) simulated events is prepared using the PYTHIA 8.212 [113] MC generator. The simulation is performed using leading-order matrix elements for all $2 \to 2$ QCD processes. Initial-state and final-state parton showering is used to simulate the effect of higher-order processes. The NNPDF 2.3 LO [114] parameterization is used for the parton distribution functions (PDF) of the proton. The charm quark and bottom quark masses are set to 1.5 GeV and 4.8 GeV respectively. The event sample is generated using the ATLAS A14 set of tuned parameters [115]. Separate samples are generated for initial states with charm or bottom-quarks to model the prompt and non-prompt production.

To enhance the available statistics in the fiducial phase space, generator filters have been developed placing cuts on the momentum of the generated muons and the pion according to the trigger thresholds. The quarks are then hadronized accordingly and only events where the quarks hadronized into $D^{\pm}$ or $D_s^{\pm}$ mesons are kept. For the purpose of efficiency, the decay branching ratios of $D^{\pm}/D_s^{\pm} \to \phi\pi$ and $\phi \to \mu\mu$ are set to 1. Table 4.1 shows the different processes generated.

The MC samples generated are separated into 3 MC campaigns, which mimic the relative amount of data collected in year 2016-2018. To strike a balance between simulation time and statistics, each process is simulated with the number of events as presented in Table 4.2. The generated events are passed through a full ATLAS detector simulation [116] based on GEANT4 [117] and processed with the same reconstruction program as used for the data.

MCID	Production quark	Process	Key
300596	bb	$D_s^+ \to \phi(\mu\mu)\pi$	bbPosDs
300597	bb	$D_s^- \to \phi(\mu\mu)\pi$	bbNegDs
300598	cc	$D_s^+ \to \phi(\mu\mu)\pi$	ccPosDs
300599	cc	$D_s^- \to \phi(\mu\mu)\pi$	ccNegDs
300750	bb	$D^+ \to \phi(\mu\mu)\pi$	bbPosD
300751	bb	$D^- \to \phi(\mu\mu)\pi$	bbNegD
300752	cc	$D^+ \to \phi(\mu\mu)\pi$	ccPosD
300753	cc	$D^- \to \phi(\mu\mu)\pi$	ccNegD

Table 4.1.: Summary of processes simulated.

Year	MC campign	Luminosity [fb^{-1}]	Number of generated events
2016	mc16a	33.40	1,000,000
2017	mc16d	44.63	1,250,000
2018	mc16e	58.79	1,750,000

Table 4.2.: Summary of MC campign.

Particle	Filter
$D^{\pm}$	$p_{\mathrm{T}} > 8000\,\mathrm{MeV}$, $\lvert\eta\rvert < 3.0$
$D_s^{\pm}$	$p_{\mathrm{T}} > 8000\,\mathrm{MeV}$, $\lvert\eta\rvert < 3.0$
μ	$p_{\mathrm{T}} > 3500\,\mathrm{MeV}$, $\lvert\eta\rvert < 3.0$
π	$p_{\mathrm{T}} > 700\,\mathrm{MeV}$, $\lvert\eta\rvert < 3.0$

Table 4.3.: Summary of kinematics filter.

Filter Threshold

To match with the kinematic region of interest, kinematic filters are added. The filter threshold is determined by the level of background and available triggers.

The range in η is set to allow the study of tracks within the ATLAS detector, and the range in p_{T} is set to allow the study of muon triggers with a p_{T} threshold down to 4 GeV. Table 4.3 shows the kinematic filters in use. The p_{T} distribution is plotted for the full set of data and MC samples as shown in Figure 4.1. It can be seen that the background level changes drastically at low p_{T}. The MC samples include prompt and non-prompt $D^{\pm}$ and $D_s^{\pm}$ events, while the data distribution contains signal and background events.

For the p_{T} distribution of the muons, the peaking structures of data are due to the different thresholds of the triggers available; while the MC distributions have a larger set of simulated triggers. The filter thresholds on the pion p_{T} were set based on the lowest threshold triggers available.

For the pion tracks, the signal-to-background ratio between 1 GeV and 2 GeV is significantly lower than in the higher p_{T} bins in Figure 4.1. Therefore, it was concluded that including tracks lower than p_{T} =1 GeV will bring no benefit, but increase the background related uncertainties drastically.

4.3. Event Selection

To select events with $D^{\pm}/D_s^{\pm}$ mesons, a set of selection criteria has been applied. Table 4.4 shows the table of selection criteria applied to both data and simulated samples. To

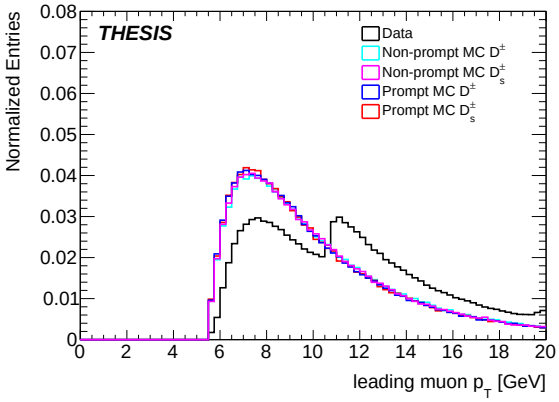

(a) p_{T} of leading muon

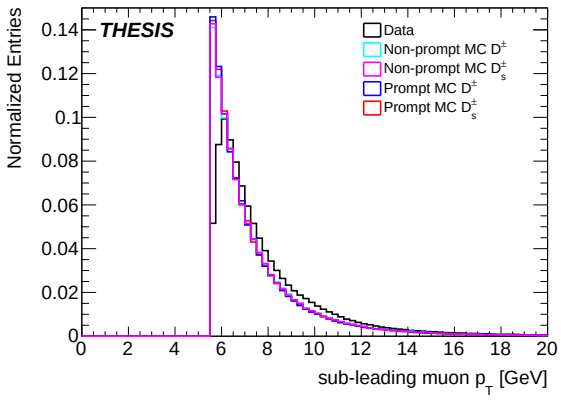

(b) p_{T} of sub-leading muon

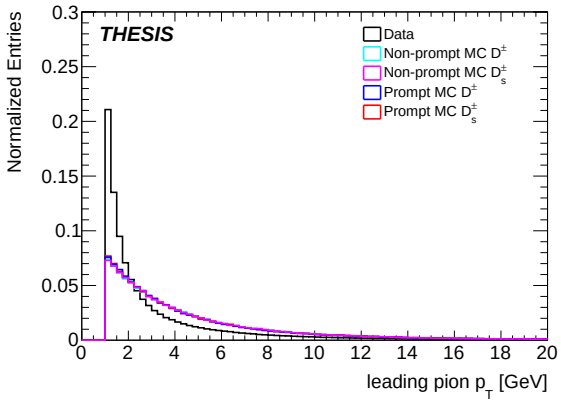

(c) p_{T} of leading pion

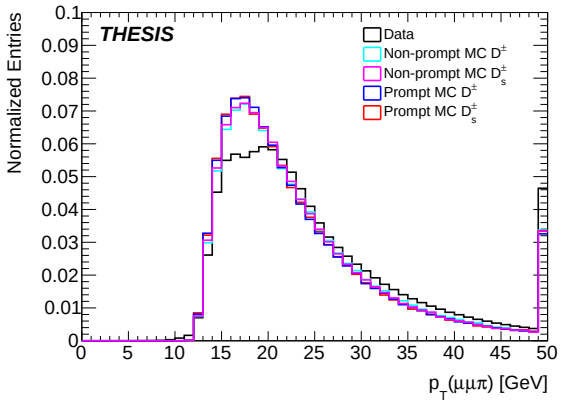

(d) p_{T} of D meson

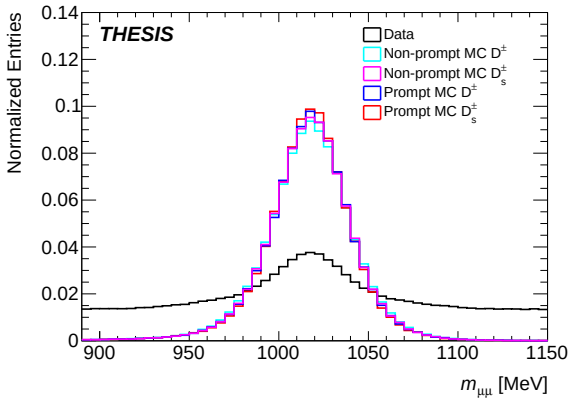

(e) invariant mass of di-muon system

Figure 4.1.: Normalized distributions of basic kinematic variables for the official MC samples and data collected. To illustrate the filter thresholds and the cut values, the selection chain and the trigger selection are not applied; therefore, the MC samples have a larger set of simulated triggers compared to data, which allows for more low p_{T} muons.

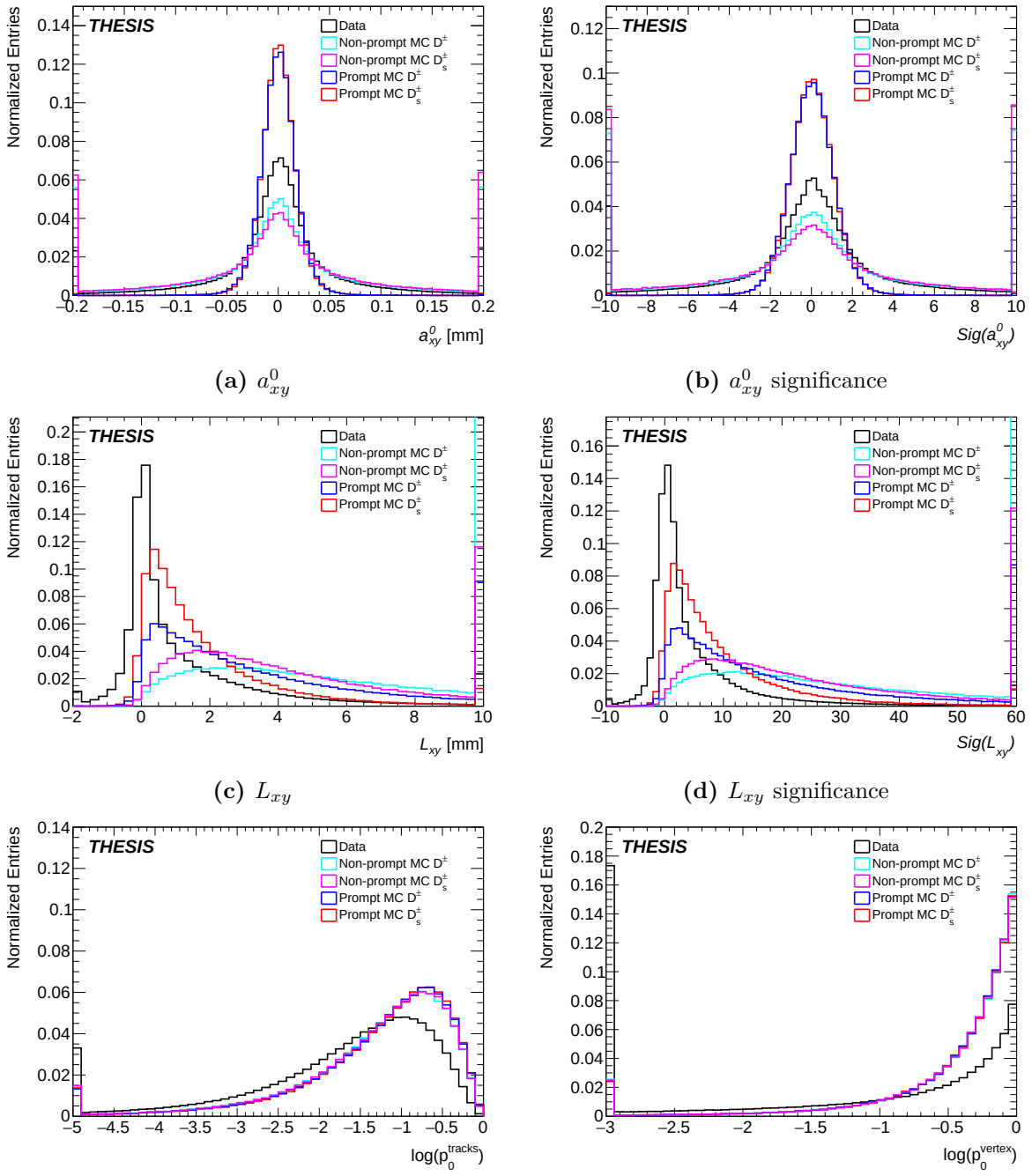

(a) a^0_{xy}

(b) a^0_{xy} significance

(c) L_{xy}

(d) L_{xy} significance

(e) log of product of track p-values

(f) log of vertex p-value

Figure 4.2.: Normalized distributions of secondary vertex variables for the official MC samples and data collected. To illustrate the cut values, the distributions before applying the selection chain are presented.

make use of the topology of detached vertices due to a relatively long lifetime of $D^{\pm}/D_s^{\pm}$ mesons, secondary vertex variables are constructed. Figure 4.1 and Figure 4.2 show the comparison between data and simulated samples for some of the variables before applying the selections. Since the data before selection contains mostly background events, the data versus simulated signal samples plots can be interpreted as background versus signal plots to illustrate the effectiveness of the selection. Although the analysis considers both prompt and non-prompt $D^{\pm}/D_s^{\pm}$ mesons as signal events, the selection criteria are specifically adjusted to extract the prompt $D_s^{\pm}$ meson signals for further analysis.

In order to identify the decay $D^{\pm}/D_s^{\pm} \to \phi(\mu\mu)\pi$, events are first required to be accepted by two-muon triggers, which pre-select muons with certain p_{T} thresholds and a loose di-muon invariant mass requirement. The exact trigger list varies per year depending on the triggers available. At least one of the two muons must pass the 6 GeV threshold; the threshold for the other muon can either be 6 GeV or 11 GeV. Reconstructed muons are selected to have a transverse momentum greater than 6 GeV and are required to pass the Loose working point requirements. Only combined ID+MS measurements of track parameters are used. Several matching criteria [118] are imposed to reject tracks that do not originate from muons (e.g. tracks from hadron decays). Events are also required to consist of at least two selected muons with opposite electric charges Q_μ. The di-muon invariant mass has to agree with the ϕ meson mass of 1020 MeV within a window that scales linearly with the pseudorapidity of the system η, i.e. $|m_{\mu\mu} - m_\phi| < \delta m(\eta)$, to account for the resolution of the detector.

In addition, one track with at least 1 GeV is required to be reconstructed in the ID. All possible di-muon plus track combinations are used as inputs to a vertex fit. The primary vertex (PV) is also refitted after removing the corresponding tracks. Due to the $D^{\pm}$ and $D_s^{\pm}$ lifetime, the three-particle secondary vertex is often separated from the PV. The characteristics of the separation between the secondary decay vertex and the PV are therefore used to reject background. The two projections of the SV displacement with respect to the PV in the transverse plane are used: $L_{xy} = |\vec{L}_T| \cos\theta_{\mathrm{xy}}$ and $a^0_{xy} = |\vec{L}_T| \sin\theta_{\mathrm{xy}}$, where $\vec{L}_T$ is the vector connecting the PV and the SV in the transverse plane, and θ_{xy} is the angle between $\vec{L}_T$ and the transverse momentum. Since a large separation in L_{xy} distributions is observed between signal and background events, an aggressive cut has been placed on the variable. To account for detector resolution, the significance of L_{xy} and a^0_{xy}, Sig(L_{xy}) and Sig(a^0_{xy}), are defined as $L_{xy}/\sigma_{L_{xy}}$ and $a^0_{xy}/\sigma_{a^0_{xy}}$, where $\sigma_{L_{xy}}$ and $\sigma_{a^0_{xy}}$ are the uncertainties on L_{xy} and a^0_{xy}, respectively.

To suppress the combinatorial background and poorly reconstructed candidates, requirements are placed on the goodness of fits of secondary vertices and tracks. Ideally, the tracks that originate from D mesons should form a common vertex, and the χ^2 of the vertex fit should be small; on the other hand, poorly reconstructed vertices, which have a large χ^2 value, are likely to be combinatorial background. The secondary vertex p-values p_0^{vertex} is defined as the probability of obtaining a χ^2 value larger than that of the reconstructed secondary vertex; cuts is place on p_0^{vertex} to reject poorly reconstructed vertices. Similarly, the p-values can be defined for the goodness of fit of tracks. Since three tracks are present, the product of track p-values p_0^{tracks} is used.

At the end of the selection chain, only the di-muon plus track candidate with the highest vertex fit probability p-value p_0^{vertex} is allowed per event. Because of detector coverage and trigger threshold, the final candidate is required to have a transverse momentum above 12 GeV and be within the pseudorapidity range of $|\eta| < 2.5$.

Base Selection	
Muon	Passing *Loose* [118] muon working point
Track	Passing *Loose* [119] working point
Tight Selection	
Triggers	Trigger selection without period matching
Di-muon invariant mass	$\lvert m_{\mu\mu} - m_\phi \rvert < 160\,\text{MeV}$
Triplet invariant mass	$1680\,\text{MeV} < m_{\text{triplet}} < 2220\,\text{MeV}$
Transverse momentum	$p_{\text{T}}^{\mu} > 6\,\text{GeV}$, $p_{\text{T}}^{\pi} > 1\,\text{GeV}$
L_{xy} significance	$\text{Sig}(L_{xy}) > 3$
a_{xy}^0 significance	$\lvert\text{Sig}(a_{xy}^0)\rvert > 4$
Vertex p-value	$log(p_0^{\text{vertex}}) > -0.8$
Products of track p-values	$log(p_0^{\text{tracks}}) > -4$
Total charge	$\lvert Q_{\text{triplet}} \rvert = 1$
Opposite charge muon	$Q_{\mu_1} Q_{\mu_2} = -1$
Final Selection	
Trigger selection tight	Trigger selection according to period stated in Table 4.5
Di-muon invariant mass tight	$\lvert m_{\mu\mu} - m_\phi \rvert < \delta m(\eta)$
Highest vertex p-value	The vertex with $\text{Max}(p_0)$ in the event

Table 4.4.: Summary of each step in the event selection.

Phi Mass Selection

Since the detector resolution is different in different η regions, the di-muon invariant mass resolution is also different. To account for this, the di-muon invariant mass selection is tightened in different η regions. Figure 4.3 shows the Gaussian distribution fitted to the di-muon invariant mass of MC samples in different bins of $|\eta|$. It can be seen that the width of the di-muon invariant mass distribution increases from around 15 MeV to 24 MeV as $|\eta|$ increases. Therefore, with a known value of $m_\phi = 1020\,\text{MeV}$, and a function $\delta m(|\eta|)$ is defined as,

$$\delta m(\eta) = 2\sigma(|\eta|) \tag{4.1}$$

where $\sigma(|\eta|)$ is the function that scales linearly in $|\eta|$ from 15 MeV to 24 MeV in the range of $|\eta| < 2.5$; the choice of 2σ ensures around 95% of signals are retained while rejecting the background effectively.

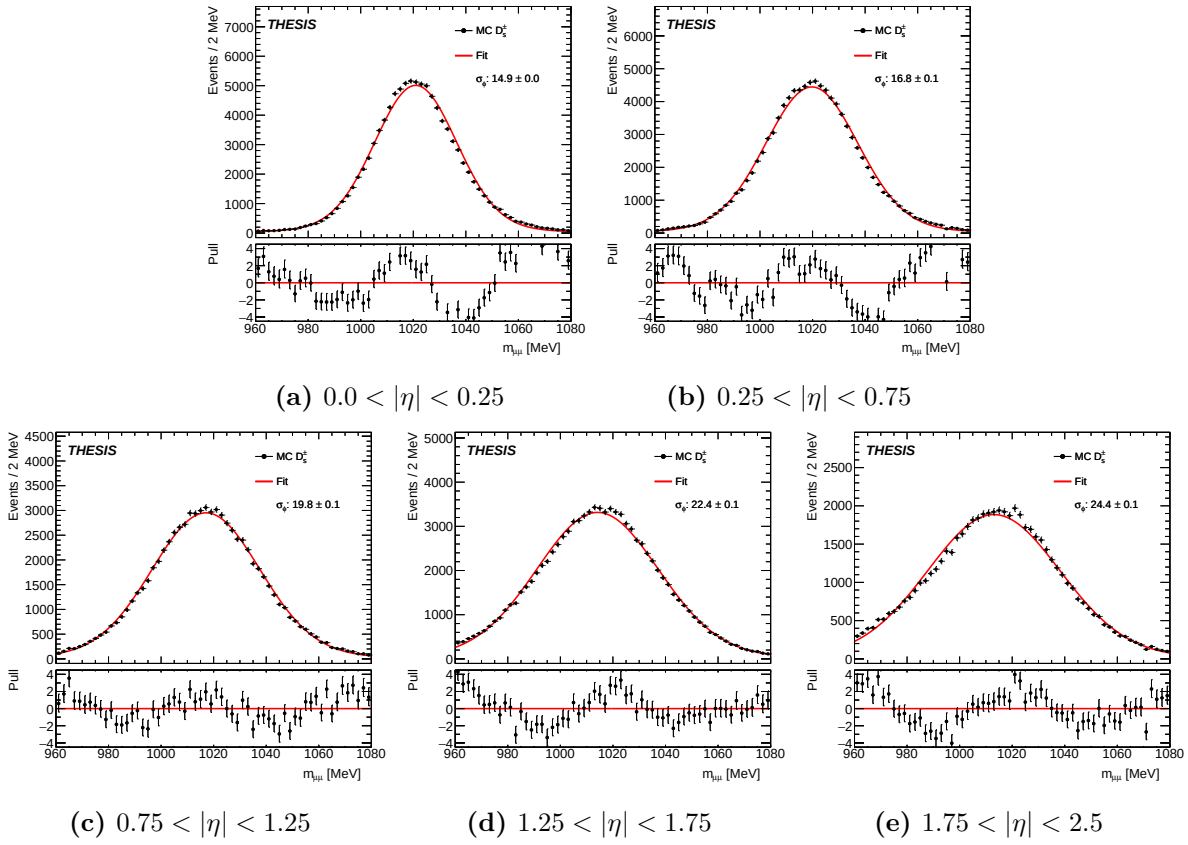

(a) $0.0 < |\eta| < 0.25$ **(b)** $0.25 < |\eta| < 0.75$

(c) $0.75 < |\eta| < 1.25$ **(d)** $1.25 < |\eta| < 1.75$ **(e)** $1.75 < |\eta| < 2.5$

Figure 4.3.: Gaussian models fitted to di-muon invariant mass in different bins of $|\eta|$ to extract the width of the distributions.

Highest Vertex P-value

In every event, multiple candidates can be reconstructed due to the presence of multiple muons and pions. However, only the SV of the best p_0^{vertex} is allowed at the end of the selection chain; the other candidates, known as alternative candidates, are discarded. To verify this choice, the vertex p-value of the alternative candidate p_0^{alt} is also studied before applying the max-p_0^{vertex} selection.

The distribution of the highest vertex p-value p_0^{vertex}, vertex p-value of the alternative candidate p_0^{alt} and the proportion of events with alternative candidates are shown in Figure 4.4. It can be seen there is only around 5% of events with alternative candidates. Among the 5% of events, the distribution of their p-value p_0^{alt} are also background like when compared to the signal distribution. Therefore, the error due to selecting the wrong candidate is much suppressed and negligible.

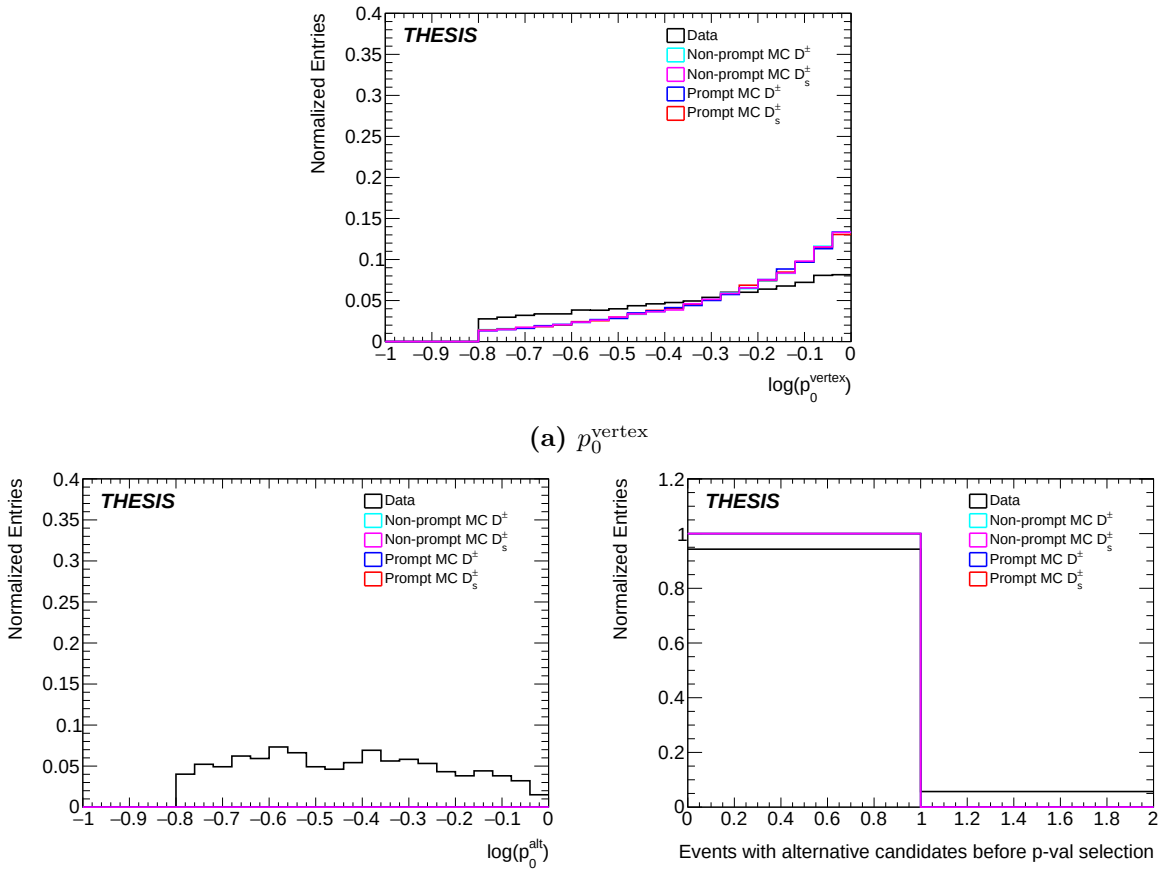

(a) p_0^{vertex}

(b) p_0^{alt}

(c) events with alternative candidates

Figure 4.4.: Distribution of p_0^{vertex}, p_0^{alt} and proportion of event with alternative candidates after all the selection, except for the highest vertex p-value selection.

4.4. Triggers

In ATLAS, the high level triggers start with "HLT" in the name and the muon triggers adopts a naming convention of "NmuY" or "muX_muY". In the former convention, N denotes the number of muons required, while Y denotes the p_{T} threshold of the muon in GeV. In the latter convention, X denotes the p_{T} threshold of the leading muon, while Y denotes the p_{T} threshold of the sub-leading muon. For example, the trigger chain 2mu6 requires two muons with p_{T} above 6 GeV. The naming convention is used in the following sections to refer to the trigger chains.

Additionally, there was a development of "nomucomb" sequence, which means that the muon concerned is not required to be matched to the MS reconstructed muon. This provides looser requirement and higher efficiency for close-by muons. From 2017 onwards, all the muon triggers are replaced by the "nomucomb" sequence; therefore, the "nomucomb" sequence is not included in the naming convention.

To accommodate the need of specific analyses, there are different topological requirements on the muons in the trigger chains. For example, "bPhi" or "bTau" denotes the requirement of di-muon invariant mass near the mass of the ϕ meson or the τ lepton, respectively.

Depending on the particular need, certain criteria on Level-1 can also be placed at the end of the trigger name. For example, "L1MU4" denotes the requirement of at least one muon with p_{T} above 4 GeV at Level-1 and "L1LFV-MU6" denotes the requirement of at least one muon with p_{T} above 6 GeV at Level-1 developed for the use of LFV study.

Both the muon p_{T} threshold and the topological requirements are important for selecting data relevant to the analysis. The trigger selection is therefore discussed in the following sections.

Trigger Selection

Unprescaled di-muon triggers are chosen to maximize the event efficiency at low-p_{T} and high-p_{T}. As the trigger menu has been developing and changing over the 4 years in Run-II, the trigger choice must adapt to the available triggers per year. For the year 2015, the collected data are not used due to the unavailability of relevant triggers and the small amount of data. The lowest-p_{T} triggers usable are the 2mu6 triggers over the data-taking years. Table 4.5 summarizes the triggers applied in this analysis.

Unique Trigger Rate

To evaluate the yield provided by each trigger, the unique trigger rate per year per range in p_{T} is evaluated using the signal MC samples. The unique trigger rate for a particular

Trigger	Periods online
2015	
Data15 is not used	
2016	
HLT_2mu6_nomucomb_bPhi	K - L
HLT_mu11_nomucomb_mu6_nomucomb_bPhi	K - L
2017	
HLT_mu11_mu6_bDimu2700	B - K
2018	
HLT_2mu6_bPhi_L1LFV-MU6	B - Q
HLT_mu11_mu6_bPhi	B - Q

Table 4.5.: Triggers required to have fired in the events analysis and the periods in which they were running online.

Trigger	Unique rate in p_{T} [GeV] ranges		
	12 to 20	20 to 30	30 to 100
2016			
HLT_2mu6_nomucomb_bPhi	0.958	0.437	0.120
HLT_mu11_nomucomb_mu6_nomucomb_bPhi	0.000	0.000	0.011
2017			
HLT_mu11_mu6_bDimu2700	1.0	1.0	1.0
2018			
HLT_2mu6_bPhi_L1LFV-MU6	0.968	0.459	0.116
HLT_mu11_mu6_bPhi	0.001	0.027	0.058

Table 4.6.: Unique trigger rate for different ranges of the $D_s^{\pm}$ mesons p_{T}. The unique rate decreases as the p_{T} increases, indicating a larger overlap between triggers for higher-p_{T}.

trigger-i in a particular data collecting period can be calculated as:

$$\text{Unique rate}_i = \frac{N_{\text{Only trigger-}i}}{N_{\text{Any trigger in list}}} \tag{4.2}$$

where $N_{\text{Only trigger-}i}$ is the number of events that fired a trigger-i without firing any other trigger in the corresponding period according to Table 4.5, and $N_{\text{Any trigger in list}}$ is the number of events that fired at least one trigger in the corresponding period according to Table 4.5. Table 4.6 shows the unique trigger rates of the triggers for different ranges of p_{T}.

3mu4 Triggers

Although the 3mu4 triggers are not used in the analysis, the possibility of using such triggers is investigated. Unlike di-muon triggers, the 3mu4 triggers require the presence of a third muon in the event. Although 3mu4 triggers are on the menu in 2018 data, the trigger can potentially give an unacceptable amount of fake event. It is realized that around 50% of the events that fired the 3mu4 triggers include a third muon that is either a fake muon or a muon that is associated with a different vertex compared to the triplet. Therefore, it is concluded that the 3rd muon that triggered the events are mostly fakes, and the trigger 3mu4 is not used due to a high level of fake miss-modelling at low-p_{T}. Figure 4.5 shows the distribution of p_{T} with and without 2mu6 and 3mu4 triggers. It can be seen that the 3mu4 triggers can contribute to the events in the low-p_{T} region, which is not used in the analysis.

2mu6 Triggers

Without 3mu4 triggers, the lowest trigger is therefore 2mu6 triggers, which are only available unprescaled in part of the data periods in 2016 and 2018. In the analysis a tight cut on the di-muon mass is implemented, which is well inside the topological requirement of the triggers. The topological cut is therefore highly efficient for the event candidates. This is our main trigger for the analysis.

mu11_mu6 Triggers

The mu11_mu6 triggers share a same muon leg of mu6 with 2mu6. Therefore, a large number of events that fire mu11_mu6 triggers also fire 2mu6; this can be observed in the 20 GeV to 30 GeV range in year 2016 and 2018. The mu11_mu6 triggers therefore only contribute a small number of events for higher p_{T} in year 2016 and 2018. However, this trigger is essential for data collected in 2017, where the unprescaled 2mu6 triggers are not available.

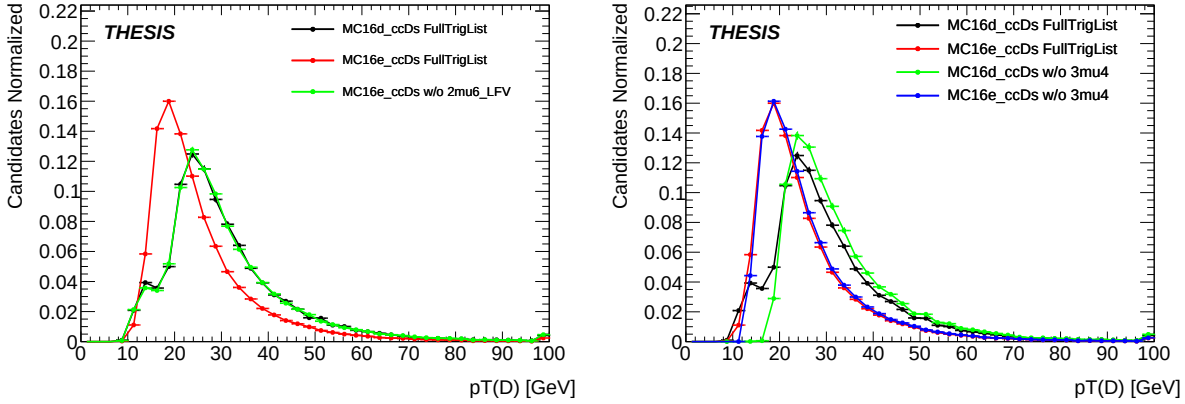

(a) Without 2mu6 **(b)** Without 3mu4

Figure 4.5.: Distribution of p_{T} with and without 2mu6 and 3mu4 triggers.

4.4.1. Trigger Matching

The fully reconstructed muon objects are matched with the trigger chain objects in the analysis. Using the trigger matching tool, a matching criterion with a recommended ΔR of 0.1 between the fully reconstructed muon and the trigger chain muon is applied. The definition of ΔR is:

$$\Delta R(\mu_{\mathrm{reco}}, \mu_{\mathrm{Trig}}) = \sqrt{(\Delta\eta)^2 + (\Delta\phi)^2} \tag{4.3}$$

where μ_{reco} represents the fully reconstructed muon object and μ_{Trig} represents the trigger chain muon object.

Since the di-muon triggers are used in the analysis, the two muons in each event must both satisfy the trigger matching requirement. Because the 2mu6 triggers are the dominating triggers, matching priority is given to 2mu6 triggers in cases where multiple matches occur.

4.4.2. Scale Factor

To correct for the difference in trigger efficiency between the MC samples and the collected data, corrections are applied to the MC samples. Therefore, a set of trigger scale factors, which is the ratio between the trigger efficiency in data and MC, needs to be extracted and applied to the MC samples.

For a di-muon trigger, the efficiency of the trigger ϵ_{Trig} can be factorized as:

$$\epsilon_{\mathrm{Trig}} = \epsilon(p_T^{\mu_1}, q^{\mu_1}\eta^{\mu_1}) \times \epsilon(p_T^{\mu_2}, q^{\mu_2}\eta^{\mu_2}) \times c(\Delta R^{\mu\mu}, y^{\mu\mu}, \tau^{\mu\mu}) \tag{4.4}$$

where ϵ represents the efficiency of a single muon as a function of the transverse momentum p_{T}, charge q and pseudorapidity η of the muon; c represents the correlation of the two muons as a function of the dimuon separation ΔR, rapidity y and lifetime τ. Therefore, the individual muon efficiency and the correlation between the two muons can be extracted separately.

The individual efficiencies and correlation for 2016, 2017 and 2018 have been collected by a data driven method using the $J/\psi \to \mu\mu$ decay. The individual muon efficiencies are extracted by the tag and probe approach, where one muon is matched to the trigger and the efficiency is evaluated on the other muon. By performing such study in MC samples and data, the ratio was then taken as the scale factor for individual muons. For the correlation factor, a loose reference trigger is used to evaluate the difference in efficiency due to the di-muon vertexing and other requirements; the ratio between MC samples and data is then taken as the scale factor for the correlation. The result of the study is a scale factor map which depends on the variables in Equation 4.4. In addition, a closure test is also performed to evaluate the uncertainty due to residual difference after applying the scale factors.

The trigger scale factor map is applied to the muons in $D_s^{\pm} \to \phi(\mu\mu)\pi$ decay; the factors are applied as individual event weights to the MC samples. The profile of the scale factors for different years, together with the uncertainties, in bins of p_{T}, η and ΔR are shown in Figure 4.6, Figure 4.7 and Figure 4.8. It can be seen that the scale factors are close to unity across different years, with a larger deviation for the central η region and low-p_{T} region. The uncertainties of the scale factors are also well under control, except for the year 2018, where the uncertainties are larger for the small ΔR and for the central η region; this is due to the non-closure and the lack of statistics for small ΔR when building the scale factor map.

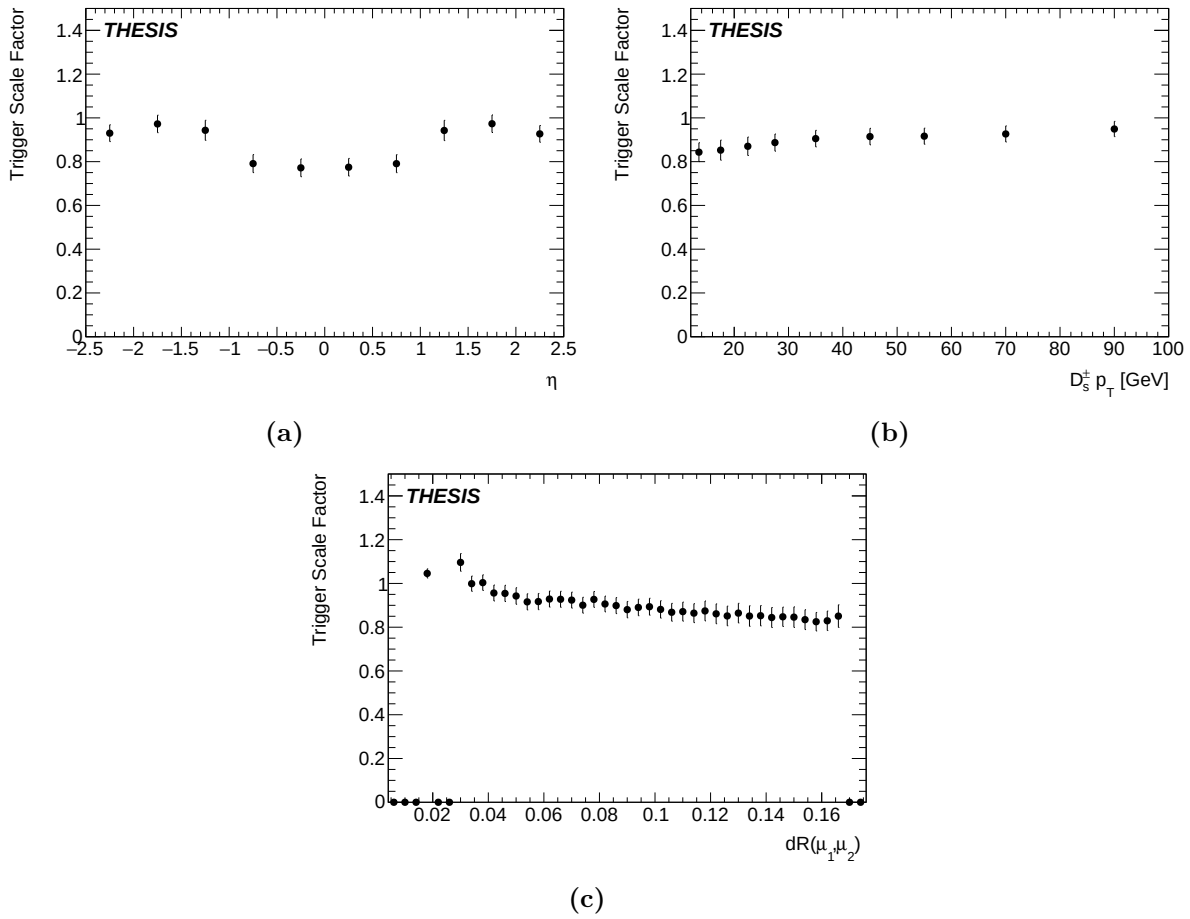

Figure 4.6.: Profile of the trigger scale factors extracted in data 2016 applied to mc16a.

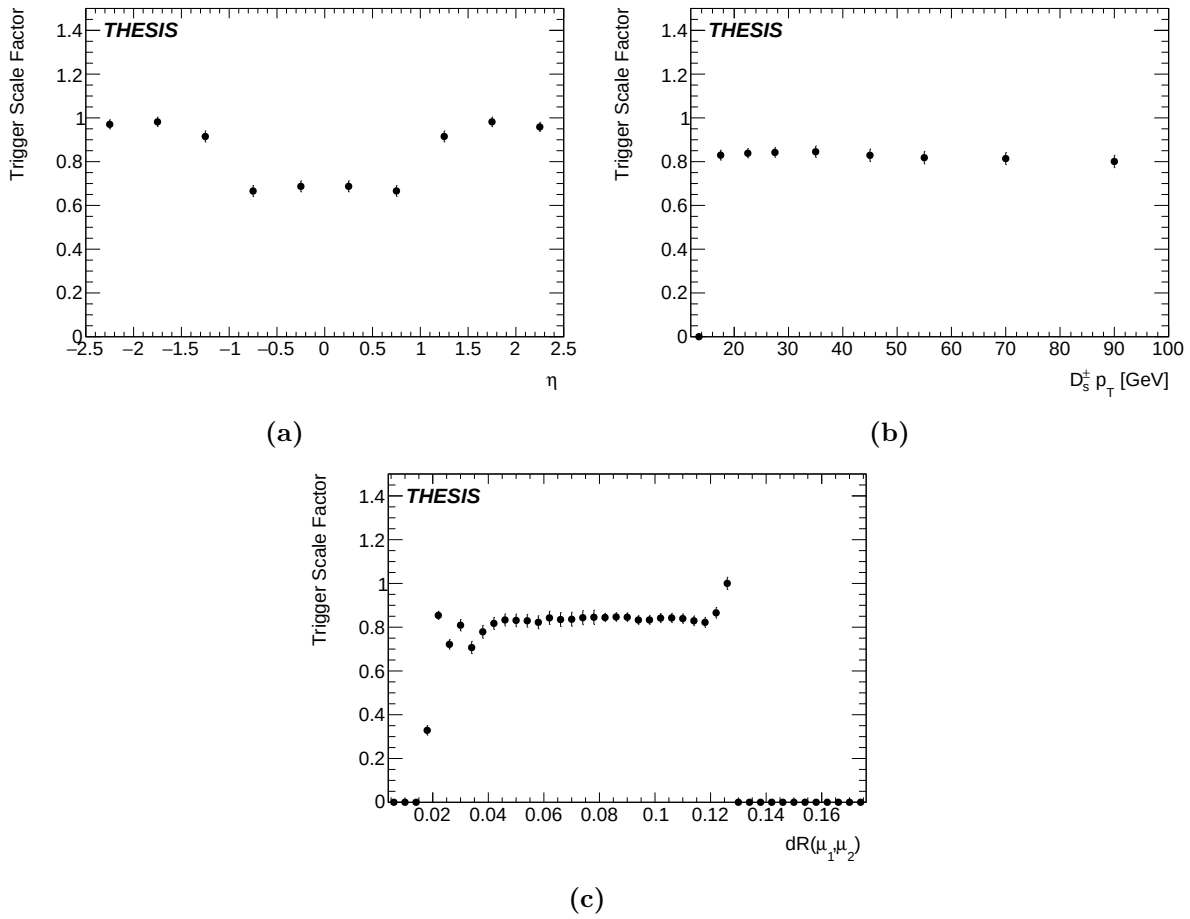

Figure 4.7.: Profile of the trigger scale factors extracted in data 2017 applied to mc16d.

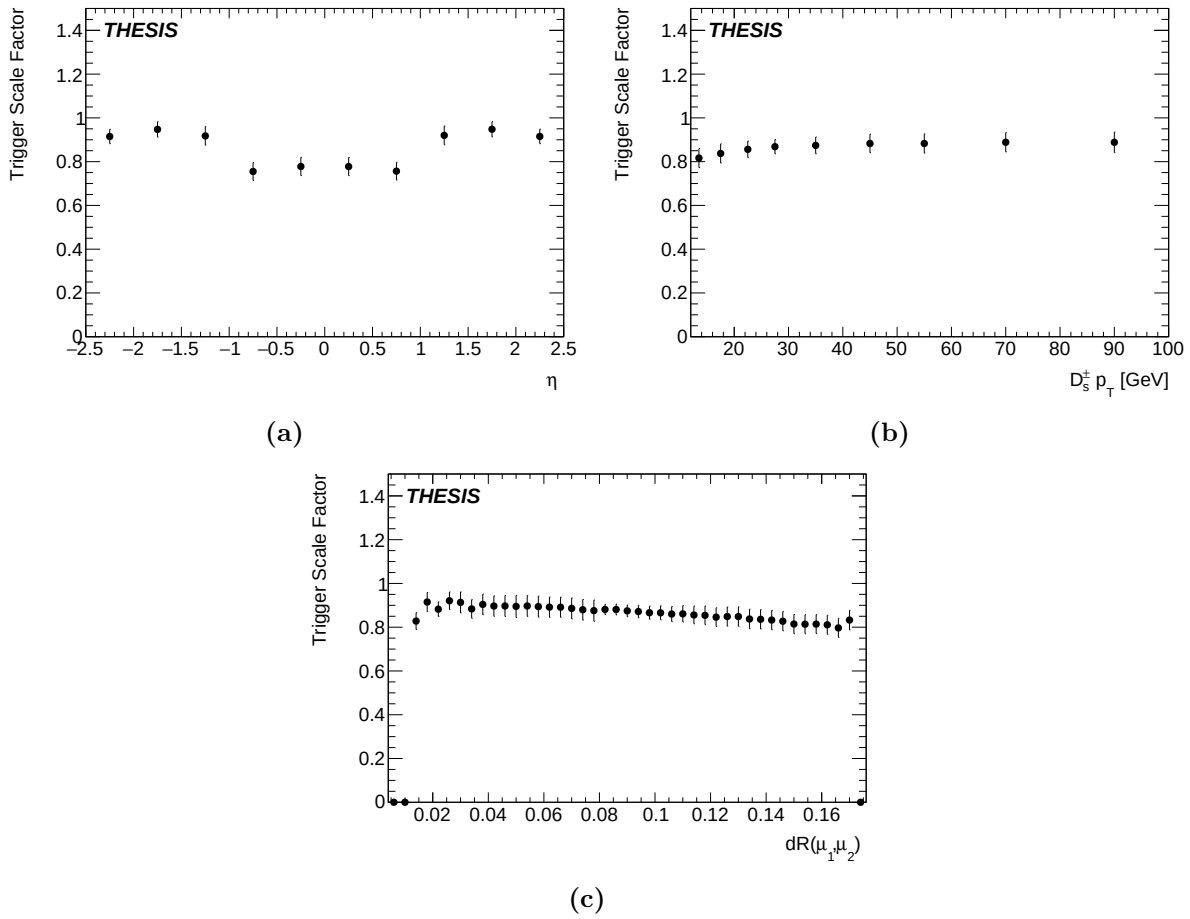

Figure 4.8.: Profile of the trigger scale factors extracted in data 2018 applied to mc16e.

Chapter 5.

Results for D Meson Production

With the selection applied in Chapter 4, the signal to background ratio is much improved compared to that before the selection; however, the signal is still not dominant over the background. Therefore, fitting procedures are defined to extract the signal yield and the non-prompt fraction in the presence of a significant background level.

To measure the cross section of D meson production accurately, systematic uncertainties have to be taken into account. In particular, systematic uncertainties due to detector effects and the choice of fit models are dominant; such effects are studied in detail.

This chapter describes the fitting procedures based on the invariant mass and lifetime of the D meson candidates. Then, the cross sections, which are calculated from the signal yield, are presented with a detailed study of the systematic uncertainties. The differential cross sections and fiducial cross sections obtained are also compared with state-of-the-art next-to-leading-order (NLO) calculations to provide theory feedback.

5.1. Signal Extraction

To extract the signal yield, the most straight forward method is to fit the invariant mass $m_{\mu\mu\pi}$ of the D meson candidates. In this approach, possibilities of using different signal and background models are investigated. Different models are tested in both MC samples and data to evaluate their performance. A combined model is then developed to include contributions from the $D^{\pm}$ meson, the $D_s^{\pm}$ meson and the combinatorial background.

5.1.1. Signal Model

Since the fit model to the invariant mass is used to extract signal yield in bins of p_{T}, η and lifetime, such a model needs to be flexible and stable enough to extract yields in subsets of data with different statistics and signal-to-background ratio. To look for the best fit model to use for the signal, a number of models are tested on MC samples. The signal model is fitted to the invariant triplet mass of the MC simulated events. A number of fit models are tested and listed below (formulas of uncommon models are also provided):

1. Gaussian: $\text{Gauss}(x;\mu,\sigma)$
2. Modified Gaussian: $\text{ModGauss}(x) = \exp[-\frac{x^{(1+\frac{1}{1+x/2})}}{2}]$
3. Breit-Wigner: $\text{BW}(x;m_0,\sigma_1)$
4. Crystal Ball: $\text{CB}(x;m_0,\sigma,\alpha,n)$
5. Bukin: $\text{Bukin}(x;x_i,\sigma_p,\zeta) = A_p \exp\left[\frac{\zeta\sqrt{\zeta^2+1}(x-x_1)\sqrt{2\ln 2}}{\sigma_p\left(\sqrt{\zeta^2+1}-\zeta\right)^2\ln\left(\sqrt{\zeta^2+1}+\zeta\right)} + \rho\left(\frac{x-x_i}{x_p-x_i}\right)^2 - \ln 2\right]$
6. ModGaussConvGauss: $\text{ModGaussConvGauss}(x';\sigma) = \text{ModGauss}(x) * \text{Gauss}(x;\mu = 0,\sigma)$
7. Voigtian: $\text{Voigtian}(x;m,\sigma_1,\sigma_2) = \text{BW}(m,\sigma_1) * \text{Gauss}(0;\mu = 0,\sigma_2)$
8. CBConvGauss: $\text{CB}(x;m_0,\sigma,\alpha,n) * \text{Gauss}(x;\sigma)$

The different fit models are fitted to the invariant triplet mass and the results are summarized in Figure 5.1 for MC16d simulated events. The best description is achieved using the Voigtian model and the Bukin models. The Bukin model is however not used due to its high number of parameters. The Voigtian model is chosen for its good description of the signal shape and its reduced number of parameters. Since both the $D^{\pm}$ and $D_s^{\pm}$ mesons have a highly similar kinematics, the Voigtian model is used as both of their signal model. Although the Bukin model is not used, it is chosen as one of the alternative models to evaluate the systematic uncertainty due to the choice of the signal model. These models are studied in greater details for systematic uncertainty evaluation.

5.1.2. Background Model

The background fit model is studied in a ϕ mass side band which is signal free: $|m_{\mu\mu} - 1020\ \text{MeV}| > 50\ \text{MeV}$. The fit model which fits best the falling background shape is found to be a quadratic exponential. The result of the side-band mass fit is shown in Figure 5.2.

5.1.3. Combined Model

For the $D^{\pm}$ and $D_s^{\pm}$ signals, the fit models $P_{D^{\pm}}$ and $P_{D_s^{\pm}}$ are the Voigtian distribution (Voigt), which is the convolution of a Breit-Wigner distribution with a Gaussian distribution. The background contribution P_{Bkg} originating mainly from combinatorics is extracted using a normalized quadratic exponential distribution (Qexp). Using RooFit [120], the

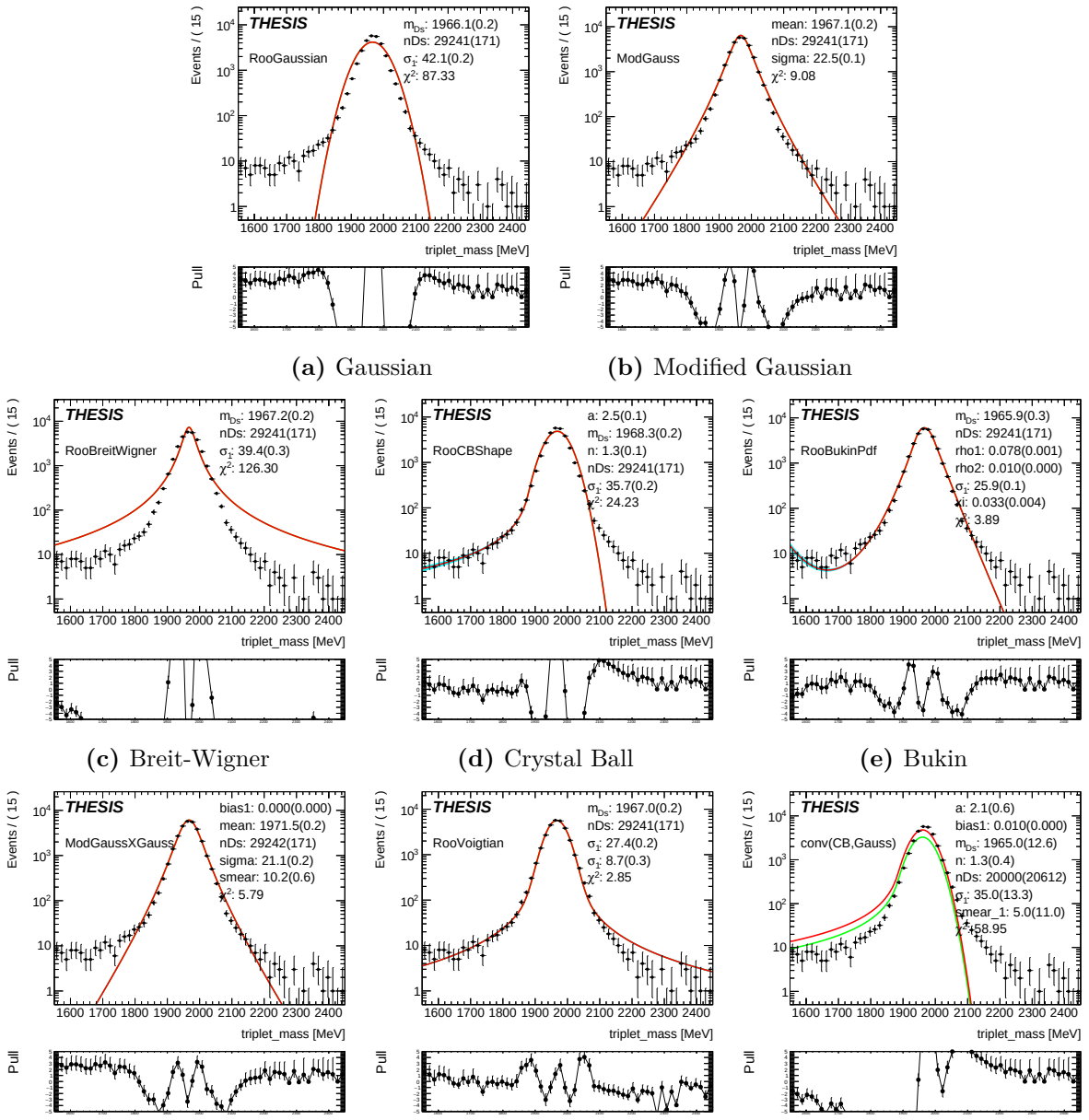

(a) Gaussian **(b)** Modified Gaussian

(c) Breit-Wigner **(d)** Crystal Ball **(e)** Bukin

(f) Modified Gaussian conv Gaussian **(g)** Voigtian **(h)** Crystal Ball conv Gaussian

Figure 5.1.: Different signal models fitted to MC $D_s^{\pm}$ samples.

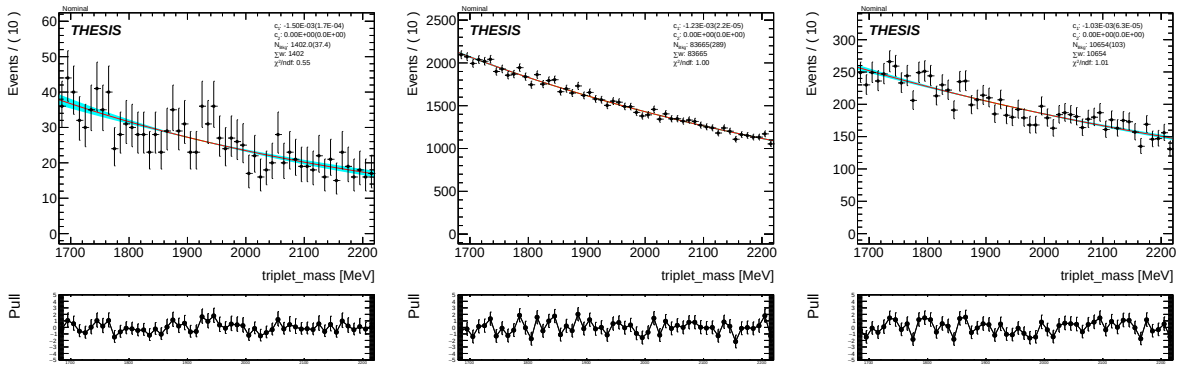

(a) low-p_{T} **(b)** mid-p_{T} **(c)** hgh-p_{T}

Figure 5.2.: Fit of the invariant triplet mass in the ϕ mass side-band for different p_{T} range.

unbinned maximum likelihood $\mathcal{L}(m)$ is implemented as:

$$
\begin{aligned}
\mathcal{L}(m) &= \frac{e^{-(S_{D^\pm}+S_{D_s^\pm}+B)}}{n!}\prod_{i=1}^{n}\left[S_{D^\pm}P_{D^\pm}(m)+S_{D_s^\pm}P_{D_s^\pm}(m)+BP_{\mathrm{Bkg}}(m)\right]\times\mathcal{G}(\Delta)\\
P_{D^\pm}(m) &= \mathrm{Voigt}(m;m_{D^\pm},\gamma_{D^\pm},\sigma_{D^\pm})\\
P_{D_s^\pm}(m) &= \mathrm{Voigt}(m;m_{D_s^\pm},\gamma_{D_s^\pm},\sigma_{D_s^\pm})\\
P_{\mathrm{Bkg}}(m) &= \mathrm{Qexp}(m;c_1,c_2)\\
\mathrm{Qexp}(m;c_1,c_2) &= A_{\mathrm{norm}}\cdot e^{(c_1m+c_2m^2)}\\
\mathcal{G}(\Delta) &= \mathrm{Gauss}(\Delta;\mu_\Delta,\sigma_\Delta)
\end{aligned}
\tag{5.1}
$$

where A_{norm} is the normalization factor of the quadratic exponential distribution, $S_{D^\pm}$, $S_{D_s^\pm}$ and B are the yield of $D^\pm$ meson, $D_s^\pm$ meson and background respectively. The Voigtian distributions of $D^\pm$ and $D_s^\pm$ mesons are parameterized by the mean parameters $m_{D^\pm}$ and $m_{D_s^\pm}$, $\gamma_{D^\pm}$ and $\gamma_{D_s^\pm}$ are the width of the Breit-Wigner distribution and the width of the Gaussian distribution are $\sigma_{D^\pm}$ and $\sigma_{D_s^\pm}$. The parameter c_1 is the linear rate parameter as in a simple exponential distribution, while the parameter c_2 is the quadratic part that is multiplied with m^2. Since the mass difference Δ between the $D_s^\pm$ and $D^\pm$ mesons is known, an additional Gaussian constraint $\mathcal{G}(\Delta)$ with mean μ_Δ and width σ_Δ is also used.

In the model, the parameters of interest are the yields $S_{D^\pm}$ and $S_{D_s^\pm}$, while the other parameters that determine the background model and the signal shape are regarded as nuisance parameters. To improve the stability of the fit model, particularly in bins with low statistics, a few empirical modifications based on fits to MC samples of $D^\pm$ and $D_s^\pm$ mesons are introduced on the nuisance parameters:

- μ_Δ is set to the mass difference according to the known values reported by the PDG [121].

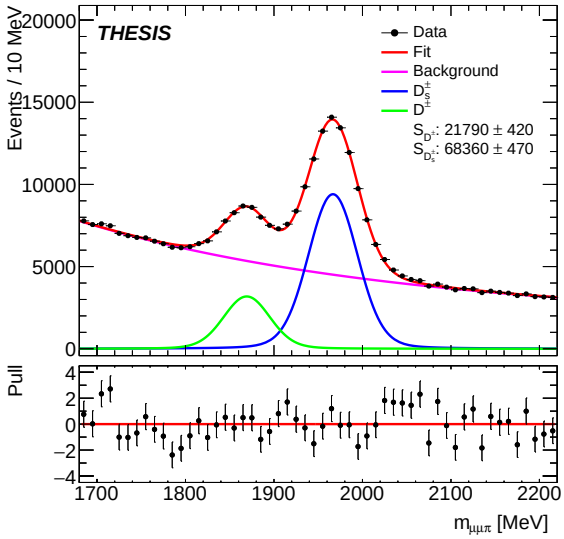

Figure 5.3.: Invariant mass of the di-muon plus track system.

- σ_Δ controls the softness of the constraint on the distance between the $D^\pm$ and $D_s^\pm$ signals. By repeatedly applying the fit to data binned in different variables, it is evaluated that the fitted mass difference $m_{D^\pm}$ - $m_{D_s^\pm}$ deviates from the value reported by PDG by 1.0 MeV on average. To avoid bias due to over-constraint, σ_Δ is set to twice this value, i.e. 2.0 MeV. Note that in PDG, the error on the mass difference is 0.09 MeV, so the constraint is applied due to resolution of the detector.

- The parameters $\gamma_{D^\pm}$ and $\gamma_{D_s^\pm}$ are fixed to 8.0 MeV, which is a number obtained by fitting to MC samples. By fixing the parameters, the correlation between $\sigma_{D^\pm/D_s^\pm}$ and $\gamma_{D^\pm/D_s^\pm}$ are eliminated. As shown in Figure 5.3 and fits to different kinematic bins in the following sections, this approach retains a good level of goodness of fit while reducing the number of fit parameters.

- Since there is a high correlation between c_1 and c_2, having both of the parameters floating can introduce a large error for some kinematic regions with lower statistics. By trial and error, it was found that setting c_2 to zero and perform a re-fit when the error on c_2 exceeds 30% can greatly improve fit stability (i.e. the quadratic exponential distribution is reduced to a simple exponential distribution).

With the empirical modifications, the fit parameters therefore are as follows: $S_{D_s^\pm}$, $S_{D^\pm}$, B, $m_{D_s^\pm}$, $m_{D^\pm}$, $\gamma_{D^\pm}$, $\sigma_{D^\pm}$, c_1 and c_2. The unbinned maximum likelihood fit on the mass spectrum is presented in Figure 5.3. It can be seen from the pull distribution that the fitted model is generally consistent with the data.

5.2. Non-prompt Fraction Extraction

In the LHC, $D^{\pm}$ and $D_s^{\pm}$ mesons can be produced promptly through the c-quarks or non-promptly through the b-quarks. For the prompt production mode, the c-quark hadronizes into a $D^{\pm}/D_s^{\pm}$ meson. Because of the relatively long lifetime of $D^{\pm}/D_s^{\pm}$ mesons, they can travel around 0.5 ps before they decay into a ϕ meson and a pion. For the non-prompt production mode, the b-quark hadronizes into B mesons, which have a typical lifetime of 1.5 ps or more. The B mesons can therefore travel a few mm before they decay into a $D^{\pm}/D_s^{\pm}$ meson, which travels further before decaying into a ϕ meson and a pion. To quantify the proportion of the two different production mechanisms, the non-prompt fraction f_{bb} is defined as the proportion of events that are non-prompt:

$$f_{bb} = \frac{S_{bb}}{S_{\mathrm{bb}} + S_{cc}} \tag{5.2}$$

where S_{bb} is the number of events originating from b-quarks and S_{cc} is the number of events originating from c-quarks. Due to the similarity of the two processes, the yields S_{bb} and S_{cc} cannot be directly extracted. The two processes mainly differ in terms of decay distance and lifetime. With the reconstructed vertex position, the pseudo-proper-lifetime (hereinafter referred to as lifetime) of $D^{\pm}$ and $D_s^{\pm}$ mesons is defined as:

$$\tau = \frac{m_{\mu\mu\pi} \cdot L_{xy}}{p_{\mathrm{T}}} \tag{5.3}$$

In this analysis, the non-prompt fraction is extracted by means of template fits to the measured lifetime. The prompt and non-prompt templates are first developed with MC samples; the parameters of each individual template are then fixed before applying a combined fit to the extracted signal from data.

5.2.1. Prompt and Non-prompt Templates

The prompt and non-prompt templates are obtained by fitting analytic models to corresponding MC samples using RooFit [120], by means of an unbinned maximum likelihood fit. The prompt contribution includes an exponential distribution (Exp) to describe the physical exponential decay of the particle, and is convoluted with the Gaussian distribution (Gauss) and the error function (Erf) to account for the detector resolution and the turn-on effect at low lifetime. The non-prompt contribution includes one exponential distribution to account for the cascade decay of the B meson, and another exponential distribution to account for the lifetime of the $D^{\pm}/D_s^{\pm}$ mesons. Similar to the prompt contribution, the distribution is also convoluted with the Gaussian distribution (Gauss) and the error function (Erf) to account for detector effects.

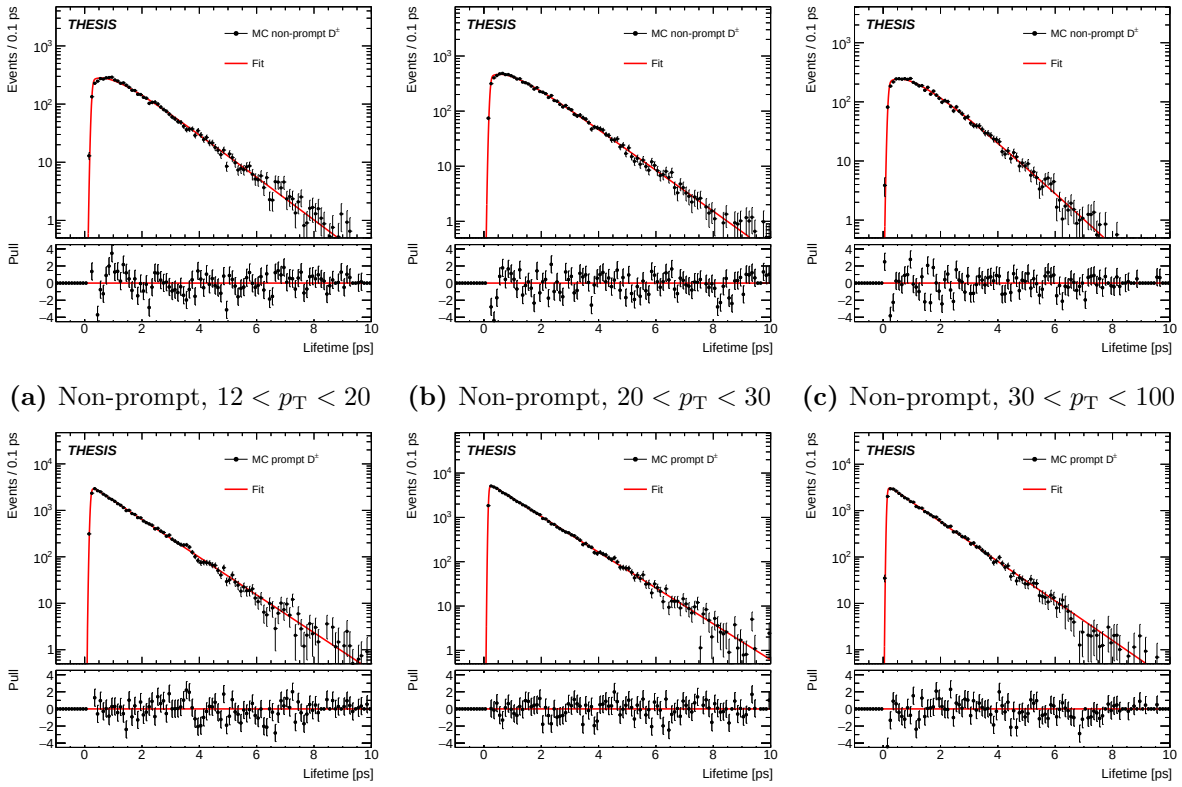

(a) Non-prompt, $12 < p_{\mathrm{T}} < 20$ **(b)** Non-prompt, $20 < p_{\mathrm{T}} < 30$ **(c)** Non-prompt, $30 < p_{\mathrm{T}} < 100$

(d) Prompt, $12 < p_{\mathrm{T}} < 20$ **(e)** Prompt, $20 < p_{\mathrm{T}} < 30$ **(f)** Prompt, $30 < p_{\mathrm{T}} < 100$

Figure 5.4.: Fit templates of the proper lifetime for $D^{\pm}$ mesons for prompt/non-prompt production and different p_{T} (in GeV) ranges.

The template for non-prompt contribution $P_{bb}(\tau)$ and the template for prompt contribution $P_{cc}(\tau)$ are defined as:

$$\begin{aligned} P_{bb}(\tau) &= \mathrm{Exp}(\tau;\tau_1^{bb}) * \mathrm{Exp}(\tau;\tau_2^{bb}) * \mathrm{Gauss}(\tau;\mu^{bb},\sigma_{\mathrm{res}}^{bb}) * \mathrm{Erf}(\tau;\tau_{\text{turn-on}}^{bb},\beta^{bb}) \\ P_{cc}(\tau) &= \mathrm{Exp}(\tau;\tau_1^{cc}) * \mathrm{Gauss}(\tau;\mu^{cc},\sigma_{\mathrm{res}}^{cc}) * \mathrm{Erf}(\tau;\tau_{\text{turn-on}}^{cc},\beta^{cc}) \end{aligned} \tag{5.4}$$

while τ is the lifetime of the secondary vertex, τ_1^{bb} and τ_1^{cc} are the lifetime component of $D^{\pm}/D_s^{\pm}$ meson, τ_2^{bb} is the lifetime component of the B meson for the non-prompt decay, μ^{bb} and μ^{cc} represent a constant shift in lifetime due to detector resolution, $\sigma_{\mathrm{res}}^{bb}$ and $\sigma_{\mathrm{res}}^{cc}$ describe the smearing due to detector resolution, $\tau_{\text{turn-on}}^{bb}$ and $\tau_{\text{turn-on}}^{cc}$ represent a constant shift in lifetime due to the turn-on effect, and β^{bb} and β^{cc} are factors multiplied to lifetime which determine the sharpness of the turn-on effect.

To improve the stability of the models, several empirical modifications, based on fits to MC samples, have been introduced:

- μ^{bb} and μ^{cc} are absorbed by $\tau_{\text{turn-on}}^{bb}$ and $\tau_{\text{turn-on}}^{cc}$ since they all represent a shift in lifetime.

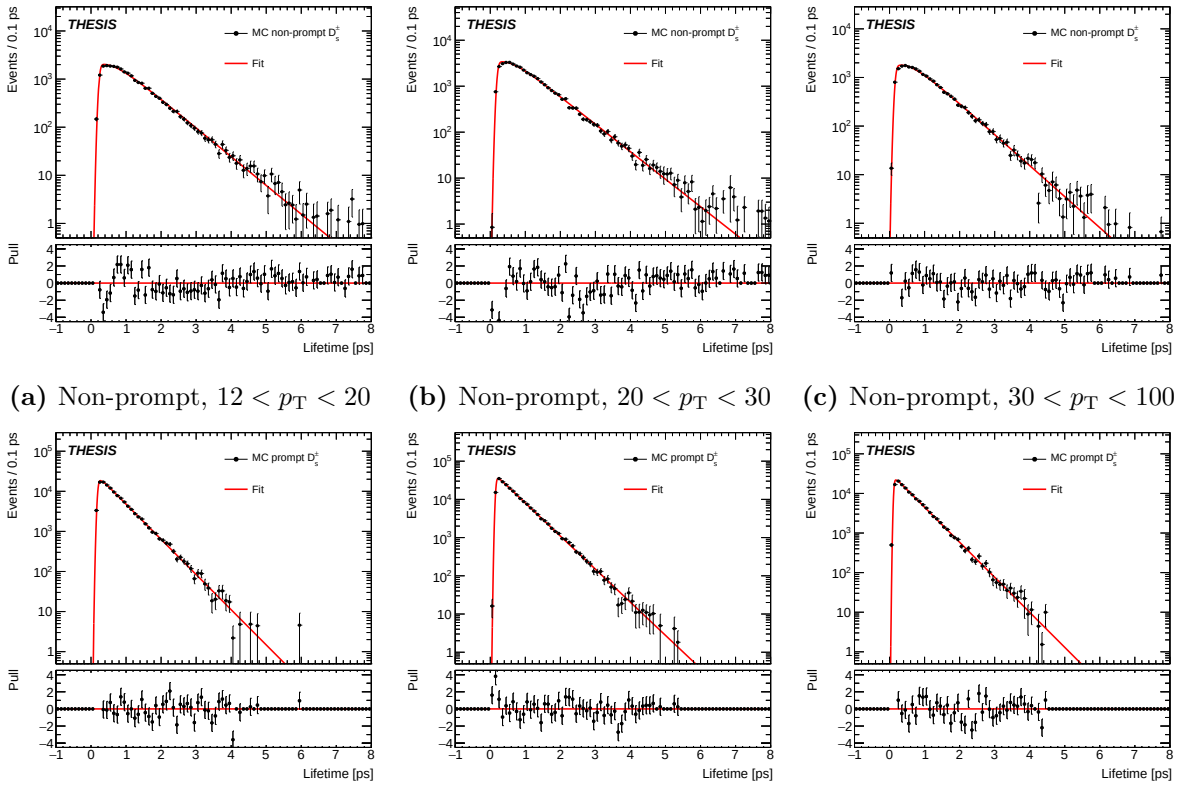

(a) Non-prompt, $12 < p_{\mathrm{T}} < 20$ **(b)** Non-prompt, $20 < p_{\mathrm{T}} < 30$ **(c)** Non-prompt, $30 < p_{\mathrm{T}} < 100$

(d) Prompt, $12 < p_{\mathrm{T}} < 20$ **(e)** Prompt, $20 < p_{\mathrm{T}} < 30$ **(f)** Prompt, $30 < p_{\mathrm{T}} < 100$

Figure 5.5.: Fit templates of the proper lifetime for $D_s^\pm$ mesons for prompt/non-prompt production and different p_{T} (in GeV) ranges.

- Since the rising slope at low lifetime cannot be captured precisely, β^{bb} is a nuisance parameter which is set to a value (i.e. 18.0) tested with MC samples, to avoid high correlation between τ_1^{bb}, τ_2^{bb} and $\sigma_{\mathrm{res}}^{bb}$.

The two templates $P_{bb}(\tau)$ and $P_{cc}(\tau)$ are fitted to non-prompt and prompt MC samples respectively. The fit parameters for the non-prompt template $P_{bb}(\tau)$ are: τ_1^{bb}, τ_2^{bb}, $\sigma_{\mathrm{res}}^{bb}$ and $\tau_{\text{turn-on}}^{bb}$. The fit parameters for the prompt template $P_{cc}(\tau)$ are: τ_1^{cc}, $\sigma_{\mathrm{res}}^{bb}$, $\tau_{\text{turn-on}}^{bb}$ and β^{cc}. Figure 5.4 and Figure 5.5 show the templates fitted to MC samples with the extracted parameters; the shapes of the templates are then fixed with the parameters extracted. From the figures, a generally good agreement can be seen between data and the fit templates, except for low lifetime, where the binned MC distribution cannot accommodate the sharply rising distribution.

Signal Extraction

Before performing a lifetime fit to extract non-prompt fraction, the signal distribution in data needs to be first extracted. The dataset is sliced into three p_{T} bins (bin boundaries are [12 GeV, 20 GeV, 30 GeV, 100 GeV]). In each bin of p_{T}, the signal shape in lifetime is

obtained by further slicing the dataset into bins of lifetime, and apply the fit model for invariant mass.

To get rid of the background contribution in data, invariant mass fits are performed in each bin; the yield N_i and the corresponding error σ_i in data are extracted. The fit models fitted to the dataset in three bins of p_{T} and bins of lifetime are shown in appendix A.

With such an approach, the fits can extract yields up to 6.0 ps for $D_s^{\pm}$ meson and 8.0 ps for $D^{\pm}$ meson before running out of statistics. However, the sharply rising shape and the peak at low lifetime cannot be accurately captured due to limitation of statistics and binning. This places a constraint on the lifetime range when performing the combined fit.

5.2.2. Combined Model

The combined model is constructed by summing the prompt and non-prompt templates fixed by fitting to MC samples. The fit model is compared to the extracted signal to calculate the χ^2:

$$\begin{aligned} S_i &= S_{\mathrm{model}} \left[f_{bb} P_{bb}(\tau) + (1 - f_{bb}) P_{cc}(\tau) \right] \\ \chi^2 &= \sum_{i=1}^{n} \frac{(N_i - S_i)^2}{\sigma_i^2} \end{aligned} \tag{5.5}$$

where S_i is the signal in a particular bin of lifetime and S_{model} is the total number of signal yield extracted in data. Using RooFit, a minimum χ^2 fit is performed on the extracted signal distribution. Since the shape parameters of individual templates are fixed, the only fit parameter and the parameter of interest is f_{bb}. Due to the limitations in signal extraction, the region with low lifetime is excluded from the fit to minimize significant error.

5.2.3. Extracted Values

The fit has been applied separately for both $D^{\pm}$ and $D_s^{\pm}$ mesons across three bins of p_{T}; in each bin of p_{T}, the individual templates and the combined models are all rebuilt. The bins are defined to capture the falling shape of f_{bb}, while ensuring enough data are present in each bin. The bin boundaries in p_{T} are: 12 GeV, 20 GeV, 30 GeV, 100 GeV. Figure 5.6 and Figure 5.7 show the extracted signal from data and the fits with the combined model. Generally good agreement is observed between the combined model and the extracted data within the fitting range.

The extracted non-prompt fraction is at fit level, i.e. post-selection. To obtain the non-prompt fraction at production level, selection efficiency and filter efficiency need to be accounted for. At fit level, the non-prompt to prompt ratio is

$$f_{\mathrm{fit}} : (1 - f_{\mathrm{fit}}) \tag{5.6}$$

Therefore, the non-prompt fraction at production level f_{prod} can be related to the non-prompt fraction extracted by the fit f_{fit} by the formula :

$$\frac{f_{\text{prod}}}{(1-f_{\text{prod}})} = \frac{f_{\text{fit}}/\epsilon_{\text{non-prompt}}}{(1-f_{\text{fit}})/\epsilon_{\text{prompt}}} \tag{5.7}$$

where $\epsilon_{\text{non-prompt}}$ and ϵ_{prompt} are the total efficiency of non-prompt and prompt processes respectively.

To evaluate the non-prompt fraction at production level, the non-prompt fraction extracted from the fit is corrected by the efficiency of MC filter, reconstruction efficiency and acceptance. These efficiencies are evaluated with MC samples, and are derived separately for prompt and non-prompt production in bins of p_{T}. Given the total efficiencies of non-prompt processes are higher than that of the prompt processes, the non-prompt fraction is expected to be lower at production level.

Figure 5.8 shows the extracted non-prompt fraction and the extracted error for both $D^{\pm}$ and $D_s^{\pm}$ in bins of p_{T}. For the $D_s^{\pm}$ meson, a reasonable error is observed; for the $D^{\pm}$ meson, a large error is observed. This is because of the lower yield and the long lifetime of the $D^{\pm}$ meson, which causes the distinguishing power of the fit to decrease due to similar prompt and non-prompt shapes.

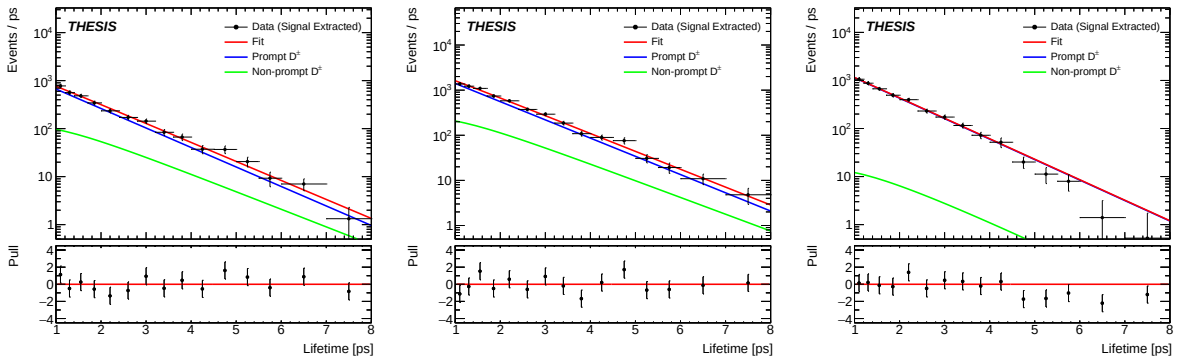

(a) $12 < p_{\text{T}} < 20$ **(b)** $20 < p_{\text{T}} < 30$ **(c)** $30 < p_{\text{T}} < 100$

Figure 5.6.: Combined fit model fitted to lifetime distribution extracted from data for $D^{\pm}$ in different p_{T} (in GeV) ranges. The prompt and non-prompt contribution is shown in blue and green respectively. The combined fit is shown in red.

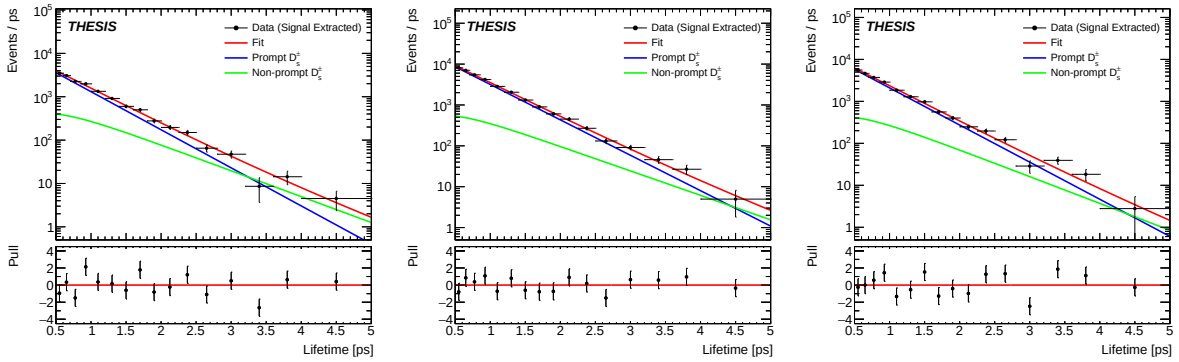

(a) $12 < p_\mathrm{T} < 20$ **(b)** $20 < p_\mathrm{T} < 30$ **(c)** $30 < p_\mathrm{T} < 100$

Figure 5.7.: Combined fit model fitted to lifetime distribution extracted from data for $D_s^\pm$ in different p_T (in GeV) ranges. The prompt and non-prompt contribution is shown in blue and green respectively. The combined fit is shown in red.

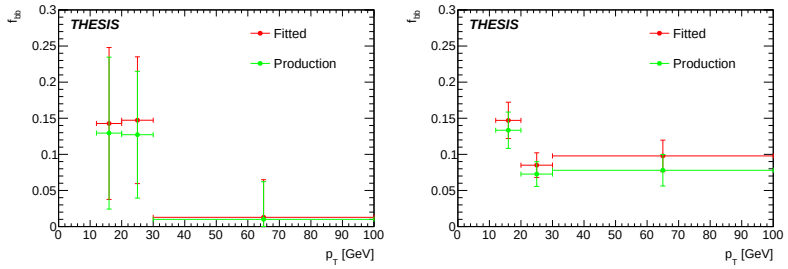

(a) $D^\pm$ **(b)** $D_s^\pm$

Figure 5.8.: Non-prompt fraction of $D^\pm$ and $D_s^\pm$ production in bins of p_T.

5.3. Efficiency

Several efficiencies have to be taken into account when calculating the differential cross section and the non-prompt fraction. The efficiencies are separated into several components. In this section, details on their nature and the procedure of how they are derived are summarized.

MC Filter Efficiency

To obtain the filter efficiency in MC simulation, an unbiased sample without muon or pion kinematics filters is generated. The kinematic distribution is then obtained and compared to the distribution with kinematics filters explicitly applied. The filter efficiency is taken as the ratio between the distributions. Figure 5.9 and Figure 5.10 show the distribution and the obtained filter efficiency.

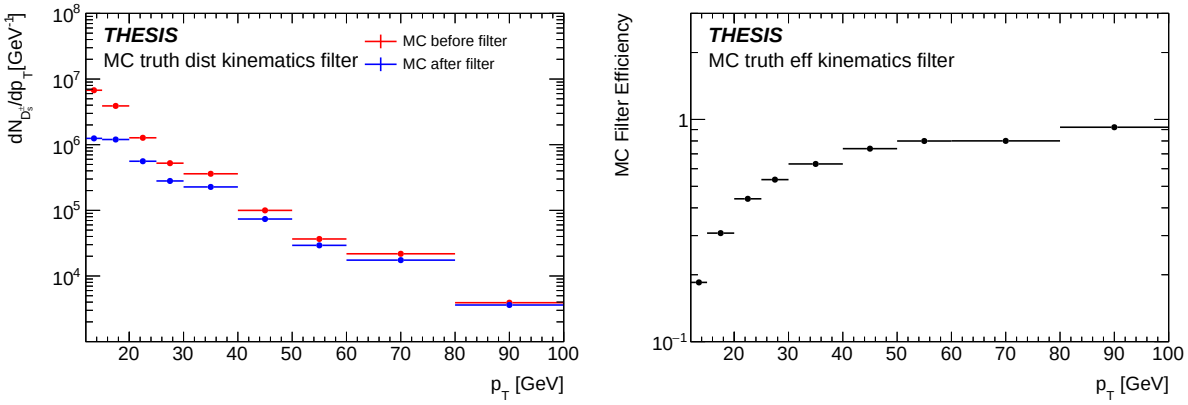

(a) Distribution in p_{T}

(b) Efficiency in p_{T}

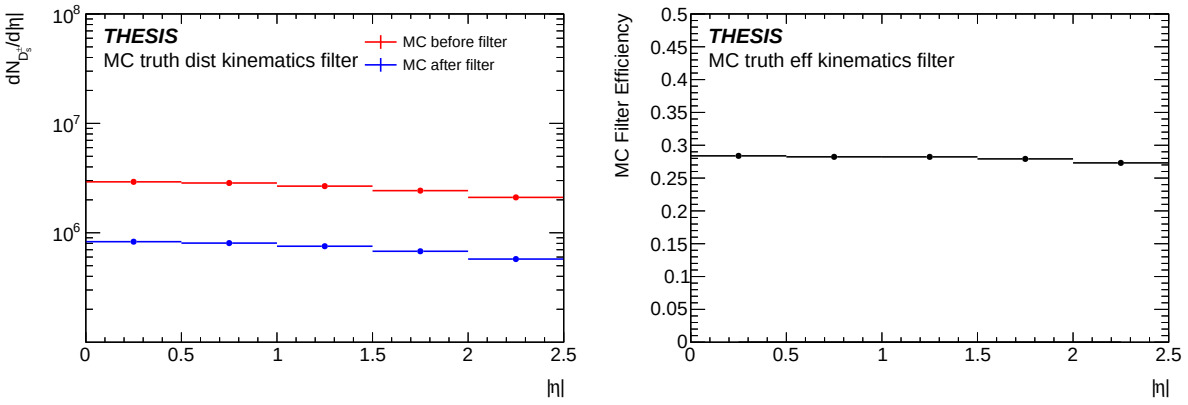

(c) Distribution in η

(d) Efficiency in η

Figure 5.9.: Distribution and efficiency of $D_s^{\pm}$ in p_{T} and η due to kinematics filters in MC samples.

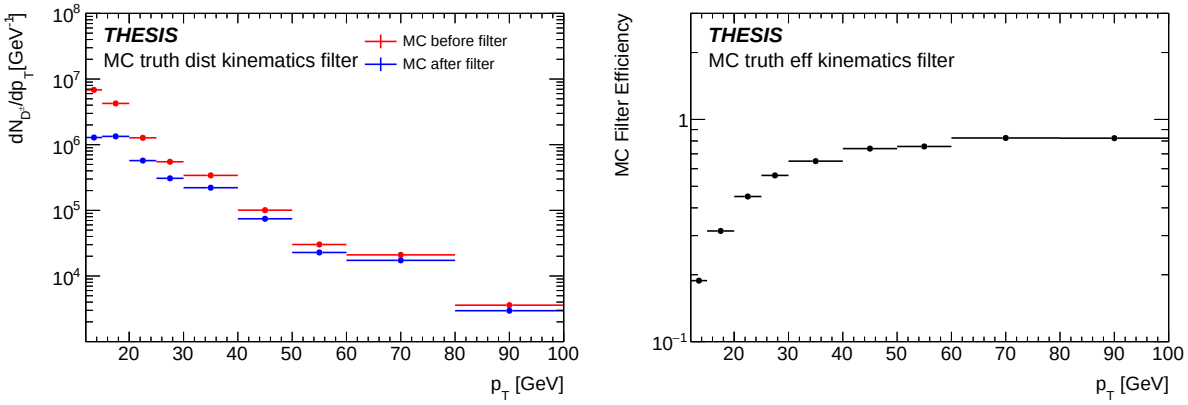

(a) Distribution in p_{T}

(b) Efficiency in p_{T}

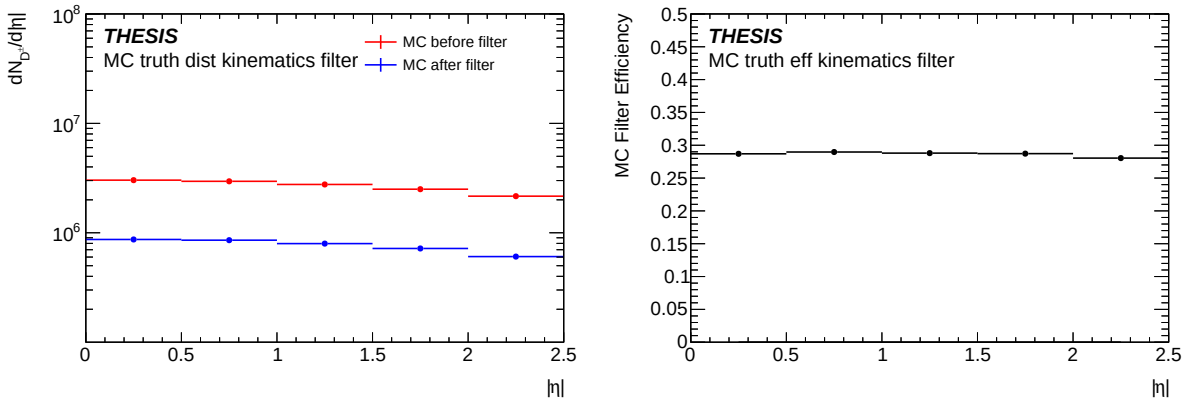

(c) Distribution in η

(d) Efficiency in η

Figure 5.10.: Distribution and efficiency of $D^{\pm}$ in p_{T} and η due to kinematics filters in MC samples.

Reconstruction Efficiency and Acceptance

To evaluate the efficiencies of different sets of cut, the p_{T} and η distribution at different levels of selection are recorded. The Analysis Object Data (AOD) level, which correspond to the reconstructed level with minimal selection applied, is used as the reference. The distribution of triplet candidates of AOD samples are recorded for different levels in the selection chain. The efficiency is taken as distribution at final level over the distribution at AOD level before selection. Figure 5.11 and Figure 5.12 show the distribution and the efficiency obtained. Note that the small efficiency at low p_{T} is due to trigger limitation, which remains to be one of the largest challenge of this analysis.

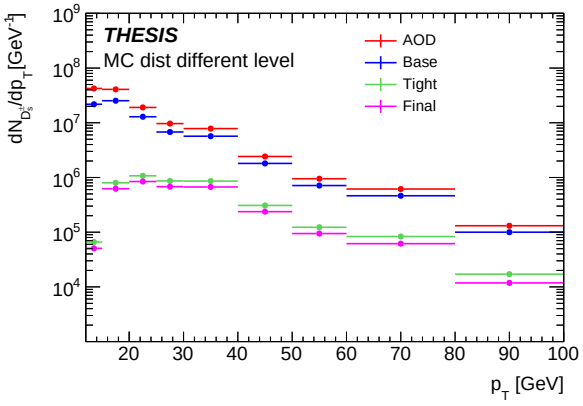

(a) Distribution in p_{T}

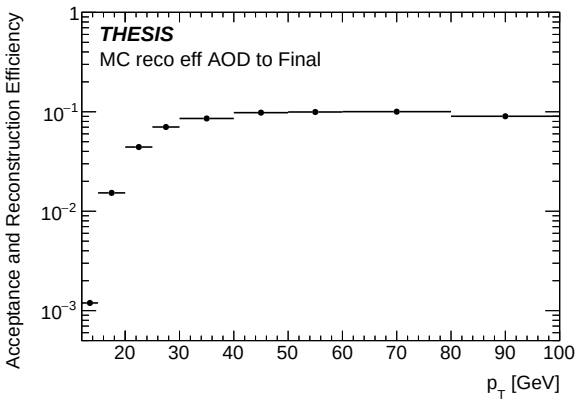

(b) Efficiency in p_{T}

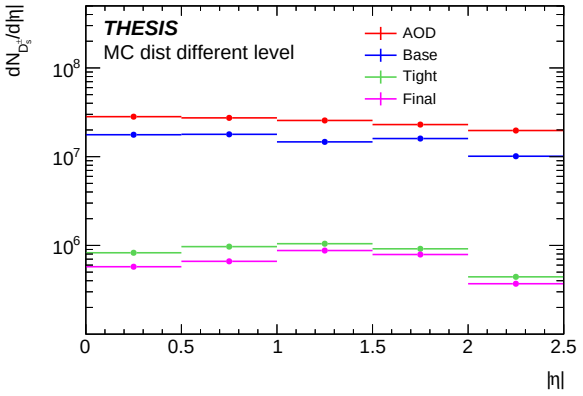

(c) Distribution in η

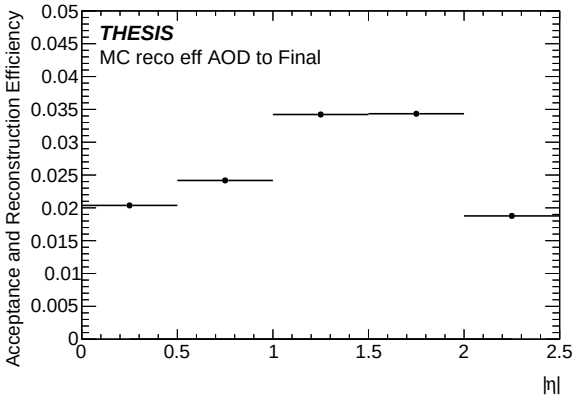

(d) Efficiency in η

Figure 5.11.: Distribution and efficiency of $D_s^{\pm}$ in p_{T} and η due to selection and acceptance in MC samples.

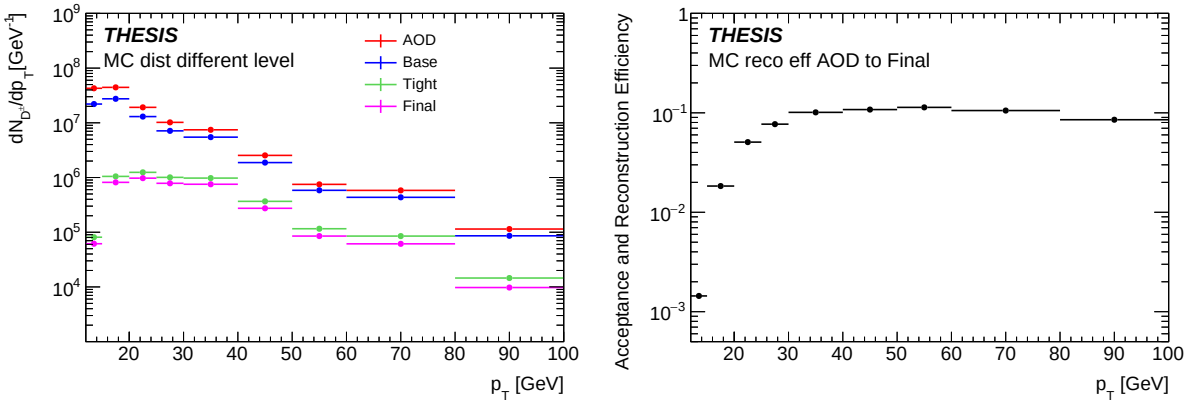

(a) Distribution in p_{T} **(b)** Efficiency in p_{T}

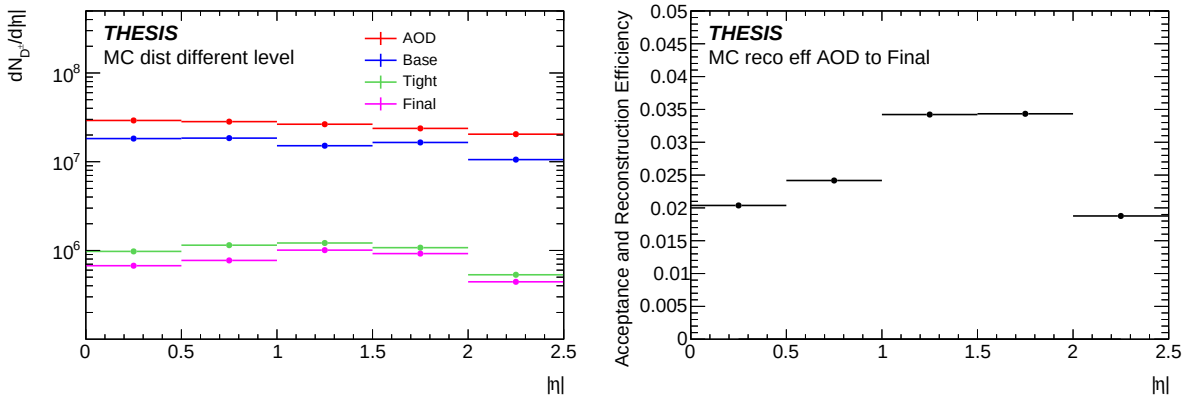

(c) Distribution in η **(d)** Efficiency in η

Figure 5.12.: Distribution and efficiency of $D^{\pm}$ in p_{T} and η due to selection and acceptance in MC samples.

5.4. Unfolding

A feasibility study of unfolding has been performed to investigate the possibility to correct for experimental effects, including the resolution and efficiency of the detector and trigger system. This allows direct comparison with particle-level predictions within the fiducial phase space.

The unfolding procedure is based on describing the relationship between the number of events measured in bins of a particular detector-level differential distribution and the yield in bins of the corresponding particle-level distribution using a single response matrix M. This matrix consists of two contributions:

- The reconstruction efficiency is measured as the ratio of the number of events which pass both the fiducial and detector event selections to the number passing the fiducial selection, as a function of $p_{\mathrm{T}}^{D_s}$ at particle level.
- A migration matrix which contains the probabilities that a particle-level event from a given fiducial bin which passes the detector selection will be found in a particular reconstructed bin. It accounts for bin-to-bin migrations.

The migration matrix is shown in Figure 5.13(a). Based on the migration matrix the response matrix is derived as the migration matrix normalized in each bin of the reconstructed p_{T}. The response matrix is shown in Figure 5.13(b). The binning is chosen such that the asymmetric binning in the migration matrix is transformed into an equidistant binning where bin i corresponds to the i-th p_{T} bin. The response matrix is then inverted to be applied on the reconstructed distribution. The inverted response matrix is shown in Figure 5.13(c).

Figure 5.14 shows the closure check based on $D_s^{\pm}$ signal samples. For the closure test the reconstructed p_{T} distribution is unfolded and compared to data. As can be seen from the ratio plot (right) the applied unfolding corrects for the p_{T} shift observed at reconstruction level.

The MC samples are weighted by the extracted b-fraction and luminosity to build the 2D distribution at final selection level. Then the response matrix is built by RooUnfold tool and inverted to unfold the $D_s^{\pm}$ signal yields, which are extracted by the mass fits.

Although the unfolding approach passed the tests, the level of correction when compared to the uncertainty is still small. On the other hand, the error of the unfolding matrix and the systematic uncertainty of the method together give a larger uncertainty compared to the correction. From the result, it is concluded that no significant bin-by-bin migration is observed between the reconstructed and particle-level distributions; statistically, no benefit can be gained from applying the unfolding procedure. Therefore, unfolding is not applied in this analysis.

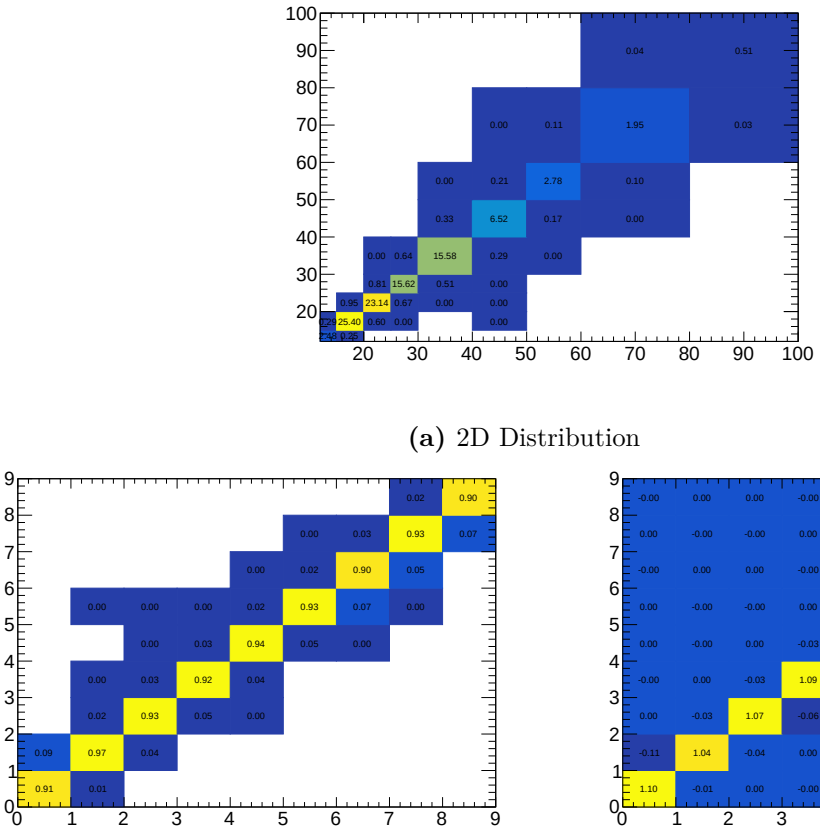

(a) 2D Distribution

(b) Response matrix

(c) Inverted response matrix

Figure 5.13.: 2D distribution, response and inverted response matrix of the transverse momentum of the $D_s^{\pm}$ meson at particle-level to reconstruction. In (a), the y-axis is the $D_s^{\pm}$ meson truth p_{T} in GeV and the x-axis is the reconstructed p_{T} in GeV. In (b) and (c), the distribution is converted to matrix, where the y-axis is the bins in truth p_{T} and the x-axis is the bins in reconstructed p_{T}.

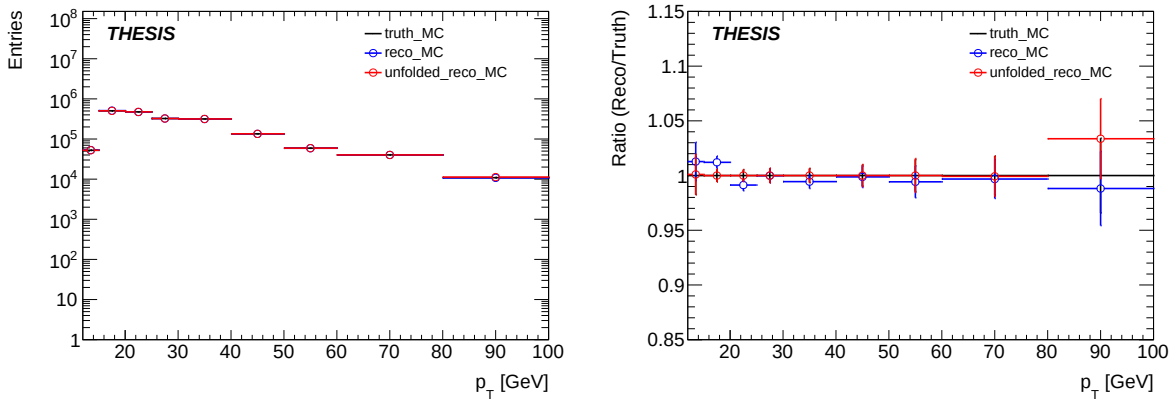

(a) (b)

Figure 5.14.: Closure test of the matrix inversion technique applied for unfolding in $D_s^{\pm}$ signal samples. Left: Transverse momentum of the triplet system at generated (black) and reconstructed (blue) level. In red the unfolded distribution is overlaid. Right: ratio of reconstructed and unfolded distribution w.r.t truth.

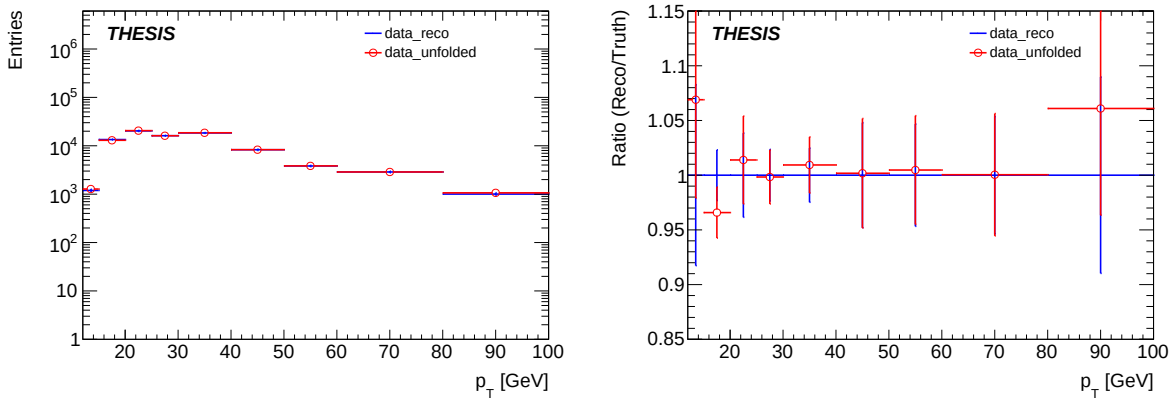

(a) (b)

Figure 5.15.: Unfolding applied to data.

Process	Branching Ratio	Percentage error
$D^{\pm} \to \phi\pi$	$(5.70 \pm 0.14)10^{-3}$	2.5%
$D_s^{\pm} \to \phi\pi$	$(4.5 \pm 0.4)10^{-2}$	8.9%
$D^{\pm} \to \phi(KK)\pi$	$(2.69^{+0.07}_{-0.08})10^{-3}$	2.6% 3.0%
$D_s^{\pm} \to \phi(KK)\pi$	$(2.22 \pm 0.06)10^{-2}$	2.7%
$\phi \to KK$	$(4.91 \pm 0.05)10^{-1}$	1.0%
$\phi \to \mu\mu$	$(2.85 \pm 0.19)10^{-4}$	6.7%

Table 5.1.: Summary of branching ratios [121] .

5.5. Cross Section

5.5.1. Signal Extraction

The differential cross section is measured in the fiducial volume defined by $12\,\text{GeV} < p_{\text{T}} < 100\,\text{GeV}$ and $|\eta| < 2.5$ for $D^{\pm}$ and $D_s^{\pm}$, inclusive for $+$ and $-$ charges. There are 9 bins of p_{T} and 5 bins in $|\eta|$. The bin boundaries in p_{T} are: 12 GeV, 15 GeV, 20 GeV, 25 GeV, 30 GeV, 40 GeV, 50 GeV, 60 GeV, 80 GeV and 100 GeV. The bin boundaries in $|\eta|$ are: 0.0, 0.5, 1.0, 1.5, 2.0, 2.5. To obtain the differential cross section in a given bin, the yields of $D^{\pm}$ and $D_s^{\pm}$ mesons in each bin are obtained by means of a fit to the triplet mass using the same procedure as described in Section 5.1.2. Figure 5.16 and Figure 5.17 show the invariant mass fit applied to different bins of p_{T} and $|\eta|$ to extract the signal. From the fits, it is observed that the performance of the fit model is consistent across bins of p_{T} and $|\eta|$, providing signal yields with reasonable statistical error. The extracted signal shapes are shown in Figure 5.18.

With the signal shapes extracted, the shape of the yield is compared to that of the MC samples. A difference in shape was observed when comparing the p_{T} distribution in MC samples and the p_{T} distribution extracted from data, which is expected, as current calculations at such momentum range is not reliable. There is in general more high p_{T} $D^{\pm}$ and $D_s^{\pm}$ and fewer low p_{T} ones in data compared to MC.For the measurements in bins of p_{T}, the effect is suppressed because the efficiencies are evaluated bin by bin in p_{T}. However, for the integral over differential cross section in $|\eta|$, the effect is not suppressed, because the efficiencies assume a mis-modelled p_{T} distribution. To correct for the p_{T} mis-modelling, a procedure of p_{T} reweighting is performed. The p_{T} reweighting profile is obtained by comparing the p_{T} distribution in MC samples versus the signal yields extracted from data.

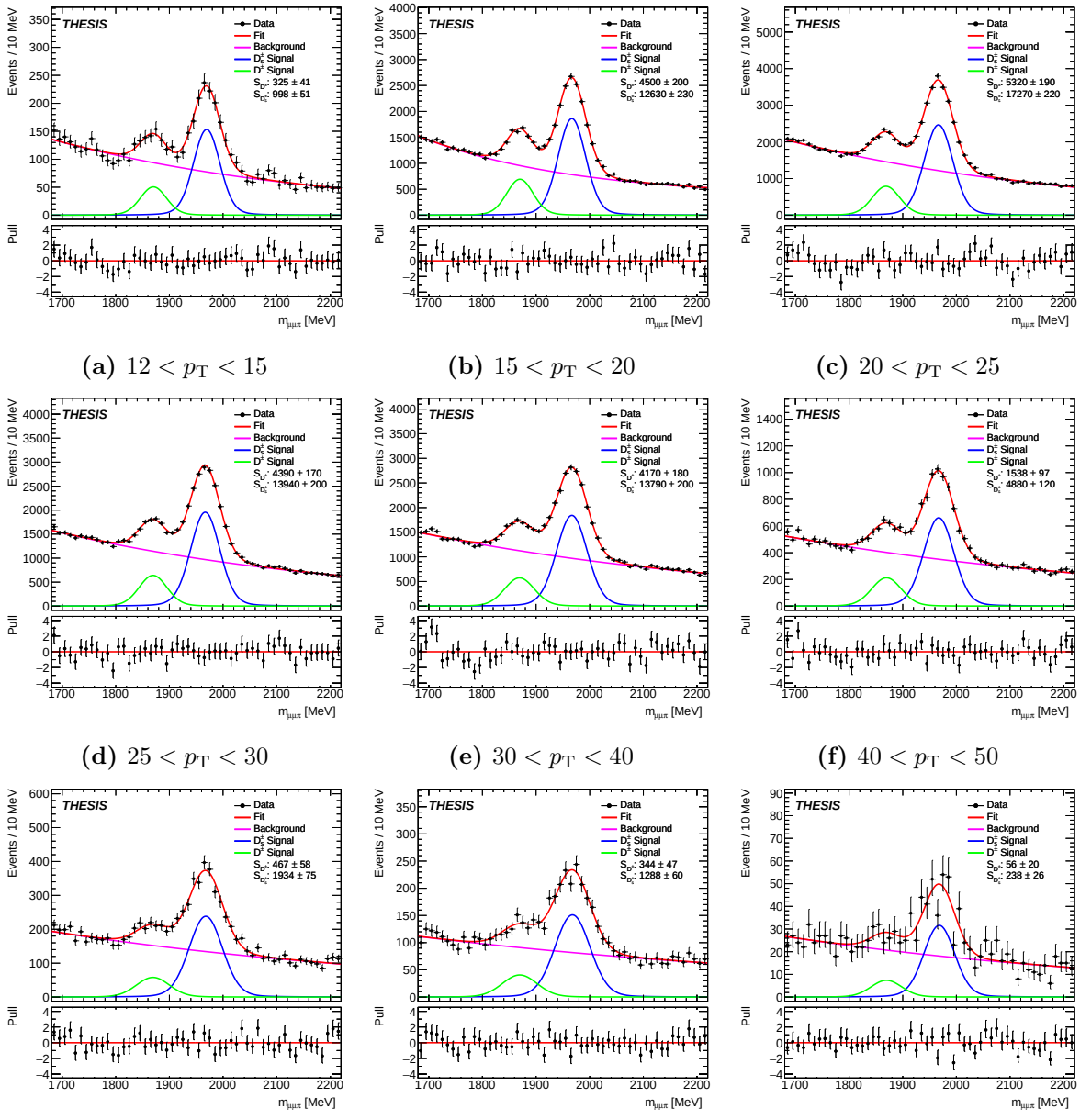

(a) $12 < p_T < 15$ **(b)** $15 < p_T < 20$ **(c)** $20 < p_T < 25$

(d) $25 < p_T < 30$ **(e)** $30 < p_T < 40$ **(f)** $40 < p_T < 50$

(g) $50 < p_T < 60$ **(h)** $60 < p_T < 80$ **(i)** $80 < p_T < 100$

Figure 5.16.: Invariant mass fit in bins of p_T (in GeV).

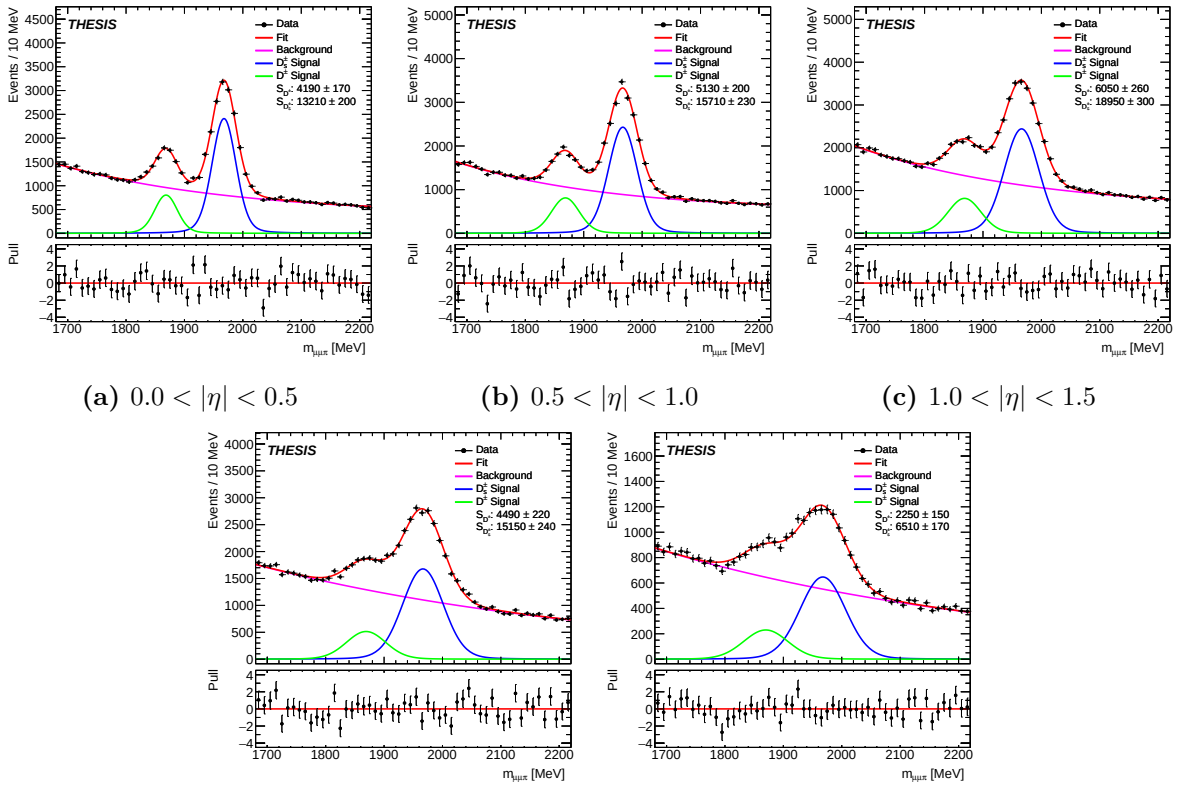

(a) $0.0 < |\eta| < 0.5$ **(b)** $0.5 < |\eta| < 1.0$ **(c)** $1.0 < |\eta| < 1.5$

(d) $1.5 < |\eta| < 2.0$ **(e)** $2.0 < |\eta| < 2.5$

Figure 5.17.: Invariant mass fit in bins of $|\eta|$.

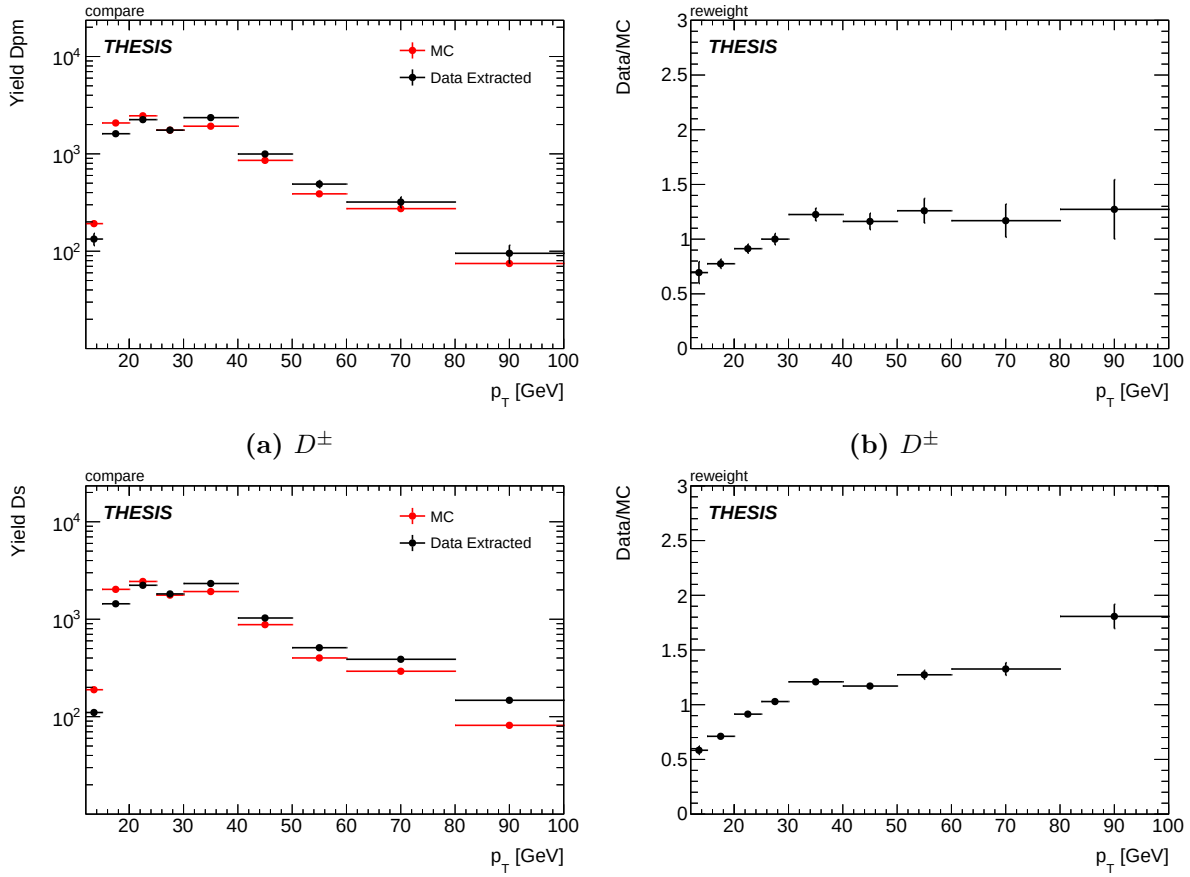

(a) $D^{\pm}$ **(b)** $D^{\pm}$

(c) $D_s^{\pm}$ **(d)** $D_s^{\pm}$

Figure 5.18.: Extracted signal yields of (a) $D^{\pm}$ and (c) $D_s^{\pm}$ in bins of p_{T} for data and MC samples; the yield ratios between data and MC samples for (b) $D^{\pm}$ and (d) $D_s^{\pm}$ in bins of p_{T} is also shown.

5.5.2. Differential Measurement

To calculate the differential measurement from the extracted yields, corrections for the reconstruction efficiency ϵ_{reco} and MC generation filter efficiency ϵ_{MC} are taken into account. The obtained yields are also divided by the bin width $\Delta p_{\text{T}}/\Delta\eta$ to account for the binning. The corresponding integrated luminosity for data obtained in 2016-2018 is calculated to be $137\,\text{fb}^{-1}$. The branching fraction of the decays are taken as the world average PDG value; the values are summarized in Table 5.1 [4]. From the table, it can be seen that a relatively large error of $BR(D_s^{\pm} \to \phi\pi)$ is quoted by PDG; therefore, the value is instead obtained by making use of $\phi \to KK$ values. The branching ratios for the $D^{\pm}$ and $D_s^{\pm}$ decays are calculated by:

$$\begin{aligned} BR(D^{\pm} \to \phi(\mu\mu)\pi) &= BR(D^{\pm} \to \phi\pi) \times BR(\phi \to \mu\mu) \\ BR(D_s^{\pm} \to \phi(\mu\mu)\pi) &= \frac{BR(D_s^{\pm} \to \phi(KK)\pi)}{BR(\phi \to KK)} \times BR(\phi \to \mu\mu) \end{aligned} \tag{5.8}$$

Thus, the differential cross section for the i-th bin in p_{T} and j-th bin in $|\eta|$ are given by the following equations:

$$\begin{aligned} \left.\frac{d\sigma}{dp_{\text{T}}}\right|_i &= \frac{S^i_{D^{\pm}/D_s^{\pm}}}{\int Ldt \times \epsilon^i_{\text{MC}} \times \epsilon^i_{\text{reco}} \times BR(D^{\pm}/D_s^{\pm} \to \phi(\mu\mu)\pi) \times \Delta^i p_{\text{T}}} \\ \left.\frac{d\sigma}{d|\eta|}\right|_j &= \frac{S^j_{D^{\pm}/D_s^{\pm}}}{\int Ldt \times \epsilon^j_{\text{MC}} \times \epsilon^j_{\text{reco}} \times BR(D^{\pm}/D_s^{\pm} \to \phi(\mu\mu)\pi) \times \Delta^j |\eta|} \end{aligned} \tag{5.9}$$

where $S^i_{D^{\pm}/D_s^{\pm}}$ and $S^j_{D^{\pm}/D_s^{\pm}}$ are the yields of $D^{\pm}$ and $D_s^{\pm}$ signals extracted in bins of p_{T} and $|\eta|$. The efficiencies ϵ^i_{MC} and ϵ^j_{MC} are also evaluated in bins of p_{T} and $|\eta|$.

5.5.3. Inclusive Measurement

Given the differential cross section measured in finite bins of p_{T} and $|\eta|$, the inclusive fiducial cross section can be calculated by summing over the fiducial differential cross section:

$$\begin{aligned} \sigma_{\text{fiducial}} &= \sum_i \left.\frac{d\sigma}{dp_{\text{T}}}\right|_i \Delta^i p_{\text{T}} \\ \sigma_{\text{fiducial}} &= \sum_j \left.\frac{d\sigma}{d|\eta|}\right|_j \Delta^j |\eta| \end{aligned} \tag{5.10}$$

where the summation over i corresponds to summing over bins of p_{T} and the summation over j corresponds to summing over bins of $|\eta|$. The value obtained by summing over p_{T} is the fiducial cross section reported in this thesis; while the value obtained by summing over $|\eta|$ provides a cross check of the p_{T} reweighting procedure. It is observed that the

two values are consistent to within 1% when summed over the ficucial volume defined by $|\eta| < 2.5$ and $p_{\mathrm{T}} > 12\,\mathrm{GeV}$.

To facilitate the use of the result as a normalization for other studies and comparison to Run-I, different fiducial volumes are considered. The lower p_{T} boundary of 12 GeV provides a value of the lowest p_{T} reach; the p_{T} boundary of 15 GeV provides a p_{T} range that guarantees trigger plateau to reduce the muon and trigger uncertainties; the p_{T} boundary of 20 GeV provides a p_{T} range compatible with the value measured in Run-I.

5.6. Systematic Uncertainties

Due to imperfect knowledge of our detector and the underlying physics, several systematic uncertainties are considered. Most the uncertainties propagate linearly to the differential cross section and thus to the fiducial cross section. Table 5.2 shows a list of systematic uncertainties and a brief description of the individual systematics that are included in the study; the breakdown of the systematics is also provided where available.

This section provides the more detailed description of the systematics. The validation of the vertex refit and the MC toy study is also presented. Finally, the systematics are combined to obtain the total systematic uncertainty.

5.6.1. Sources

The following groups of systematic uncertainty sources are considered:

Muon reconstruction The uncertainty in muon parameters is dominated by the uncertainty on the description of the detector material. Muons are smeared with the known detector resolution; then the selection of muon is performed on the smeared muons to evaluate the differences due to the smearing.

Tracking The track parameters have uncertainty primarily due to the uncertainty on the description of the inner detector. Track parameters, including the impact parameters and momentum, are smeared with the known detector resolution. The track selection is then applied on the smeared tracks to evaluate the differences due to the smearing. Track selection efficiency is also varied to account for fake tracks. The uncertainties on the track parameters are also propagated to the vertex variables by means of secondary vertex refits.

Pileup reweighting The pileup reweighting is a weight applied to MC samples to match the pileup distribution in data. Such weight is varied to account for the imperfect knowledge of pileup variation run by run.

Trigger Because of the relatively tight cut on the di-muon invariant mass, the signal events lie well inside the topological selection of the trigger. Therefore, the trigger uncertainty is mainly due to triggering of individual muons and the correlation between the two muons.

Systematics	Brief Description
Muon Reconstruction	
MUON_SAGITTA_DATASTAT	Statistical error on the charge dependant corrections
MUON_SAGITTA_RESBIAS	Variations in the momentum scale
MUON_CB	Variations in the CB track resolution directly
MUON_SCALE_CB	Variations in the momentum scale corrections to CB track directly
MUON_SCALE_CB_ELOSS	Variations in the energy loss corrections to CB track directly
MUON_EFF_RECO_STAT	Statitical error on the $p_{\mathrm{T}} > 15$ GeV component of the SF
MUON_EFF_RECO_SYS	Systematic error on the $p_{\mathrm{T}} > 15$ GeV component of the SF
MUON_EFF_RECO_STAT_LOWPT	Statitical error on the $p_{\mathrm{T}} < 15$ GeV component of the SF
MUON_EFF_RECO_SYS_LOWPT	Systematic error on the $p_{\mathrm{T}} < 15$ GeV component of the SF
Tracking	
TRK_RES_D0_MEAS	Uncertainties on the impact parameter resolution
TRK_RES_Z0_MEAS	Uncertainties on the impact parameter resolution
TRK_BIAS_D0_WM	Residual aligment uncertainties
TRK_BIAS_Z0_WM	Residual aligment uncertainties
TRK_BIAS_QOVERP_SAGITTA_WM	Residual aligment uncertainties
TRK_EFF_TIGHT_GLOBAL	Uncertainties on the efficiency and fake rate
Pileup Reweighting	
PRW_DATASF	Uncertainties on pileup weight
Others	
Trigger	Uncertainties on di-muon triggers
MC Size	Uncertainties due to limited number of events simulated
Luminosity	Uncertainties on luminosity recorded
Fit model	Uncertainties on choice of fit models
Non-prompt Fraction	Uncertainties on non-prompt weight when combining MC samples

Table 5.2.: Systematic uncertainties and brief description. For systematics with specific key names, the key names are also listed.

The discrepancy between data and simulated muons has been studied using $J/\psi \to \mu\mu$ events, with data collected in individual years from 2016 to 2018. A scale factor with corresponding systematic error is assigned to correct for the discrepancy.

MC Size The uncertainty due to a limited number of events of the dataset simulated by MC simulation.

Luminosity The uncertainty in the integrated luminosity of the combined dataset from 2016, 2017 and 2018 is 0.84%, using the same methodology as in Ref [122], and obtained using the LUCID-2 detector [123] for the primary luminosity measurements, complemented by measurements using the inner detector and calorimeters.

Fit models The fit model systematics can be separated into contributions from the signal model and the background model. MC toys are generated according to the distribution obtained from data; fits with alternative models are then applied to the MC toys. For the signal model, the Bukin model and triple Gaussian models are chosen as alternative models. For the background model, the simple exponential model is taken as the alternative model. By repeatedly fitting the nominal models and the alternative models to the MC toys, the distributions of the yield estimators are obtained. The maximum yield difference between the nominal model and the alternative models is taken as the systematic uncertainties.

Non-prompt fraction The non-prompt fraction is the relative weight between prompt and non-prompt MC samples. By varying the non-prompt fraction, the uncertainty is propagated to the overall efficiencies. The level of uncertainty is suppressed because of the similar efficiency between prompt and non-prompt processes.

Branching ratio The uncertainty of the branching ratios as in Table 5.1.

5.6.2. Vertex Refit

After applying the systematic uncertainties on tracks and muons, the vertex parameters are expected to change. Since the primary vertices typically contains tens of tracks, the parameter is mostly unchanged. For the secondary vertices, the sensitivity is much larger in comparison. Therefore, the refit is only applied to the secondary vertex. To perform a light and fast refit to account for systematic uncertainties, the refit tool ELExtrapolator(ELE) is adopted. The tool takes the three inner detector tracks of the selected secondary vertices, perform a refit, and provides the refitted vertex coordinates.

The coordinates obtained by the refit are compared to the vertex given by standard BPHY tool. Figure 5.19 and Figure 5.20 shows the comparison of the coordinates and resolution of the two tools. Comparing the $x-$coordinates of the vertices, it is observed that the difference between the two tool is of order 0.005 mm while the resolution of the vertex is of order 0.1 mm. The corresponding L_{xy} distributions are also shown in Figure 5.21. Although the vertex resolution of vertices provided by the ELE tool (ELE vertex) are slightly worse, the differences are insignificant for the purpose of the measurements presented. Given the small difference, the ELE vertex is therefore used for further calculation of

the vertex variables and evaluation of the track systematics. In particular, the level of the track and vertex resolution is propagated to the L_{xy} and its significance, as shown in Figure 5.22 and Figure 5.23. Table 5.3 summarizes the level of resolution, level of smearing and level of difference introduced by the ELE tool.

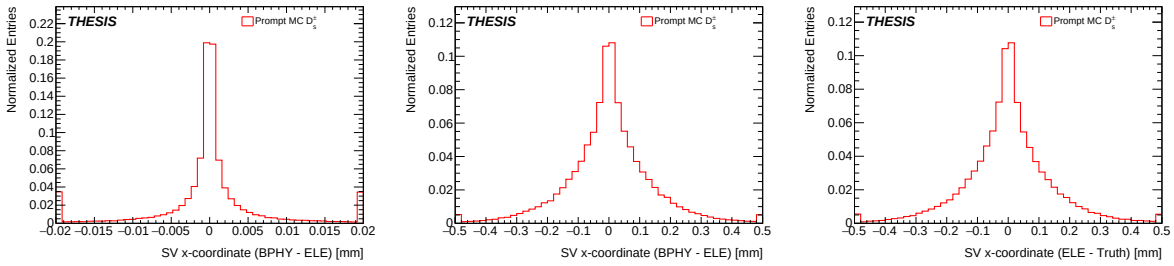

(a) Difference between tools **(b)** BPHY resolution **(c)** ELE resolution

Figure 5.19.: Comparing x-coordinates of BPHY tool secondary vertex and ELE tool secondary vertex.

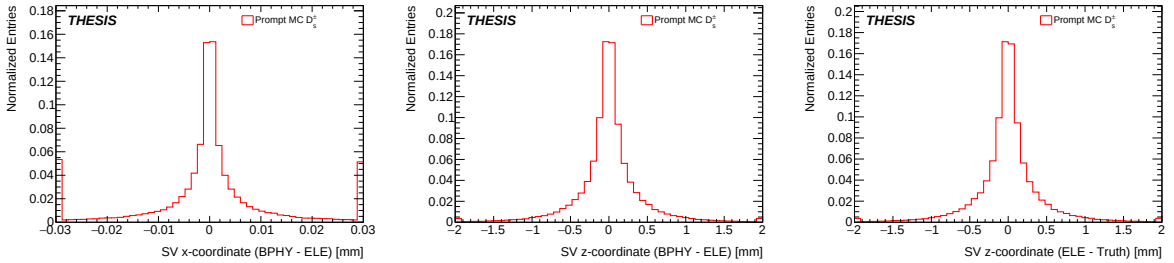

(a) Difference between tools **(b)** BPHY resolution **(c)** ELE resolution

Figure 5.20.: Comparing z-coordinates of BPHY tool secondary vertex and ELE tool secondary vertex.

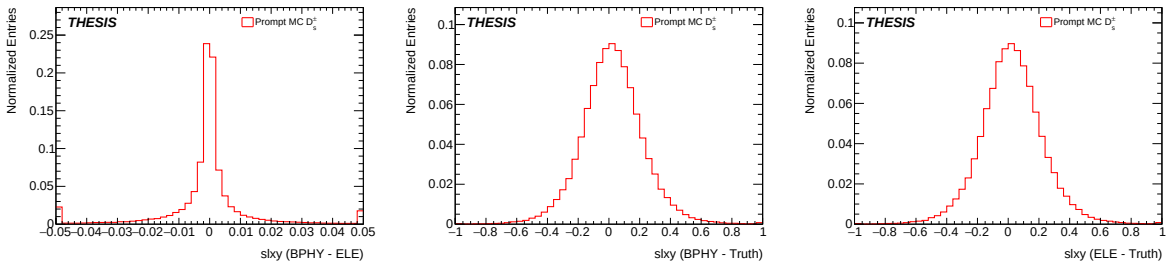

(a) Difference between tools **(b)** BPHY resolution **(c)** ELE resolution

Figure 5.21.: Comparing L_{xy} of BPHY tool secondary vertex and ELE tool secondary vertex.

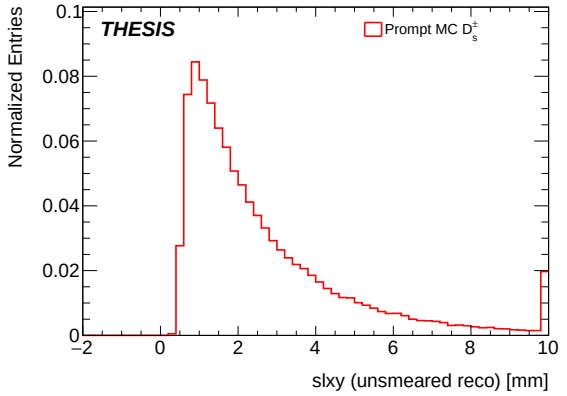

(a) Unsmeared distribution

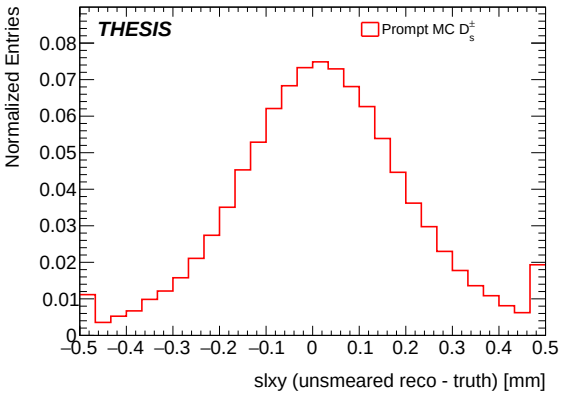

(b) Unsmeared resolution

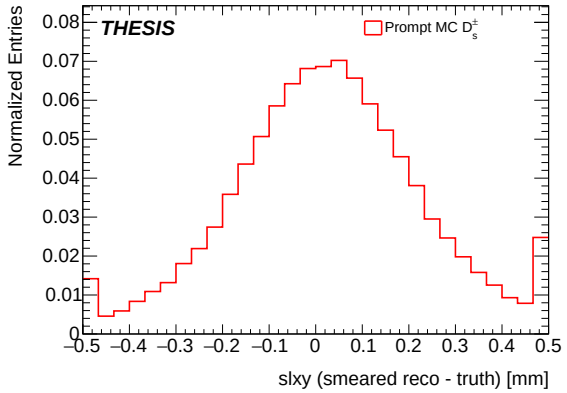

(c) Smeared resolution

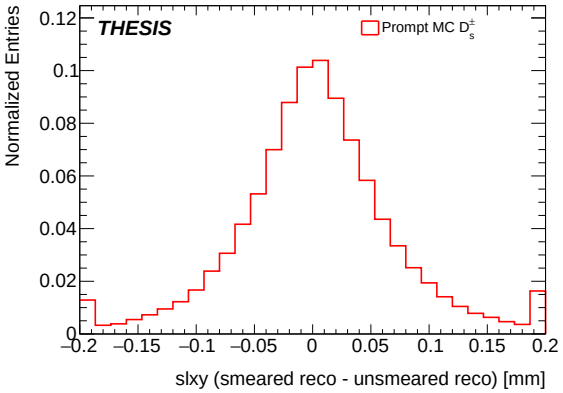

(d) Smeared minus unsmeared

Figure 5.22.: Effect of track smearing on L_{xy}.

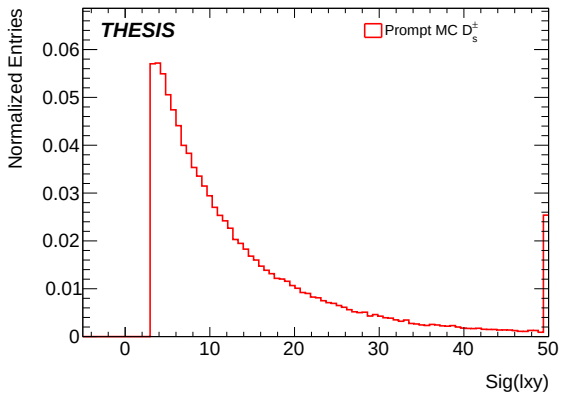

(a) Unsmeared distribution

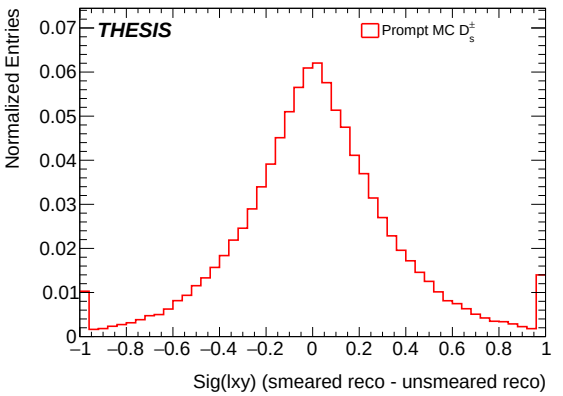

(b) Smeared minus unsmeared

Figure 5.23.: Effect of track smearing on sig(L_{xy}).

	Resolution [mm]	Track smearing [mm]	ELE bias [mm]
Pion d0	0.02	0.005	-
SV x-coordinate	0.05	0.02	0.002
L_{xy}	0.15	0.05	0.005
Sig(L_{xy})	-	0.2	-

Table 5.3.: Comparison of approximate level of resolution, level of smearing introduced by track systematics and level of bias introduced by ELE vertex refit tool.

5.6.3. Alternative Models

To evaluate the modelling systematics, alternative models are tested against the nominal models. In appendix B, the nominal model and the alternative models are fitted to the invariant mass distributions in bins of different p_{T} and $|\eta|$ for comparison. By comparing the nominal model against the alternative models, differences in the level of few % are observed in the yields extracted.

For the signal systematics, the Bukin model and the triple Gaussian models are chosen as the alternative models. Fits are first performed on the MC samples to obtain the parameters of the models. The procedure is repeated in different bins of p_{T} and $|\eta|$. Figure B.1 and Figure B.2 shows the Bukin model fitted to the invariant mass of $D^{\pm}$ and $D_s^{\pm}$ MC samples in bins of different p_{T} and $|\eta|$. Figure B.3 and Figure B.4 shows the triple Gaussian model fitted to the invariant mass of $D^{\pm}$ and $D_s^{\pm}$ MC samples in bins of different p_{T} and $|\eta|$. Then the parameters are fixed and the fits are performed to the data. Figure B.5 and Figure B.6 shows the Bukin model and the triple Gaussian models fitted to the invariant mass of data in bins of different p_{T} and $|\eta|$.

For the background systematics, the simple exponential model is tested against the quadratic exponential model in the nominal model. Figure B.7 shows the exponential model fitted to the invariant mass in data.

5.6.4. MC Toy Study

To evaluate the difference between using different alternative models in greater accuracy, hundreds of MC toy datasets are generated based on the data distribution. For each MC toy, the nominal model and the alternative models are fitted. The difference in the yields are then calculated. The distribution of the extracted yield is then fitted with a Gaussian function. The difference in the mean of the Gaussian function compared to the nominal is taken as the systematic uncertainty. The obtained values are summarized in Table 5.4 and Table 5.5.

	$D_s^{\pm}$ meson yield [Counts]			
Range	Nominal	Bukin	TripleGauss	ExpBkg
$0.0 < \|\eta\| < 0.5$	12975	12318	12542	12588
$0.5 < \|\eta\| < 1.0$	15376	14775	14819	14709
$1.0 < \|\eta\| < 1.5$	18695	18611	18414	18003
$1.5 < \|\eta\| < 2.0$	15132	14828	15053	14784
$2.0 < \|\eta\| < 2.5$	6865	6933	6897	6476
$12 < p_{\mathrm{T}} < 15$	1006	1038	1014	968
$15 < p_{\mathrm{T}} < 20$	12308	12559	12742	11834
$20 < p_{\mathrm{T}} < 25$	17413	17629	17749	16995
$25 < p_{\mathrm{T}} < 30$	13898	13924	14154	13767
$30 < p_{\mathrm{T}} < 40$	13975	13992	14159	13634
$40 < p_{\mathrm{T}} < 100$	8659	8793	8798	8266

Table 5.4.: Summary of the $D_s^{\pm}$ meson yield extracted by the MC toy study.

	$D^{\pm}$ meson yield [Counts]			
Range	Nominal	Bukin	TripleGauss	ExpBkg
$0.0 < \|\eta\| < 0.5$	4101	3979	3983	3728
$0.5 < \|\eta\| < 1.0$	5019	4628	4741	4421
$1.0 < \|\eta\| < 1.5$	6013	5733	5794	5362
$1.5 < \|\eta\| < 2.0$	4731	4834	4421	4434
$2.0 < \|\eta\| < 2.5$	2508	2989	2446	2235
$12 < p_{\mathrm{T}} < 15$	356	362	359	331
$15 < p_{\mathrm{T}} < 20$	4385	4685	4472	3953
$20 < p_{\mathrm{T}} < 25$	5583	5794	5588	5202
$25 < p_{\mathrm{T}} < 30$	4502	4785	4476	4352
$30 < p_{\mathrm{T}} < 40$	4353	4637	4252	4039
$40 < p_{\mathrm{T}} < 100$	2680	3074	2671	2372

Table 5.5.: Summary of the $D^{\pm}$ meson yield extracted by the MC toy study.

5.6.5. Combining Systematics

The combination procedure is separated into two steps: averaging and categorization.

Each class of systematic uncertainty is first evaluated bin by bin, e.g. in bins of p_{T} and $|\eta|$. Since the systematic uncertainty is also affected by limited MC statistics, each class of uncertainty is averaged to reduce fluctuation, which is given by the formula:

$$\delta = \frac{|\delta_{up}| + |\delta_{down}|}{2} \tag{5.11}$$

where δ_{up} and δ_{down} are the systematic uncertainty evaluated by varying the systematics parameter up and down respectively. Before averaging, it is also checked that all the systematic profiles show a symmetric envelope shape in bins of p_{T} and $|\eta|$. Then the averaged systematics are further categorized into muon, track, pileup and so on. The categorized systematics are finally combined to give the final systematics.

Figure 5.24 and Figure 5.25 show the systematic uncertainty profiles of $D^{\pm}$ and $D_s^{\pm}$ mesons in bins of p_{T} and $|\eta|$. The largest systematic uncertainties are mainly contributed by the branching ratios, followed by trigger uncertainty and background modelling. For $D_s^{\pm}$, the combined uncertainty is around 10%, while that of $D^{\pm}$ is around 20%, due to a lower yield, which is more sensitive to the choice of background model.

5.7. Results

5.7.1. Theoretical Prediction

FONLL

The FONLL prediction is extracted bin-by-bin per p_{T} and $|\eta|$ through a web interface. For $D^{\pm}$ meson production, both contributions from b and c quarks are considered. The FONLL prediction for $D^{\pm}$ meson production is given by the following formula:

$$\begin{aligned}
\frac{d\sigma^{bb}_{D^{\pm}}}{dp_{\mathrm{T}}} &= \sigma^{\mathrm{inclusive}}_{bb} \times 2 f_{b\to D^{\pm}} \times \frac{1}{\delta p_{\mathrm{T}}} \\
\frac{d\sigma^{cc}_{D^{\pm}}}{dp_{\mathrm{T}}} &= \sigma^{\mathrm{inclusive}}_{cc} \times 2 f_{c\to D^{\pm}} \times \frac{1}{\delta p_{\mathrm{T}}} \\
\frac{d\sigma^{bb}_{D^{\pm}}}{d|\eta|} &= \sigma^{\mathrm{inclusive}}_{bb} \times 2 f_{b\to D^{\pm}} \times \frac{1}{\delta |\eta|} \\
\frac{d\sigma^{cc}_{D^{\pm}}}{d|\eta|} &= \sigma^{\mathrm{inclusive}}_{cc} \times 2 f_{c\to D^{\pm}} \times \frac{1}{\delta |\eta|}
\end{aligned} \tag{5.12}$$

where $\sigma^{\mathrm{inclusive}}_{bb}$ and $\sigma^{\mathrm{inclusive}}_{cc}$ are the predicted cross section in the kinematic region of interest for the b and c quarks, $f_{b\to D^{\pm}}$ and $f_{c\to D^{\pm}}$ are the fragmentation function of the quark

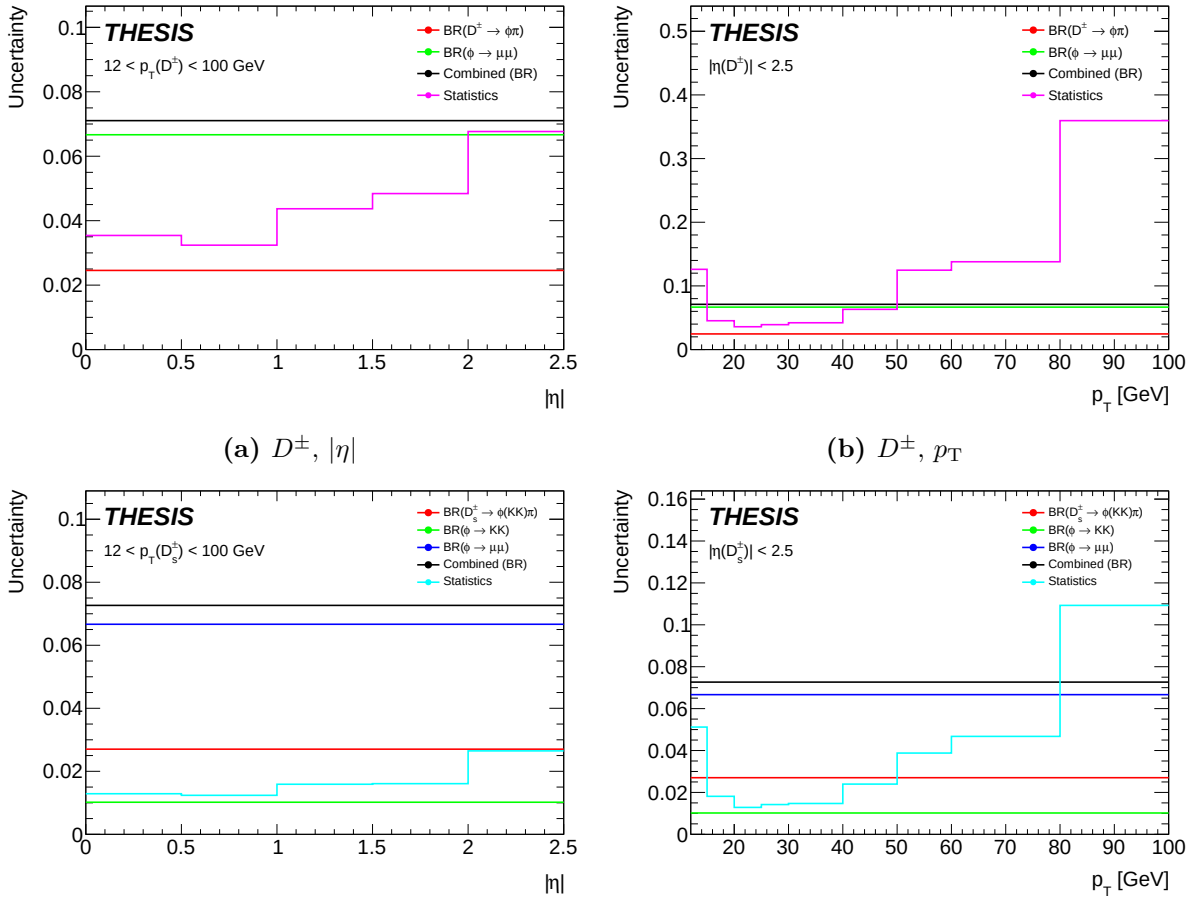

(a) $D^{\pm}$, $|\eta|$ **(b)** $D^{\pm}$, p_{T}

(c) $D_s^{\pm}$, $|\eta|$ **(d)** $D_s^{\pm}$, p_{T}

Figure 5.24.: Relative branching ratio and statistical uncertainties for $D^{\pm}$ and $D_s^{\pm}$ mesons in bins of p_{T} and $|\eta|$.

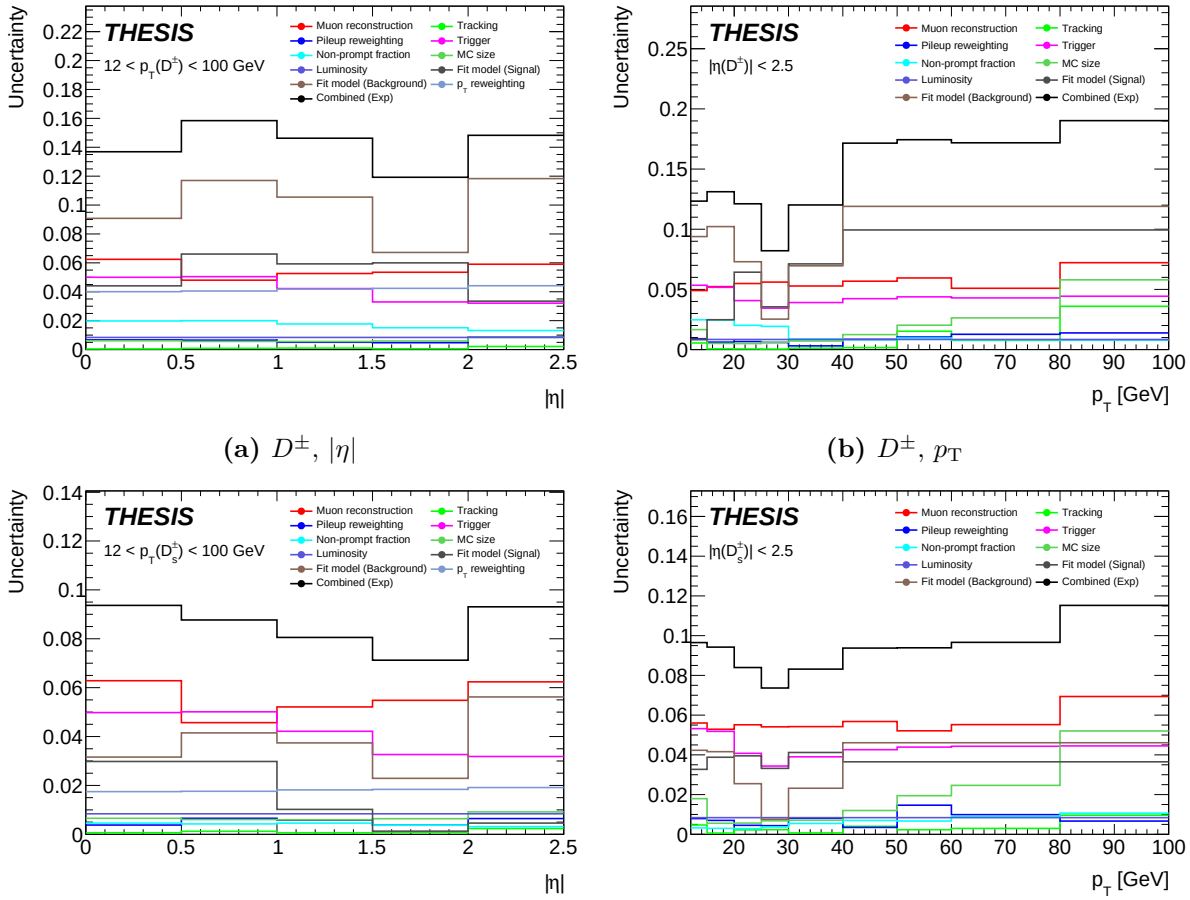

(a) $D^{\pm}$, $|\eta|$ **(b)** $D^{\pm}$, p_{T}

(c) $D_s^{\pm}$, $|\eta|$ **(d)** $D_s^{\pm}$, p_{T}

Figure 5.25.: Relative experimental systematic uncertainties for $D^{\pm}$ and $D_s^{\pm}$ mesons in bins of p_{T} and $|\eta|$.

taken from LEP measurements, δp_{T} and $\delta|\eta|$ are the bin width in p_{T} and η. There is also a factor of 2, which accounts for the inclusive measurement of both positive and negative charged $D^{\pm}$ mesons. The fragmentation fractions are taken from LEP measurements [124]; Table 5.6 shows the fragmentation fractions for b quarks and c quarks hadronize to $D^{\pm}$ and $D_s^{\pm}$ mesons.

Process	Fragmentation fraction $f \pm \delta_{\mathrm{stat}} \pm \delta_{\mathrm{syst}}$
$b \to D^{\pm}$	$0.223 \pm 0.011 \pm 0.005$
$b \to D_s^{\pm}$	$0.138 \pm 0.009 \pm 0.006$
$c \to D^{\pm}$	$0.225 \pm 0.010 \pm 0.005$
$c \to D_s^{\pm}$	$0.092 \pm 0.008 \pm 0.005$

Table 5.6.: Fragmentation fractions for b quarks and c quarks hadronize to $D^{\pm}$ and $D_s^{\pm}$ mesons.

GM-VFNS

The GM-VFNS prediction is provided in bins of p_{T} and $|\eta|$ for both $D^{\pm}$ and $D_s^{\pm}$ mesons by the author of the paper [125]. The original values provided are in bins of rapidity y, instead of pseudorapidity η. Upon discussion with the authors, it is advised to neglect the small error due to the difference between y and η given the large theoretical uncertainty and the D mesons are reasonably boosted.

	Differential cross section [µb]		
Range	Data ($\frac{d\sigma}{d\|\eta\|} \pm \delta_{\mathrm{stat}} \pm \delta_{\mathrm{syst}}$)	FONLL ($\frac{d\sigma}{d\|\eta\|} \pm \delta_{\mathrm{theory}}$)	GM-VFNS ($\frac{d\sigma}{d\|\eta\|} \pm \delta_{\mathrm{theory}}$)
$0.0 < \|\eta\| < 0.5$	$(5.72 \pm 0.19 \pm 0.83)$	$(4.80^{+1.27}_{-0.93})$	$(6.41^{+1.33}_{-1.07})$
$0.5 < \|\eta\| < 1.0$	$(5.92 \pm 0.20 \pm 1.04)$	$(4.65^{+1.23}_{-0.90})$	$(6.22^{+1.29}_{-1.04})$
$1.0 < \|\eta\| < 1.5$	$(5.00 \pm 0.22 \pm 0.77)$	$(4.34^{+1.15}_{-0.84})$	$(5.84^{+1.21}_{-0.97})$
$1.5 < \|\eta\| < 2.0$	$(3.63 \pm 0.18 \pm 0.48)$	$(3.88^{+1.03}_{-0.75})$	$(5.26^{+1.08}_{-0.87})$
$2.0 < \|\eta\| < 2.5$	$(3.30 \pm 0.23 \pm 0.80)$	$(3.30^{+0.88}_{-0.65})$	$(4.50^{+0.92}_{-0.75})$

Table 5.7.: Differential cross section of $D^{\pm}$ meson within $12 < p_{\mathrm{T}} < 100$ GeV in bins of $|\eta|$.

	Differential cross section [pb/GeV]		
Range [GeV]	Data ($\frac{d\sigma}{dp_{\mathrm{T}}} \pm \delta_{\mathrm{stat}} \pm \delta_{\mathrm{syst}}$)	FONLL ($\frac{d\sigma}{dp_{\mathrm{T}}} \pm \delta_{\mathrm{theory}}$)	GM-VFNS ($\frac{d\sigma}{dp_{\mathrm{T}}} \pm \delta_{\mathrm{theory}}$)
$12 < p_{\mathrm{T}} < 15$	$(1.85 \pm 0.23 \pm 0.24)10^6$	$(1.87^{+0.56}_{-0.39})10^6$	$(2.45^{+0.58}_{-0.44})10^6$
$15 < p_{\mathrm{T}} < 20$	$(696 \pm 31 \pm 111)10^3$	$(628^{+157}_{-117})10^3$	$(854^{+166}_{-138})10^3$
$20 < p_{\mathrm{T}} < 25$	$(206 \pm 7 \pm 26)10^3$	$(195^{+40}_{-32})10^3$	$(276^{+44}_{-39})10^3$
$25 < p_{\mathrm{T}} < 30$	$(92.0 \pm 3.6 \pm 11.2)10^3$	$(75.3^{+13.3}_{-11.3})10^3$	$(109.6^{+14.8}_{-14.2})10^3$
$30 < p_{\mathrm{T}} < 40$	$(28.1 \pm 1.2 \pm 3.9)10^3$	$(25.0^{+3.9}_{-3.4})10^3$	$(37.5^{+4.3}_{-4.4})10^3$
$40 < p_{\mathrm{T}} < 50$	$(8.72 \pm 0.55 \pm 1.85)10^3$	$(6.97^{+0.93}_{-0.86})10^3$	$(10.76^{+0.99}_{-1.12})10^3$
$50 < p_{\mathrm{T}} < 60$	$(3.03 \pm 0.33 \pm 0.65)10^3$	$(2.47^{+0.30}_{-0.29})10^3$	$(3.89^{+0.30}_{-0.37})10^3$
$60 < p_{\mathrm{T}} < 80$	$(1.07 \pm 0.13 \pm 0.23)10^3$	$(0.75^{+0.08}_{-0.08})10^3$	$(1.21^{+0.08}_{-0.10})10^3$
$80 < p_{\mathrm{T}} < 100$	$(182 \pm 63 \pm 42)$	(186^{+19}_{-19})	(308^{+16}_{-24})

Table 5.8.: Differential cross section of $D^{\pm}$ meson within $|\eta| < 2.5$ in bins of p_{T}.

	Differential cross section [µb]	
Range	Data ($d\frac{d\sigma}{d\lvert\eta\rvert} \pm \delta_{\mathrm{stat}} \pm \delta_{\mathrm{syst}}$)	GM-VFNS ($\frac{d\sigma}{d\lvert\eta\rvert} \pm \delta_{\mathrm{theory}}$)
$0.0 < \lvert\eta\rvert < 0.5$	$(2.57 \pm 0.03 \pm 0.32)$	$(2.69^{+0.56}_{-0.45})$
$0.5 < \lvert\eta\rvert < 1.0$	$(2.59 \pm 0.03 \pm 0.30)$	$(2.62^{+0.55}_{-0.44})$
$1.0 < \lvert\eta\rvert < 1.5$	$(2.21 \pm 0.04 \pm 0.24)$	$(2.46^{+0.51}_{-0.41})$
$1.5 < \lvert\eta\rvert < 2.0$	$(1.79 \pm 0.03 \pm 0.18)$	$(2.22^{+0.46}_{-0.37})$
$2.0 < \lvert\eta\rvert < 2.5$	$(1.42 \pm 0.04 \pm 0.17)$	$(1.90^{+0.39}_{-0.32})$

Table 5.9.: Differential cross section of $D_s^{\pm}$ meson within $12 < p_{\mathrm{T}} < 100$ GeV in bins of $|\eta|$.

	Differential cross section [pb/GeV]	
Range [GeV]	Data ($\frac{d\sigma}{dp_{\mathrm{T}}} \pm \delta_{\mathrm{stat}} \pm \delta_{\mathrm{syst}}$)	GM-VFNS ($\frac{d\sigma}{dp_{\mathrm{T}}} \pm \delta_{\mathrm{theory}}$)
$12 < p_{\mathrm{T}} < 15$	$(851 \pm 44 \pm 102)10^3$	$(1020^{+241}_{-185})10^3$
$15 < p_{\mathrm{T}} < 20$	$(303 \pm 5 \pm 35)10^3$	$(362^{+71}_{-59})10^3$
$20 < p_{\mathrm{T}} < 25$	$(101 \pm 1 \pm 11)10^3$	$(119^{+19}_{-17})10^3$
$25 < p_{\mathrm{T}} < 30$	$(42.1 \pm 0.6 \pm 4.2)10^3$	$(47.5^{+6.5}_{-6.2})10^3$
$30 < p_{\mathrm{T}} < 40$	$(14.5 \pm 0.2 \pm 1.5)10^3$	$(16.4^{+1.9}_{-1.9})10^3$
$40 < p_{\mathrm{T}} < 50$	$(3.81 \pm 0.09 \pm 0.43)10^3$	$(4.74^{+0.45}_{-0.50})10^3$
$50 < p_{\mathrm{T}} < 60$	$(1.48 \pm 0.06 \pm 0.17)10^3$	$(1.72^{+0.14}_{-0.17})10^3$
$60 < p_{\mathrm{T}} < 80$	$(483 \pm 21 \pm 56)$	(539^{+37}_{-47})
$80 < p_{\mathrm{T}} < 100$	$(79.1 \pm 8.8 \pm 10.5)$	$(138.1^{+7.7}_{-10.8})$

Table 5.10.: Differential cross section of $D_s^{\pm}$ meson within $|\eta| < 2.5$ in bins of p_{T}.

5.7.2. Measured Values

The measured differential cross section and the theory prediction are shown in Figure 5.26. Table 5.7, Table 5.8, Table 5.9 and Table 5.10 summarize the measured differential cross section for $D^{\pm}$ and $D_s^{\pm}$ mesons together with the prediction. The fiducial cross section is summarized in Table 5.11 including the theory prediction as available.

For the $D^{\pm}$ meson, a good agreement is observed at low-p_{T} for both the GM-VFNS and FONLL prediction give; the FONLL prediction is in general slightly lower than the measured differential cross section, while the GM-VFNS prediction is slightly higher. For higher-p_{T}, the GM-VFNS prediction gives a larger value than the measured differential cross section, while the FONLL prediction is still consistent with measured values. When comparing in bins of $|\eta|$, a good agreement is observed for both prediction, as it is dominated by p_{T}.

For the $D_s^{\pm}$ meson, only the GM-VFNS prediction is available for comparison. A similar behavior is observed; the GM-VFNS prediction gives a larger value than the measured differential cross section for both p_{T} and $|\eta|$, with a trend of larger deviation at higher p_{T}.

To compare with the values measured in Run-I, the difference in fiducial volume, particularly in $|\eta|$ needs to be taken into account. Since the distribution and differential cross section in bins of $|\eta|$ is rather flat and well modelled by MC simulation, the ratio between fiducial volume of $|\eta| < 2.1$ and $|\eta| < 2.5$ is derived from MC simulation. The scaled values are shown in Table 5.12; the ratio of Run-II to Run-I is evaluated to be 1.59 ± 0.38 for $D^{\pm}$ meson and 1.90 ± 0.34 for $D_s^{\pm}$ meson respectively.

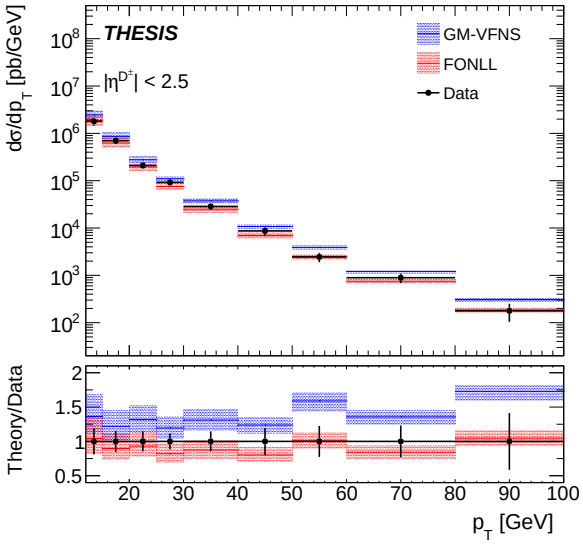

(a) $D^\pm \frac{d\sigma}{dp_T}$

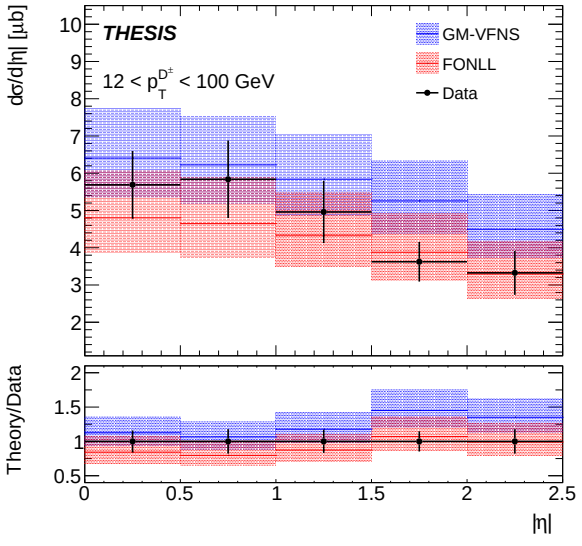

(b) $D^\pm \frac{d\sigma}{d\eta}$

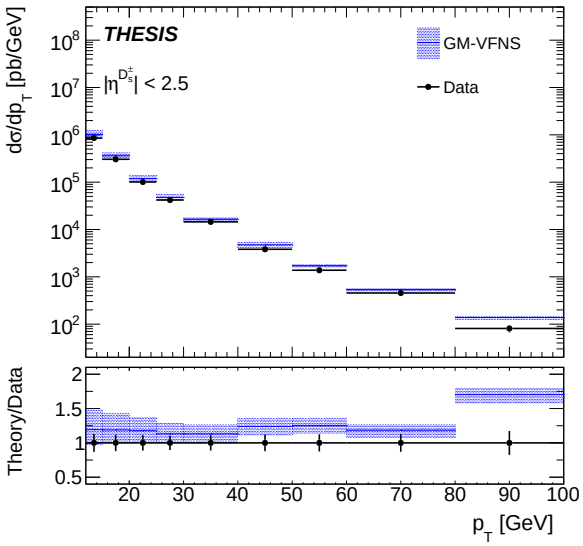

(c) $D_s^\pm \frac{d\sigma}{dp_T}$

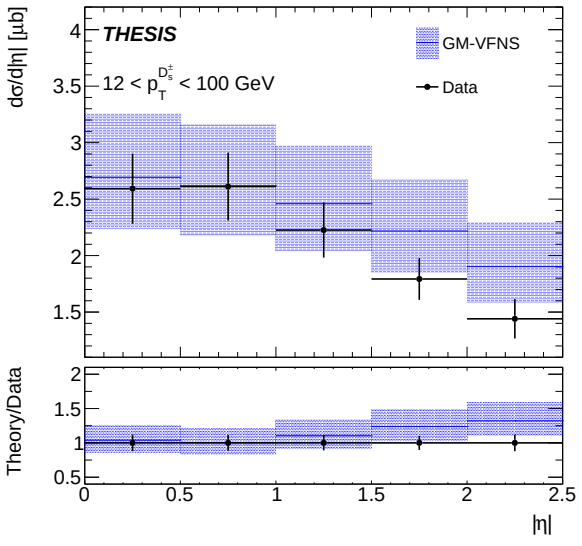

(d) $D_s^\pm \frac{d\sigma}{d\eta}$

Figure 5.26.: Measured differential cross section in bins of p_T (within $|\eta|$<2.5) and $|\eta|$ (within $12 < p_T < 100$ GeV) for $D^\pm$ and $D_s^\pm$. The measured values with the combined error are represented by the data points, while the theory prediction from GM-VFNS and FONLL are shown in blue and red respectively.

	$D_s^\pm$ Inclusive cross section at $\sqrt{s} = 13\,\text{TeV}$ [nb]	
Fiducial volume	ATLAS	GM-VFNS
	$\sigma \pm \delta_{\text{stat}} \pm \delta_{\text{syst}}$	$\sigma \pm \delta_{\text{theory}}$
$p_\text{T} > 12\,\text{GeV}, \lvert\eta\rvert < 2.5$	$4990 \pm 360 \pm 580$	5940^{+1230}_{-990}
$p_\text{T} > 15\,\text{GeV}, \lvert\eta\rvert < 2.5$	$2440 \pm 190 \pm 270$	2880^{+510}_{-440}
$p_\text{T} > 20\,\text{GeV}, \lvert\eta\rvert < 2.5$	$925 \pm 59 \pm 97$	1070^{+150}_{-140}

	$D^\pm$ Inclusive cross section at $\sqrt{s} = 13\,\text{TeV}$ [nb]		
Fiducial volume	ATLAS	GM-VFNS	FONLL
	$\sigma \pm \delta_{\text{stat}} \pm \delta_{\text{syst}}$	$\sigma \pm \delta_{\text{theory}}$	$\sigma \pm \delta_{\text{theory}}$
$p_\text{T} > 12\,\text{GeV}, \lvert\eta\rvert < 2.5$	$10900 \pm 900 \pm 1500$	14100^{+2900}_{-2300}	10500^{+2400}_{-1700}
$p_\text{T} > 15\,\text{GeV}, \lvert\eta\rvert < 2.5$	$5390 \pm 580 \pm 810$	6750^{+1180}_{-1020}	4860^{+930}_{-720}
$p_\text{T} > 20\,\text{GeV}, \lvert\eta\rvert < 2.5$	$1920 \pm 150 \pm 260$	2480^{+350}_{-330}	1720^{+270}_{-220}

Table 5.11.: Inclusive $D^\pm$ and $D_s^\pm$ meson production cross section in different fiducial volumes defined by $|\eta| < 2.5$ and different p_T thresholds.

	$D_s^\pm$ Inclusive cross section [nb]	
	ATLAS $\sqrt{s} = 13\,\text{TeV}$	ATLAS $\sqrt{s} = 7\,\text{TeV}$
Fiducial volume	$\sigma \pm \delta_{\text{stat}} \pm \delta_{\text{syst}}$	$\sigma \pm \delta_{\text{total}}$
$p_\text{T} > 20\,\text{GeV}, \lvert\eta\rvert < 2.1$	$814 \pm 52 \pm 85$	512 ± 104

	$D^\pm$ Inclusive cross section [nb]	
	ATLAS $\sqrt{s} = 13\,\text{TeV}$	ATLAS $\sqrt{s} = 7\,\text{TeV}$
Fiducial volume	$\sigma \pm \delta_{\text{stat}} \pm \delta_{\text{syst}}$	$\sigma \pm \delta_{\text{total}}$
$p_\text{T} > 20\,\text{GeV}, \lvert\eta\rvert < 2.1$	$1690 \pm 130 \pm 230$	888 ± 97

Table 5.12.: Inclusive $D^\pm$ and $D_s^\pm$ production cross section compared to Run-I results.

5.8. Summary and Discussion

Lifetime and invariant mass fit models have been developed and tested in both MC samples and data. The lifetime fits allow the extraction of the non-prompt fraction and show that the data can be well described by combining the prompt and non-prompt MC samples. The invariant mass fits allow the extraction of the signal yield in bins of kinematic variables, i.e. p_T and $|\eta|$.

By extracting the signal yield of $D^{\pm}$ and $D_s^{\pm}$ meson, the differential cross section is measured in bins of p_{T} and $|\eta|$ within the fiducial volume of $|\eta| < 2.5$ and $12 < p_{\mathrm{T}} < 100$ GeV. The measured values are compared with the GM-VFNS and FONLL prediction, showing a good agreement at low-p_{T}. In general, the GM-VFNS prediction gives a larger value than the measured differential cross section, while the FONLL prediction gives a smaller value. When comparing the uncertainties, the measured values have an uncertainty ranging from 10% to 15% at low-p_{T}, while the theory prediction has an uncertainty of 25% to 30%; the measurement shows a clear advantage in precision. The fiducial cross section is also measured and compared with the theory prediction, showing a good agreement within the same level of uncertainty.

This is the first time in the LHC that the $D_s^{\pm}$ meson production is measured differentially up to 100 GeV in transverse momentum p_{T}, providing theory feedback in an unexplored kinematic region. The measured values are mainly limited by the systematic uncertainties, due to triggering, background modelling and muon reconstruction. These uncertainties are studied in a data-driven way, and the combined systematic uncertainty is estimated to be around 10%. In the future operation of the ATLAS experiment, these uncertainties are expected to be reduced with more data and improved calibration.

Chapter 6.

Prospects of Searches for $\tau \to 3\mu$ Decay Using the $D_s^{\pm}$ Meson

Lepton-flavour-violating (LFV) processes are essential to search for new physics beyond the Standard Model. Although LFV processes are extremely rare and therefore limited by the statistics of experiments, the observation of such processes would be a clear sign of new physics.

In run-II, the improvements in luminosity, trigger and energy provide a great chance for searches of different LFV decays. In particular, the large production rate of $D_s^{\pm}$ mesons at the LHC allows for using it as a source of the τ lepton. Currently, the official search for the $D_s^{\pm} \to \tau(3\mu)\nu$ decay within the ATLAS experiment is still ongoing; the search region is still blinded, and therefore no official result will be presented. This chapter describes the preliminary study of the $D_s^{\pm} \to \tau(3\mu)\nu$ decay, the prospects of such study and the synergy with the $D_s^{\pm} \to \phi(\mu\mu)\pi$ decay study.

6.1. Motivation

The LFV $\tau \to 3\mu$ decay has been searched during run-I in the $W \to \tau(3\mu)\nu$ decay. With the high-p_{T} and detached τ event signature, ATLAS achieved a great rejection of the background and set an upper limit of 3.76×10^{-7} on $BR(\tau \to 3\mu)$ at 90% confidence level.

In run-II, more channels are explored to search for the LFV $\tau \to 3\mu$ decay. One particular channel of interest is the $D_s^{\pm} \to \tau(3\mu)\nu$ decay. This particular channel is chosen because of the high production rate of $D_s^{\pm}$ meson and high branching ratio of $D_s^{\pm} \to \tau\nu$ at a value of $BR(D_s^{\pm} \to \tau\nu) = 5.3 \pm 0.1\%$ [121]. However, due to the lower energy of the production processes, it is a more challenging channel with significant difficulty in triggering and background rejection. Moreover, there is a prerequisite to make use of the $D_s^{\pm}$ meson as the source of τ - the production of the $D_s^{\pm}$ meson needs to be well understood.

Assuming one can extract the signal yield of the $D_s^\pm \to \tau(3\mu)\nu$ decay, the branching ratio of $\tau \to 3\mu$ can be calculated using the formula:

$$BR(\tau \to 3\mu) = \frac{N_{D_s^\pm \to \tau(3\mu)\nu}}{N_{D_s^\pm \to \tau\nu}}, \tag{6.1}$$

where $N_{D_s^\pm \to \tau(3\mu)\nu}$ is the number of signal events measured and $N_{D_s^\pm \to \tau\nu}$ is the number of events that a $D_s^\pm$ meson decays into τ lepton. In the formula, the $D_s^\pm \to \tau(3\mu)\nu$ signal yield is normalized by the number of $D_s^\pm$ meson produced, which is measured using the $D_s^\pm \to \phi(\mu\mu)\pi$ decay as presented in Chapter 5. Therefore, the $D_s^\pm \to \phi(\mu\mu)\pi$ channel is called the normalization channel, while the $D_s^\pm \to \tau(3\mu)\nu$ channel is called the signal channel.

The reason for choosing the $D_s^\pm \to \phi(\mu\mu)\pi$ as the normalization channel for the $D_s^\pm$ meson production measurement is that the similarity in final state compared to $D_s^\pm \to \tau(3\mu)\nu$ can provide a good cross-check and potentially minimize the systematic uncertainties. With such purpose in mind, both the $D_s^\pm \to \phi(\mu\mu)\pi$ and the $D_s^\pm \to \tau(3\mu)\nu$ channels are studied with a common MC simulator, software framework and analysis tool.

6.2. Simulation and MC Samples

To study the target channel, the $D_s^\pm \to \tau(3\mu)\nu$ decay has been simulated to generate MC samples for the study. Like the $D_s^\pm \to \phi(\mu\mu)\pi$ decay, the $D_s^\pm \to \tau(3\mu)\nu$ decay is simulated using the Pythia8(A14 tune) and NNPDF23LO pdf set. Likewise, the prompt and non-prompt samples are simulated to account for production from b and c quarks. To efficiently simulate the events, all the τ produced are set to decay into 3μ, i.e. $BR(\tau \to 3\mu) = 1$.

Similar to the $D_s^\pm \to \phi(\mu\mu)\pi$ decay, the search of $D_s^\pm \to \tau(3\mu)\nu$ decay is also limited by the muon trigger thresholds; this is one of the main challenges of the analysis. Although general di-muon triggers can be used to trigger the $D_s^\pm \to \tau(3\mu)\nu$ events, the trigger thresholds and trigger topology greatly reduce the signal efficiency. For instance, the di-muon trigger 2mu6 triggers requires a pair of muons with $p_\mathrm{T} > 6\,\mathrm{GeV}$, while the third muon in the $\tau \to 3\mu$ decay is only reconstructed by the muon spectrometer above 4 GeV; all the muons are also required to be within $|\eta| < 2.5$. This limits the lowest measurable τ lepton p_T to around 16 GeV. Moreover, the trigger topology requirement bPhi also limits that the invariant mass of the pair of muons to be near the ϕ meson mass, which greatly reduce the muons firing the trigger. Therefore, 3-muon triggers are essential to trigger the $\tau \to 3\mu$ events.

In early Run-II, the lowest threshold 3-muon trigger is the 3mu6 trigger, which requires at least 3 muons with $p_\mathrm{T} > 6$ GeV. Over the course of Run-II, lower threshold triggers are developed, and a lower trigger threshold of 3mu4 is developed. With such trigger, the requirement is relaxed to 3-muons with $p_\mathrm{T} > 4$ GeV in 2017 and 2018. For events with higher p_T, the mu11_mu6 trigger is also used, which requires a pair of muons with $p_\mathrm{T} >$ 11 GeV and 6 GeV, respectively.

To efficiently simulate events passing these triggers, a mixed kinematic filter is implemented to produce samples that can be accepted by the available trigger and the detector. The kinematic filter is set to require either 3 muons all with $p_{\mathrm{T}} > 3.5\,\mathrm{GeV}$ or the leading muon with $p_{\mathrm{T}} > 10.5\,\mathrm{GeV}$, the second muon with $p_{\mathrm{T}} > 5.5\,\mathrm{GeV}$ and the third muon with $p_{\mathrm{T}} > 2\,\mathrm{GeV}$.

6.3. Reconstruction and Event Selection

The reconstruction of the $D_s^\pm \to \tau(3\mu)\nu$ decay is similar to the $D_s^\pm \to \phi(\mu\mu)\pi$ decay, with the main difference being the number of muons. Therefore, a common software framework has been developed to perform the reconstruction and selection; this is essential to minimize the difference between the two channels and to cross-check the analysis. For instance, by acquiring the tracks of the three muon candidates, the τ lepton is reconstructed as a displaced secondary vertex, with the same set of variables as the $\mu\mu\pi$ vertex in Chapter 5.

To distinguish the signal from the background, the following variables are used, similar to those in the $D_s^\pm \to \phi(\mu\mu)\pi$ decay analysis, e.g. the 3μ invariant mass, the SV-PV distance and the lifetime. Figure 6.1 shows the normalized distributions of the secondary vertex variables and the 3μ invariant mass of the MC samples against data collected.

6.3.1. Validation Using the $D_s^\pm \to \phi(\mu\mu)\pi$ Decay

Although the $D_s^\pm \to \tau(3\mu)\nu$ decay is not yet observed and thus no direct validation is available, the $D_s^\pm \to \phi(\mu\mu)\pi$ decay is well established and can be used to indirectly validate the simulation and analysis. For variables in use, the corresponding variables are constructed in the $D_s^\pm \to \phi(\mu\mu)\pi$ study as close as possible for validation.

To validate the consistency of the MC generator between the signal and normalization channel, the kinematics of the $D_s^\pm$ meson produced in the signal and normalization samples are compared. Figure 6.2 shows the normalized distributions of the p_{T} and η of the $D_s^\pm$ meson at truth level without any MC filter placed on the decay products; the only selection made is the fiducial volume of $p_{\mathrm{T}}\,(D_s^\pm) > 12$ GeV and $|\eta(D_s^\pm)| < 2.5$. It can be seen that the p_{T} and $|\eta|$ distributions of the $D_s^\pm$ meson in both processes are consistent, while the τ produced has a slightly lower p_{T} compared to the $D_s^\pm$ meson. This is expected because the τ lepton carries most of the energy of the $D_s^\pm$ meson in the $D_s^\pm \to \tau\nu$ decay. It can be concluded that the MC generator is consistent between the signal and normalization channel; the τ produced (in the fiducial volume defined by the kinematics of the $D_s^\pm$ meson) are also within the p_{T} and $|\eta|$ range detectable by the ATLAS detector.

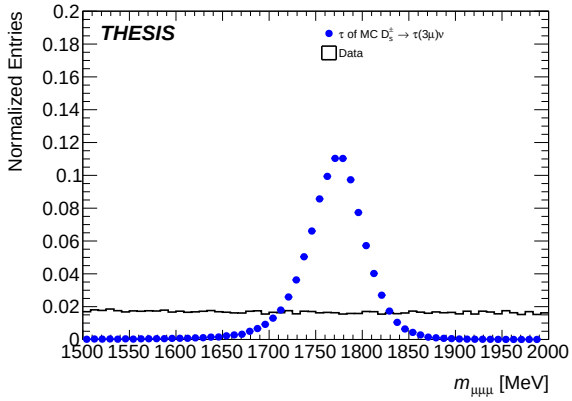

(a) 3μ invariant mass

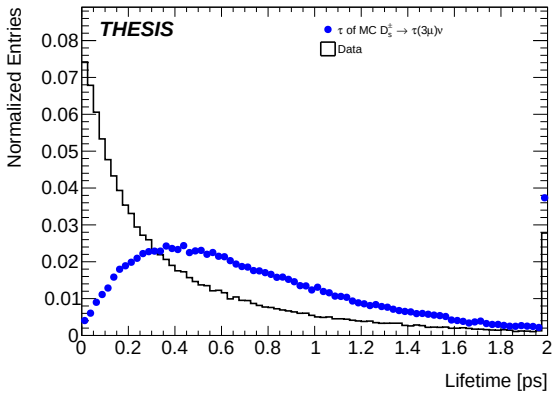

(b) 3μ lifetime

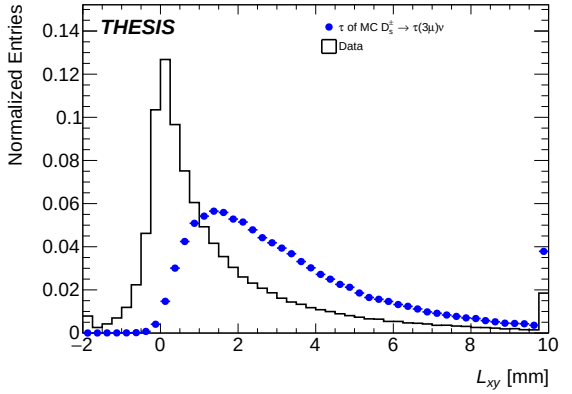

(c) L_{xy}

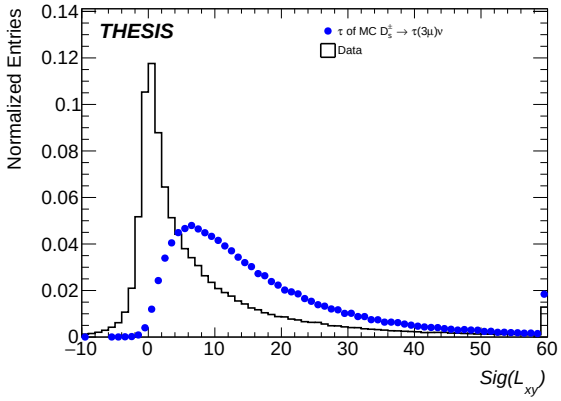

(d) L_{xy} significance

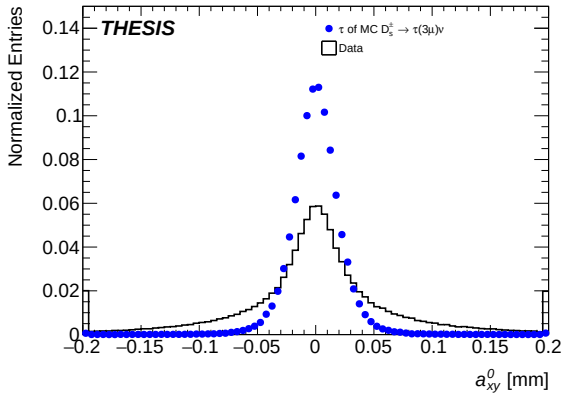

(e) a^0_{xy}

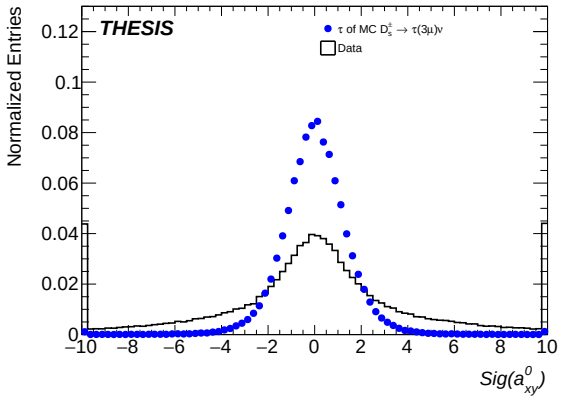

(f) a^0_{xy} significance

Figure 6.1.: Normalized distributions of selected variables for the MC samples and data collected. To illustrate the distinguishing power of each variable, the distributions before applying the selection chain are presented.

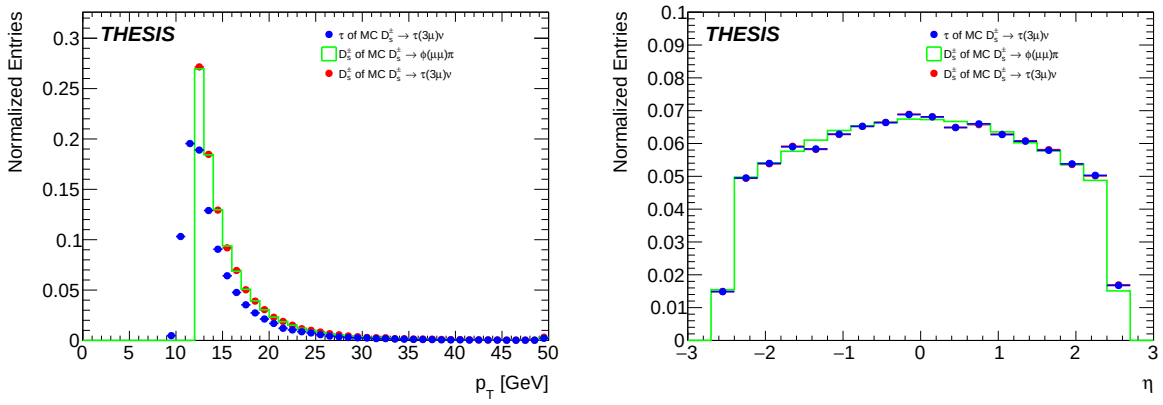

(a) p_T of $D_s^\pm$ **(b)** η of $D_s^\pm$

Figure 6.2.: Normalized distributions of p_T and η of the $D_s^\pm$ meson and τ lepton in the MC samples. The $D_s^\pm$ meson at truth level are required to be within the fiducial volume of $p_\mathrm{T} > 12$ GeV and $|\eta| < 2.5$; no other kinematic filters are applied.

6.4. Expected Yield

To optimize the sensitivity, machine learning algorithms are trained to distinguish MC signal samples against the data post-selection. In run-I and early run-II, boosted decision tree (BDT) algorithms have been developed to distinguish the signal from the background [126, 127]. Such algorithms take the input variables that are independent of the three-muon invariant mass, and provide a machine learning score that increases with signal-to-background ratio. With the machine learning score obtained, the data above a certain score is selected; then, the signal and background yields are extracted by means of a fit applied to the three-muon invariant mass.

In Reference [127], it is demonstrated that a BDT algorithm with 19 input variables, consisting of mostly kinematic variables, vertexing variables and missing momentum variables can significantly improve the signal-to-background ratio. Currently, efforts to improve machine learning models are underway by exploring various approaches, including neural networks and gradient boosted decision trees. These methods, combined with increased statistical data, allow for a better exploitation of the correlations between input variables, thereby enhancing the signal-to-background ratio. Since no result can be quoted at the moment of writing, the benchmark of machine learning algorithm is taken as the BDT algorithm presented in Reference [127].

In case no signal is observed, the obtained background yield is used to calculate the upper limit of the branching ratio of $\tau \to 3\mu$. In general, for a one bin counting experiment with a background, the total yield can be written as:

$$N = \mu S + B, \tag{6.2}$$

where N is the total number of events in the region of interest, μ is the signal strength, S is the signal yield and B is the background yield.

Given a known luminosity and production cross-section, the number of expected $\tau \to 3\mu$ events $N_{D_s^\pm \to \tau(3\mu)\nu}$ can be rewritten as:

$$N_{D_s^\pm \to \tau(3\mu)\nu} = \mathcal{L}\sigma_{D_s^\pm} BR(D_s^\pm \to \tau\nu) BR(\tau \to 3\mu)\epsilon, \tag{6.3}$$

where $\mathcal{L}$ is the integrated luminosity, $\sigma_{D_s^\pm}$ is the production cross-section of $D_s^\pm$ meson, $BR(D_s^\pm \to \tau\nu)$ is the branching ratio of $D_s^\pm \to \tau\nu$, $BR(\tau \to 3\mu)$ is the branching ratio of $\tau \to 3\mu$ and ϵ is the total simulation, acceptance and selection efficiency (hereinafter referred to as total efficiency). Therefore, the signal strength μ and the signal yield S can be interpreted as:

$$\mu = BR(\tau \to 3\mu), \tag{6.4}$$
$$S = \mathcal{L}\sigma_{D_s^\pm} BR(D_s^\pm \to \tau\nu)\epsilon, \tag{6.5}$$

where the signal strength μ is exactly our branching ratio of interest. Therefore, the signal yield S can be calculated from the measured $D_s^\pm$ meson production cross-section, the luminosity recorded by ATLAS, the known branching ratio of $D_s^\pm \to \tau\nu$ and the total efficiency is taken from MC simulation. In this case, the signal strength of one means that all the τ decays into 3μ, while the signal strength of zero means that no τ decays into 3μ. Assuming the absence of a signal, the background yield B is taken as the number of data events observed in the signal region.

6.4.1. Signal Efficiency

Because of the updated fiducial volume, the total acceptance and selection efficiency needs to be updated compared to previous studies. With the p_T range changed from $p_\mathrm{T} > 10$ GeV to $p_\mathrm{T} > 12$ GeV, the value of the cross section decreases while the total efficiency increases, due to the removal of events at lower p_T that are harder to trigger on.

For the MC filter efficiency, this is studied the same way as in the $D_s^\pm \to \phi(\mu\mu)\pi$ measurement. By first generating a large sample without the filters, and applying the MC filters on individual muons, the efficiency of the MC filter is estimated to be 10.9% for $D_s^\pm$ meson within the fiducial volume of $p_\mathrm{T} > 12$ GeV and $|\eta| < 2.5$.

For the selection efficiency, this is studied with the updated selection and detector calibration. Without the machine learning score selection, the selection efficiency is evaluated to 15.2%. Because of the complexity of distinguishing the signal from combinatorial background, the machine learning selection is currently being improved, and no result can be quoted at the moment of writing. For the sensitivity estimate presented, the machine learning selection efficiency is taken as 31% as presented in Ref [127].

6.5. Systematics Update

To evaluate the upper limit precisely, the systematic uncertainties need to be evaluated and accounted for. While the ATLAS collaboration currently optimizes the full run-II study, early studies have made certain assumptions about systematic uncertainties. In particular, given that the $D_s^\pm$ meson production cross-section is known, the fiducial volume and the cross section values need to be updated accordingly. This section reviews the previous studies presented in Ref [128] and Ref [127], updates the systematic uncertainties as currently known and estimates the sensitivity of the search for the $\tau \to 3\mu$ decay in the $D_s^\pm$ channel. The updated estimated systematic uncertainties of the signal and background yield extraction are summarized in Table 6.1.

Signal Yield Uncertainties	
Cross section	12.7%
Trigger	7.2%
Muon	6.5%
Background Yield Uncertainties	
Fit	6.3%
Model	6.2%
Negligible Uncertainties	
Luminosity	-
Tracking	-
Non-prompt fraction	-

Table 6.1.: Estimated systematic uncertainties. The background yield uncertainties are based on previous study of Reference [127]. The cross section, trigger and muon uncertainties are estimated from that of the $D_s^\pm$ normalization channel.

From Equation (6.5), it can be seen that the signal yield can be affected by two sources of systematic uncertainties: the production cross section of the $D_s^\pm$ meson and the total efficiency. As presented in Ref [128], the main source of signal systematic uncertainties are exactly these two sources. Because of the lack of direct measurement at the time, the prospect study made use of the FONLL B and D meson production cross-sections in the fiducial volume defined by $p_\mathrm{T} > 10$ GeV and $|\eta| < 2.5$. Consequently, a large cross section uncertainty between 17% to 23% was obtained; this systematic uncertainty thus dominates over the other sources. Given the current measurement of the $D_s^\pm$ meson production cross-section, the systematic uncertainty of the production cross-section is much reduced to 12%. Moreover, the fiducial volume of $p_\mathrm{T} > 10$ GeV and $|\eta| < 2.5$ is known to be impractical given the trigger limitation; it is updated to $p_\mathrm{T} > 12$ GeV and $|\eta| < 2.5$.

The uncertainty introduced by selection efficiency is not discussed in Ref [128], but it is expected to be primarily due to triggering and muon selection; such uncertainty is estimated to be 15% according to Ref [127]. Because the signal process shares a similar kinematics with the $D_s^\pm \to \phi(\mu\mu)\pi$ decay, some of the systematic uncertainties can be estimated using this decay. Although the trigger uncertainty of the 3_mu4 trigger remains unresolved due to the complexity of 3-muon correlation, the uncertainty for the mu11_mu6 trigger is available. Considering that approximately one-third of the signal events are triggered by the mu11_mu6 trigger, which has a significantly lower uncertainty, the trigger uncertainty is assumed to be two-third of the estimated 3-muon trigger uncertainty (11%), resulting in 7.2%. As for the muon systematic uncertainties, the systematics of selecting three muons is estimated to be the maximum value across the p_T bins in $D_s^\pm \to \phi(\mu\mu)\pi$ decay, which is 6%. Other uncertainties, including the tracking, vertexing and luminosity uncertainties are shown to be negligible in both the $D_s^\pm \to \phi(\mu\mu)\pi$ decay study and the early $D_s^\pm \to \tau(3\mu)\nu$ study.

On the other hand, the background yield is affected by the systematics related to the fitting procedure and model choice when extracting the yield from data. While Ref [128] initially assumed a 15% background uncertainty for various scenarios, this estimate has since been significantly improved with higher statistics. With the updated fitting model and increased statistics, Ref [127] has shown that the fitting uncertainty and modelling uncertainty can both be evaluated to 6.3% and 6.2%, respectively, for 120 events observed in the signal region.

6.6. Sensitivity Estimate

With the updated signal efficiency and updated systematic uncertainties, the sensitivity of the search for the $\tau \to 3\mu$ decay in the $D_s^\pm$ channel can be estimated. Given the ongoing development and interest in knowing the improvements introduced by more precise $D_s^\pm$ production measurement, the prospects of three scenarios for both run-II and high-luminosity LHC (HL-LHC) are presented.

For run-II, the measured luminosity of 140 fb^{-1} is used, and the $D_s^\pm$ meson production cross-section is taken from the measurement in Chapter 5. The background yield is taken from the early study, which is 120 events. For HL-LHC, the estimated luminosity of 3000 fb^{-1} is used, and the anticipated center-of-mass energy of 14 TeV is used. Given this energy increase, the $D_s^\pm$ meson production cross-section and the number of background events are also scaled up linearly assuming linear scale with the luminosity; while this may not be the case, the scaling is used as a first approximation.

Since the cross section is measured using the $D_s^\pm \to \phi(\mu\mu)\pi$ decay, and the $D_s^\pm \to \tau(3\mu)\nu$ decay is searched in the same $D_s^\pm$ meson phase space, the systematic uncertainty of the cross section is correlated with the selection uncertainties. For instance, the tracking, luminosity, trigger and muon uncertainties are all experimental uncertainties that come from the same sources for both decay channels. Therefore, a significant positive correlation is expected between the signal yield uncertainties and the cross section uncertainties.

For the sensitivity estimation presented, the systematic uncertainties are assumed to be uncorrelated for simplicity according to Table 6.1; this is a conservative assumption, and the sensitivity can be improved once the correlation is taken into account.

For both the run-II and the HL-LHC, additional scenarios are considered for comparison. To study the effect of uncertainties on the cross section, the scenario where the uncertainty on the $D_s^\pm$ meson production cross-section is taken as 20% is added to compare with run-II; this represents the typical uncertainty given by GM-VFNS and FONLL calculation. In addition to the uncertainty improvement, the analysis can also be improved by more advanced machine learning algorithms, which can impact physics object reconstruction and background rejection. To account for the potential improvements of the machine learning based selection, the scenario where the background yield is reduced by five times is also added for comparison.

In each scenario, the expected signal is determined using Equation (6.5). In each case, the expected limit on the branching ratio of $\tau \to 3\mu$ is calculated using the profile likelihood method, where the asimov data yield is taken as the expected background yield to assume that no signal is observed. By using the *pyhf* package [129, 130], the expected limit is obtained by hypothesis test with the signal strength μ, which is the branching ratio of interest in this case. The results of the sensitivity estimate are summarized in Table 6.2 and Table 6.3. The CL_s (also known as the modified p-value) against the BR for the run-II and HL-LHC scenarios are shown in Figure 6.3 and Figure 6.4, respectively. The curve of the expected limit is shown in black and the 1σ and 2σ bands are shown in green and yellow, respectively. The upper limit is the value of BR where the CL_s curve crosses the red line, which is the 90% confidence level line (or equivalently p-value = 0.1 line).

By comparing the scenarios that incorporate theory error, it can be observed that the improvement of the $D_s^\pm$ meson production cross-section measurement can enhance the expected limit by 5%. While comparing with the ML enhanced scenario, the expected limit is much improved due to a much lower background yield. In particular, the Run-II (Enhanced ML) scenario even performs significantly better than the HL-LHC scenario. Of course, improvements in ML algorithms are not guaranteed; however, such scenarios illustrate the potential improvement of the search for the $\tau \to 3\mu$ decay. Moreover, given the larger amount of background yield potentially in the HL-LHC, machine learning algorithms can be tuned to reject background more aggressively, even at the cost of lower signal efficiency. Additionally, the machine learning selection in use is based on a "limit scan" on the machine learning score in the early run-II study, which is also expected to improve given larger amount of data. Therefore, the HL-LHC scenario only serves as a baseline scenario, which will definitely be improved greatly. Note that other than the $D_s^\pm$ meson, the B mesons can also contribute to the signal and background; although a preliminary study has been shown in Ref [127], it is not included in the estimation above.

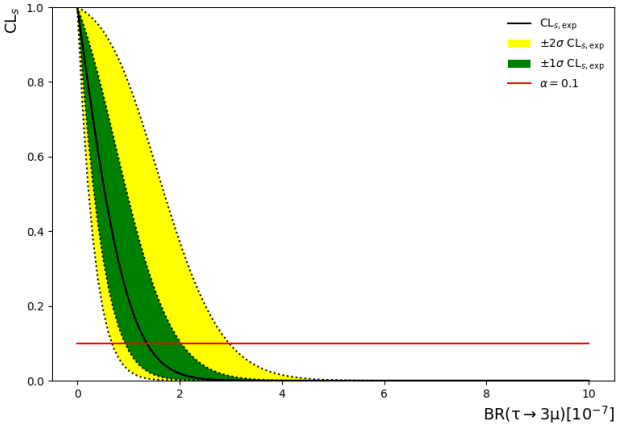

(a) Run-II (Updated error)

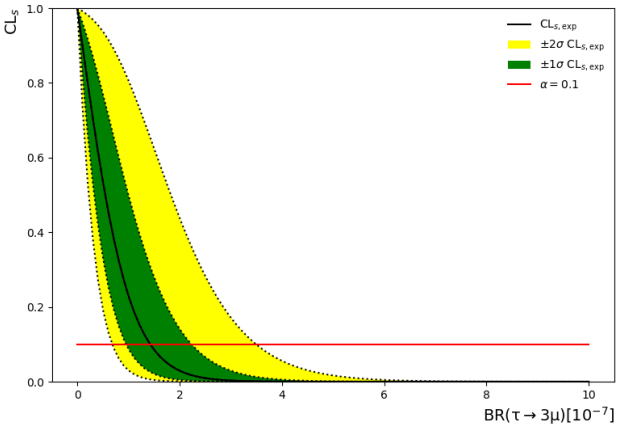

(b) Run-II (Old theory error)

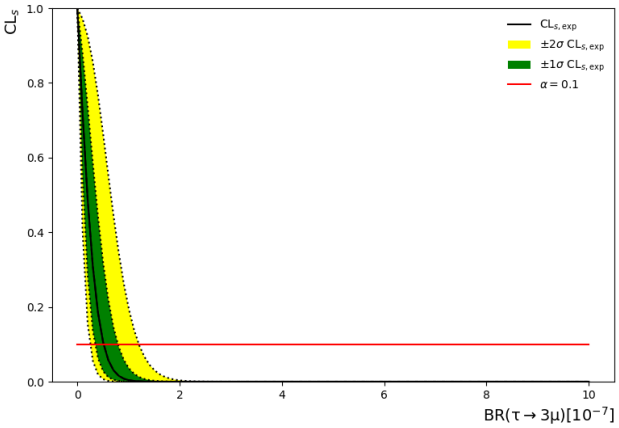

(c) Run-II (Improved ML)

Figure 6.3.: Expected limits on the branching ratio of $\tau \to 3\mu$ for different scenarios using Run-II data.

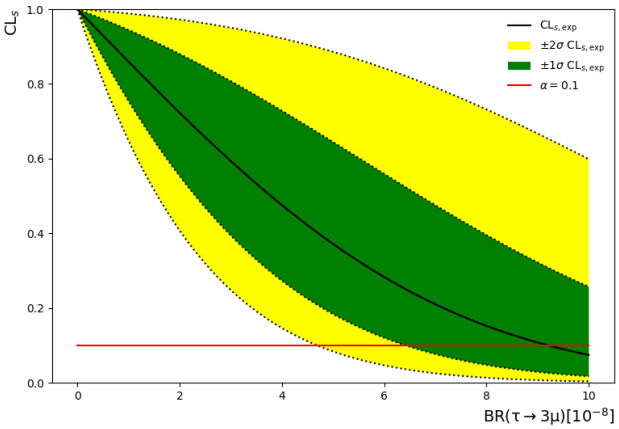

(a) HL-LHC (Updated error)

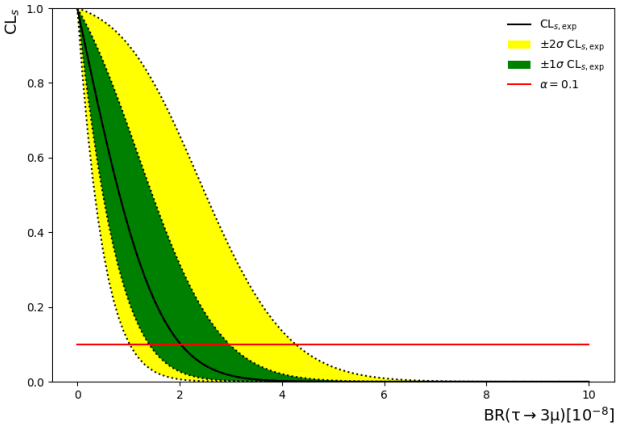

(b) HL-LHC (Improved ML)

Figure 6.4.: Expected limit on the branching ratio of $\tau \to 3\mu$ for different scenarios using HL-LHC luminosity projection.

	Run-II		
	Updated error	Old theory error	Improved ML
Luminosity [fb^{-1}]	140	140	140
Center-of-mass energy [TeV]	13	13	13
$D_s^{\pm}$ cross section [10^9 fb]	4.99 (12%)	4.99 (20%)	4.99 (12%)
Total efficiency	0.52%	0.52%	0.52%
Background yield	120	120	24
Expected limit on BR($\tau \to 3\mu$)	1.36×10^{-7}	1.43×10^{-7}	5.16×10^{-8}

Table 6.2.: Expected limits on BR($\tau \to 3\mu$) in run-II for different scenarios based on early run-II study in $D_s^{\pm}$ channel only.

	HL-LHC	
	Updated error	Improved ML
Luminosity [fb^{-1}]	3000	3000
Center-of-mass energy [TeV]	14	14
$D_s^{\pm}$ cross section [10^9 fb]	5.37 (12%)	5.37 (12%)
Total efficiency	0.51%	0.51%
Background yield	2769	554
Expected limit on BR($\tau \to 3\mu$)	9.19×10^{-8}	2.02×10^{-8}

Table 6.3.: Expected limits on BR($\tau \to 3\mu$) projected to HL-LHC based on early run-II study in $D_s^{\pm}$ channel only.

Chapter 7.

Conclusion and Discussion

In this thesis, the measurements of $D^{\pm}$ and $D_s^{\pm}$ meson production cross-sections with the ATLAS detector is presented as the main finding, which provides a direct test of QCD calculation schemes. Compared to the run-I analysis performed by ATLAS, the run-II analysis takes advantage of a higher center-of-mass energy of 13 TeV and increased luminosity to study the rarer processes of $D^{\pm}/D_s^{\pm} \to \phi(\mu\mu)\pi$. Moreover, the production of the $D_s^{\pm}$ meson is of particular interest for the search of the lepton-flavour-violating $\tau \to 3\mu$ decay; the prospect of which is also outlined in this thesis.

Because of the relatively light mass of the D mesons compared to LHC energy scale, the D meson signal suffer from large background contamination and a limited trigger efficiency. Thanks to the improvements in triggering, tracking and muon reconstruction algorithms, D mesons can be efficiently reconstructed and measured down to $p_{\mathrm{T}} = 12\,\mathrm{GeV}$. The reconstruction of the D mesons is based on requiring two muon tracks and one pion track to form a secondary vertex with a displaced decay length. By making use of the vertex variables and requiring the invariant mass of the di-muon system to be near the ϕ mass, the background can be much suppressed.

To extract the signal yield, the invariant mass distribution of the D meson candidates is fitted with a combined model that describes the signal and the background. It has been shown that the invariant mass fit model is able to describe the data well, and capable of extracting the signal yield in the data collected by the ATLAS detector, particularly in bins of different variables of the D meson candidates for further analysis. Therefore, the signal models have been carefully validated and the stability of the fit model has been demonstrated. For instance, the background-free p_{T}, $|\eta|$ and lifetime distribution of the D meson signal in the data is extracted by fitting the invariant mass distribution bin-by-bin in those variables. The resultant signal distribution enables the measurement of the non-prompt fraction and the differential cross sections of the D mesons.

The presented differential cross sections of the D meson production are compared to the state-of-the-art QCD calculations, such as the GM-VFNS and FONLL calculations. The results show consistency with both calculation schemes; the difference between the measured values and the calculations are within the uncertainties. This is the first time in the LHC that the $D_s^{\pm}$ meson production is measured differentially up to 100 GeV in transverse momentum p_{T}, providing theory feedback in an unexplored kinematic region.

When comparing the percentage error, the measured values presented are found to range from 10% to 20% in low p_{T} to intermediate p_{T} range, primarily due to the systematic uncertainties. Such level of error is significantly lower than the percentage error of the QCD calculations, which are found to be around 20% to 30%, due to the uncertainties related to the mass scales. The fiducial cross section is also measured within the region of $|\eta| < 2.5$ and different p_{T} thresholds of $p_{\mathrm{T}} > 12\,\mathrm{GeV}$, $p_{\mathrm{T}} > 15\,\mathrm{GeV}$ and $p_{\mathrm{T}} > 20\,\mathrm{GeV}$, which shows the same level of agreement with the QCD calculations. The values and comparison presented will be useful for the improvement of the QCD calculations and the understanding of the charm quark production.

Although the presented results are mostly limited by the systematic uncertainties, several improvements can be made to the analysis to reduce the uncertainties with upcoming run-III of the LHC. For instance, the detector systematics, trigger systematics and background systematics can be improved by the increased statistics, as these uncertainties are evaluated in a data driven manner. In particular, the $D^{\pm}$ meson values are limited by the background systematics, which can be improved if the background can be better understood; a higher statistics can also allow placing tighter cuts to lower the background level.

Another potential improvement is the optimization of the trigger. In this analysis, most of the statistics are provided by the bPhi triggers, which place a window on the invariant mass of the di-muon system. For the $D_s^{\pm} \to \phi(\mu\mu)\pi$ decay specifically, the resolution of the invariant mass is found to be much smaller than the window at trigger level. This implies that the bPhi and the corresponding L1 item can be optimized to have a narrower window specifically to accept $\phi(\mu\mu)$ events, potentially down to muons with $p_{\mathrm{T}} > 4\,\mathrm{GeV}$.

Based on the measured fiducial cross section of the $D_s^{\pm}$ meson, the related searches for the lepton-flavour-violating $D_s^{\pm} \to \tau(3\mu)\nu$ decay is also outlined. In previous studies, the fiducial cross section is a major systematic uncertainty in the measurement of the branching ratio of $\tau \to 3\mu$. The improved fiducial cross section provides a normalization of a much lower uncertainty. Since the previous prospect took the FONLL calculation as the reference, the improved fiducial cross section will improve such systematic uncertainty from 20% to 12%, directly improving the sensitivity of the search for the $\tau \to 3\mu$ decay. By updating the systematics and evaluating the expected upper limit based on early run-II study, the expected sensitivity of HL-LHC is also estimated. Although the sensitivity is not expected to reach the level of the current best limit, the result highlights the need of a more powerful and aggressively tuned machine learning algorithm to separate the signal from the background.

To conclude, the presented measurement of the $D^{\pm}$ and $D_s^{\pm}$ meson production cross-sections is a definite improvement over the previous run-I analysis. The results provide theory feedback and a direct improvement of lepton-flavour-violating τ decay searches. In the coming years, the LHC will continue to provide more data, which will allow improved results for lepton-flavour-violating processes.

Appendix A.

Signal Extraction in Bins of Lifetime

The invariant mass fits of the full dataset per bins in lifetime and p_{T} are shown in this appendix.

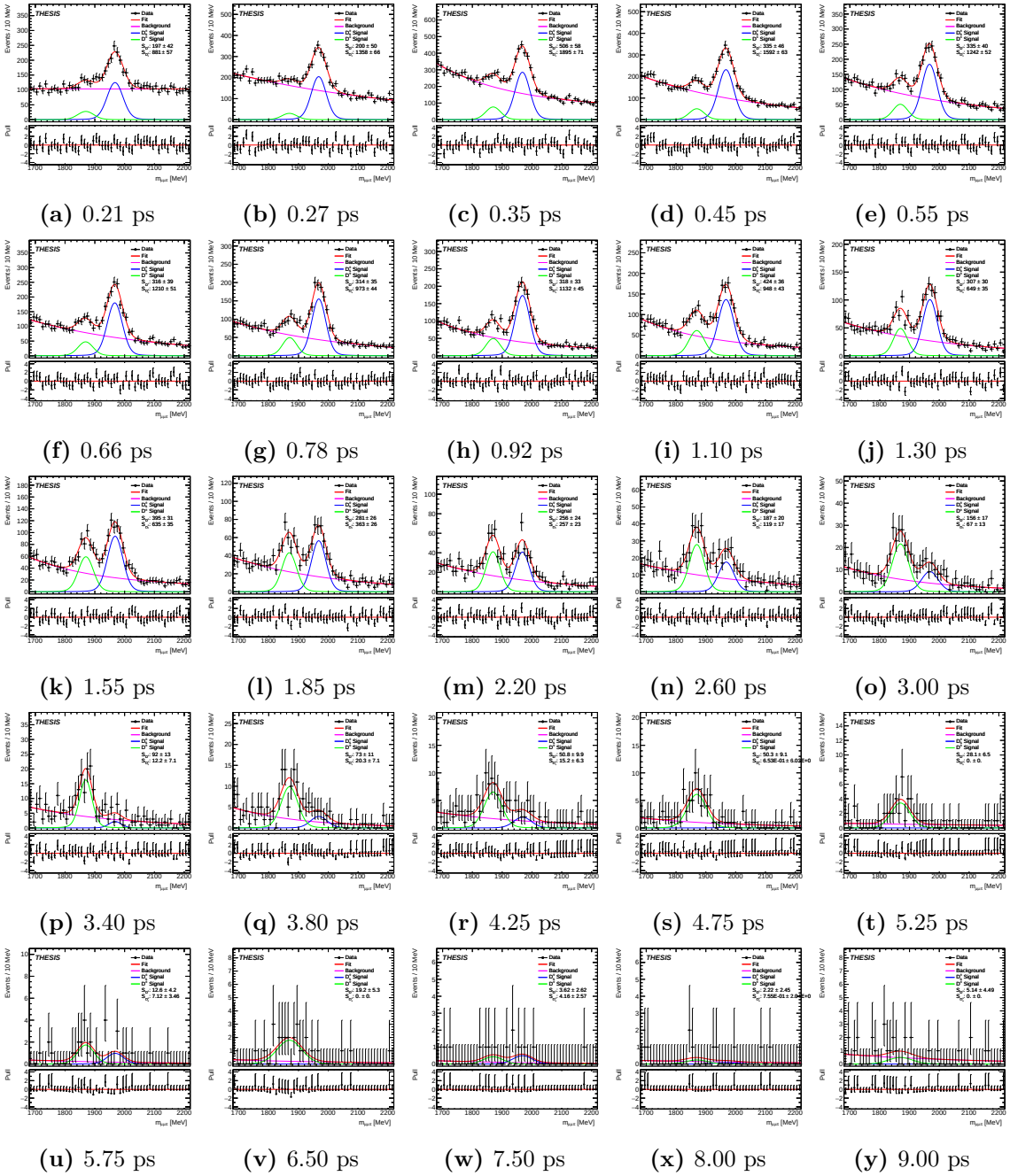

(a) 0.21 ps **(b)** 0.27 ps **(c)** 0.35 ps **(d)** 0.45 ps **(e)** 0.55 ps

(f) 0.66 ps **(g)** 0.78 ps **(h)** 0.92 ps **(i)** 1.10 ps **(j)** 1.30 ps

(k) 1.55 ps **(l)** 1.85 ps **(m)** 2.20 ps **(n)** 2.60 ps **(o)** 3.00 ps

(p) 3.40 ps **(q)** 3.80 ps **(r)** 4.25 ps **(s)** 4.75 ps **(t)** 5.25 ps

(u) 5.75 ps **(v)** 6.50 ps **(w)** 7.50 ps **(x)** 8.00 ps **(y)** 9.00 ps

Figure A.1.: Fit model for invariant mass applied to the dataset in the p_{T} bin of 12 GeV to 20 GeV and different bins of lifetime.

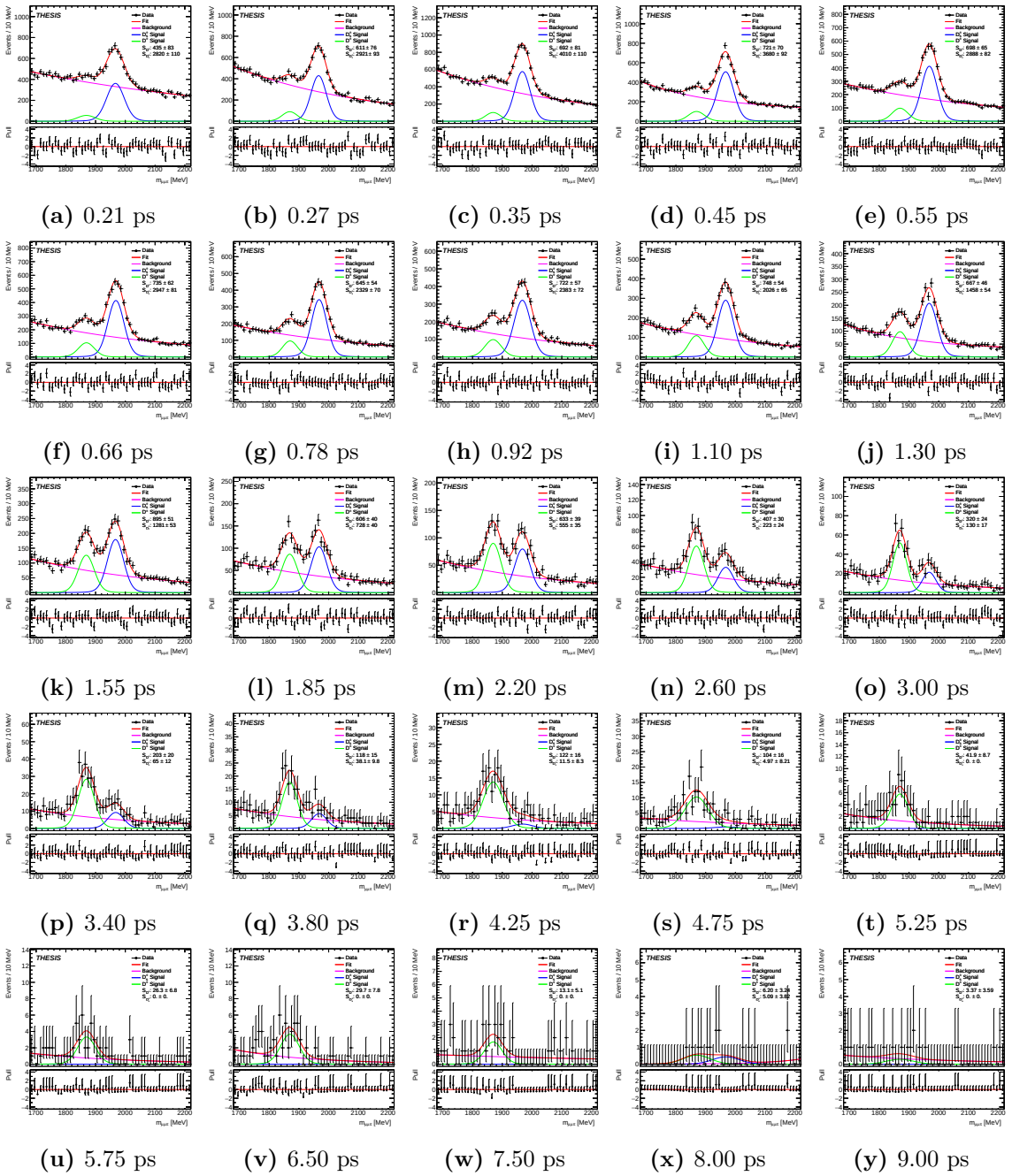

(a) 0.21 ps **(b)** 0.27 ps **(c)** 0.35 ps **(d)** 0.45 ps **(e)** 0.55 ps

(f) 0.66 ps **(g)** 0.78 ps **(h)** 0.92 ps **(i)** 1.10 ps **(j)** 1.30 ps

(k) 1.55 ps **(l)** 1.85 ps **(m)** 2.20 ps **(n)** 2.60 ps **(o)** 3.00 ps

(p) 3.40 ps **(q)** 3.80 ps **(r)** 4.25 ps **(s)** 4.75 ps **(t)** 5.25 ps

(u) 5.75 ps **(v)** 6.50 ps **(w)** 7.50 ps **(x)** 8.00 ps **(y)** 9.00 ps

Figure A.2.: Fit model for invariant mass applied to the dataset in the p_{T} bin of 20 GeV to 30 GeV and different bins of lifetime.

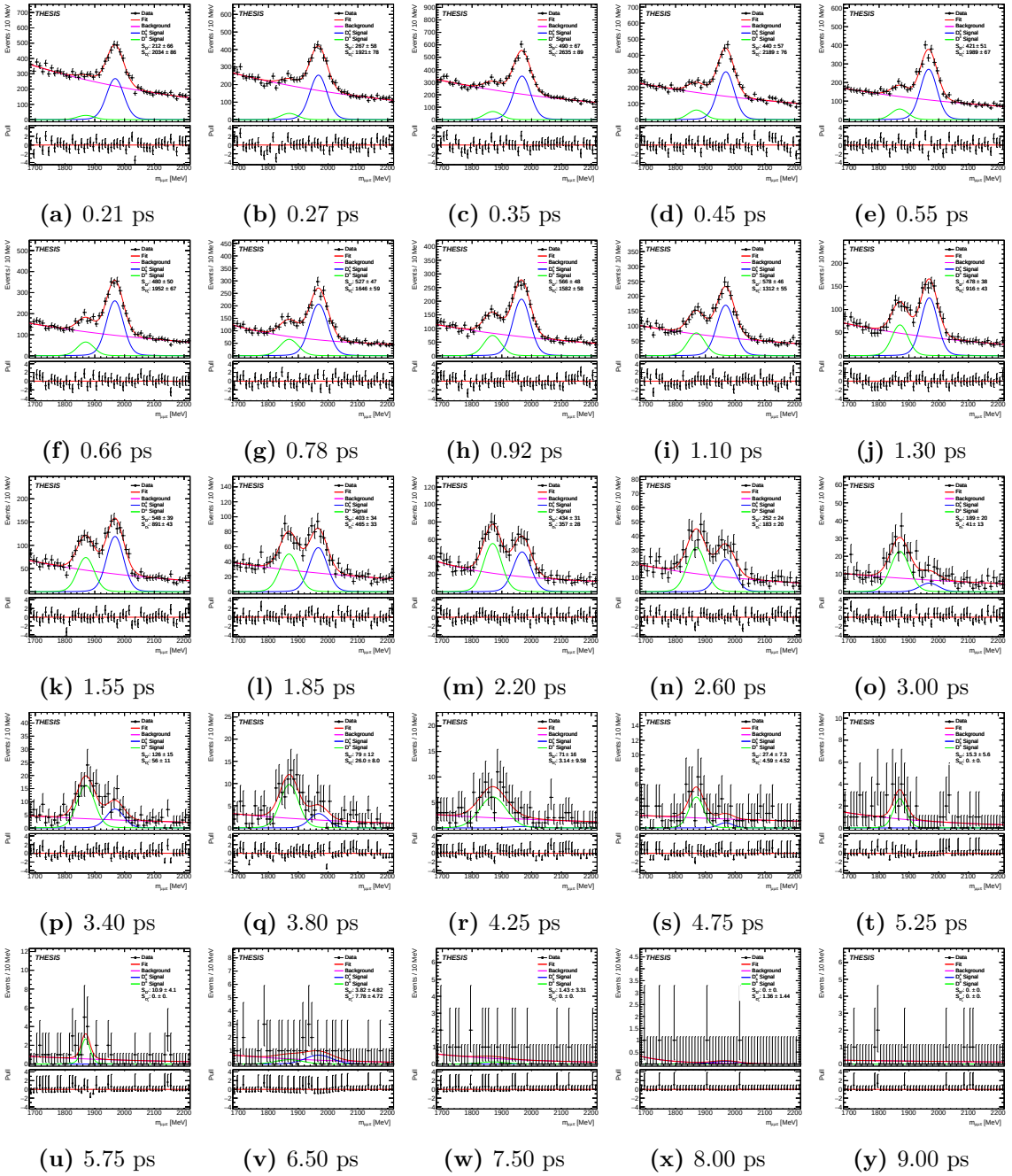

(a) 0.21 ps **(b)** 0.27 ps **(c)** 0.35 ps **(d)** 0.45 ps **(e)** 0.55 ps

(f) 0.66 ps **(g)** 0.78 ps **(h)** 0.92 ps **(i)** 1.10 ps **(j)** 1.30 ps

(k) 1.55 ps **(l)** 1.85 ps **(m)** 2.20 ps **(n)** 2.60 ps **(o)** 3.00 ps

(p) 3.40 ps **(q)** 3.80 ps **(r)** 4.25 ps **(s)** 4.75 ps **(t)** 5.25 ps

(u) 5.75 ps **(v)** 6.50 ps **(w)** 7.50 ps **(x)** 8.00 ps **(y)** 9.00 ps

Figure A.3.: Fit model for invariant mass applied to the dataset in the p_{T} bin of 30 GeV to 100 GeV and different bins of lifetime.

Appendix B.

MC Toy Study of Alternative Fit Models

The invariant mass of different models fitted to the full dataset in bins of p_{T} and $|\eta|$ are shown in this appendix.

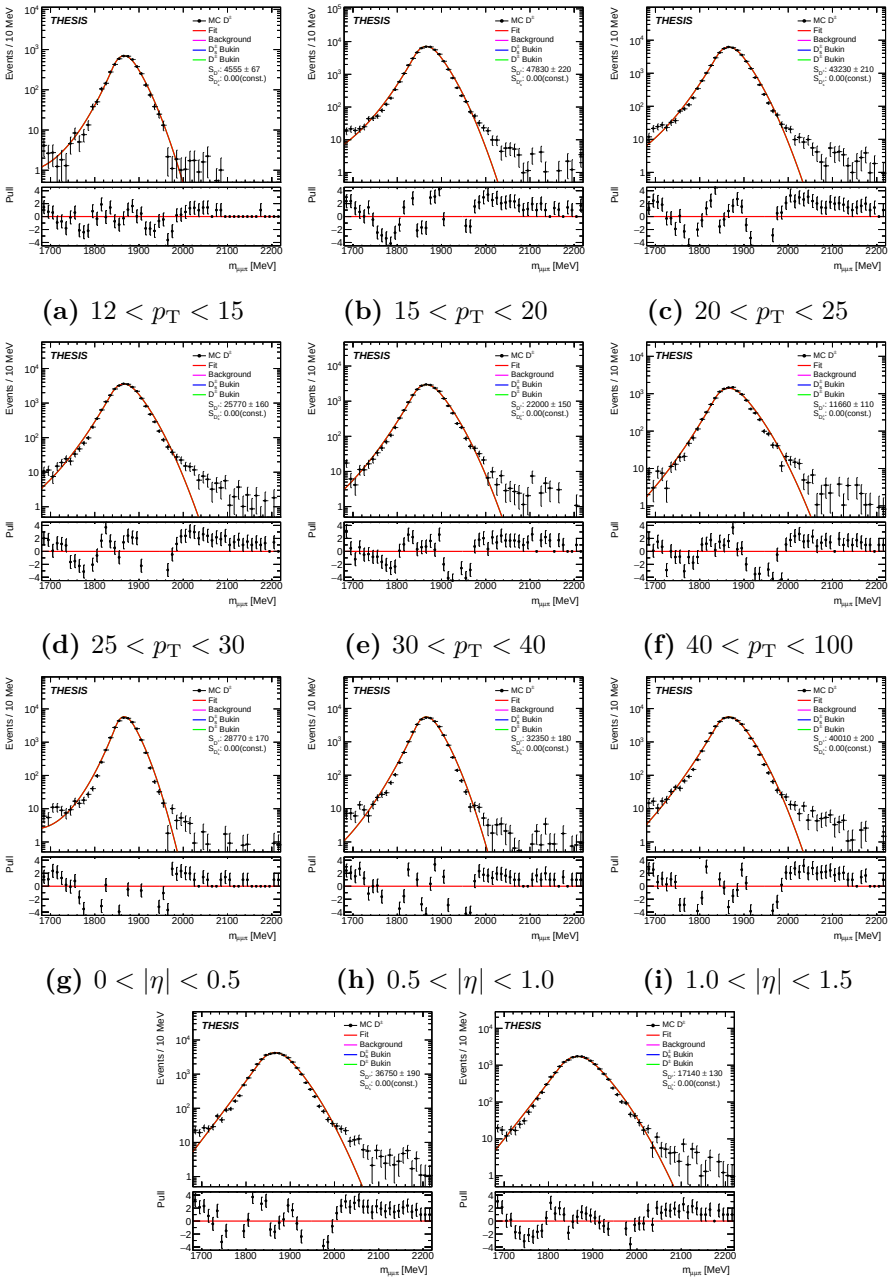

(a) $12 < p_{\mathrm{T}} < 15$ **(b)** $15 < p_{\mathrm{T}} < 20$ **(c)** $20 < p_{\mathrm{T}} < 25$

(d) $25 < p_{\mathrm{T}} < 30$ **(e)** $30 < p_{\mathrm{T}} < 40$ **(f)** $40 < p_{\mathrm{T}} < 100$

(g) $0 < |\eta| < 0.5$ **(h)** $0.5 < |\eta| < 1.0$ **(i)** $1.0 < |\eta| < 1.5$

(j) $1.5 < |\eta| < 2.0$ **(k)** $2.0 < |\eta| < 2.5$

Figure B.1.: Bukin model fitted to the invariant mass of $D^{\pm}$ MC samples in bins of different p_{T} (in GeV) and $|\eta|$.

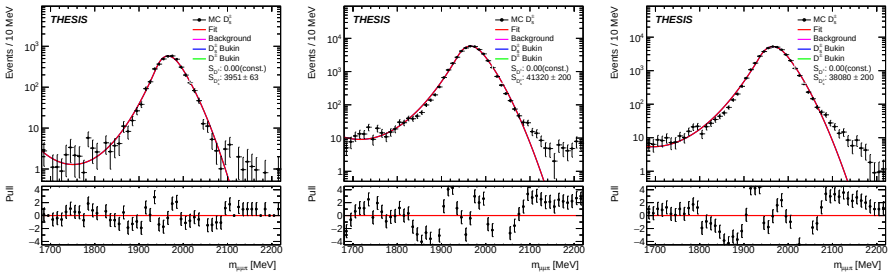

(a) $12 < p_{\mathrm{T}} < 15$

(b) $15 < p_{\mathrm{T}} < 20$

(c) $20 < p_{\mathrm{T}} < 25$

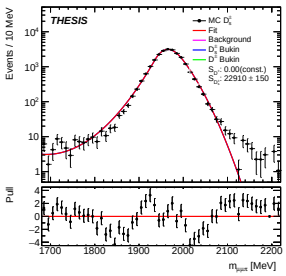

(d) $25 < p_{\mathrm{T}} < 30$

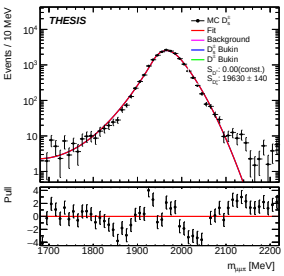

(e) $30 < p_{\mathrm{T}} < 40$

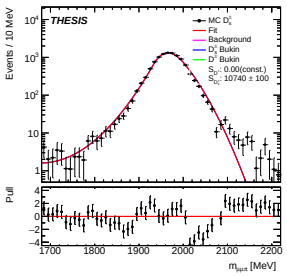

(f) $40 < p_{\mathrm{T}} < 100$

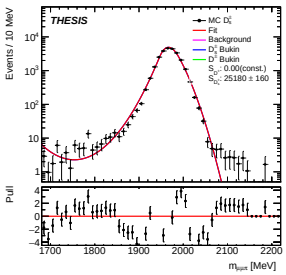

(g) $0 < |\eta| < 0.5$

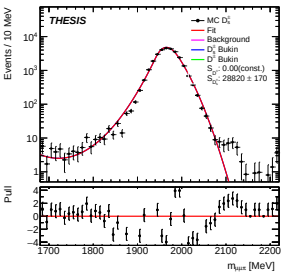

(h) $0.5 < |\eta| < 1.0$

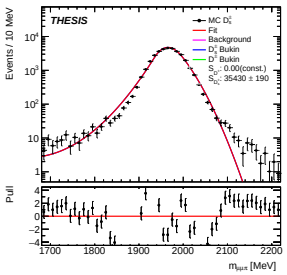

(i) $1.0 < |\eta| < 1.5$

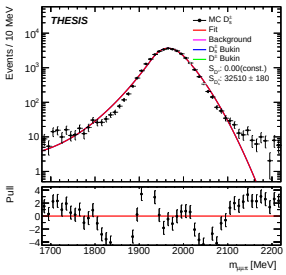

(j) $1.5 < |\eta| < 2.0$

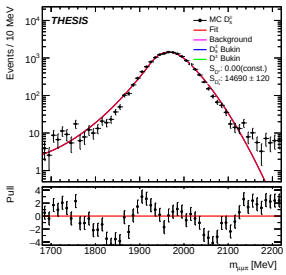

(k) $2.0 < |\eta| < 2.5$

Figure B.2.: Bukin model fitted to the invariant mass of $D_s^{\pm}$ MC samples in bins of different p_{T} (in GeV) and $|\eta|$.

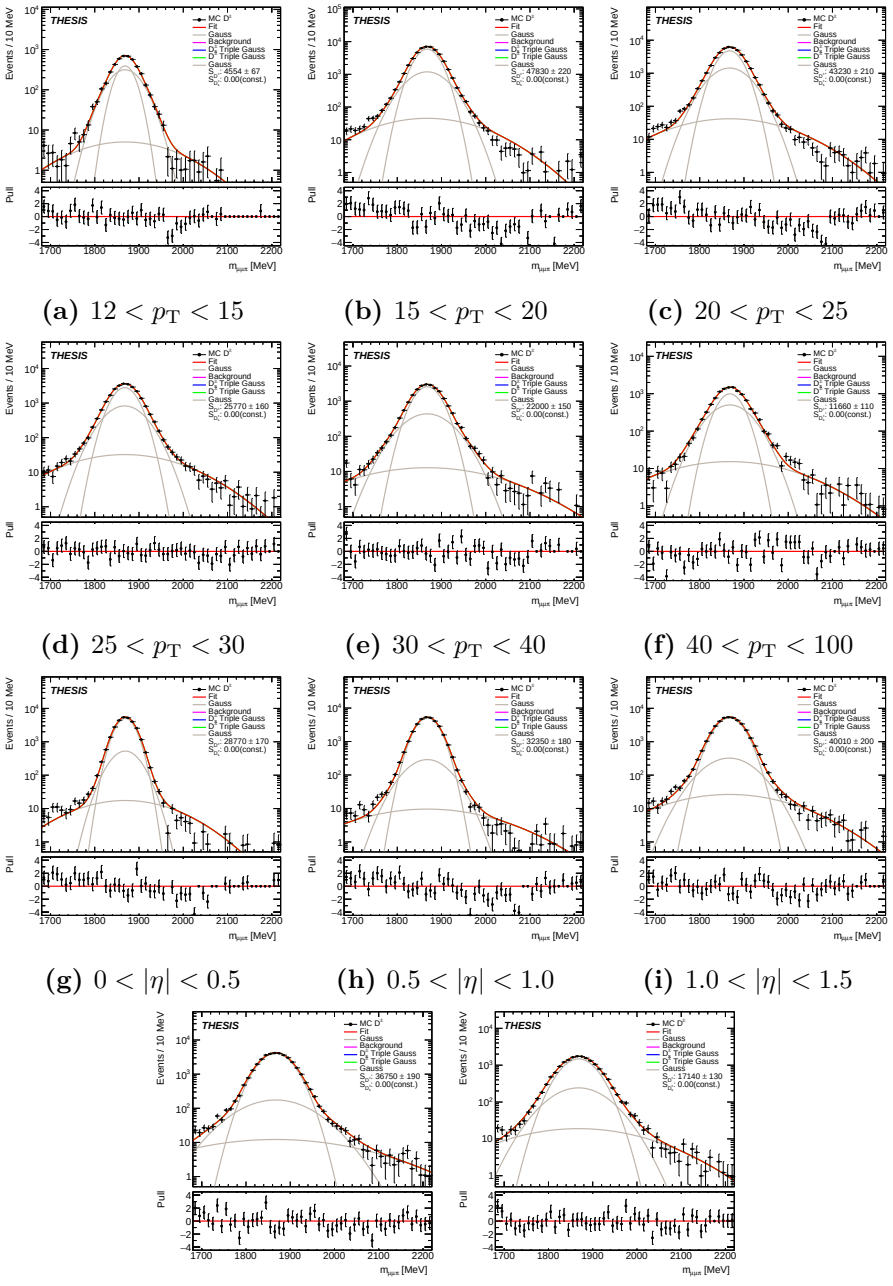

(a) $12 < p_{\mathrm{T}} < 15$ **(b)** $15 < p_{\mathrm{T}} < 20$ **(c)** $20 < p_{\mathrm{T}} < 25$

(d) $25 < p_{\mathrm{T}} < 30$ **(e)** $30 < p_{\mathrm{T}} < 40$ **(f)** $40 < p_{\mathrm{T}} < 100$

(g) $0 < |\eta| < 0.5$ **(h)** $0.5 < |\eta| < 1.0$ **(i)** $1.0 < |\eta| < 1.5$

(j) $1.5 < |\eta| < 2.0$ **(k)** $2.0 < |\eta| < 2.5$

Figure B.3.: Triple Gaussian model fitted to the invariant mass of $D^{\pm}$ MC samples in bins of different p_{T} (in GeV) and $|\eta|$.

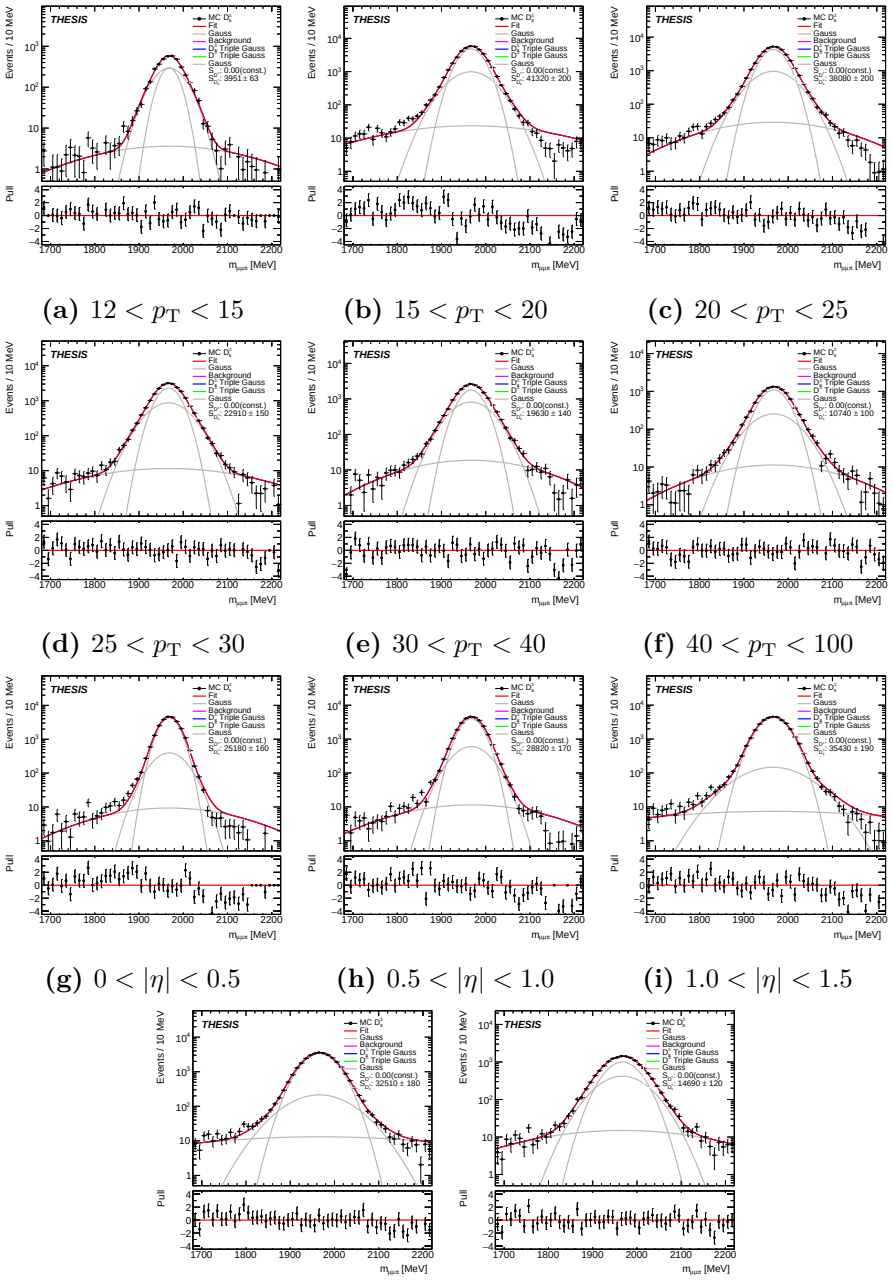

(a) $12 < p_{\mathrm{T}} < 15$ **(b)** $15 < p_{\mathrm{T}} < 20$ **(c)** $20 < p_{\mathrm{T}} < 25$

(d) $25 < p_{\mathrm{T}} < 30$ **(e)** $30 < p_{\mathrm{T}} < 40$ **(f)** $40 < p_{\mathrm{T}} < 100$

(g) $0 < |\eta| < 0.5$ **(h)** $0.5 < |\eta| < 1.0$ **(i)** $1.0 < |\eta| < 1.5$

(j) $1.5 < |\eta| < 2.0$ **(k)** $2.0 < |\eta| < 2.5$

Figure B.4.: Triple Gaussian model fitted to the invariant mass of $D_s^{\pm}$ MC samples in bins of different p_{T} (in GeV) and $|\eta|$.

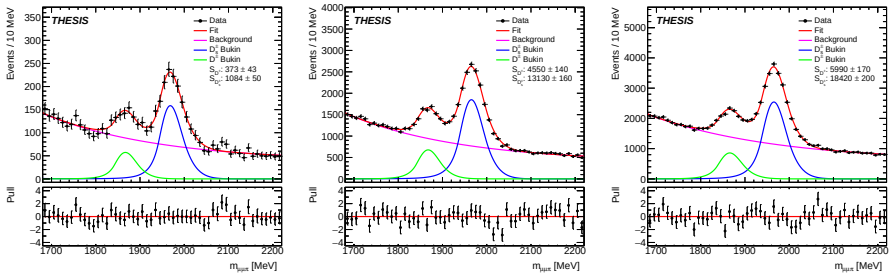

(a) $12 < p_{\mathrm{T}} < 15$ **(b)** $15 < p_{\mathrm{T}} < 20$ **(c)** $20 < p_{\mathrm{T}} < 25$

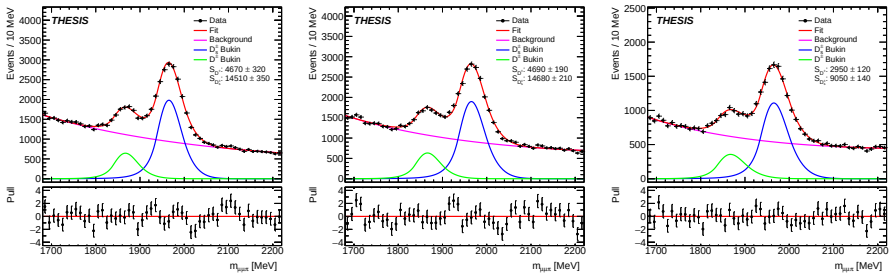

(d) $25 < p_{\mathrm{T}} < 30$ **(e)** $30 < p_{\mathrm{T}} < 40$ **(f)** $40 < p_{\mathrm{T}} < 100$

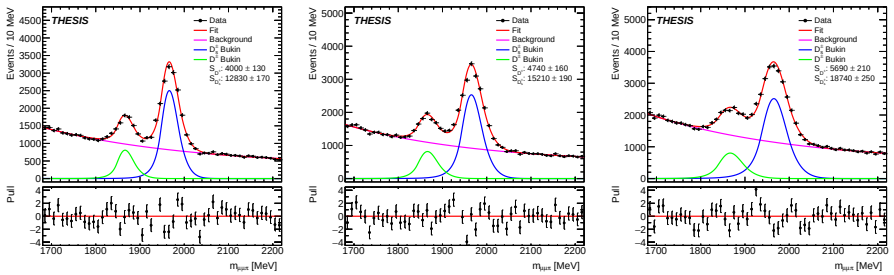

(g) $0 < |\eta| < 0.5$ **(h)** $0.5 < |\eta| < 1.0$ **(i)** $1.0 < |\eta| < 1.5$

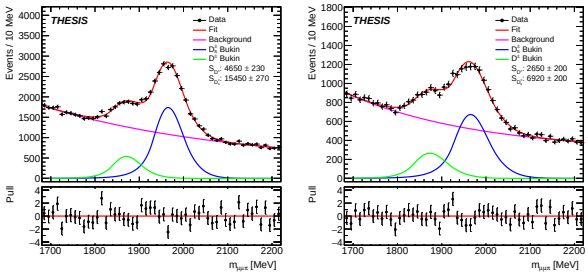

(j) $1.5 < |\eta| < 2.0$ **(k)** $2.0 < |\eta| < 2.5$

Figure B.5.: Nominal model modified by the Bukin model (fixed by MC) fitted to the invariant mass of data in bins of different p_{T} (in GeV) and $|\eta|$.

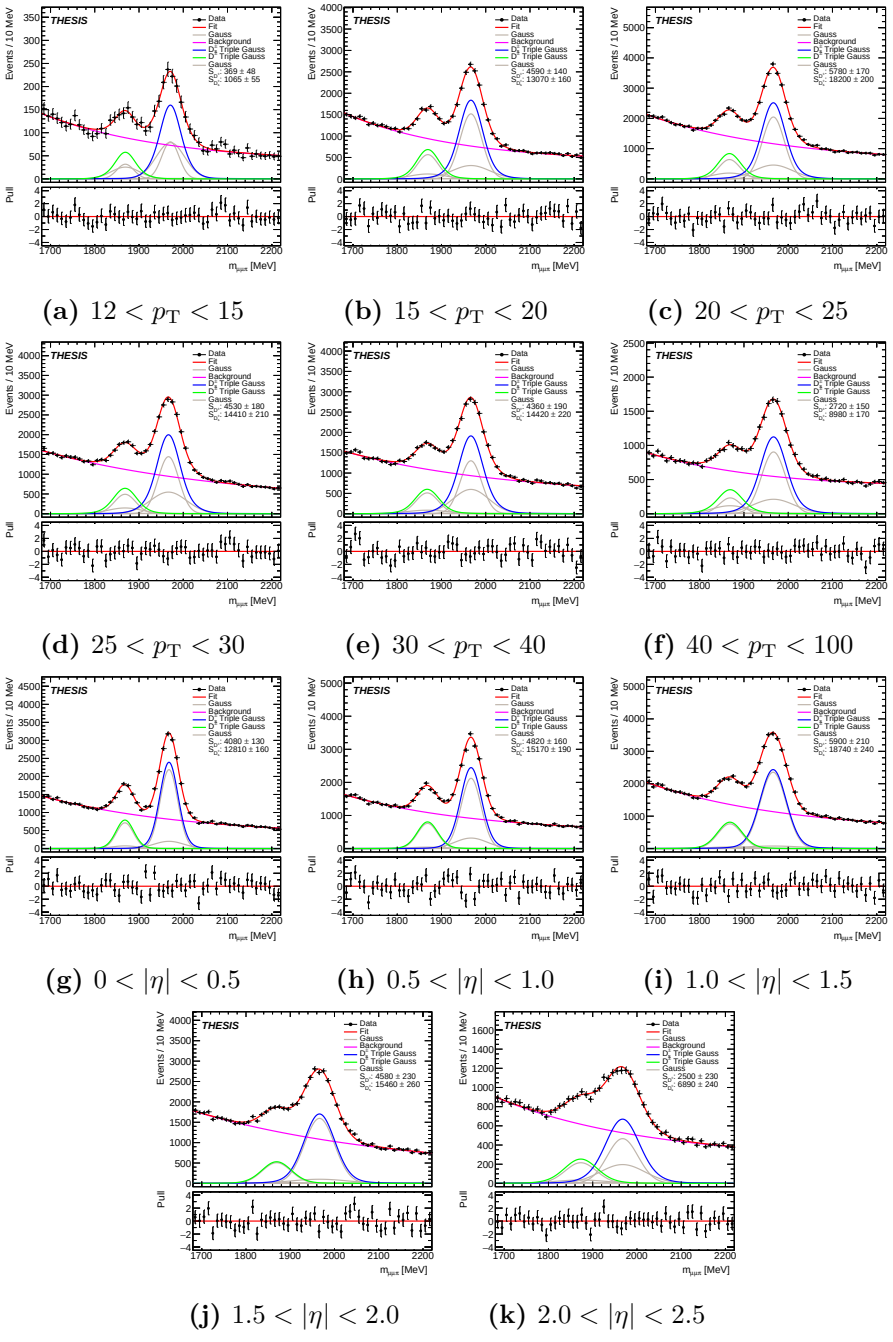

(a) $12 < p_T < 15$ **(b)** $15 < p_T < 20$ **(c)** $20 < p_T < 25$

(d) $25 < p_T < 30$ **(e)** $30 < p_T < 40$ **(f)** $40 < p_T < 100$

(g) $0 < |\eta| < 0.5$ **(h)** $0.5 < |\eta| < 1.0$ **(i)** $1.0 < |\eta| < 1.5$

(j) $1.5 < |\eta| < 2.0$ **(k)** $2.0 < |\eta| < 2.5$

Figure B.6.: Nominal model modified by the Triple Gaussian model (fixed by MC) fitted to the invariant mass of data in bins of different p_T (in GeV) and $|\eta|$.

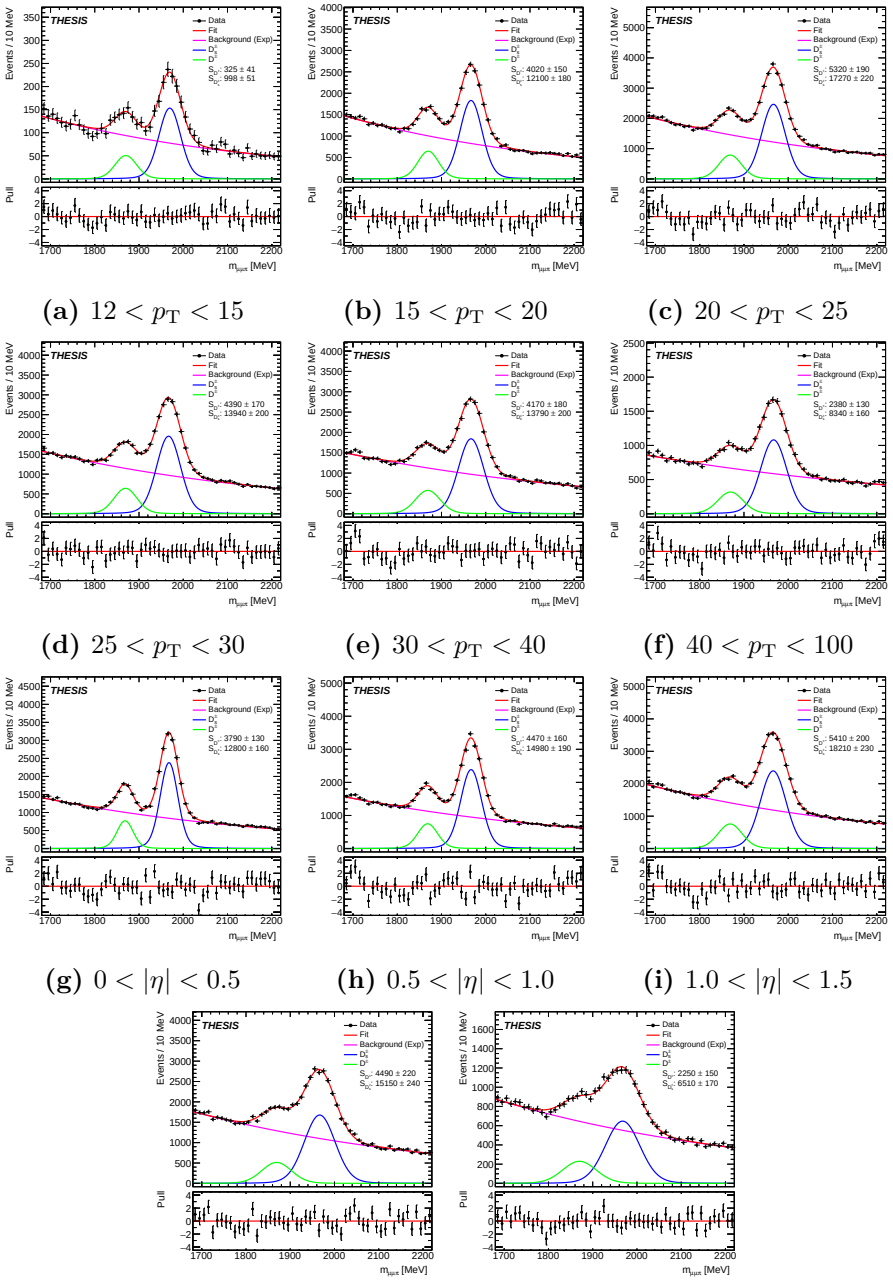

(a) $12 < p_{\mathrm{T}} < 15$ **(b)** $15 < p_{\mathrm{T}} < 20$ **(c)** $20 < p_{\mathrm{T}} < 25$

(d) $25 < p_{\mathrm{T}} < 30$ **(e)** $30 < p_{\mathrm{T}} < 40$ **(f)** $40 < p_{\mathrm{T}} < 100$

(g) $0 < |\eta| < 0.5$ **(h)** $0.5 < |\eta| < 1.0$ **(i)** $1.0 < |\eta| < 1.5$

(j) $1.5 < |\eta| < 2.0$ **(k)** $2.0 < |\eta| < 2.5$

Figure B.7.: Nominal model modified by simple exponential background fitted to the invariant mass of data in bins of different p_{T} (in GeV) and $|\eta|$.

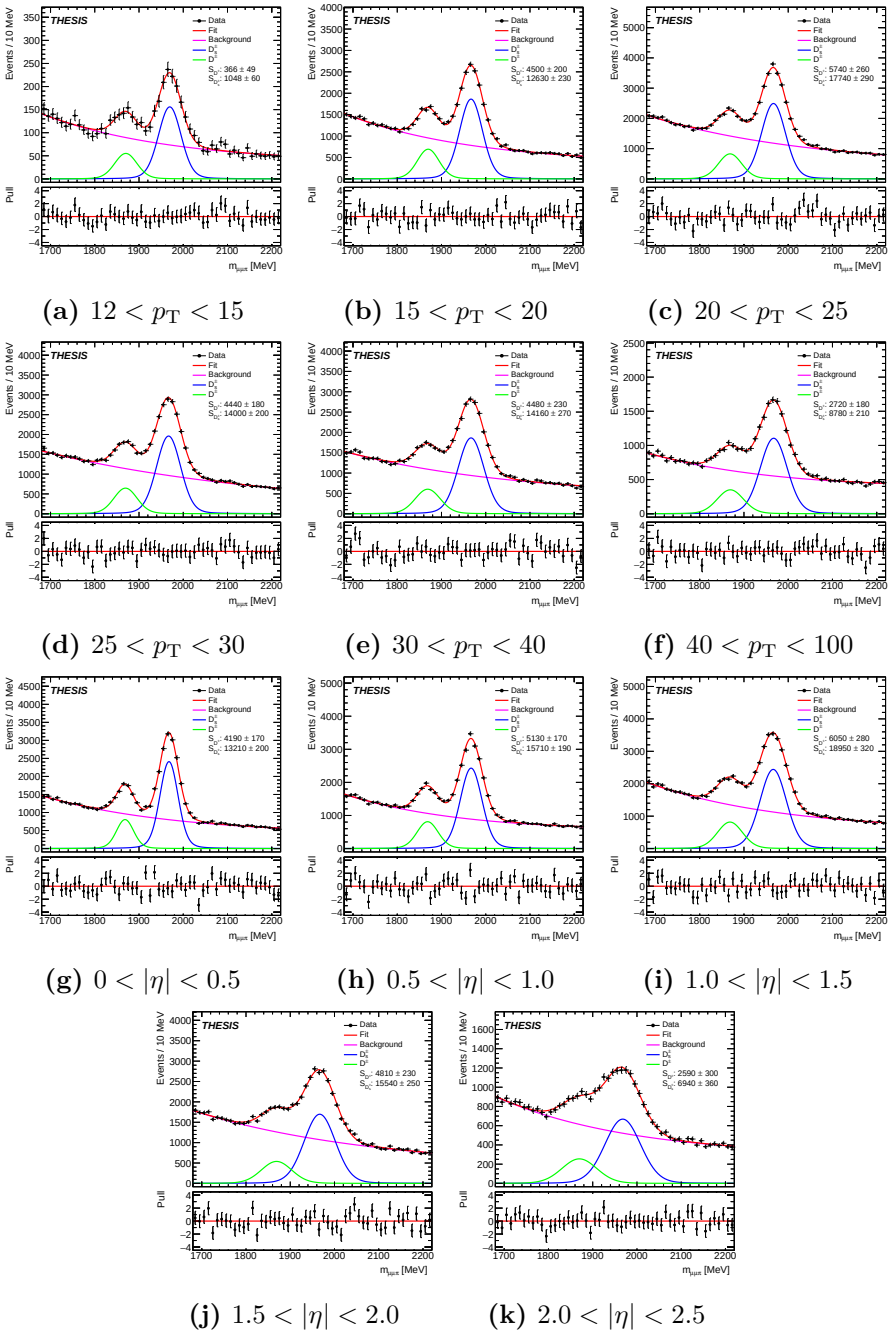

(a) $12 < p_{\mathrm{T}} < 15$ **(b)** $15 < p_{\mathrm{T}} < 20$ **(c)** $20 < p_{\mathrm{T}} < 25$

(d) $25 < p_{\mathrm{T}} < 30$ **(e)** $30 < p_{\mathrm{T}} < 40$ **(f)** $40 < p_{\mathrm{T}} < 100$

(g) $0 < |\eta| < 0.5$ **(h)** $0.5 < |\eta| < 1.0$ **(i)** $1.0 < |\eta| < 1.5$

(j) $1.5 < |\eta| < 2.0$ **(k)** $2.0 < |\eta| < 2.5$

Figure B.8.: Nominal model fitted to the invariant mass of data in bins of different p_{T} (in GeV) and $|\eta|$.

Research Data Management

This thesis research has been carried out under the research data management policies of the Nationaal Instituut voor Kernfysica en Hoge-Energiefysica (Nikhef), and the High Energy Physics department of Radboud University.

The datasets used in this thesis are based on the proton-proton collision data collected by the ATLAS collaboration at the Large Hadron Collider at CERN during the Run 2 operation in 2015-2018. The raw output data of the ATLAS experiment are stored at CERN and the associated computing centers, including Stichting Academisch Rekencentrum Amsterdam (SARA) in Amsterdam. They are accessible through membership and associate-membership of the ATLAS collaboration. A sizeable part of the processed data are also directly accessible through the ATLAS Open Data project (`https://atlas.cern/Resources/Opendata`), which has been set up and maintained by CERN directly. The processed and analyzed data are stored on servers maintained by Nikhef (`https://kb.nikhef.nl/ct/Stoomboot_cluster.html`). Data directly underlying publications are made available through the HEPData repository (`https://www.hepdata.net`).

The data processing and analysis tools are developed by the ATLAS collaboration and are maintained in the ATLAS software repository. The main tools used in this thesis are as follows:

- The ATLAS software framework Athena [131] (`https://gitlab.cern.ch/atlas/athena/-/tree/21.2`)
- Data processing framework (`https://gitlab.cern.ch/Tau3Mu/ELTau3Mu`)
- Statistics and plotting tools (`https://gitlab.cern.ch/ELBrain/PyAnalysisTools`)

Samenvatting

Het Standaardmodel en verder

Het Standaardmodel is een succesvolle theorie gebleken bij het beschrijven van de fysica op een fundamenteel niveau. Met slechts 17 fundamentele deeltjes en hun interacties, is het Standaardmodel in staat om de elektromagnetische, zwakke en sterke krachten te beschrijven, evenals het Higgs-mechanisme dat massa geeft aan de deeltjes. De fundamentele deeltjes in het Standaardmodel worden getoond in Fig.S1.

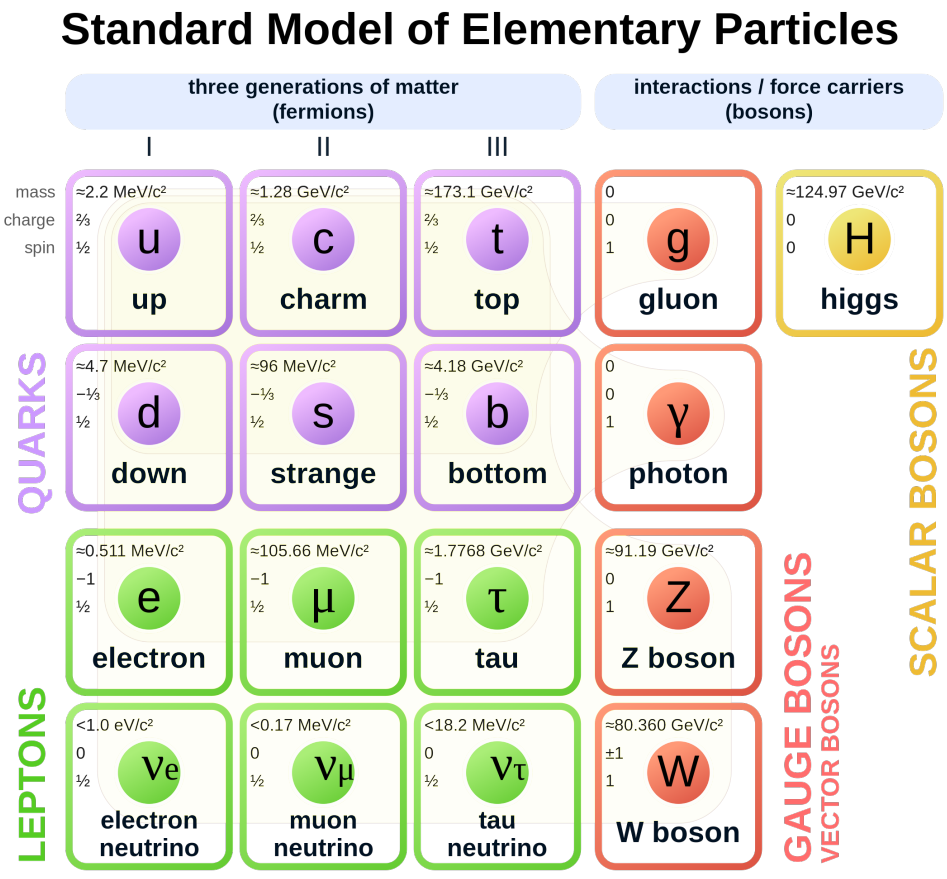

Fig. S1.: Fundamentele deeltjes in het Standaardmodel, gegroepeerd in verschillende sectoren. De massa, elektrische lading en spin worden ook getoond voor elk deeltje[5].

Echter, het Standaardmodel is nog steeds niet compleet en er blijven nog veel open vragen onbeantwoord. Deze open vragen betreffen de meest fundamentele vragen in de fysica, zoals de oorsprong van alles, symmetrieën en behoudswetten. In het bijzonder is het Standaardmodel ook uitgedaagd door de ontdekking van neutrino-oscillatie, wat impliceert dat neutrino's massa hebben. Bovendien biedt het Standaardmodel geen beschrijving van de zwaartekracht, en verklaart het niet de donkere materie en donkere energie die in het universum worden waargenomen. Daarom wordt algemeen aangenomen dat een uitbreiding van het Standaardmodel nodig is.

Aan de meer praktische kant, geven huidige theorieën niet altijd voorspellingen met de hoge precisie die experimentele behoeften voldoet. Vooral in het geval van de sterke kracht betekent de complicatie in perturbatieve uitbreiding en beperkt begrip van partondistributie dat de voorspellingen niet altijd betrouwbaar zijn. Om het Standaardmodel te perfectioneren, moeten verschillende deeltjes en hun interacties in groot detail bestudeerd worden.

Kansen bij de LHC

De Large Hadron Collider (LHC) die bij CERN in gebruik is, is een versneller die energie in protonen injecteert en deze met extreem hoge energie laat botsen. Tijdens zijn tweede bedrijfsperiode in 2015-2018 heeft de LHC protonen gebotst met een energie in het massamiddelpunt van 13 TeV en een snelheid van 40 miljoen botsingsgebeurtenissen per seconde. Bij zo'n hoge energie is de productie van een breder scala aan deeltjes mogelijk, waardoor gezocht kan worden naar deeltjes met een hogere massa, inclusief de nieuwe deeltjes die worden voorspeld door theorieën die verder gaan dan het Standaardmodel. De hoge gebeurtenissnelheid betekent ook dat zeldzame processen met hoge statistieken kunnen worden bestudeerd, wat eerder niet mogelijk was. Met de botsingsgegevens verzameld door de ATLAS- en CMS-detectoren, werd het Higgs-boson ontdekt in 2012, en veel andere metingen zijn gemaakt om het Standaardmodel te testen en te zoeken naar nieuwe fysica.

Meting van de productie van D mesonen

Van de Standaardmodeldeeltjes die in de LHC worden geproduceerd, is één groep deeltjes die bijzonder interessant is, de D mesonen. De D mesonen bestaan uit een c quark en een lichte quark, en kunnen in de LHC worden geproduceerd via een initiële c quark of een b quark. Huidige theorieën kunnen de verhouding van productie via b quark niet betrouwbaar voorspellen, noch kan de algehele productiesnelheid met hoge precisie worden voorspeld, vanwege de massaschalen in de berekening.

De uitgevoerde analyse vertrouwt op het ontwikkelen van stabiele pasmodellen om de signaalvorm van de D mesonen te extraheren om de productiedoorsnede te evalueren. De resultaten worden vergeleken met de meest geavanceerde QCD-berekeningen, zoals de GM-VFNS en FONLL berekeningen en worden getoond in Fig. S2. Het wordt aangetoond

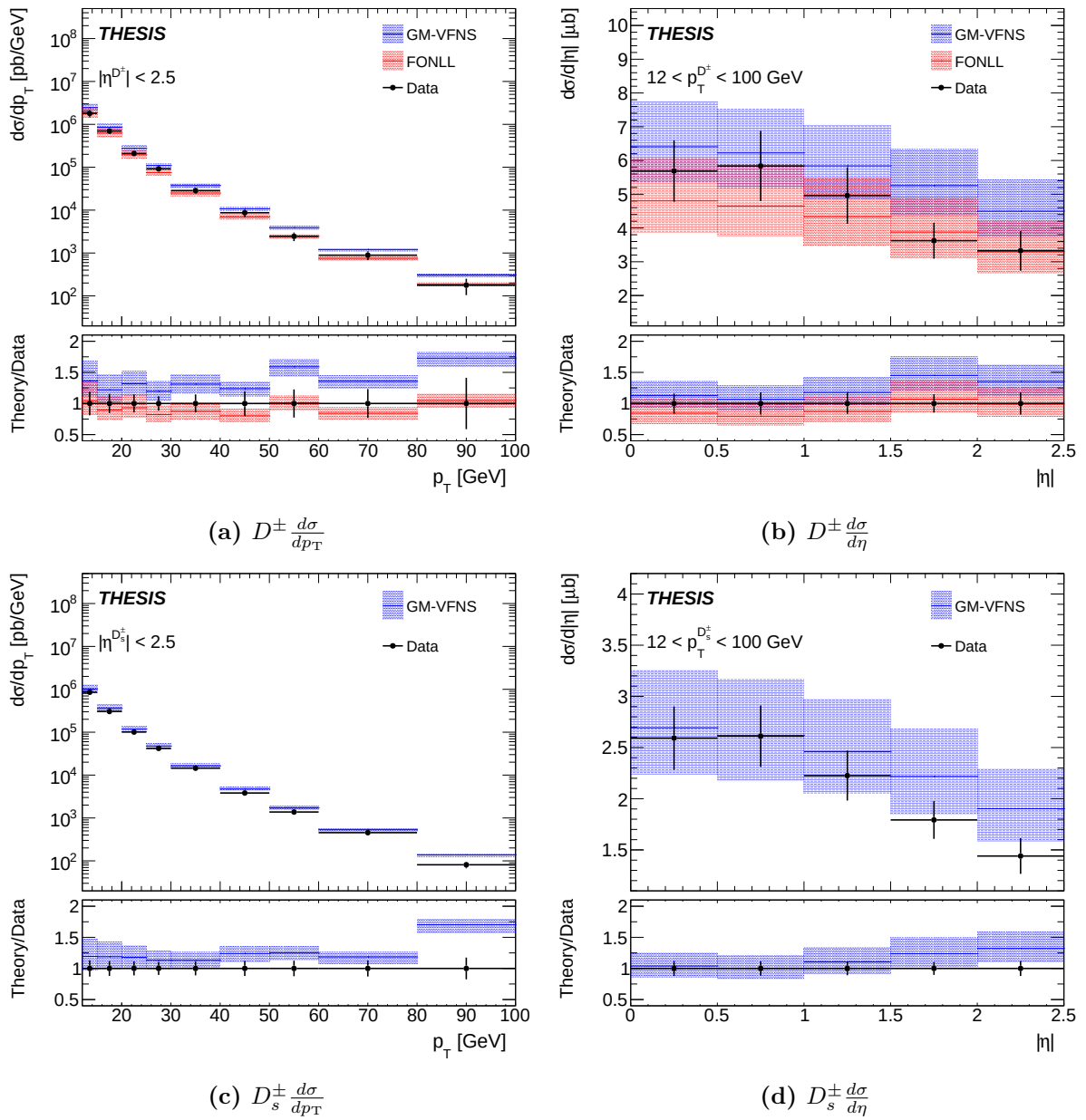

(a) $D^{\pm}\frac{d\sigma}{dp_{\mathrm{T}}}$ **(b)** $D^{\pm}\frac{d\sigma}{d\eta}$

(c) $D_s^{\pm}\frac{d\sigma}{dp_{\mathrm{T}}}$ **(d)** $D_s^{\pm}\frac{d\sigma}{d\eta}$

Fig. S2.: Differentiële doorsnede voor $D^{\pm}$ en $D_s^{\pm}$ per p_{T} en $|\eta|$. De gemeten waarden met de gecombineerde fout worden vertegenwoordigd door de datapunten, terwijl de theorievoorspelling van GM-VFNS en FONLL respectievelijk in blauw en rood worden getoond.

dat de differentiële doorsnede met redelijke precisie kan worden gemeten tot 100 GeV in p_{T}; het niveau van onzekerheid toont ook een grote verbetering ten opzichte van de berekeningsschema's.

Hoewel er geen verrassingen zijn gevonden, noch verwacht worden, zijn de metingen bij de LHC uniek in de zin dat de $D_s^{\pm}$ mesonen geproduceerd worden in een breed bereik van transversale impuls p_{T}, wat niet beschikbaar is in andere experimenten; dit is belangrijk

voor het begrijpen van de productie van charme quarks en de onderliggende processen bij verschillende energie schalen. Dergelijke feedback van de theorie is essentieel voor verdere verbetering van de berekeningsschema's.

Verbetering in LFV τ verval zoektochten

Met de gemeten productiesnelheid van het $D_s^{\pm}$ meson wordt het vooruitzicht van het zoeken naar het lepton-smaak-schendende $D_s^{\pm} \to \tau(3\mu)\nu$ verval herzien. Het wordt gerealiseerd dat de belangrijkste systematische onzekerheid in de meting van de vertakkingsverhouding van $\tau \to 3\mu$ de fiduciale doorsnede van het $D_s^{\pm}$ meson is. Dergelijke onzekerheid wordt verlaagd van 20% naar 12% met de verbeterde meting, wat de gevoeligheid van de zoektocht naar het $\tau \to 3\mu$ verval met 5% verbetert.

Summary

The Standard Model and beyond

The Standard Model has been a successful theory in describing physics at a fundamental level. With only 17 fundamental particles and their interactions, the Standard Model is able to describe the electromagnetic, weak and strong forces, as well as the Higgs mechanism that gives mass to the particles. The fundamental particles in the Standard Model are shown in Fig. S1.

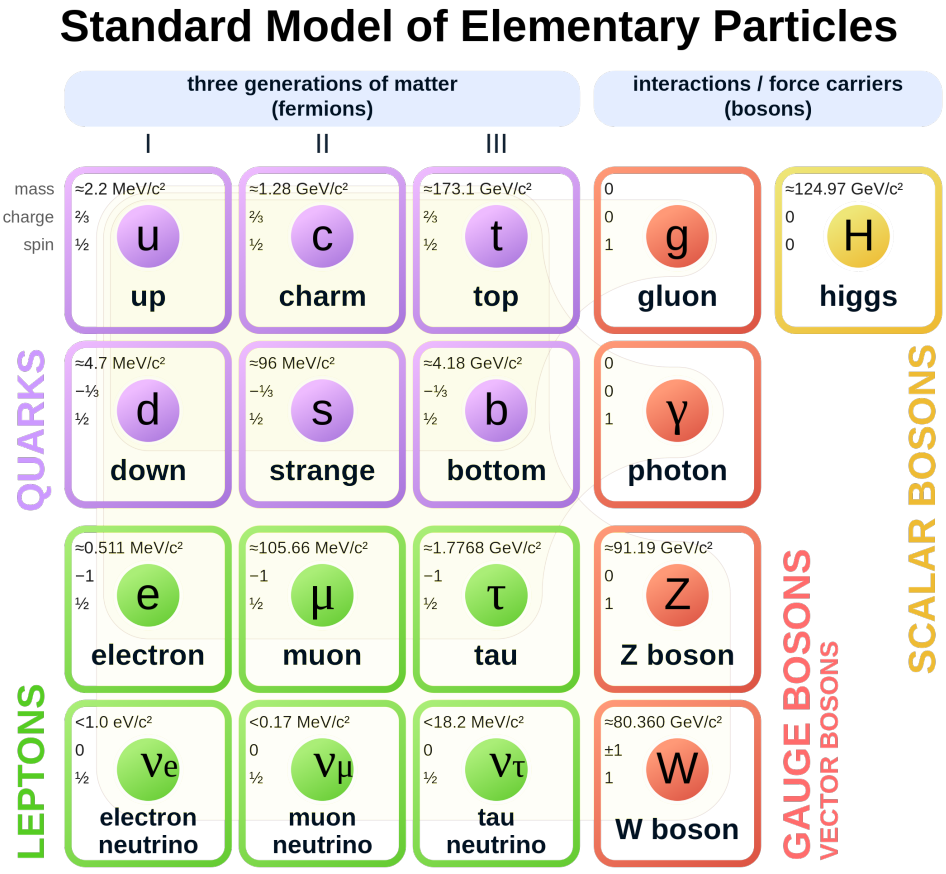

Fig. S1.: Fundamental particles in the Standard Model, grouped into different sectors. The mass, electric charge and spin are also shown for each particle [5].

However, the Standard Model is still not complete and there are still many open questions that remain unanswered. These open questions relate to the most fundamental questions in physics, such as the origin of everything, symmetries and conservation laws. In particular, the Standard Model has also been challenged by the discovery of neutrino oscillation, which implies that neutrinos have mass. Moreover, the Standard Model does not provide a description of gravity, and it does not explain the dark matter and dark energy that are observed in the universe. Therefore, it is widely believed that an extension to the Standard Model is needed.

On the more practical side, current theories do not always make predictions with sufficiently high precision to satisfy the needs of experimental measurements. Especially in the case of the strong force, the complication in perturbative expansion and limited understanding of parton distribution means that the predictions are not always reliable. To perfect the Standard Model, different particles and their interactions need to be studied in great detail.

Opportunity at the LHC

The Large Hadron Collider (LHC) operating at CERN is an accelerator that injects energy into protons and collides them at extremely high energy. During its second operation run in 2015-2018, the LHC has collided protons at the center-of-mass energy of 13 TeV with a rate of 40 million collision events per second. At such high energy, the production of a wider variety of particles is possible, allowing the search of particles of a higher mass, including the new particles that are predicted by the theories beyond the Standard Model. The high event rate also means rare processes can be studied with high statistics that was not possible before. With the collision data collected by the ATLAS and CMS detectors, the Higgs boson was discovered in 2012, and many other measurements have been made to test the Standard Model and search for new physics.

Measurement of D meson production

Out of the Standard Model particles produced in the LHC, one group of particles that is of particular interest is the D mesons. The D mesons are made of a c quark and a light quark, and they can be produced in the LHC via either an initial c quark or a b quark. Current theories cannot predict the proportion of production via b quark reliably, nor can the overall production rate be predicted to high precision, due to mass scales in the calculation.

The analysis performed relies on developing stable fit models to extract the signal shape of the D mesons to evaluate the production cross section. The results are compared to the state-of-the-art QCD calculations, such as the GM-VFNS and FONLL calculations and shown in Fig. S2. It is demonstrated that the differential cross section can be measured with reasonable precision up to 100 GeV in p_{T}; the level of uncertainty also shows a great improvement over the calculation schemes. This is the first time in the LHC that the $D_s^{\pm}$

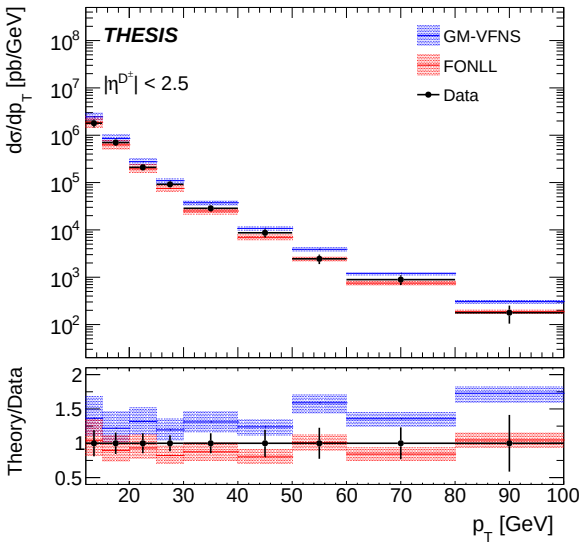

(a) $D^\pm \frac{d\sigma}{dp_T}$

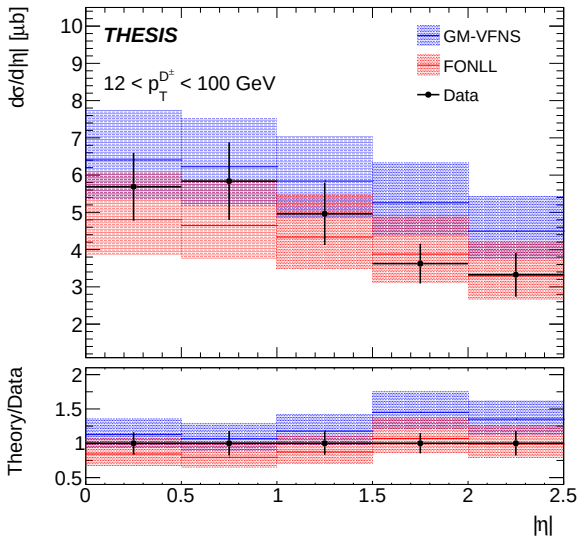

(b) $D^\pm \frac{d\sigma}{d\eta}$

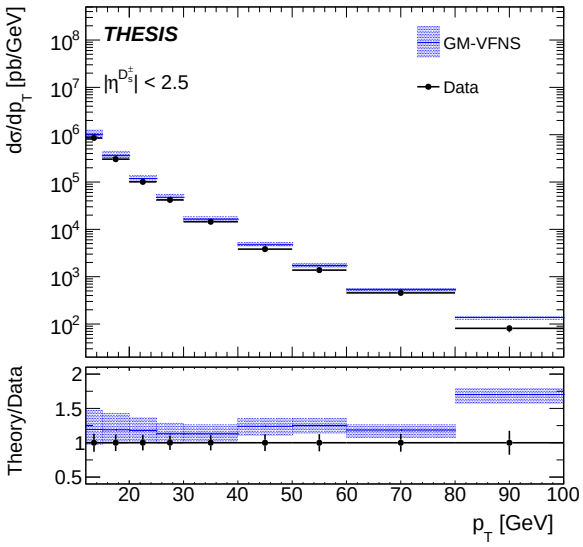

(c) $D_s^\pm \frac{d\sigma}{dp_T}$

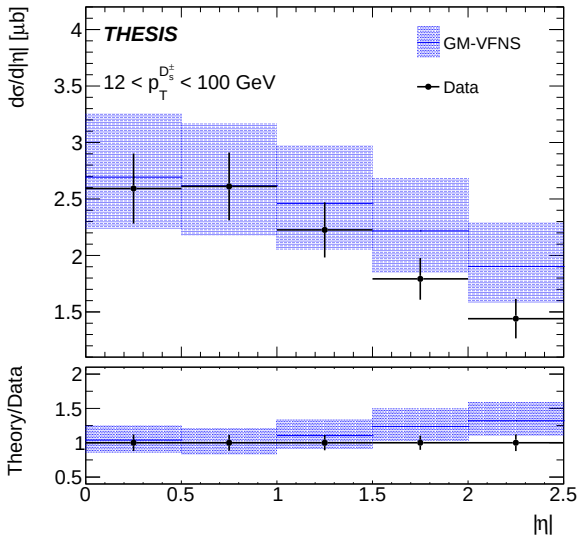

(d) $D_s^\pm \frac{d\sigma}{d\eta}$

Fig. S2.: Differential cross section for $D^\pm$ and $D_s^\pm$ per p_T and $|\eta|$. The measured values with the combined error are represented by the data points, while the theory prediction from GM-VFNS and FONLL are shown in blue and red respectively.

meson production is measured differentially up to high p_T, providing theory feedback in an unexplored kinematic region.

Although no surprise is found, nor is it expected, the measurements at the LHC are unique in the sense that the $D_s^\pm$ mesons are produced in a wide range of transverse momentum p_T, which is not available in other experiments; this is important for understanding the production of charm quarks and the underlying processes at different energy scales. Such theory feedback is essential for further improvement of the calculation schemes.

Improvement in LFV τ decay searches

With the production rate of the $D_s^{\pm}$ meson measured, the prospect of searching for the lepton-flavour-violating $D_s^{\pm} \to \tau(3\mu)\nu$ decay is revisited. It is realized that the main systematic uncertainty in the measurement of the branching ratio of $\tau \to 3\mu$ is the fiducial cross section of the $D_s^{\pm}$ meson. Such uncertainty is reduced from 20% to 12% with the improved measurement, which improves the sensitivity of the search for the $\tau \to 3\mu$ decay by 5%.

Bibliography

[1] D. Griffiths, *Introduction to Elementary Particles*, Wiley, 2008 (cit. on p. 3).

[2] M. Thomson, *Modern Particle Physics*, Cambridge University Press, 2013 (cit. on pp. 3, 6, 12).

[3] M. K. Gaillard, P. D. Grannis, and F. J. Sciulli, *The Standard model of particle physics*, Rev. Mod. Phys. **71** (1999) S96, DOI: 10.1103/RevModPhys.71.S96, arXiv: hep-ph/9812285 (cit. on p. 3).

[4] R. L. Workman et al., *Review of Particle Physics*, PTEP **2022** (2022) 083C01, DOI: 10.1093/ptep/ptac097 (cit. on pp. 3, 13, 14, 89).

[5] C. MissMJ, "Standard Model of Elementary Particles", 2023, URL: https://en.wikipedia.org/wiki/File:Standard_Model_of_Elementary_Particles.svg (cit. on pp. 4, 137, 141).

[6] J. Goldstone, A. Salam, and S. Weinberg, *Broken Symmetries*, Phys. Rev. **127** (1962) 965, DOI: 10.1103/PhysRev.127.965 (cit. on p. 4).

[7] P. W. Higgs, *Broken symmetries, massless particles and gauge fields*, Phys. Lett. **12** (1964) 132, DOI: 10.1016/0031-9163(64)91136-9 (cit. on p. 4).

[8] P. W. Higgs, *Broken Symmetries and the Masses of Gauge Bosons*, Phys. Rev. Lett. **13** (1964), ed. by J. C. Taylor 508, DOI: 10.1103/PhysRevLett.13.508 (cit. on p. 4).

[9] M. Carena, M. Olechowski, S. Pokorski, and C. E. M. Wagner, *Electroweak symmetry breaking and bottom - top Yukawa unification*, Nucl. Phys. B **426** (1994) 269, DOI: 10.1016/0550-3213(94)90313-1, arXiv: hep-ph/9402253 (cit. on p. 4).

[10] C.-N. Yang and R. L. Mills, *Conservation of Isotopic Spin and Isotopic Gauge Invariance*, Phys. Rev. **96** (1954), ed. by J.-P. Hsu and D. Fine 191, DOI: 10.1103/PhysRev.96.191 (cit. on p. 5).

[11] R. P. Feynman, *The Qualitative Behavior of Yang-Mills Theory in (2+1)-Dimensions*, Nucl. Phys. B **188** (1981) 479, DOI: 10.1016/0550-3213(81)90005-5 (cit. on p. 5).

[12] M. Gell-Mann, *The Eightfold Way: A Theory of strong interaction symmetry* (1961), DOI: 10.2172/4008239 (cit. on p. 5).

[13] M. Gell-Mann, *A Schematic Model of Baryons and Mesons*, Phys. Lett. **8** (1964) 214, DOI: 10.1016/S0031-9163(64)92001-3 (cit. on p. 5).

[14] D. J. Gross and F. Wilczek, *Ultraviolet Behavior of Nonabelian Gauge Theories*, Phys. Rev. Lett. **30** (1973), ed. by J. C. Taylor 1343, DOI: 10.1103/PhysRevLett.30.1343 (cit. on p. 5).

[15] H. D. Politzer, *Reliable Perturbative Results for Strong Interactions?*, Phys. Rev. Lett. **30** (1973), ed. by J. C. Taylor 1346, DOI: 10.1103/PhysRevLett.30.1346 (cit. on p. 5).

[16] E. Fermi, *An attempt of a theory of beta radiation. 1.*, Z. Phys. **88** (1934) 161, DOI: 10.1007/BF01351864 (cit. on p. 5).

[17] S. Weinberg, *A Model of Leptons*, Phys. Rev. Lett. **19** (1967) 1264, DOI: 10.1103/PhysRevLett.19.1264 (cit. on p. 5).

[18] S. L. Glashow, J. Iliopoulos, and L. Maiani, *Weak Interactions with Lepton-Hadron Symmetry*, Phys. Rev. D **2** (1970) 1285, DOI: 10.1103/PhysRevD.2.1285 (cit. on p. 5).

[19] N. Cabibbo, *Unitary Symmetry and Leptonic Decays*, Phys. Rev. Lett. **10** (1963) 531, DOI: 10.1103/PhysRevLett.10.531 (cit. on p. 5).

[20] M. Kobayashi and T. Maskawa, *CP Violation in the Renormalizable Theory of Weak Interaction*, Prog. Theor. Phys. **49** (1973) 652, DOI: 10.1143/PTP.49.652 (cit. on p. 5).

[21] P. A. M. Dirac, *Quantum theory of emission and absorption of radiation*, Proc. Roy. Soc. Lond. A **114** (1927) 243, DOI: 10.1098/rspa.1927.0039 (cit. on p. 5).

[22] S. Tomonaga, *On a relativistically invariant formulation of the quantum theory of wave fields*, Prog. Theor. Phys. **1** (1946) 27, DOI: 10.1143/PTP.1.27 (cit. on p. 5).

[23] J. S. Schwinger, *On Quantum electrodynamics and the magnetic moment of the electron*, Phys. Rev. **73** (1948) 416, DOI: 10.1103/PhysRev.73.416 (cit. on p. 5).

[24] J. F. Gunion, H. E. Haber, G. L. Kane, and S. Dawson, *The Higgs Hunter's Guide*, vol. 80, 2000 (cit. on pp. 6, 18).

[25] S. Weinberg, *Implications of Dynamical Symmetry Breaking*, Phys. Rev. D **13** (1976), [Addendum: Phys.Rev.D 19, 1277–1280 (1979)] 974, DOI: 10.1103/PhysRevD.19.1277 (cit. on p. 6).

[26] P. D. Mannheim, *Mass Generation, the Cosmological Constant Problem, Conformal Symmetry, and the Higgs Boson*, Prog. Part. Nucl. Phys. **94** (2017) 125, DOI: 10.1016/j.ppnp.2017.02.001, arXiv: 1610.08907 [hep-ph] (cit. on p. 6).

[27] Ponor, "Standard Model All Feynman diagram vertices", 2023, URL: https://commons.wikimedia.org/wiki/File:Standard_Model_%E2%80%93_All_Feynman_diagram_vertices.svg (cit. on p. 7).

[28] J. Woithe, G. J. Wiener, and F. F. Van der Veken, *Lets have a coffee with the Standard Model of particle physics!*, Phys. Educ. **52** (2017) 034001, DOI: 10.1088/1361-6552/aa5b25 (cit. on p. 6).

[29] T. D. Lee and C.-N. Yang, *Question of Parity Conservation in Weak Interactions*, Phys. Rev. **104** (1956) 254, DOI: 10.1103/PhysRev.104.254 (cit. on p. 8).

[30] S. L. Glashow, *Partial Symmetries of Weak Interactions*, Nucl. Phys. **22** (1961) 579, DOI: 10.1016/0029-5582(61)90469-2 (cit. on p. 8).

[31] R. D. Peccei and H. R. Quinn, *CP Conservation in the Presence of Instantons*, Phys. Rev. Lett. **38** (1977) 1440, DOI: 10.1103/PhysRevLett.38.1440 (cit. on p. 9).

[32] F. Wilczek, *Problem of Strong P and T Invariance in the Presence of Instantons*, Phys. Rev. Lett. **40** (1978) 279, DOI: 10.1103/PhysRevLett.40.279 (cit. on p. 9).

[33] G. Steigman, *Observational tests of antimatter cosmologies*, Ann. Rev. Astron. Astrophys. **14** (1976) 339, DOI: 10.1146/annurev.aa.14.090176.002011 (cit. on p. 10).

[34] A. D. Sakharov, *Violation of CP Invariance, C asymmetry, and baryon asymmetry of the universe*, Pisma Zh. Eksp. Teor. Fiz. **5** (1967) 32, DOI: 10.1070/PU1991v034n05ABEH002497 (cit. on p. 10).

[35] Y. Fukuda et al., *Evidence for oscillation of atmospheric neutrinos*, Phys. Rev. Lett. **81** (1998) 1562, DOI: 10.1103/PhysRevLett.81.1562, arXiv: hep-ex/9807003 (cit. on p. 10).

[36] Q. R. Ahmad et al., *Direct evidence for neutrino flavor transformation from neutral current interactions in the Sudbury Neutrino Observatory*, Phys. Rev. Lett. **89** (2002) 011301, DOI: 10.1103/PhysRevLett.89.011301, arXiv: nucl-ex/0204008 (cit. on p. 10).

[37] K. Abe et al., *Indication of Electron Neutrino Appearance from an Accelerator-produced Off-axis Muon Neutrino Beam*, Phys. Rev. Lett. **107** (2011) 041801, DOI: 10.1103/PhysRevLett.107.041801, arXiv: 1106.2822 [hep-ex] (cit. on p. 10).

[38] B. Pontecorvo, *Mesonium and anti-mesonium*, Sov. Phys. JETP **6** (1957) 429 (cit. on p. 10).

[39] B. Pontecorvo, *Neutrino Experiments and the Problem of Conservation of Leptonic Charge*, Zh. Eksp. Teor. Fiz. **53** (1967) 1717 (cit. on pp. 10, 12).

[40] L. Wolfenstein, *Neutrino Oscillations in Matter*, Phys. Rev. D **17** (1978) 2369, DOI: 10.1103/PhysRevD.17.2369 (cit. on p. 10).

[41] H. Georgi and S. L. Glashow, *Unity of All Elementary Particle Forces*, Phys. Rev. Lett. **32** (1974) 438, DOI: 10.1103/PhysRevLett.32.438 (cit. on p. 10).

[42] H. Georgi, *The State of the ArtGauge Theories*, AIP Conf. Proc. **23** (1975), ed. by H. C. C. E. W. Carlson 575, DOI: 10.1063/1.2947450 (cit. on p. 10).

[43] H. Fritzsch and P. Minkowski, *Unified Interactions of Leptons and Hadrons*, Annals Phys. **93** (1975) 193, DOI: 10.1016/0003-4916(75)90211-0 (cit. on p. 10).

[44] F. Zwicky, *Die Rotverschiebung von extragalaktischen Nebeln*, Helv. Phys. Acta **6** (1933) 110, DOI: 10.1007/s10714-008-0707-4 (cit. on p. 11).

[45] V. C. Rubin and W. K. Ford Jr., *Rotation of the Andromeda Nebula from a Spectroscopic Survey of Emission Regions*, Astrophys. J. **159** (1970) 379, DOI: 10.1086/150317 (cit. on p. 11).

[46] J. H. Oort, *The force exerted by the stellar system in the direction perpendicular to the galactic plane and some related problems*, Bull. Astron. Inst. Netherlands **6** (1932) 249 (cit. on p. 11).

[47] J. A. Tyson, R. A. Wenk, and F. Valdes, *Detection of systematic gravitational lens galaxy image alignments - Mapping dark matter in galaxy clusters*, Astrophys. J. Lett. **349** (1990) L1, DOI: 10.1086/185636 (cit. on p. 11).

[48] M. Bartelmann and P. Schneider, *Weak gravitational lensing*, Phys. Rept. **340** (2001) 291, DOI: 10.1016/S0370-1573(00)00082-X, arXiv: astro-ph/9912508 (cit. on p. 11).

[49] D. Clowe et al., *A direct empirical proof of the existence of dark matter*, Astrophys. J. Lett. **648** (2006) L109, DOI: 10.1086/508162, arXiv: astro-ph/0608407 (cit. on p. 11).

[50] Z. Maki, M. Nakagawa, and S. Sakata, *Remarks on the unified model of elementary particles*, Prog. Theor. Phys. **28** (1962) 870, DOI: 10.1143/PTP.28.870 (cit. on p. 12).

[51] P. F. de Salas, D. V. Forero, C. A. Ternes, M. Tortola, and J. W. F. Valle, *Status of neutrino oscillations 2018: 3σ hint for normal mass ordering and improved CP sensitivity*, Phys. Lett. B **782** (2018) 633, DOI: 10.1016/j.physletb.2018.06.019, arXiv: 1708.01186 [hep-ph] (cit. on p. 12).

[52] F. Capozzi, E. Lisi, A. Marrone, D. Montanino, and A. Palazzo, *Neutrino masses and mixings: Status of known and unknown 3ν parameters*, Nucl. Phys. B **908** (2016) 218, DOI: 10.1016/j.nuclphysb.2016.02.016, arXiv: 1601.07777 [hep-ph] (cit. on p. 12).

[53] I. Esteban, M. C. Gonzalez-Garcia, M. Maltoni, T. Schwetz, and A. Zhou, *The fate of hints: updated global analysis of three-flavor neutrino oscillations*, JHEP **09** (2020) 178, DOI: 10.1007/JHEP09(2020)178, arXiv: 2007.14792 [hep-ph] (cit. on p. 12).

[54] M. Aker et al., *Direct neutrino-mass measurement with sub-electronvolt sensitivity*, Nature Phys. **18** (2022) 160, DOI: 10.1038/s41567-021-01463-1, arXiv: 2105.08533 [hep-ex] (cit. on p. 12).

[55] I. Esteban, M. C. Gonzalez-Garcia, M. Maltoni, T. Schwetz, and A. Zhou, "Three-neutrino fit based on data available in November 2022", 2022, URL: http://www.nu-fit.org/?q=node/256 (cit. on p. 13).

[56] A. M. Abdullahi et al., *The present and future status of heavy neutral leptons*, J. Phys. G **50** (2023) 020501, DOI: 10.1088/1361-6471/ac98f9, arXiv: 2203.08039 [hep-ph] (cit. on p. 14).

[57] G. Hernández-Tomé, G. López Castro, and P. Roig, *Flavor violating leptonic decays of τ and μ leptons in the Standard Model with massive neutrinos*, Eur. Phys. J. C **79** (2019), [Erratum: Eur.Phys.J.C 80, 438 (2020)] 84, DOI: 10.1140/epjc/s10052-019-6563-4, arXiv: 1807.06050 [hep-ph] (cit. on p. 15).

[58] P. Blackstone, M. Fael, and E. Passemar, *$\tau \to \mu\mu\mu$ at a rate of one out of 10^{14} tau decays?*, Eur. Phys. J. C **80** (2020) 506, DOI: 10.1140/epjc/s10052-020-8059-7, arXiv: 1912.09862 [hep-ph] (cit. on pp. 15, 17).

[59] Y. S. Amhis et al., *Averages of b-hadron, c-hadron, and τ-lepton properties as of 2018*, Eur. Phys. J. C **81** (2021) 226, DOI: 10.1140/epjc/s10052-020-8156-7, arXiv: 1909.12524 [hep-ex] (cit. on p. 15).

[60] S. Banerjee et al., *Snowmass 2021 White Paper: Charged lepton flavor violation in the tau sector* (2022), arXiv: 2203.14919 [hep-ph] (cit. on pp. 15, 16).

[61] R. V. Harlander, S. Y. Klein, and M. Lipp, *FeynGame*, Comput. Phys. Commun. **256** (2020) 107465, DOI: 10.1016/j.cpc.2020.107465, arXiv: 2003.00896 [physics.ed-ph] (cit. on pp. 15, 17–19).

[62] M. Ardu and G. Pezzullo, *Introduction to Charged Lepton Flavor Violation*, Universe **8** (2022) 299, DOI: 10.3390/universe8060299, arXiv: 2204.08220 [hep-ph] (cit. on p. 17).

[63] G. Lopez Castro and N. Quintero, *Lepton number violation in tau lepton decays*, Nucl. Phys. B Proc. Suppl. **253-255** (2014), ed. by K. Hayasaka and T. Iijima 12, DOI: 10.1016/j.nuclphysbps.2014.09.004, arXiv: 1212.0037 [hep-ph] (cit. on p. 17).

[64] H. Novales-Sánchez, M. Salinas, and J. J. Toscano, *About heavy neutrinos: Lepton-flavor violation in decays of charged leptons*, J. Phys. G **45** (2018) 095004, DOI: 10.1088/1361-6471/aad53c, arXiv: 1710.08474 [hep-ph] (cit. on p. 17).

[65] J. C. Pati and A. Salam, *Lepton Number as the Fourth Color*, Phys. Rev. D **10** (1974), [Erratum: Phys.Rev.D 11, 703–703 (1975)] 275, DOI: 10.1103/PhysRevD.10.275 (cit. on p. 17).

[66] I. Dorner, S. Fajfer, A. Greljo, J. F. Kamenik, and N. Konik, *Physics of leptoquarks in precision experiments and at particle colliders*, Phys. Rept. **641** (2016) 1, DOI: 10.1016/j.physrep.2016.06.001, arXiv: 1603.04993 [hep-ph] (cit. on p. 17).

[67] I. Dorner and A. Greljo, *Leptoquark toolbox for precision collider studies*, JHEP **05** (2018) 126, DOI: 10.1007/JHEP05(2018)126, arXiv: 1801.07641 [hep-ph] (cit. on p. 17).

[68] R. Benbrik, M. Chabab, and G. Faisel, *Lepton Flavour Violating τ and μ decays induced by scalar leptoquark* (2010), arXiv: 1009.3886 [hep-ph] (cit. on p. 18).

[69] G. C. Branco et al., *Theory and phenomenology of two-Higgs-doublet models*, Phys. Rept. **516** (2012) 1, DOI: 10.1016/j.physrep.2012.02.002, arXiv: 1106.0034 [hep-ph] (cit. on p. 18).

[70] F. J. Botella, G. C. Branco, and M. N. Rebelo, *Invariants and Flavour in the General Two-Higgs Doublet Model*, Phys. Lett. B **722** (2013) 76, DOI: 10.1016/j.physletb.2013.03.022, arXiv: 1210.8163 [hep-ph] (cit. on p. 18).

[71] A. Crivellin, A. Kokulu, and C. Greub, *Flavor-phenomenology of two-Higgs-doublet models with generic Yukawa structure*, Phys. Rev. D **87** (2013) 094031, DOI: 10.1103/PhysRevD.87.094031, arXiv: 1303.5877 [hep-ph] (cit. on p. 18).

[72] I. P. Ivanov, V. Keus, and E. Vdovin, *Abelian symmetries in multi-Higgs-doublet models*, J. Phys. A **45** (2012) 215201, DOI: 10.1088/1751-8113/45/21/215201, arXiv: 1112.1660 [math-ph] (cit. on p. 18).

[73] I. P. Ivanov and C. C. Nishi, *Symmetry breaking patterns in 3HDM*, JHEP **01** (2015) 021, DOI: 10.1007/JHEP01(2015)021, arXiv: 1410.6139 [hep-ph] (cit. on p. 18).

[74] M. Maniatis and O. Nachtmann, *Stability and symmetry breaking in the general three-Higgs-doublet model*, JHEP **02** (2015), [Erratum: JHEP 10, 149 (2015)] 058, DOI: 10.1007/JHEP10(2015)149, arXiv: 1408.6833 [hep-ph] (cit. on p. 18).

[75] A. E. C. Hernández, S. Kovalenko, M. Maniatis, and I. Schmidt, *Fermion mass hierarchy and $g-2$ anomalies in an extended 3HDM Model*, JHEP **10** (2021) 036, DOI: 10.1007/JHEP10(2021)036, arXiv: 2104.07047 [hep-ph] (cit. on p. 18).

[76] E. Mobs, "The CERN accelerator complex - August 2018. Complexe des accélérateurs du CERN - Août 2018", General Photo, 2018, URL: https://cds.cern.ch/record/2636343 (cit. on p. 22).

[77] T. S. Pettersson and P. Lefèvre, *The Large Hadron Collider: conceptual design*, tech. rep. CERN-AC-95-05-LHC, 1995, URL: https://cds.cern.ch/record/291782 (cit. on pp. 23, 25).

[78] ATLAS Collaboration, *Luminosity Public Results Run 2*, URL: https://twiki.cern.ch/twiki/bin/view/AtlasPublic/LuminosityPublicResultsRun2 (visited on 03/08/2021) (cit. on pp. 23–25).

[79] CERN, *Restarting the LHC: Why 13 Tev?*, 2014, URL: https://cds.cern.ch/record/1998739 (cit. on p. 24).

[80] B. Salvachua, *Overview of Proton-Proton Physics during Run 2*, tech. rep., 2019, URL: https://cds.cern.ch/record/2750272 (cit. on pp. 24, 25).

[81] T. A. Collaboration, *The ATLAS Experiment at the CERN Large Hadron Collider*, Journal of Instrumentation **3** (2008) S08003, DOI: 10.1088/1748-0221/3/08/S08003 (cit. on pp. 26–29, 31).

[82] A. Collaboration, "ATLAS Track Reconstruction", 2024, URL: https://atlassoftwaredocs.web.cern.ch/trackingTutorial/idoverview/ (cit. on p. 34).

[83] T. Cornelissen et al., *The new ATLAS track reconstruction (NEWT)*, J. Phys. Conf. Ser. **119** (2008), ed. by R. Sobie, R. Tafirout, and J. Thomson 032014, DOI: 10.1088/1742-6596/119/3/032014 (cit. on p. 34).

[84] M. Aaboud et al., *Performance of the ATLAS Track Reconstruction Algorithms in Dense Environments in LHC Run 2*, Eur. Phys. J. C **77** (2017) 673, DOI: 10.1140/epjc/s10052-017-5225-7, arXiv: 1704.07983 [hep-ex] (cit. on pp. 34, 35).

[85] G. Aad et al., *A neural network clustering algorithm for the ATLAS silicon pixel detector*, JINST **9** (2014) P09009, DOI: 10.1088/1748-0221/9/09/P09009, arXiv: 1406.7690 [hep-ex] (cit. on p. 34).

[86] R. Fruhwirth, *Application of Kalman filtering to track and vertex fitting*, Nucl. Instrum. Meth. A **262** (1987) 444, DOI: 10.1016/0168-9002(87)90887-4 (cit. on p. 35).

[87] *Track Reconstruction Performance of the ATLAS Inner Detector at $\sqrt{s} = 13$ TeV*, tech. rep., All figures including auxiliary figures are available at https://atlas.web.cern.ch/Atlas/GROUPS/PHYSICS/PUBNOTES/ATL-PHYS-PUB-2015-018: CERN, 2015, URL: https://cds.cern.ch/record/2037683 (cit. on p. 36).

[88] F. Meloni, *Primary vertex reconstruction with the ATLAS detector*, JINST **11** (2016), ed. by C. Gemme and L. Rossi C12060, DOI: 10.1088/1748-0221/11/12/C12060 (cit. on p. 36).

[89] *Development of ATLAS Primary Vertex Reconstruction for LHC Run 3* (2019) (cit. on p. 36).

[90] R. Fruhwirth, W. Waltenberger, and P. Vanlaer, *Adaptive vertex fitting*, J. Phys. G **34** (2007) N343, DOI: 10.1088/0954-3899/34/12/N01 (cit. on p. 37).

[91] G. Aad et al., *Muon reconstruction performance of the ATLAS detector in protonproton collision data at $\sqrt{s}$ =13 TeV*, Eur. Phys. J. C **76** (2016) 292, DOI: 10.1140/epjc/s10052-016-4120-y, arXiv: 1603.05598 [hep-ex] (cit. on p. 38).

[92] M. Aaboud et al., "Momentum resolution improvements with the inclusion of the Alignment Errors On Track", 2018, URL: https://atlas.web.cern.ch/Atlas/GROUPS/PHYSICS/PLOTS/MUON-2018-003/index.html (cit. on p. 39).

[93] G. Aad et al., *Muon reconstruction and identification efficiency in ATLAS using the full Run 2 pp collision data set at $\sqrt{s} = 13$ TeV*, Eur. Phys. J. C **81** (2021) 578, DOI: 10.1140/epjc/s10052-021-09233-2, arXiv: 2012.00578 [hep-ex] (cit. on pp. 38, 39).

[94] W. Lampl et al., *Calorimeter clustering algorithms: Description and performance* (2008) (cit. on p. 40).

[95] M. Aaboud et al., *Electron reconstruction and identification in the ATLAS experiment using the 2015 and 2016 LHC proton-proton collision data at $\sqrt{s} = 13$ TeV*, Eur. Phys. J. C **79** (2019) 639, DOI: 10.1140/epjc/s10052-019-7140-6, arXiv: 1902.04655 [physics.ins-det] (cit. on p. 40).

[96] M. Aaboud et al., *Measurement of the photon identification efficiencies with the ATLAS detector using LHC Run 2 data collected in 2015 and 2016*, Eur. Phys. J. C **79** (2019) 205, DOI: 10.1140/epjc/s10052-019-6650-6, arXiv: 1810.05087 [hep-ex] (cit. on p. 40).

[97] M. Aaboud et al., *Measurement of the photon identification efficiencies with the ATLAS detector using LHC Run-1 data*, Eur. Phys. J. C **76** (2016) 666, DOI: 10.1140/epjc/s10052-016-4507-9, arXiv: 1606.01813 [hep-ex] (cit. on p. 40).

[98] G. Aad et al., *Electron and photon performance measurements with the ATLAS detector using the 20152017 LHC proton-proton collision data*, JINST **14** (2019) P12006, DOI: 10.1088/1748-0221/14/12/P12006, arXiv: 1908.00005 [hep-ex] (cit. on pp. 40, 41).

[99] S. Schramm, *ATLAS Jet Reconstruction, Calibration, and Tagging of Lorentz-boosted Objects*, EPJ Web Conf. **182** (2018), ed. by Y. Aharonov, L. Bravina, and S. Kabana 02113, DOI: 10.1051/epjconf/201818202113 (cit. on p. 42).

[100] G. Aad et al., *Topological cell clustering in the ATLAS calorimeters and its performance in LHC Run 1*, Eur. Phys. J. C **77** (2017) 490, DOI: 10.1140/epjc/s10052-017-5004-5, arXiv: 1603.02934 [hep-ex] (cit. on p. 42).

[101] M. Cacciari, G. P. Salam, and G. Soyez, *The anti-k_t jet clustering algorithm*, JHEP **04** (2008) 063, DOI: 10.1088/1126-6708/2008/04/063, arXiv: 0802.1189 [hep-ph] (cit. on p. 42).

[102] G. Aad et al., *ATLAS b-jet identification performance and efficiency measurement with $t\bar{t}$ events in pp collisions at $\sqrt{s} = 13$ TeV*, Eur. Phys. J. C **79** (2019) 970, DOI: 10.1140/epjc/s10052-019-7450-8, arXiv: 1907.05120 [hep-ex] (cit. on pp. 42, 43).

[103] T. Barillari et al., *Local hadronic calibration* (2009) (cit. on p. 43).

[104] *Measurement of the tau lepton reconstruction and identification performance in the ATLAS experiment using pp collisions at $\sqrt{s} = 13$ TeV* (2017) (cit. on p. 43).

[105] *Reconstruction, Identification, and Calibration of hadronically decaying tau leptons with the ATLAS detector for the LHC Run 3 and reprocessed Run 2 data* (2022) (cit. on p. 44).

[106] G. Aad et al., *Performance of Missing Transverse Momentum Reconstruction in Proton-Proton Collisions at 7 TeV with ATLAS*, Eur. Phys. J. C **72** (2012) 1844, DOI: 10.1140/epjc/s10052-011-1844-6, arXiv: 1108.5602 [hep-ex] (cit. on p. 44).

[107] M. Aaboud et al., *Performance of missing transverse momentum reconstruction with the ATLAS detector using proton-proton collisions at $\sqrt{s} = 13$ TeV*, Eur. Phys. J. C **78** (2018) 903, DOI: 10.1140/epjc/s10052-018-6288-9, arXiv: 1802.08168 [hep-ex] (cit. on p. 45).

[108] C. R. Schmidt, *QCD phenomenology of charm production at HERA*, AIP Conf. Proc. **407** (1997), ed. by J. Repond and D. Krakauer 381, DOI: 10.1063/1.53608, arXiv: hep-ph/9706496 (cit. on p. 48).

[109] ATLAS Collaboration, *The ATLAS Experiment at the CERN Large Hadron Collider*, JINST **3** (2008) S08003, DOI: 10.1088/1748-0221/3/08/S08003 (cit. on p. 49).

[110] ATLAS Collaboration, *Measurement of $D^{*\pm}$, $D^{\pm}$ and $D_s^{\pm}$ meson production cross sections in pp collisions at $\sqrt{s} = 7$ TeV with the ATLAS detector*, Nucl. Phys. B **907** (2016) 717, DOI: 10.1016/j.nuclphysb.2016.04.032, arXiv: 1512.02913 [hep-ex] (cit. on p. 49).

[111] CMS Collaboration, *Measurement of prompt open-charm production cross sections in proton–proton collisions at $\sqrt{s} = 13$ TeV*, JHEP **11** (2021) 225, DOI: 10.1007/JHEP11(2021)225, arXiv: 2107.01476 [hep-ex] (cit. on p. 49).

[112] ALICE Collaboration, *Measurement of the non-prompt D-meson fraction as a function of multiplicity in proton−proton collisions at $\sqrt{s} = 13$ TeV* (2023), arXiv: 2302.07783 [nucl-ex] (cit. on p. 49).

[113] T. Sjöstrand, S. Mrenna, and P. Z. Skands, *A brief introduction to PYTHIA 8.1*, Comput. Phys. Commun. **178** (2008) 852, DOI: 10.1016/j.cpc.2008.01.036, arXiv: 0710.3820 [hep-ph] (cit. on p. 50).

[114] R. D. Ball et al., *Parton distributions for the LHC Run II*, JHEP **04** (2015) 040, DOI: 10.1007/JHEP04(2015)040, arXiv: 1410.8849 [hep-ph] (cit. on p. 50).

[115] ATLAS Collaboration, *ATLAS Pythia 8 tunes to 7 TeV data*, ATL-PHYS-PUB-2014-021, 2014, URL: https://cds.cern.ch/record/1966419 (cit. on p. 50).

[116] ATLAS Collaboration, *The ATLAS Simulation Infrastructure*, Eur. Phys. J. C **70** (2010) 823, DOI: 10.1140/epjc/s10052-010-1429-9, arXiv: 1005.4568 [physics.ins-det] (cit. on p. 50).

[117] S. Agostinelli et al., *GEANT4—a simulation toolkit*, Nucl. Instrum. Meth. A **506** (2003) 250, DOI: 10.1016/S0168-9002(03)01368-8 (cit. on p. 50).

[118] ATLAS Collaboration, *Studies of the muon momentum calibration and performance of the ATLAS detector with pp collisions at* $\sqrt{s} = 13$ *TeV* (2022), arXiv: 2212.07338 [hep-ex] (cit. on pp. 54, 55).

[119] ATLAS Collaboration, *Early Inner Detector Tracking Performance in the 2015 Data at* $\sqrt{s} = 13$ *TeV*, ATL-PHYS-PUB-2015-051, 2015, URL: https://cds.cern.ch/record/2110140 (cit. on p. 55).

[120] W. Verkerke and D. Kirkby, *The RooFit toolkit for data modeling*, 2003, arXiv: physics/0306116 [physics.data-an] (cit. on pp. 68, 72).

[121] R. L. Workman et al., *Review of Particle Physics*, PTEP **2022** (2022) 083C01, DOI: 10.1093/ptep/ptac097 (cit. on pp. 70, 85, 107).

[122] ATLAS Collaboration, *Luminosity determination in pp collisions at* $\sqrt{s} = 13$ *TeV using the ATLAS detector at the LHC* (2022), arXiv: 2212.09379 [hep-ex] (cit. on p. 92).

[123] ATLAS Collaboration, *The new LUCID-2 detector for luminosity measurement and monitoring in ATLAS*, JINST **13** (2018) P07017, DOI: 10.1088/1748-0221/13/07/P07017 (cit. on p. 92).

[124] L. Gladilin, *Fragmentation fractions of c and b quarks into charmed hadrons at LEP*, Eur. Phys. J. C **75** (2015) 19, DOI: 10.1140/epjc/s10052-014-3250-3, arXiv: 1404.3888 [hep-ex] (cit. on p. 100).

[125] M. Benzke et al., *Prompt neutrinos from atmospheric charm in the general-mass variable-flavor-number scheme*, Journal of High Energy Physics **2017** (2017) 21, DOI: 10.1007/JHEP12(2017)021 (cit. on p. 100).

[126] G. Aad et al., *Probing lepton flavour violation via neutrinoless* $\tau \longrightarrow 3\mu$ *decays with the ATLAS detector*, Eur. Phys. J. C **76** (2016) 232, DOI: 10.1140/epjc/s10052-016-4041-9, arXiv: 1601.03567 [hep-ex] (cit. on p. 111).

[127] M. Bedognetti, "Pushing the Limits - A search for the Lepton Flavour Violating decay $\tau \to 3\mu$ within Heavy Flavour Jets with the ATLAS Detector", PhD thesis: University of Radboud, 2020, URL: https://www.nikhef.nl/pub/services/biblio/theses_pdf/thesis_M_Bedognetti.pdf (cit. on pp. 111–115).

[128] ATLAS Collaboration, *Prospects for lepton flavour violation measurements in $\tau \to 3\mu$ decays with the ATLAS detector at the HL-LHC*, ATL-PHYS-PUB-2018-032, 2018, URL: https://cds.cern.ch/record/2647956 (cit. on pp. 113, 114).

[129] L. Heinrich, M. Feickert, and G. Stark, *pyhf: v0.7.6*, version 0.7.6, https://github.com/scikit-hep/pyhf/releases/tag/v0.7.6, DOI: 10.5281/zenodo.1169739, URL: https://doi.org/10.5281/zenodo.1169739 (cit. on p. 115).

[130] L. Heinrich, M. Feickert, G. Stark, and K. Cranmer, *pyhf: pure-Python implementation of HistFactory statistical models*, Journal of Open Source Software **6** (2021) 2823, DOI: 10.21105/joss.02823 (cit. on p. 115).

[131] A. Collaboration, *Athena: The ATLAS Software Framework*, ATL-SOFT-PUB-2020-001, 2020, URL: https://cds.cern.ch/record/2712577 (cit. on p. 135).

Acknowledgements

Completing a PhD is a long and challenging journey that marks a significant milestone in my life. It is a time to reflect on and acknowledge the people who have supported me along the way. I would like to take this opportunity to thank everyone who has helped me during my PhD.

Firstly, I would like to extend my deepest gratitude to my promotor, Nicolo. I am truly grateful for the opportunity to work with you. During times when I felt lost, you always helped me identify what was most important. Beyond physics topics, you have also given me invaluable career advice, which I will always remember. I greatly appreciate your patience and guidance over the past years.

My sincerest thanks go to my co-promotor, Peter. I recall the tremendous effort you put into guiding and conversing with me during the COVID-19 lockdown. During those times, you were one of the few people I talked to regularly. Thank you for your help and support throughout my PhD.

I must also thank my past supervisor, Olga. It was very kind of you to offer me a PhD position, allowing me to begin this journey. I still remember our discussions at Nikhef and CERN; talking to you was always inspiring and encouraging. It was a shock that you left us so early, but I will never forget your enthusiasm and positivity.

I would like to give huge thanks to Marcus, who daily supervised me during the first two years of my PhD. You patiently answered all my questions, no matter how trivial, and helped me understand the technical details in our field. It was truly a pleasure to work closely with you and learn directly from you.

I am also grateful to the members of my thesis committee for your valuable feedback and support, which helped to improve my work. Your kind words have encouraged me to continue my research, and I will pass this encouragement on to the students and colleagues I work with.

I would like to thank my fellow PhD students and staff members at Nikhef. I enjoyed our coffee breaks, lunches, and various events together. Matteo, thank you for your support since I joined the team. We had many conversations; you taught me a lot, and invited me to numerous parties and dinners. I always enjoy hearing from you; you have been like a big brother to me. Terry, thank you for all your help since the time I first visited CERN. You have always been helpful all these years. Thank you, Pepijn, for being my officemate; we had some nice chats. Alice, thank you for sharing the office with me and for the pleasant conversations. I started to enjoy a bit more sunlight after spending years

in the Netherlands; I wonder what you would think about that. Kawa, thank you for spending so much time with me during the lockdown. I always enjoy listening to your interesting and entertaining stories.

Thank you to my flatmates, Youjia and Miao, for sharing the apartment with me. You have made my life in the Netherlands more enjoyable. I appreciate all the fun times we had together.

There are many more people I met and worked with during my PhD. I would like to thank all of you for your support and encouragement. I would also like to thank my friends and my family, who have always been there for me, even though they are far away. I am grateful for having all of you in my life.

Thanks again to you, who are reading this. I appreciate your time and interest in my work. Best wishes to you all.